A statistical approach to the analysis of surface pressure measurements on a pitching delta wing

by

Martyn Leonard Edward Jupp

A dissertation submitted to the Faculty of Engineering, at the University of Glasgow in fulfilment of the requirements for the degree of

Doctor of Philosophy

The research was carried out in the Department of Aerospace Engineering University of Glasgow

December 1999

Martyn Jupp

SUMMARY

Detailed experiments have been carried out on a 60° delta wing with sharp leading-edges. The instantaneous pressure distribution on one half of the leeward surface of the wing has been measured over a range of incidence using a large number of closely spaced pressure transducers coupled to an advanced data acquisition system capable of sampling at a high rate. The advantages of high spatial and temporal resolution pressure measurements lie in the ability to obtain high quality statistical data of the pressure fluctuations over the whole surface of the wing. This data has been used in a detailed statistical analysis involving the calculation of mean/instantaneous pressure, RMS pressure and signal power distributions, as well as frequency spectra of pressure fluctuations and the cross-correlation function of two pressure signals.

A number of observations have been made regarding the mean/instantaneous pressure, RMS pressure and signal power distributions, the power spectra of the pressure fluctuations and the cross-correlation spectra which have been supported by the results from smoke visualisation tests. In the static, pitch up and pitch down cases, the position and general condition of the leading-edge vortex are indicated by a localised ridge of high suction emanating from the apex of the wing extending towards the trailing-edge. Similarly, the rate of vorticity production, axial pressure gradient and the initial axial velocity of the flow, together with the wing incidence, determine the condition of the vortex flow at a given chord position. For the static and pitch up cases, it is suggested that a 'primary' region of high RMS pressure located inboard of the vortex core is indicative of the attachment region of the primary vortex. Similarly, a 'secondary' region of high RMS pressure located outboard of the primary vortex core is indicative of the separation region of the secondary vortex structure. The deceleration and

eventual stagnation of the axial velocity within the vortex core, which acts as a pre-cursor to vortex breakdown, is indicated by a 'waisting' of the contours in the region of high RMS pressure inboard of the vortex core. Similarly, the onset of the fully broken down state is indicated by an expansion of the same RMS pressure contours immediately downstream of the waist and is accompanied by a characteristic change in the frequency signature of the pressure fluctuations. In the pitch down cases, it is submitted that the change from bluff-body behaviour at high angles of incidence to the restoration of the primary vortex core at the apex of the wing is indicated by the outboard movement of a region of high RMS pressure situated along the wing centreline and its subsequent recession from the wing apex. Again, this change is accompanied by a characteristic change in the frequency signature of the pressure fluctuations. Following vortex restoration, two regions of high RMS pressure become apparent, suggesting that the 'primary' region of high RMS pressure located inboard of the vortex core is again indicative of the attachment region of the primary vortex and the secondary region of high RMS pressure located outboard of the primary vortex core is again indicative of the separation region of the secondary vortex structure.

The results of a frequency analysis show for static, pitch up and pitch down cases, that the excitation frequency of pressure fluctuations is not only dependent on chordwise vortex breakdown position, but also strongly dependent on the post-breakdown growth of the vortex in a streamwise direction, and therefore, dependent on the downstream measurement point distance. At a given chord position, the frequency of pressure fluctuations has been shown to be higher during pitch up and pitch down motions compared with the static case. It is suggested for each motion type, that these characteristics are probably caused by different phenomena outside of changes in vortex condition.

DEDICATION

This work is dedicated to the memory of my parents Len and Ivy. They gave me so much during my formative years and since, but above all, they endowed me with the confidence to believe that this might be possible and the determination to make it so. For these, I will be eternally grateful.

ACKNOWLEDGEMENTS

The wind tunnel tests reported in this study were carried out with funding from the Engineering and Physical Sciences Research Council (EPSRC), GKN Westland Helicopters Ltd., the Defence Evaluation & Research Agency (DERA) and Glasgow University under contract GR/H48330. I would like to acknowledge the additional support of the EPSRC through RS Quota award 96300150 and the support provided for the flow visualisation activities by the Nuffield Foundation.

A huge vote of thanks go to my supervisors, Frank and Richard. Their knowledge, experience, common sense, patience and good humour have all played an equal part in making this project a success. I am also indebted to Prof. R. Galbraith for his continual support and encouragement. Thanks also go to Tom, for his valued friendship and beer during my time in a foreign land. To Garry, and Maxine for fun, philosophy, more friendship and more beer. To Sharon, Chris, Neil, Aileen, Xabier, Dave and Theresa - TFI Friday ! To Mark (Mr O.), Matt, Karen, Hannah, Nicky, Flo and Andy C. (Dave), for care and refuge from all of this madness when I've most needed it. To Dot & Fred and Hilary for picking up the phone once in a while. You are **all** the best.

TABLE OF CONTENTS

...Continued

...Continued

LIST OF FIGURES

...Continued

...Continued

...Continued

...Continued

...Continued

...Continued

...Continued

...Continued

NOMENCLATURE

SYMBOLS

c	root chord, (m).
C_L	lift coefficient.
$C_{L,p}$	potential lift coefficient.
$C_{L,v}$	vortex lift coefficient.
C_M	pitching moment coefficient.
C_N	normal force coefficient.
C_P	pressure coefficient.
C_l	rolling moment coefficient.
C_{Sp}	potential lift leading-edge suction coefficient.
E	signal energy magnitude.
f	frequency, (Hz).
f	relating to the frequency domain.
f_s	sampling frequency, (Hz).
g	Sychev parameter, $r/U_\infty .c.\tan^2\varepsilon.\cos\alpha$
H	total head, (Pa).
k	reduced pitch rate, $c(\partial\alpha/\partial t)/2U_\infty$.
K	reduced oscillation frequency, $2\pi fc/U_\infty$.
K_p	potential lift constant.
K_v	vortex lift constant.
n	non-dimensional frequency parameter, $(fc/U)\sin\alpha$.

Continued...

n_m	modified non-dimensional frequency parameter, (fc.Cot Λ/U) sin α .
p	pressure, (Pa).
q	swirl parameter, (Γ_∞/2π.δ.δw).
r	cylindrical polar co-ordinate/equivalent vortex radius (m).
r*	radial distance from the vortex centreline, (m).
Re	Reynolds number based on root chord.
Ro	Rossby number, W/r* Ω.
R_{mr}	vortex energy ratio, ($\int_0^r V_x^2$ rdr /$\int_0^r V_\theta^2$ rdr).
s	local semi-span, (m).
t	time, (s).
t	relating to the time domain.
u	radial velocity component.
U_∞	mean freestream velocity, (ms^{-1}).
v	swirl velocity component.
w	axial velocity component.
W	axial velocity, (ms^{-1}).
x	chordwise distance from apex, (m).
x/c	non-dimensional chord position.
y	spanwise distance from wing centreline. (m)
y/s	non-dimensional span position.
z	distance normal to the plane of the wing surface, (m).
z/s	non-dimensional vertical height.
z	cylindrical polar co-ordinate.

Continued...

$2s$	local span, (m).
α	model incidence, (°).
α_0	swirl ratio of velocity, V_θ/V_w.
α_v	helix angle of velocity, (°).
β	degree of sideslip, (°).
β_0	swirl ratio of vorticity, ζ_θ/ζ_w
δ	vortex core radius (m).
δw	axial velocity scale in a q-vortex
χ	axial co-ordinate.
ε	apex half-angle, (°).
ϕ	swirl angle, (°).
Γ_∞	vortex circulation.
ζ	component of vorticity.
γ	complex phase velocity.
κ	axial wave number.
Λ	wing sweep angle, (°).
θ	azimuthal co-ordinate.
ρ	fluid density, (kgm^{-3}).
Ω	angular velocity of the inner vortex core, ($rads^{-1}$).
υ	viscosity, (Nsm^{-2}).
τ_0	α_0/β_0.
ψ	stream function.

Continued...

ABBREVIATIONS

AR	Aspect Ratio.
CCF	Cross-Correlation Function.
D*A	Digital to Analogue.
DAT	Digital Audio Tape.
FIR	Finite Impulse Response.
LDA	Laser-Doppler Anemometry.
LDV	Laser-Doppler Velocimetry.
PC	Personal Computer.
PIV	Particle Image Velocimetry.
PSD	Power Spectral Density.
RIB	Run Information Block.
RMS	Root-Mean-Square.

SUBSCRIPTS

bd	location of vortex breakdown.
BD-TE	vortex breakdown reaches the trailing-edge.
eff	effective.
max	maximum value.
m	modified.
s	scale (i.e. parameter used for non-dimensionalisation purposes)
te	trailing-edge.
w	axial.
θ	azimuthal.

Chapter 1

1. INTRODUCTION

1.1 WHY STUDY DELTA WINGS?

The development of the jet engine in the 1930's, with its potential for higher flying speeds, was the catalyst for prolific levels of research into high-speed flight during the 1940's and beyond. The pace of research progress was brisk, the apparent urgency fuelled by tension between East and West at the beginning of the Cold War. As a result, 1947 saw the Bell X-1 leap off the drawing board, through the sound barrier and into the record books after just three years of development. The flights of the Bell X-1 proved that aircraft could fly safely in the then unknown aerodynamic region around Mach 1, in spite of the lack of theory and experimental data concerning aerodynamic characteristics in the transonic region. Prior to the flights of the Bell X-1, knowledge had been gained through aircraft exceeding design airspeed limitations when put, either deliberately or accidentally, into a steep dive. The end result often had fatal consequences. On approaching the sound barrier, the effects of compressibility led to a loss of lift over the wings and a loss of elevator control as a critical Mach Number was reached. To make matters worse, the loss of lift and the resulting reduced downwash angle of the flow behind the wings, tended to increase the effective angle of attack at which the flow met the horizontal tail. The lift generated by the tail would therefore increase, pulling the aircraft into a steeper dive that the pilot was then unable to control.

The idea of using swept wings to counteract the problems of compressibility was first introduced in a paper by Adolf Busemann at the 1935 Volta Conference (Anderson (1997)). Busemann's ideas failed to impress the visiting American delegates led by Theodore von Kármán, but led to an exhaustive research programme in Germany which produced a mass of technical data by the end of the Second World War. Busemann's paper was based on the idea that the aerodynamic characteristics of a wing are mainly governed by the component of the flow velocity perpendicular to the leading-edge. As the angle of wing sweep (Λ) is increased, the component of velocity perpendicular to the leading-edge will decrease and the onset of compressibility effects on the wing will be delayed. After the end of the Second World War, American researchers were able to study the German data and were keen to apply the newly gained knowledge to their own designs. On 1st October 1947, two weeks before the record breaking flight of the Bell X-1, the North American XP-86, later to become the highly successful F-86 'Sabre', made its first flight. Less than a year later, the same aircraft was placed into a shallow dive and went supersonic. This was the first time that an aircraft designed for combat had exceeded the speed of sound (Anderson (ibid.)).

The progression from the simple swept wing to the delta wing design was not long in coming. The Convair XF-92A (a fore-runner of the F-102 Delta Dagger) first flew in 1948, and the British-designed Avro 707 took to the skies in 1949. The Avro 707 was a scale-model of the proposed Avro 698, which later became the highly successful 'Vulcan' strategic bomber. The advantages of the delta wing design are numerous (Friemer (1996)). A combined aerodynamic and structural benefit is given by the long root chord which provides absolute wing thickness together with a high fineness ratio required for low wave drag at supersonic speeds. This allows a lighter but stronger wing structure with high volumetric efficiency maximising the internal fuel and store carrying capacity. The delta

planform is not however, without its disadvantages. Aircraft designs using this configuration tend to exhibit aerodynamic instability about the pitch axis under stall conditions at all subsonic speeds (Friemer (1996)). Similarly, at low speed and high angles of incidence in pre-stall conditions, manoeuvres employing a roll/yaw content or externally applied lateral aerodynamic forces can lead to self-induced, unstable oscillations about the roll axis which are often coupled with a lateral yawing motion (Jobe (1996)). This non-linear and discontinuous rolling moment characteristic, or so-called 'wing rock' phenomenon, is prevalent in aircraft with particularly slender delta wings, i.e. with an aspect ratio (AR) less than unity. In the 1950's and 1960's, the problems posed by such undesirable characteristics and the complex nature of stability augmentation and control devices required to overcome them, shifted popular thinking in terms of aircraft design, away from the delta planform and towards simpler swept wing designs. There have been a few notable exceptions including the Anglo/French Concorde high speed transport, and the Dassault Mirage and General Dynamics F-16 fighters. Each aircraft has been highly successful and each is still in service today 30 years on, their longevity a testament to the effort put into, and perhaps the extravagant cost of, the research and design process.

The growing sophistication of onboard computers for control and stability augmentation, and significant advances in propulsion and materials technology, has greatly expanded the potential manoeuvring envelope of current and future combat aircraft. These advances, coupled with the development in recent years of short-range, all-aspect capability air-to-air missiles and sophisticated medium-range, radar-guided weapons, have led to significant changes in two areas of fighter combat strategy. Short-range combat, previously limited to forward-firing weapons only, was characterised by two or more engaged aircraft making a series of sustained turns to gain the upper hand. Convergence to a firing position was dependent on achieving a better turn-rate than the opponent. Combat

effectiveness was, therefore, very sensitive to thrust/weight ratio and wing loading. Herbst (1983) has shown, via results obtained in extensive computer combat modelling, manned combat simulation and flight testing, that the most combat-effective pre-launch manoeuvring tactic, using modern all-aspect short-range weapons, is provided by a head-on firing position. The attainment of this position is crucially dependent on superior instantaneous manoeuvre capability, rather than sustained performance. Similarly, medium-range combat has moved on from semi-active guided missiles and the use of stand-off tactics. Herbst was able to show, via air combat modelling using the latest generation radar-guided medium-range missiles, that aircraft would now have to perform very rapid dynamic manoeuvres in order to achieve a firing position, (in terms of relative aspect, speed and altitude), which provided a target hit with the minimum counter-hit probability. The change in short-range combat characteristics toward unsteady manoeuvre performance in the low subsonic regime and the need for supersonic manoeuvrability in medium-range combat are contradictory design requirements. This presents a significant design problem if both mission types are to be performed by the same aircraft. In finding a solution to this problem, designers of current and future combat aircraft have turned again to the delta wing planform. The Eurofighter 2000 programme and the Future Offensive Aircraft (FOA) are examples of the genre that have brought the delta wing to the forefront. The renewed interest in delta wings from a design point of view has done a great deal to rekindle research interest in this area.

1.2 THE DELTA WING FLOW-FIELD

Aircraft utilising delta wings can be designed for effective high-speed performance such that they are able to generate lift in the conventional sense, that is, using camber, twist or small angles of incidence. However, at higher angles of

incidence, vortices are formed above the leeward surface of the wing and additional lift can be generated because the highest velocities of the flow, at the periphery of the vortex sub-core, can be as much as three times that of the freestream. The associated low pressures generated by this increased flow velocity increasingly dominate the total lift curve of the wing as the incidence is increased to high values. The vast majority of experimental research into delta wing vortex flows uses a model wing planform having an isosceles triangle shape without an associated fuselage, i.e. the model has a single apex, two leading-edges and a single trailing-edge. The terminology used in the following explanation assumes such a model.

1.2.1 *The static flowfield*

The dominant features of delta wing flows at high incidences are a pair of vortical structures known as the primary vortices. Their centrelines extend from the wing apex, along a ray located somewhere inboard of each leading-edge and into the wake beyond the trailing-edge of the wing. These primary vortices are formed when the attached approach flow on the windward surface of the wing turns outboard and heads towards either leading-edge. Unable to negotiate the sharp leading-edge turn, the flow separates from the wing surface and forms a free shear layer or vortex sheet. The combined influence of the bound vorticity in the shear layer and a spanwise pressure gradient, (which, on the leeward surface is positive towards the wing centreline), results in the shear layer moving around the leading edge and inboard over the top surface of the wing, rolling up in a spiral fashion to form the two vortex cores. The leading-edge vortex can be divided into three regions: 1) The shear layer, which feeds vorticity into the vortex along the entire leading-edge of the wing, tends to grow in thickness with increasing distance from the leading-edge. 2) The rotational core, which is approximately 30% of the local semi-span in diameter, contains vorticity that is assumed to be distributed continuously. Vorticity is transported downstream along the rotational core and is

shed from the trailing-edge enabling the vortex to remain stationary above the wing surface. 3) The viscous sub-core, which has a diameter approximately 5% of the local semi-span and rotates as a solid body. It is defined as a region in which the gradients of local head, static pressure and velocity are very high. The roll up of the shear layer and the vortex regions are shown in Figure 1.1.

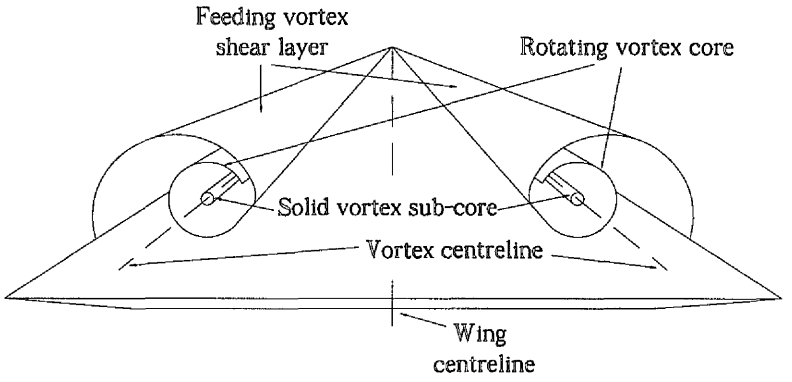

Figure 1.1 - Roll up of shear layers & principle vortex regions.

Lambourne & Bryer (1961) showed that for a static wing, the location and height above the wing of each vortex centreline is chiefly dependent on angle of incidence, sweep angle and leading-edge profile. The creation of the primary vortices causes the attached boundary layer on the leeward surface underneath each structure to turn outboard towards the leading-edge. This outflow meets a spanwise pressure gradient, which is adverse in the direction of the leading-edge, causing the flow to separate into a secondary shear layer. This, in turn, rolls up into a secondary vortex structure rotating in opposition to its primary parent. The principle flowfield and topological surface features are shown in Figure 1.2.

The main effect of the secondary vortex is to displace the primary vortex upwards and inwards. The effect is greater if the boundary layer is laminar, i.e., separation occurs earlier, thereby increasing the size of the secondary vortex structure.

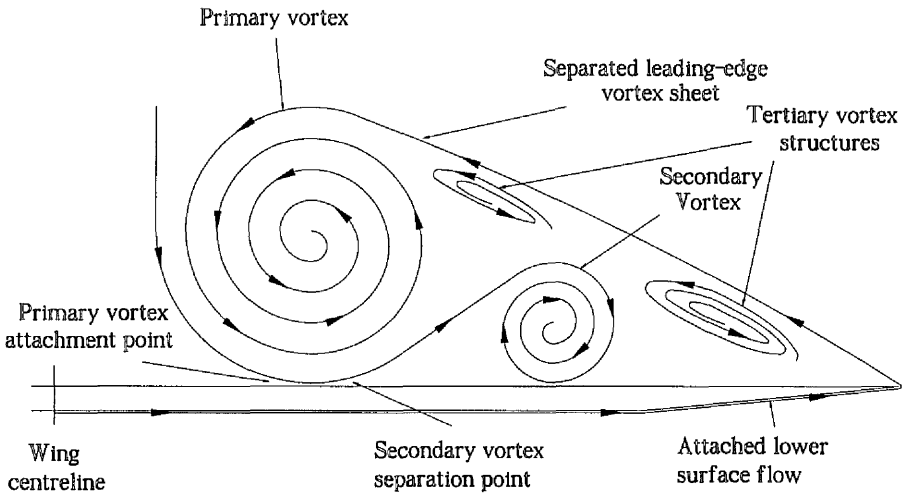

Figure 1.2 - Topological features of the vortex flowfield.

The generated primary vortices tend to grow in strength as the wing incidence is increased further and allows the generation of useable lift to continue at angles of incidence beyond the recognised stall condition of conventional wings. In cases with highly swept wings (AR < 1.0), an increase in vortex lift with an increase in incidence can be non-linear. The dominance of the theoretical total lift curve by the vortex lift component is illustrated in Figure 1.3 (taken from Polhamus (1971)). The increased benefits of vortex lift are not, however, inexhaustible. At some value of incidence and at some position along the vortex core, a transformation takes place causing the axial velocity of the flow to stagnate and the vortex to dissipate into large scale turbulence. This phenomenon is known as 'vortex breakdown' or 'vortex bursting'. With a subsequent increase in incidence,

the vortex breakdown stagnation point progresses upstream towards the apex of the wing heralding a decrease in vortex lift followed by the onset of stall.

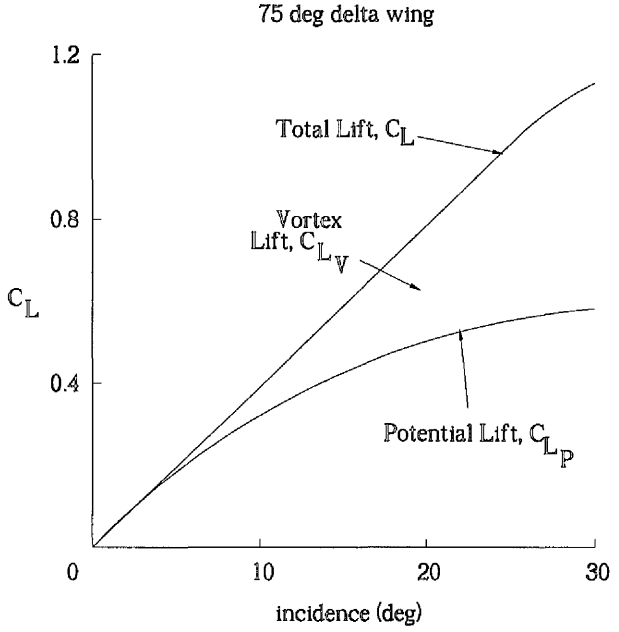

Figure 1.3 - Diagram showing the influence of vortex lift on the total lift curve (from Polhamus (1971))

1.2.2 *Slender wing rock*

Dynamic manoeuvres about the roll axis or lateral excitation forces at low speeds and high incidences have long been known to generate highly non-linear aerodynamic effects on delta wings. The upward motion of one half of the delta wing leads to a convective time lag in the corresponding motion of the leading-edge vortex. This in turn causes a momentary reduction in the height above the wing surface of the rising vortex. It has been shown by Levin & Katz (1984) that such a movement of the leading-edge vortex towards the wing surface will generate an increase in suction. At the same time, the downward moving leading-

edge finds its vortex momentarily lifting away and detaching from the wing surface causing a corresponding decrease in suction. An illustration of this effect is shown in Figure 1.4. The combination of the two effects generates an unstable dynamic rolling moment that can, in certain circumstances, overcome the in-built wing damping forces. The roll amplitude increases until it reaches its limit-cycle magnitude, where the destabilising effect is balanced by a restoring moment, itself induced by the lifted-off vortex re-attaching itself to the wing surface. This happens as a consequence of the increased roll angle, where the effective apex half-angle (ε_{eff}) on the falling half of the wing increases, causing the lifted-off vortex to attach again. This action produces the restoring rolling moment which provides the positive aerodynamic 'spring' needed for the rigid-body oscillation in roll to begin. At this point of balance a discontinuous change in vortex induced lift and associated rolling moment occurs as described by Ericsson (1990).

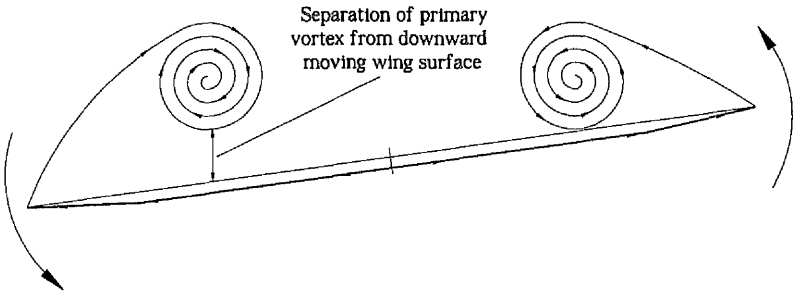

Figure 1.4 - An illustration of vortex separation caused by a rolling motion

It is clear that delta wings with sufficiently high in-built wing damping forces are not likely to suffer from 'wing-rock' problems. Indeed, it was shown by Levin & Katz (1984) using a free-to-roll experimental set-up, that self induced slender wing rock could not be induced in wings of AR > 1.0. Where it did occur, a considerable reduction in the value of the normal force coefficient (C_N) was

observed, when compared to the static case. For all wings where slender wing rock occurs, the effect of vortex breakdown, when it is induced by an increase in incidence, is to reduce the suction produced by the leading-edge vortices. This has been shown by Er-El *et al* (1989) to reduce the measured value of the rolling moment coefficient (C_l) when compared with the non-breakdown case. Hence, the presence of vortex breakdown will suppress wing rock motion.

1.2.3 *Sideslip*

The problems of induced wing rock are not confined to pure rolling manoeuvres. Under conditions of sideslip, each leading-edge of the wing experiences an change in effective sweep angle (Λ_{eff}). The edge leading into the flow will see a decrease in effective sweep angle, whereas the edge trailing-edge will see an increase in effective sweep angle. The effect of a decrease in Λ_{eff} will be to cause a stronger vortex with increased suction which is more susceptible to vortex breakdown. Similarly, an increase in Λ_{eff} will cause a weaker vortex with reduced suction and a delay in the onset of breakdown. Guglieri & Quagliotti (1997) showed the effect of increasing degrees of sideslip (β) on static normal force, pitching moment and rolling moment coefficients with respect to incidence. The effect of increasing sideslip on static normal force and pitching moment is to reduce, both the magnitude of C_N and C_M at a given incidence, and the magnitude of C_{Nmax} and C_{Mmax} prior to stall. It also reveals an increased negative static rolling moment at a given incidence. $-C_{Rmax}$ occurs at an incidence just prior to the arrival of vortex breakdown at the trailing-edge of the wing on the windward side. These levels of rolling moment may be great enough to induce wing rock on delta wings of very low aspect ratio (Ericsson (1984)). As breakdown progresses up the wing on the windward side, the rolling moment becomes less negative. At some point, the lift capability of the leeward vortex becomes greater than the windward vortex and the rolling moment becomes positive. C_{Rmax} occurs when the windward

vortex breakdown reaches the apex of the wing. The rolling moment remains positive until the leeward vortex breakdown also reaches the wing apex, after which it becomes negative again before stabilising.

1.2.4 *Pitching motions*

The type of motion employed in vortex behaviour studies on pitching delta wings may be divided into three generic classes: 1) plunging motions, 2) sinusoidal or harmonic motions and 3) ramp-type motions. All three classes of motion have important parts to play in the understanding of delta wing flows. For example, the consequences of rapid changes in incidence during plunging and small amplitude sinusoidal forcing are important in the understanding of stall and flutter stability, whereas ramp-type motions are more directly related to practical aircraft manoeuvres. It was suggested by Ashley *et al* (1991), that concerns about stall and flutter stability on the Concorde high-speed transport aircraft prompted some of the first unsteady investigations. Lambourne *et al* (1969) carried out water-tunnel dye-injection visualisation tests on three delta-shaped plates with leading-edge sweep angles of 60°, 70° and 80°. They observed the formation and growth of vortices during plunging tests at various plunge velocities. They reported a transient phase in vortex formation which saw a spanwise movement of the vortex core centreline from the leading-edge to a steady state position inboard. They concluded that the vortex flow over a delta wing following a sudden plunge can be regarded as reaching this steady-state condition in a time-scale of approximately one convective chord-length. Maltby *et al* (1963) carried out smoke visualisation tests on a 76° flat plate model in oscillatory motion. They observed a hysteretic phase lag of up to 60° in the height of the vortex core above the wing surface during the motion. Jarrah (1990) and Green (1998) showed for ramp-type pitch up cases that the flow is characterised by a spanwise shift of each vortex system outboard at a given incidence, when compared to the static case. Both

studies showed that the vortices tended to move further outboard with an increase in pitch rate. This is accompanied by an increasing delay in the growth of the main vortex core and a delay in the subsequent upstream progression of vortex breakdown, i.e. breakdown passes a given chordwise position at a higher incidence with increasing pitch rate. In the ramp-type pitch down case, the primary vortex is seen to begin its 'restoration' at the wing apex. The point of vortex core restoration moves progressively towards the wing trailing edge with a decrease in incidence. When compared with the static case, there is a delay in the progression of vortex core restoration, which tends to pass a given chordwise location at a lower incidence with an increase in pitch rate magnitude. Following the vortex restoration, Green (1998) showed that the location of the vortex centreline tended to shift inboard at a given incidence compared with the static case. Again, the effect is more marked with increasing pitch rate magnitude.

1.2.5 *Vortex breakdown*

The phenomenon of vortex breakdown is the major limiting factor in the aerodynamic performance of aircraft utilising delta wings. As a consequence, the wing will experience a gradual loss of suction peak pressure as breakdown progresses upstream, resulting in a reduction in lift and a reduction in the magnitude of the nose down pitching moment. The phenomenon and its effects has greatly interested researchers since it was apparently first observed by Peckham & Atkinson (1957) and defined by Lambourne & Bryer (1961). It can be characterised by a sudden increase in the vortex core diameter accompanied by a decrease in axial and circumferential velocity followed by large scale turbulent dissipation. It should be noted that the deceleration and expansion of the vortex core does take place over a finite length of the vortex axis and this has led to problems in the past in defining the vortex breakdown position. To get around this problem, McKernan *et al* (1988) assumed a chordwise breakdown region which extends to five or six times the vortex core diameter. Despite many years

of research into the phenomenon, a clear picture of its exact nature is still not yet available. However, a great deal of work has been carried out in many areas of experimental research, in theoretical methods and in computational studies, such that a great many pieces of the puzzle are in place. The following sections are designed to highlight the important aspects of this work and serves as an introduction to, and a justification of, the current study programme.

1.3 VORTEX BREAKDOWN - A SURVEY OF RESEARCH

1.3.1 *Experimental research*

During forty years of experimental research, a number of experimental programmes have analysed a wide range of flowfield characteristics in an effort to find the causes of vortex breakdown. These experiments can be grouped together under the following five general topic headings. 1) Diverging tube investigations on the nature of the physical phenomenon using visualisation and flowfield measurement techniques for a range of confined vortices under strictly controlled test conditions. 2) Visualisation of the response of vortex breakdown to changes in delta wing geometry and test conditions. 3) Investigations into the structure of the delta wing leading-edge vortex and the conditions that determine its breakdown through flowfield measurements. 4) Measurement of the unsteady forces and moments on delta wings using load data. 5) Studies of vortex breakdown on delta wings using surface pressure measurements.

1.3.1.1 *Visualisation and flowfield measurements - Diverging-tube experiments*

A great deal of experimental work has been carried out in diverging-tubes using water and dye visualisations and Laser-Doppler Anemometry (LDA) measurements. This is because it is considered that the essential parameters such as Reynolds Number, swirl magnitude and downstream pressure gradients are more easily controlled in a confined environment. It is not proposed to go into

great detail describing this work, however, it is important that two principle pieces of work and their findings are presented in the literature survey to enable comparisons to be made when regarding delta wing phenomena.

It was shown by Sarpkaya (1974) using LDA measurements, that the vortex breakdown position is sensitive to the pressure gradient along the core of the vortex, i.e. an increasingly adverse pressure gradient tended to precipitate breakdown. Similarly, it was also shown by visualisation that an increase in either inlet swirl angle or Reynolds number also tended to encourage the phenomenon and promote the upstream movement of the breakdown position after initiation. A later series of experiments were reported by Faler & Leibovich (1977) who, by varying the swirl angle and/or Reynolds number, were able to identify a total of six different classes of breakdown, the spiral or S-type and bubble or B-type being the most common with the other four types sharing the characteristics of these two. All types exhibit a sudden deceleration in axial velocity and a breakdown to turbulence, however it is the expansion of the vortex core that defines each type. S-type breakdown is an asymmetric spiralling of the vortex core which remains intact for a few turns of the spiral before breaking down into turbulence. The sense of the spiral winding is opposite to the direction of rotation of the upstream vortex, however, the direction of rotation of the fluid within the spiral winding is the same as the upstream vortex as shown in Figure 1.5. B-type breakdown, is characterised by a stagnation point on the vortex axis followed by an axisymmetric diffusion of the vortex core over a bubble-shaped region. The bubble is usually two to three upstream core diameters in length. The downstream end of the bubble is usually open and irregular, and into which the flow recirculates before either; immediately breaking down into turbulence, or reforming into a vortex core briefly before breaking down again in a spiral fashion (Figure 1.6).

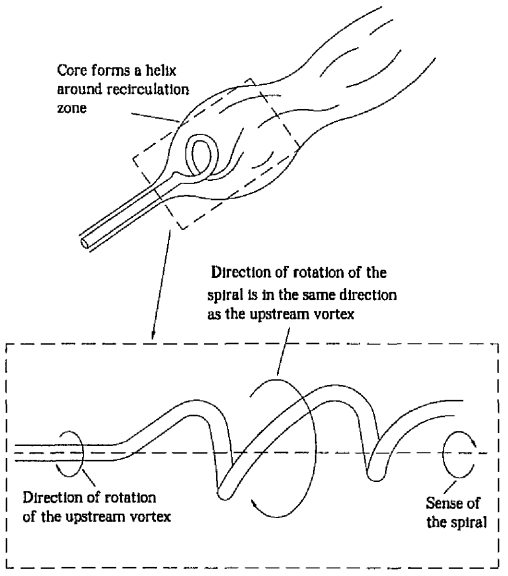

Figure 1.5 - Spiral or S-Type vortex breakdown.

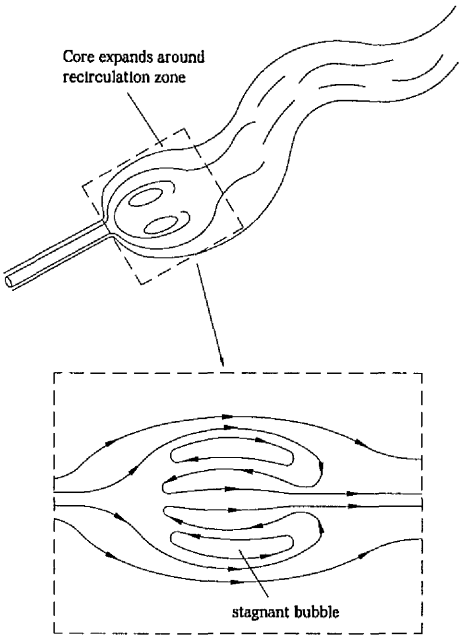

Figure 1.6 - Bubble or B-Type vortex breakdown.

1.3.1.2 *Visualisation - Delta wings*

The first observation of vortex breakdown on a delta wing was reported by Peckham & Atkinson (1957). Subsequent articles by Elle (1958) and Peckham (1958) independently showed that the position along the vortex at which breakdown occurs depends primarily on a combination of leading-edge sweep and angle of incidence. For a given delta wing at low angles of incidence, the breakdown occurs in the vortex some way downstream of the trailing-edge. With an increase in incidence or a decrease in sweep angle, the breakdown moves upstream until it reaches the trailing-edge of the wing. With a further increase in incidence or decrease in sweep angle, the breakdown point moves upstream towards the wing apex.

Lambourne & Bryer (1961) described experiments on a delta wing using both surface-oil and dye-injection visualisation together with relatively crude pressure measurements. As a result of these experiments, they defined vortex breakdown as (quote): "*A structural change at some position along a vortex from a strong regular spiral motion to a weaker turbulent motion.*" They noted that this change was characterised by a sudden deceleration of the flow along the vortex axis followed by an expansion of the vortex core and breakdown to large scale turbulence which resembles the wake behind a bluff body. Lambourne & Bryer observed only the two most common forms of breakdown seen in diverging tube experiments. They noted that the S-type breakdown was more commonly observed on static delta wings with the B-type appearing occasionally and then only briefly before taking up the spiral form. Other observers notably Parker (1977), have since reported only B-type breakdown on delta wings, whereas Johari & Moreira (1998) observed both types at various incidences and sweep angles with no specific trends apparent in the breakdown type observed.

From their experiments, Lambourne & Bryer (ibid.) were able to show one

particularly important feature of the delta wing vortex breakdown flowfield. They showed that for delta wings with sharp leading-edges, the position of vortex breakdown for a given sweep angle and angle of incidence is largely independent of Reynolds number in the range $1.0x10^4 \leq Re \leq 4.6x10^6$. Indeed, the later review by Erickson (1982) was able to extend the range to $9.8x10^3 \leq Re \leq 4.0x10^7$. The independence of vortex breakdown position with respect to Reynolds number for sharp-edged wings is true only because shear layer separation is fixed at the leading-edge. Erickson (ibid.) argued that boundary layer laminar/turbulent transition on wings with round leading-edges and flaps would still be sensitive to Reynolds number. Lee & Ho (1990) gathered results from a number of sources and showed that for sharp-edged wings the flow did indeed separate at the leading-edge producing high suction. On wings with elliptic or round leading-edges, separation occurred downstream of the leading-edge. The position of separation depended on the Reynolds number and the local curvature which determined the pressure gradient. Vortex formation was then delayed and the lift produced was significantly lower.

Gad-El-Hak & Ho (1985) and Gad-El-Hak & Blackwelder (1987) carried out oscillatory tests on delta wings with sweep angles of 45° and 60° at Reynolds numbers in the range $2.5x10^4$ to $3.5x10^5$. The tests were carried out using a mean incidence of 15°, with amplitudes of 5° to 15°, and reduced frequencies of $K = 0.05$ to 0.3. Each study identified a hysteretic phase lag in the formation of the primary vortex and its eventual breakdown. Atta & Rockwell (1990) carried out water channel experiments on three geometrically similar delta wings with a sweep angle of $\Lambda = 52°$, at Reynolds Numbers in the range 2900 to 13400. The wings of various sizes were oscillated in pitch at mean incidences of 10° and 20°, with an amplitude of 20°, over a range of reduced frequencies from $K = 0.025$ to 1.7. The dynamic hysteresis loops of vortex development and breakdown were

compared as functions of reduced frequency. At a reduced frequency of K = 0.025, the hysteresis loop was seen as a clockwise variation in the position of vortex breakdown with respect to incidence. The general trends and the direction of each hysteresis loop was maintained for higher values of K ranging from 0.05 to 0.13. For these reduced frequencies, the formation of the vortex core was identified on a downstream region of the wing during up-stroke motion moving upstream towards the wing apex with increasing incidence. Conversely, vortex breakdown was observed to move in a downstream direction on the down-stroke motion of the wing. At a higher value of reduced frequency, K = 0.28, the loop tended towards a figure of eight form. This was characterised by a gradual appearance of the vortex core on the upstroke with breakdown occurring in the usual fashion, but accompanied by a drastic shift in phase. At still higher values of reduced frequency, in the range K = 0.76 to 1.6, a dramatic change in the form of the hysteresis loop was seen, such that the sense of the loop was found to be in the opposite direction. This change was manifest as the onset of ejection of the vortex core from the apex region of the wing, followed by the abrupt onset of vortex breakdown. In addition to their observations of the primary vortex, Atta & Rockwell (1990) also focused their attention on the secondary vortex. They found that its development and breakdown were shifted in phase with respect to that of the primary vortex. A consistent trend was apparent in the data in that the secondary vortex system breakdown always preceded that of the primary. As a consequence, immediately prior to the onset of primary vortex breakdown, there exists a region of reverse flow between the leading-edge of the wing and the core of the primary vortex.

Wolffelt (1986), Jarrah (1990) and Green (1998) carried out ramp-type pitching tests on 60° and 76° delta wings at Reynolds numbers ranging from 1.0×10^4 to 1.1×10^6. For a series of pitch up cases, each observed an increasing delay in the

growth of the main vortex core and a delay in the subsequent upstream progression of vortex breakdown, i.e. breakdown passed a given chordwise position at a higher incidence with increasing pitch rate. In the pitch down cases, the primary vortex was seen to begin its 'restoration' at the wing apex. The point of vortex core restoration moved progressively towards the wing trailing edge with a decrease in incidence. When compared with the static case, there was a delay in the progression of vortex core restoration, which tended to pass a given chordwise location at a lower incidence with an increase in pitch rate magnitude. It was found that a reduced pitch rate magnitude as low as $k = 0.007$ produced significant departures from the static case. Miau *et al* (1992) carried out similar pitch up and pitch down tests on four flat-plate delta wing models with sweep angles of 59°, 63.4°, 67° and 70°. The tests were carried out at Reynolds numbers of 9000 to 11000 and reduced pitch rates of $k = 0.01$ to 0.073. In choosing the incidence limits of the pitching motion for each test, Miau *et al* were careful to choose the limits of incidence at which vortex breakdown was always present on the wing in the static case, i.e., for each planform, those incidences where breakdown was either immediately upstream of the trailing-edge or just downstream of the wing apex. From their observations, they were able to suggest that, in the pitch up case, the delay can be divided into two parts. The first delay takes place immediately after the wing is set in motion. That is, the vortex breakdown point remains at its initial position for a certain length of time and then moves upstream at almost constant velocity. The trends revealed in the data showed that this delay became more pronounced as the value of k increased. For $k = 0.01$ or higher, a second delay was observed during the pitch up motion. Upstream propagation of the breakdown point was seen to slow down or hold still at some values of incidence. It was noted that the chordwise position of this propagation 'plateau' shifted upstream and the corresponding incidence values got higher as pitch rate was increased. In the pitch down cases, the first delay,

seen previously in the pitch up cases, was again apparent, however, unlike the pitch up cases, no second delay was found in the pitching motion.

1.3.1.3 *Flow-field measurements - Delta wings*

A number of research programmes have successfully measured the transient flow-field characteristics of delta wings over a wide range of angles of incidence. These have been used principally for comparison with theoretical investigations and also to quantify the qualitative flowfield information supplied by visualisation experiments. Many different methods of flowfield measurement have been adopted and these are summarised below:

Velocity probe measurements One popular technique to obtain such measurements has been to insert a range of probes into the flowfield to obtain velocity data. However, it has been appreciated for a number of years that the physical presence of the probe tends to have a detrimental effect on the flow. Payne *et al* (1987) carried out experiments using a seven hole probe arrangement to investigate this problem. They concluded that probe-induced vortex breakdown can occur ahead of the location when natural breakdown would have normally occurred downstream. The susceptibility to probe-induced breakdown was found to be particularly high on wings with a lower sweep angle. When the probe is inserted downstream of the natural breakdown location, then the breakdown location is largely unaffected. Given these limitations, they concluded that the seven hole probe is reasonably accurate for velocity measurements where breakdown is not induced or indeed, after breakdown has passed. However, in the breakdown region the accuracy was deemed to be poor.

Within the bounds of velocity probe application, a number of researchers have provided very good and detailed information on the vortex flowfield. Visser & Nelson (1993) used a cross-wire velocity probe to measure the distribution of

velocity, axial vorticity and circulation above a 75° flat-plate delta wing at two incidences for a range of chordwise locations. They observed that the majority of pre-breakdown positive axial vorticity is concentrated about the primary vortex axis in a region approximately twice the diameter of the vortex sub-core. Similarly, a region of negative vorticity was observed in the area of the secondary vortex. They also reported that the growth of vortex circulation with distance from the apex was linear over the forward half of the wing surface. The rate of growth was seen to decrease, however, aft of the mid-chord location. Using the local semi-span as a scaling quantity, Visser & Nelson (1993) showed that the behaviour of vortex circulation was conical in nature and that it also increased in a linear manner with increase in incidence for a given chordwise station. Honkan & Andreopoulous (1997) used a novel velocity probe with good spatial resolution to measure the fluctuating spatial and temporal velocity and vorticity distributions on a 45° delta wing. They measured large vorticity fluctuations, of the order three to six times the mean vorticity between the low speed side of the shear layer and the surface of the wing. Indeed, they showed that the vortex shear layer reattachment zone inboard of the vortex core and the region of secondary separation are associated with intense turbulent activity whilst the vortex core is largely turbulence free.

Non-intrusive techniques LDA measurements were obtained by Payne *et al* (1988). Their principle observation was a sudden change in the mean axial velocity distribution from a jet-like profile with core velocities up to three times the freestream prior to breakdown, to a wake-like profile downstream. In addition to their flow visualisation data, Miau *et al* (1992), used LDA measurements taken over a cross-sectional plane of 300 grid points to obtain velocity distributions during ramp-type pitching motions. Their pitch up test results confirmed their observation of delays in the upstream vortex breakdown progression during

visualisation experiments. They were able to use their LDA results to verify that the lag in pitch up was a combination of two delays. The first delay was found to be caused by the underdevelopment of the primary vortex when compared with the static case. The second delay was caused by the suppression of the primary vortex by the secondary separation immediately after the initiation of the pitching motion. This is itself caused by the growth of the secondary separation region that grows to a size that is larger than that found in the static case. In pitch down tests, Miau *et al* (1992) also showed that there is a delay in vortex restoration progression downstream caused by the underdevelopment of the primary vortex. Like their visualisation tests, no second delay in the pitch down case was apparent in the LDA results. Laser-Doppler Velocimetry (LDV) data were presented by Cornelius (1995) for a generic fighter configuration model with a 76° chined forebody and 56° sweep wing at a Reynolds number of 1.25×10^6. Cornelius obtained axial and cross-flow velocity measurements to calculate vorticity and turbulent kinetic energy contours above the wing surface. Using these measurements, he was able to formulate Rossby parameters consistent with Ludwieg's spiral instability analysis. The significance of these Rossby parameters is discussed further in Section 1.4.2.

Particle-Image Velocimetry (PIV) images were obtained by Magness *et al* (1992) for a 75° delta wing during ramp pitching motions. The tests used reduced pitch rates in the range, $k = 0.025$ to 0.15. They showed a marked difference in the cross-flow vorticity distribution in the pitch up cases when compared with either the static case, or pitch down cases at a similar pitch rate. At an incidence of 45°, the levels of vorticity were found to be higher and the vorticity distribution more coherent in the pitch up cases than was found in the static or pitch down cases. Also, for the pitch up cases only, a series of vortical structures were seen to be entrained into the vortex core from the leading-edge shear layer. In the static and

pitch down cases at the same incidence, the vortex core was found to be disordered and lacking coherence and the vortical structures emanating from the leading-edge were found not to wrap into the vortex, but instead, were convected downstream. Lin & Rockwell (1995) used PIV measurements over another 75° delta wing to calculate and trace the evolution of azimuthal vorticity contours and streamline patterns after the cessation of a pitch up manoeuvre. The wing was pitched to an incidence of 50° at a reduced pitch rate of $k = 0.15$. They observed a switch in sign of the azimuthal vorticity contours at the apex of the breakdown bubble and concluded that the vorticity concentrations within the observed breakdown bubble are associated with an antisymmetrical streamline pattern suggesting a helical instability. Cipolla & Rockwell (1995) used PIV measurements to calculate the cross-flow vorticity distribution over a pitching 45° delta wing in oscillatory motion. They were able to show the phase relationship between the wing motion and the flow structure, showing that it is possible to generate flow patterns that are phase-locked at every cycle, as well as every other cycle, of wing motion. In a later paper, Cipolla *et al* (1998) showed that, by combining the spatial and temporal components of the snapshot proper orthogonal decomposition analysis of experimental PIV measurements, coherent flow structures that evolve in space and time can be analysed effectively and the progress of vortex breakdown can be traced with a good degree of accuracy.

1.3.1.4 *Load Measurements - Delta wings*

Research into vortex breakdown has also been motivated by the need to understand its effects on the aerodynamic loading of the delta wing. Onset of vortex breakdown above a delta wing has been correlated with the initiation of the non-linear portion of the wing lift curve for flow past a stationary wing by Hummel & Srinivasan (1966). They carried out three-component balance measurements for delta wings of varying aspect ratio observing that the lift, drag

and pitching moment all undergo an abrupt deterioration as the location of vortex breakdown moves upstream over the trailing edge of the wing. It was shown by Jarrah (1989 & 1990) using six-component airload measurements, that the hysteretic lag in vortex breakdown, first observed by Gad-El-Hak & Ho (1985) during visualisation experiments, also occurred in the corresponding values of lift, drag and pitching moment.

1.3.1.5 *Pressure measurements - Delta wings*

One of the earliest accounts of the use of pressure measurements on a delta wing were reported by Lawford & Beauchamp (1961). They used four variable-capacitance type pressure transducers on the leeward surface of a 70° flat-plate delta wing. One transducer was mounted at $x/c = 0.4$, $y/s = 0.66$ and three more were equally-spaced across the semi-span from $y/s = 0.35$ to 0.83 at a chord station of $x/c = 0.8$. The root-mean-square (RMS) intensity of pressure fluctuations were measured and presented for each transducer. The results showed a sharp rise in the magnitude of pressure fluctuations at an incidence of 31° in the case of the aft transducers, and at 35° in the case of the forward transducer. Similarly, the frequency spectra of pressure fluctuations were calculated and presented for the forward transducer and the aft transducer closest to the leading-edge. The results reveal the appearance of a narrow band of frequencies that come to dominate the frequency spectrum at a similar incidence as the sharp rise of pressure fluctuations. The centre frequency of this dominant band was shown to be higher in the case of the forward transducer.

For thirty years after Lawford & Beauchamp, very few studies were made of delta wing flows using surface pressure measurements. It is possible that limitations of data acquisition technology severely limited the potential to obtain sufficiently detailed information. Similarly, the cost of such systems when compared to other experimental tools was likely to be prohibitive. Even recent studies, notably

Rediniotis *et al* (1990), Thompson *et al* (1990) and Gursul & Yang (1995), have either used limited spatial resolution or have focused on specific sections of the wing. Very rarely have detailed full-surface pressure data been presented. Where this has been possible, e.g. Vaughan & Wood (1995), results have exhibited a low pressure ridge associated with the leading edge vortex. However, no distinct response in the local pressure has been detected during vortex breakdown. Rather, it was proposed by Greenwell & Wood (1992), that the shape of the spanwise pressure distribution may be sensitive to the vortex state and may, thus, provide a basis for identifying breakdown.

Significantly, most of these studies limited themselves to the measurement of mean pressure distributions and have, therefore, neglected the potentially valuable information contained in the time-varying signal. Where the time-varying signal has been studied i.e., Gursul (1994), Mabey (1996), Woods & Wood (1996) and Woods (1999), the work has been primarily targeted at determining post-breakdown buffet characteristics of the wing flow. In this respect, much valuable information has been forthcoming and has provided useful insight into the buffet phenomenon. In some cases additional information on the evolution and structure of the leading-edge vortex system has also been obtained.

The study by Gursul (1994), which describes a series of static experiments on 60°, 65°, 70° and 75° delta wing planforms, found that the pressure frequency spectra in the post-breakdown region of the wing exhibited a dominant frequency component that was not present prior to breakdown. It was established that this frequency was associated with the helical mode instability of the vortex breakdown field. Gursul found that it was possible to use its presence as an indication of the progression of breakdown over the wing. Analyses of frequency spectra and RMS values of surface pressure fluctuations on novel wing planforms were conducted by Woods and Wood (1996). In general, the results obtained

were consistent with those of Gursul (1994) although an additional higher buffet frequency was identified in the region of vortex attachment on one of the wings. It was noted there existed a peak in the RMS value of the surface pressure near the attachment line of the primary vortex.

The research into pitching delta wings using pressure measurements is extremely limited. The only detailed information available concerns pressure data obtained from oscillating delta wings at various reduced frequencies. A study by Thompson *et al* (1990) into oscillating delta wings used ensemble-averaged pressure data to identify a similar lag or hysteresis effect in pressure measurements as that seen in force measurements and visualisation experiments detailed previously. The degree of lag being chiefly dependent on the frequency of oscillation, even to the extent that the lag can be as much as 180°, (i.e. the lift generated by the wing can be at a maximum at the incidence corresponding to minimum lift in the static case and visa versa), Gursul & Yang (1995) suggested that this phase lag is very closely associated with the external pressure gradient generated by the wing. The deficiencies in the literature regarding pressure measurements are discussed in Section 1.5.

1.4 NUMERICAL METHODS

Accompanying the literature survey on experimental research is the following survey of numerical methods which examines three main areas in the field of vortex breakdown research: 1) Theories of vortex breakdown. 2) Empirical vortex breakdown prediction methods. 3) Computational studies.

1.4.1 *Theories of vortex breakdown*

Alongside the experimental observations made since the late fifties, a number of theoretical explanations have been put forward concerning the nature and causes

of vortex breakdown. Theoretical studies can be categorised roughly according to whether breakdown is considered to be associated with: 1) Instability caused by axisymmetric/spiral disturbances or non-linear interactions. 2) Departure from predicted lift and drag-due-to-lift characteristics. 3) Wave phenomena resulting in numerical failure 4) Stagnation of the flow along the vortex axis. 5) The generation of negative azimuthal vorticity in the primary vortex rotating core.

1.4.1.1 *Instability*

Jones (1960) was the first to suggest that hydrodynamic instability might be responsible for vortex breakdown. The theory is based on a linear stability analysis applied to the axisymmetric laminar Navier-Stokes equations. However, Jones was unable to define a criterion that could be applied generally. The idea was later pursued by Ludwieg (1965) who suggested that after the onset of instability, spiral disturbances could amplify, induce an asymmetry in the vortex core and subsequently lead to stagnation. Lessen *et al* (1974) studied the inviscid stability of the Q-vortex (i.e. q remains constant) to infinitesimal non-axisymmetric disturbances with normal modes of the form:

$$(\exp[i(\kappa\chi - n\theta - \kappa\gamma t)] \qquad (1.1)$$

where : κ = axial wave number, χ = axial co-ordinate, n = azimuthal wave number, θ = azimuthal co-ordinate, and γ = complex phase velocity.

For negative wave-numbers (i.e. helical wave paths opposite in sense to the vortex rotation) the amplification rate increases with respect to swirl parameter (q) to a maximum at $q = 0.85$ and decreases again becoming negative at $q > 1.58$ whereafter the flow is stable to all disturbances. Garg & Leibovich (1979) and Escudier *et al* (1988) have both reported values of q which result from fitting Q-vortex velocity profiles to their experimental data for flows exhibiting

breakdown. Garg & Leibovich found that q = 0.8 was the smallest value at any location, whereas upstream of breakdown it was always significantly greater than 1.5 and downstream it was less than 1.5. It was claimed that this suggests stability to axisymmetric disturbances everywhere, and an instability to helical disturbances downstream of the breakdown region. In all theories of hydrodynamic instability, breakdown is analogous to laminar-turbulent transition.

1.4.1.2 *Departure from lift predictions*

Polhamus (1971) was the first to develop a theory using the analogy of a two-dimensional laminar separation and reattachment bubble when regarding the separation and subsequent reattachment of the flow over delta wings. This theory can be used to predict the low-speed lift and drag-due-to-lift characteristics of sharp-edged delta planforms. The total lift generated by the wing is given by:

$$C_L = K_p \sin\alpha \cos\alpha + K_v \sin^2\alpha \cos\alpha \qquad (1.2)$$

Where: K_p = potential flow lift constant equal to the normal force slope given by small disturbance potential flow lifting surface theory. K_v = vortex lift constant equal to $\partial C_{Sp}/\partial\alpha^2$, such that C_{Sp} = potential flow leading-edge suction coefficient.

Polhamus showed that predicted lift values showed good agreement with experimental values for wings with aspect ratios in the range 1.5 to 0.7. These values were measured at incidences where visualisation tests under similar experimental conditions had shown an absence of vortex breakdown over the wing. A subsequent significant deviation of experimental results from theoretical results at higher incidences was thought to be indicative of the arrival and upstream progression of vortex breakdown from the trailing-edge to the apex.

1.4.1.3 *Wave Phenomena*

Squire (1960) was the first to attempt to connect vortex breakdown with wave-motion. He considered the possibility of the existence of standing waves on a cylindrical vortex motion for which the stream function satisfies the following equation for inviscid flow:

$$\frac{\partial^2\psi}{\partial x^2} + \frac{\partial^2\psi}{\partial r^2} - \frac{1}{r}\cdot\frac{\partial\psi}{\partial r} = \frac{r^2}{\rho}\cdot\frac{dH}{d\psi} - \frac{1}{2}\cdot\frac{dK^2}{d\psi} \qquad (1.3)$$

where: (for inviscid flow) the total head H and circulation $2\pi K$ are functions of the stream function (ψ) alone.

Squire assumed that if standing waves could exist, then small disturbances coming from downstream will propagate in the upstream direction and ultimately provoke breakdown. He proposed that for a 'supercritical' flow, long waves propagating against the flow are carried downstream and do not affect events in the upstream direction, whereas for a 'subcritical' flow, long waves may propagate upstream, and hence for some limit situation, standing waves can exist on the flow.

Benjamin (1962) on the other hand proposed that vortex breakdown is a transition between two conjugate swirling flow states A and B, each of which is a solution of the equation for inviscid cylindrical flow:

$$\frac{\partial^2\psi}{\partial r^2} - \frac{1}{r}\cdot\frac{\partial\psi}{\partial r} = \frac{r^2}{\rho}\cdot\frac{dH}{d\psi} - K\cdot\frac{dK^2}{d\psi} \qquad (1.4)$$

Benjamin showed that if flow A is supercritical then flow B is sub-critical in direct analogy with the shock/hydraulic jump in open channel flow. The critical state theory is based on the assumption that a columnar vortex can support

axisymmetric standing waves. Benjamin, like Squire before him, found that the critical condition for the existence of standing waves is :

$$\text{Swirl Ratio } (\alpha_0) \quad = \quad V_\theta/V_x \geq 1.2 \tag{1.5}$$

By decreasing the axial velocity component, or by increasing the swirl velocity component, (i.e. by increasing α and/or decreasing Λ), a supercritical flow is driven towards subcritical. Thus, if this assumption is correct, vortex breakdown can be thought of as the ability or not of the flow to sustain standing waves.

1.4.1.4 *Stagnation*

One feature of the flow that has already been described as an essential aspect of vortex breakdown is the deceleration and eventual stagnation of the flow at the vortex axis. In the 1960's, a number of numerical calculations were carried out using the quasi-cylindrical form of the equations of motion to calculate the axial development of the vortex flow. The quasi-cylindrical equations are of the form :

$$\frac{\partial u}{\partial r} + \frac{u}{r} + \frac{\partial w}{\partial z} = 0 \tag{1.6}$$

$$\frac{v^2}{r} = \frac{1}{\rho}\frac{\partial p}{\partial r} \tag{1.7}$$

$$u\frac{\partial v}{\partial r} + \frac{uv}{r} + w\frac{\partial v}{\partial z} = \nu\left(\frac{\partial^2 v}{\partial r^2} + \frac{1}{r}\frac{\partial v}{\partial r} - \frac{v}{r^2}\right) \tag{1.8}$$

$$\frac{\partial w}{\partial r} + w\frac{\partial w}{\partial z} = -\frac{1}{\rho}\frac{\partial p}{\partial z} + \nu\left(\frac{\partial^2 w}{\partial r^2} + \frac{1}{r}\frac{\partial w}{\partial r}\right) \tag{1.9}$$

Where r and z are cylindrical polar co-ordinates, u, v and w are the radial, swirl and axial components of velocity respectively, p, ρ and ν are pressure, density and viscosity. The boundary conditions are those that a viscous fluid must satisfy on the axis of symmetry, namely $u = v = \partial w/\partial r = 0$ at $r = 0$ and in addition, a condition such as a prescribed pressure distribution at the edge of the vortex core.

If at some location along the vortex core, the calculations of the quasi-cylindrical vortex core show appreciable axial gradients instead of small axial gradients, then there also must be appreciable axial gradients in the corresponding real vortex core, even though the quasi-cylindrical approximation fails. The idea is that, this occurrence of large axial gradients or the failure of the quasi-cylindrical approximation, corresponds to the arrival of vortex breakdown. A number of investigators used these equations in different ways. The calculations of Gartshore (1962) and Mager (1972) were of the momentum-integral type, whereas Bossel (1969) uniquely divided the flow in the vicinity of breakdown into four regions which he then matched together. Hall (1964), using this technique was first to demonstrate that the axial pressure gradient is composed of two components: 1) The imposed external pressure gradient 2) The swirl contribution. In a later paper, Hall (1972) brought together the quasi-cylindrical approximation theory and the critical state theory of Benjamin (1962) to build a framework for explaining vortex breakdown. He stated that a vortex core that is initially supercritical will tend towards the critical state with increasing distance downstream. That is, if the swirl is large enough and the conditions at the edge of the core are appropriate. The development is described by the quasi-cylindrical approximation which shows that such an approach to the critical is accompanied by a retardation of the axial flow that is most pronounced near the vortex axis. At or near the critical condition, the axial gradients increase beyond limits and the quasi-cylindrical approximation fails. The abruptness of the change in core

structure is explained by the existence of the critical state, which also explains the significance of the magnitude of swirl in breakdown as described by Benjamin.

1.4.1.5 *Azimuthal Vorticity*

A number of investigators, notably Brown & Lopez (1990), Nelson & Visser (1993) and Boffadossi (1996) have suggested that the distribution of vorticity in the flow is a crucial factor in vortex breakdown. Their observations have shown that the onset of negative azimuthal vorticity, i.e. where the swirl ratio of velocity (α_0) exceeds the swirl ratio of vorticity (β_0), is a necessary condition for the onset of breakdown. In fact, the attainment of zero or negative axial velocity is only possible if azimuthal vorticity becomes negative. Nelson & Visser have examined this theory experimentally, (see also Lin & Rockwell (1995)), whilst Brown & Lopez have tested this condition against numerical Navier-Stokes equations of swirling pipe flow and found the numerical solution would diverge rapidly only if:

$$\tau_0 \quad = \quad \alpha_0/\beta_0 > 1 \qquad (1.10)$$

Boffadossi (ibid.) used the theory originated by Brown & Lopez to develop a criterion for vortex breakdown using a computational method based on the unsteady formulation of a non-linear vortex-lattice scheme. This scheme used Rankine vortices with a viscous core diffusion model physically consistent with the turbulent diffusion mechanism of continuous shear layers. In his paper, Boffadossi predicts vortex breakdown for a series of thin delta wings and plots his results against a series of experimental data to very good effect.

1.4.2 *Empirical vortex breakdown prediction methods*

Examples of successful empirical vortex breakdown prediction methods are very few in number. The earliest example was that of Lambourne & Bryer (1961) who,

in addition to their visualisation results, suggested that if vortex breakdown location is plotted as a function of:

$$x/c_{(bd)} = \cos^{-1}(\cos\alpha \sin\Lambda) \qquad (1.11)$$

then the results for different sweep angles show a tendency to collapse onto a single curve. Similarly, Lee & Ho (1990) suggested that swirl angle based on the geometry of the wing also provides a good correlation with breakdown location based on experimental results. This swirl angle ϕ, was calculated from the perpendicular and axial velocity components along the leading-edge:

$$\tan\phi = \sin\alpha / (\cos\alpha \sin\Lambda) \qquad (1.12)$$

Jumper *et al* (1993) proposed a single criterion for vortex breakdown over slender delta wings where, according to slender wing theory, circulation was assumed to increase linearly with streamwise distance. Jumper *et al* found that vortex breakdown occurred when :

$$\Gamma/U_\infty c = 0.132. \qquad (1.13)$$

Gursul (1995) applied the methods of Lambourne & Bryer, Lee & Ho and Jumper et al to a large database of published vortex breakdown location data. This study showed that all three methods produced a high degree of scatter, particularly near the trailing-edge of the wing. Gursul proposed a different criterion based on the variation of $\Gamma/U_\infty x$, which is related to the rate of increase of circulation along the streamwise direction, and showed a good correlation over the whole length of the wing.

Spall *et al* (1987) proposed a criterion for the onset of vortex breakdown using an appropriately defined local Rossby number which was used to delineate the region where breakdown occurs. The Rossby number (or inverse swirl ratio) was

defined as Ro = $W/r^* \Omega$, where r^* is the radial distance from the vortex centreline where swirl velocity is at a maximum, W represents the axial velocity at r^* and Ω is the rotation rate of the vortex inner-core. Spall *et al* showed, for a series of experimental and computational results, that vortex breakdown tends to occur at Rossby numbers of 0.65 and below for wing-tip vortices. For leading-edge vortices the critical Rossby number was increased to approximately 1.2.

Traub (1996) presented a series of expressions to predict the chordwise variation of vortex breakdown with incidence for a number of delta wings. Traub's method was based on the work of Hemsch & Luckring (1990) who showed that, by using Sychev similarity parameters, the vortex strength at the trailing-edge of slender wings could be correlated. The parameter was given in the form:

$$g = AK^{1.2} = \Gamma/U_\infty c_r \tan^2\varepsilon \cos\alpha \qquad (1.14)$$

where A = constant (given a value of 4.63 by Visser & Nelson (1993)), K is given by

$$K = \tan\alpha/\tan\varepsilon \qquad (1.15)$$

Using the results of Visser & Nelson (1993) and slender wing theory assumptions of conical flow, Traub arrived at the following equations in terms of non-dimensional circulation:

$$\Gamma/U_\infty c_r = 4.63 \tan^{0.8}\varepsilon \tan^{1.2}\alpha \cos\alpha \qquad (1.16)$$

$$\tan\alpha_{BD\text{-}TE} = 13.47 \tan\varepsilon\, e^{-6.9\varepsilon} \qquad (1.17)$$

$$x/c_{(bd)} = (\Gamma_{BD\text{-}TE}/\Gamma_{\alpha > BD\text{-}TE})^3 \qquad (1.18)$$

Having calculated the incidence at which breakdown reaches the trailing-edge of the wing from Eq. (1.17), it is possible to use Eq. (1.16) to calculate the non-dimensional circulation at $\alpha_{BD\text{-}TE}$ and other incidences where breakdown progresses upstream of the trailing-edge. Hence, Eq. (1.18) can then be used to track the progress of breakdown from trailing-edge to apex. Traub's results showed reasonable agreement with experimental data for delta wings of sweep angles ranging from 65° to 80°.

1.4.3 *Computational studies*

The following section is designed to provide an overview of computational studies of vortex breakdown from a historical point of view. The treatment of this work is not exhaustive, however, it aims to present the most significant developments in the field.

Those early investigators who did not use the quasi-cylindrical approximation, examples being Kopecky & Torrance (1973) and Grabowski & Berger (1976), tended to confine themselves to calculations involving laminar flow using the full Navier-Stokes equations, subject only to restrictions of axial symmetry, steadiness and incompressibility. Later investigations have been able to use the vastly increased computing power of super-computers and, more recently, computing cluster technology. Thomas *et al* (1990) applied an upwind-biased finite-volume algorithm to the laminar flow over the leeward surface of a delta wing with AR =1.0 (i.e. sweep angle ≈ 76°), for incidence angles in the range 0° to 40°. The differencing was second order spatially accurate and a multi-grid algorithm was used to promote convergence to the steady state. The results compared well with experimental values of CL_{max} at a Reynolds number of 0.95×10^6. At 40°, an enlargement of the vortex diameter, thought to indicate vortex breakdown, was

evident in the computational results extending from x/c = 0.6 to just beyond the trailing-edge.

Agrawal *et al* (1992) used a computational algorithm based on a thin-layer approximation of the three-dimensional, time dependent, conservation law form of the compressible Navier-Stokes equations. Like the previous example, the code used an upwind-biased spatial differencing scheme, with either flux difference splitting or flux vector splitting for the pressure and convective terms and central differencing for the shear stress and heat transfer terms. From their results, Agrawal *et al* were able to identify the presence of vortex breakdown, if not the exact breakdown location, from the contours of axial velocity.

The first three-dimensional representation of vortex breakdown was shown by Modiano & Murman (1994), who solved the Euler equations for inviscid, compressible flow using an adaptive grid method. Refinement was used to add nodes in the region of the vortex and other interesting flow features. From their results, Modiano & Murman were able to predict the presence of vortex breakdown in its spiral form in good agreement with experimental data.

The first computational results apparent in the literature for transient vortex breakdown above a delta wing subject to ramp-type pitching manoeuvres, was presented by Visbal (1994). The flows were simulated by the solution of the full three-dimensional Navier-Stokes equations on a moving grid using the implicit Beam-Warming algorithm. An assessment of the effects of numerical resolution were carried out in comparison with experimental results. This assessment suggested that the computational method was able to capture the basic dynamics and initial stages of vortex breakdown on the pitching wing. The most important

finding of this work was that the pressure gradient along the vortex axis played a dominant role in the initiation of breakdown.

At this stage, vortex formation and development near the apex of delta wings was poorly represented in conventional grids due to dissimilar length scales of the flow and the grid. Kumar (1996) overcame this problem by introducing an embedded conical grid surrounding the wing. Using this method, the computed Euler solutions showed that the vortex could be well resolved right from the apex, even at low incidences, and the prediction of vortex breakdown was improved over a conventional grid set-up.

A further application of the Beam-Warming algorithm on a 65° delta wing has been made by Gordnier (1997). The use of both block tri-diagonal and diagonal inversion schemes with sub-iterations was investigated. The effects of time-step size and grid resolution were also discussed. Gordnier identified bubble (B-type) breakdown as being present for short periods during transient upstream movement of the vortex breakdown location during ramp pitching manoeuvres and identified a three-dimensional stagnation point at the head of the breakdown region.

1.5 UNRESOLVED ISSUES AND THE CURRENT STUDY PROGRAMME

Extensive experimental research using a wide range of techniques has greatly advanced the understanding of the physical mechanisms that make up the complex vortex flow-field on delta wings. The work carried out on flutter and stall stability, control and buffet characteristics have gone a long way to making large aircraft safer and to reducing fatigue life across the board. However, the history of research into high incidence flight dynamics and its associated aerodynamics on delta wings has seen a gradual evolution from concentration on

the avoidance of undesirable phenomena such as 'wing rock', toward increasing interest in such constructive ideas as 'super-manoeuvres'. Considering this point of view, it is apparent that there are significant gaps in the literature regarding the use of pressure measurements during delta wing ramp-type motions. The following areas, in particular, have been identified as those where information is scarce or non-existent: 1) The general use of whole surface pressure measurements to identify topological features of the flow as they interact with the wing surface. 2) The measurement of pressure fluctuations and the effect on these measurements of the arrival of vortex breakdown. 3) The use of the time varying pressure signal to track the progress of vortex breakdown over the wing surface. 4) Analysis of pitching wing buffet characteristics in the post-breakdown state.

The objectives of the current study programme are twofold: 1) To analyse pressure data obtained during an earlier research programme. The analysis takes the form of a detailed examination of time varying pressure signals in static and ramp-pitching cases using a range of statistical analysis techniques. 2) To carry out flow visualisation experiments to act as a validation tool for the pressure data analysis. The aims of the work can be summarised as follows: 1) To provide an insight into significant flow-field features including vortex breakdown, as they impinge on the wing surface. 2) To determine a reliable and robust method of tracking the progress of vortex breakdown for static, pitch up and pitch down cases. 3) To examine wing buffet characteristics during pitching motions.

The previous research programme, also carried out at Glasgow University, obtained surface pressure measurements during a series of experiments on a 60° delta wing. The upper surface of the delta wing was highly instrumented on one side with miniature surface mounted pressure transducers. These were connected to a powerful two-hundred channel data acquisition system that has the capability to acquire data at the rate of 50kHz per channel. This equipment allowed surface

pressure data to be obtained at high spatial and temporal resolution over a wide range of incidence and pitch rates. A complementary series of low-speed flow visualisation tests have been conducted in the present study programme to provide supplementary qualitative flowfield information. Analysis of collected test data in static, pitch up and pitch down cases indicate that it is possible, on the basis of surface pressure measurements alone, to monitor the structure and location of the leading edge vortex system. Similarly, the progression of breakdown towards the apex of the wing with increasing incidence in the static and pitch up cases, and the restoration of the vortex core with reducing incidence in the pitch down cases, can both be tracked with a high degree of confidence. Using full-surface contour plots of the upper surface mean and RMS pressure distributions and single point signal analysis methods, i.e. frequency spectra, signal energy and cross-correlation functions, in each case, it is be possible to provide an insight into the principal surface features of the flow not addressed by previous experimental investigations. The following chapters detail the work carried out.

Chapter 2

2. EXPERIMENTAL METHODS

Two types of wind tunnel tests took place, namely pressure measurement tests and smoke flow visualisation tests. The tests, which took place in two different facilities at Glasgow University, are described as follows.

2.1 PRESSURE MEASUREMENT TESTS

2.1.1 *Model design and construction.*

The delta wing used in the pressure test programme was machined from a solid block of aluminium. It had a leading-edge sweep of 60°, a root-chord (c) of 800mm and a trailing edge span ($2s_{te}$) of 923.8mm (wing area = 0.369m^2). The wing had a flat leeward surface, a contoured windward surface (shown in Figure 2.1), giving a thickness ratio of 9.0%. The leading and trailing edges were bevelled on the windward side at angles of 14° and 10° respectively. The model was designed to accommodate 192 Kulite Type CJQH-187 differential pressure transducers located primarily on the starboard side of both the leeward and windward surfaces. The location of the leeward surface and windward surface transducers is shown in Figures 2.2 and 2.3 respectively. The model was constructed such that the standard nose section could be removed and replaced with a rounded nose section. The rounded nose had a radius of 50mm which reduced the root chord by 6.25%. It had a bevelled leading-edge similar to its standard counterpart providing a unique opportunity to investigate the effect of the apex geometry on vortex formation and breakdown. Details of the rounded nose section are shown in Figure 2.4.

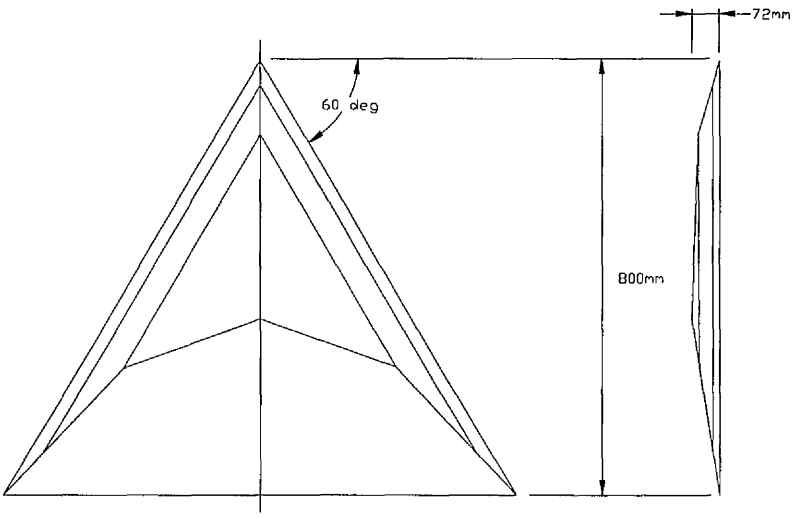

Figure 2.1 - Delta wing model windward surface

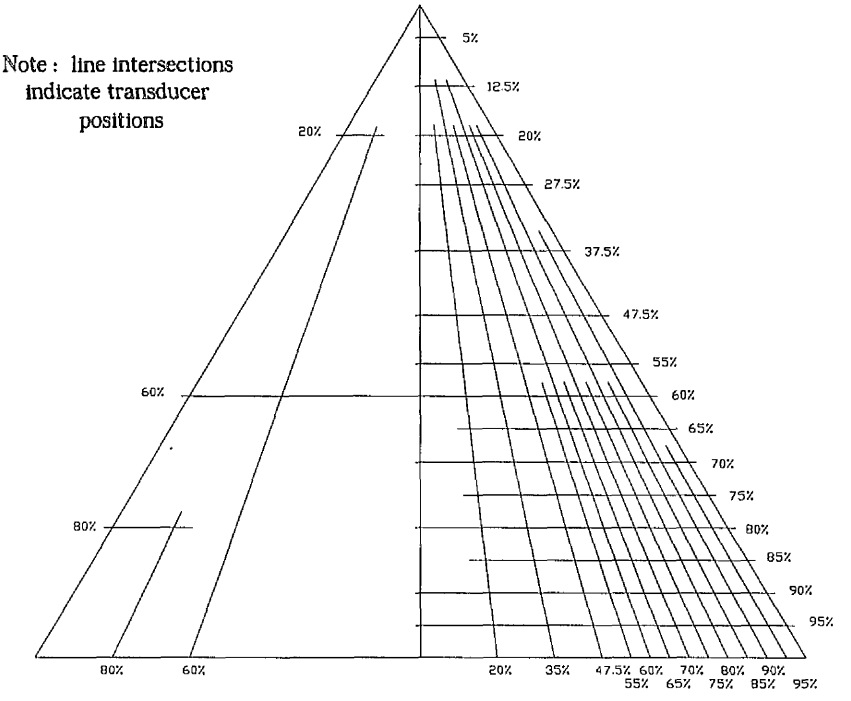

Figure 2.2 - Leeward surface pressure transducer locations

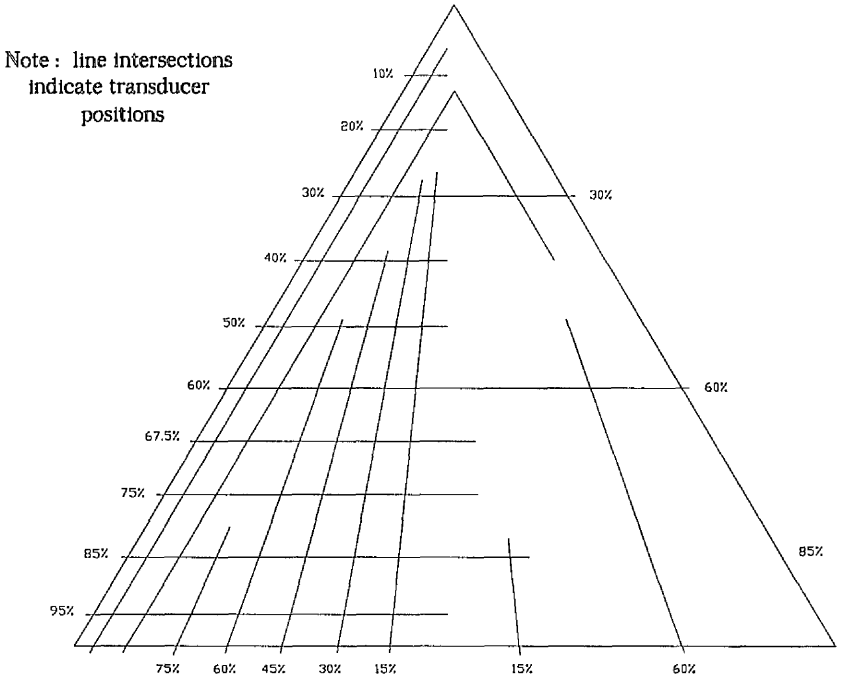

Figure 2.3 - Windward surface pressure transducer locations.

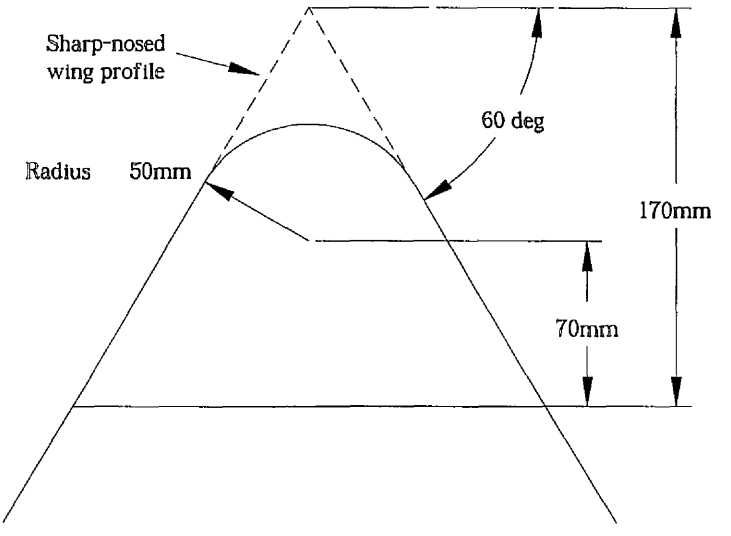

Figure 2.4 - Details of rounded nose section.

2.1.2 *The pressure measurement test facility.*

The pressure measurement tests were conducted in the University's Handley-Page wind-tunnel facility. This is a closed-return type wind tunnel with an octagonal test section measuring 2.13m by 1.61m (working area = 2.667m^2). This gave a model-span to tunnel width ratio of 43.4% and a model blockage (not including strut fairings) of 1.25% to 9.27% over the incidence range $0° \leq \alpha \leq 42°$. The model was mounted leeward side up, and was supported by three vertical struts attached to the windward surface, one placed at the quarter chord position and two at the trailing-edge. The forward strut was rigidly fastened to a support structure mounted on a concrete floor below the wind tunnel. The two rear struts were connected to a hydraulic actuation mechanism which provided a wide range of movement in pitch and instantaneous incidence measurement to an accuracy of $\pm$ 0.1°. A schematic diagram of the wind-tunnel facility is shown in Figure 2.5.

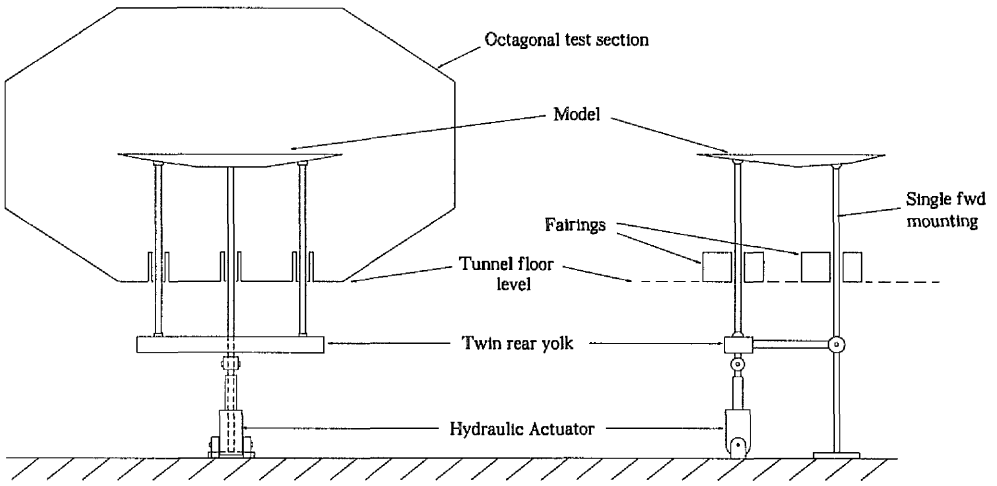

Figure 2.5 - A schematic diagram of the Handley-Page wind tunnel facility (used in conjunction with the data acquisition system).

2.1.3 *The data acquisition system.*

Data acquisition was carried out by a PC equipped with a 486 processor, programmed using TEAM 256 software. The PC was configured and interfaced with proprietary Bakker Electronics BE256 modules that provided the necessary analogue to digital conversion. The system had 200 channels, each capable of sampling at 50kHz. Six channels not taken up by transducers were used to sample temperature, model acceleration (x3), reference dynamic pressure and model incidence. Two channels were left empty. The signals from each transducer were delivered to a specially designed signal conditioning unit of modular construction, and each module contained its own control board. The control board was capable of automatic offset and gain adjustment by sampling the minimum and maximum output of each transducer during each run and adjusting the gains automatically as required. A schematic diagram of the path of data flow is shown in Figure 2.6.

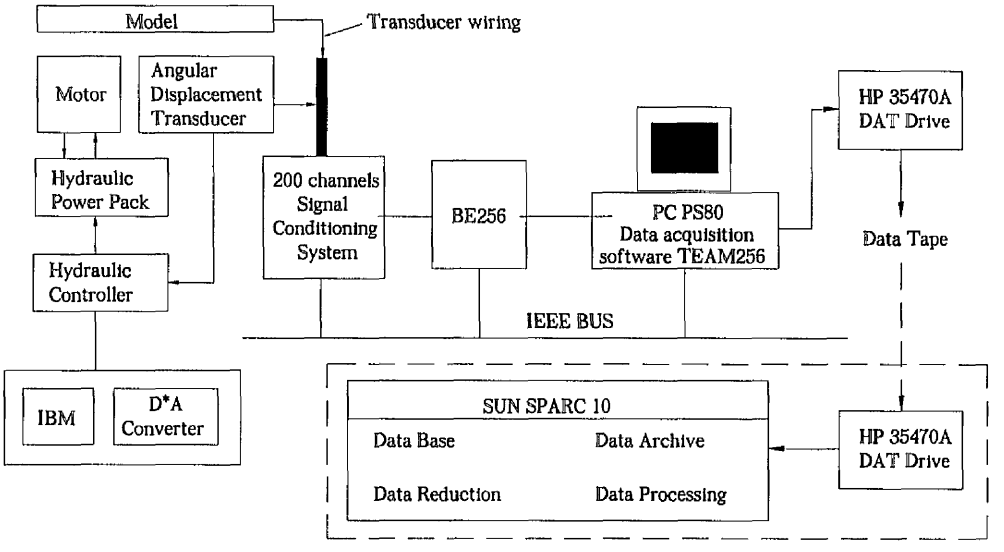

Figure 2.6 - A schematic diagram of the path of data flow in the data acquisition system and model control.

2.1.4 *Pressure test procedure - static case*

The pressure test model was set at a starting incidence of -5°. The wing was then pitched up in 1° increments to + 42°. A suitable period was allowed prior to data collection at each incidence and the pressure data were then sampled at a frequency of 1.0kHz for a period of 2s. The total data set was divided into three 'runs' each covering an arc of 16°, giving a data set of 32000 samples per run. The mean free stream velocity was measured at $50ms^{-1}$, which gave a Mach number of 0.16 and a Reynolds number of $2.7x10^6$ based on root chord.

2.1.5 *Pressure test procedure - pitching cases.*

During testing, the pressure test model was set at a starting incidence of -5° (pitch up cases) or 39° (pitch down cases). The wing was then pitched up or down through an arc of 45°. Data collection was initiated on commencement of the pitching motion and continued for a suitable period after cessation of the motion to allow the flow to settle. The data set per cycle was 8000 samples and four cycles were combined to give a total data set of 32000 samples. For each pitch rate, the sampling frequency was set such that a minimum of 6000 samples were collected during the motion phase of the cycle. The nominal Reynolds number was again set at $2.7x10^6$. The pressure data in either static or pitching cases were not corrected for tunnel blockage effects.

2.2 SMOKE FLOW VISUALISATION TESTS

2.2.1 *Model design and construction.*

The models tested in the flow visualisation facility were geometrically similar to the model used for the pressure measurement tests in each of its two nose configurations. The sharp-nosed model had a root chord of 346mm and a trailing edge span of 400mm. Each model was constructed in two parts. The main body,

which included the contoured shape of the windward surface, was machined from solid aluminium and was used to house a plenum chamber that was supplied with smoke. The main body upper surface was machined to leave pathways (shown in Figure 2.7) for the smoke along the entire length of both leading-edges. Each model was completed by a 2mm thick flat plate with edges bevelled to match the main body. The two parts fitted together provided slots located 2mm below the top surface of the model enabling smoke to be ejected along the whole leading-edge. The models were mounted in a similar fashion to the pressure measurement tests. The mechanism for pitching the models was provided by a lead-screw and flange nut assembly below the tunnel floor. The two rear support struts were attached to the nut by a yoke, which as the screw shaft rotated, was constrained to move in the vertical direction.

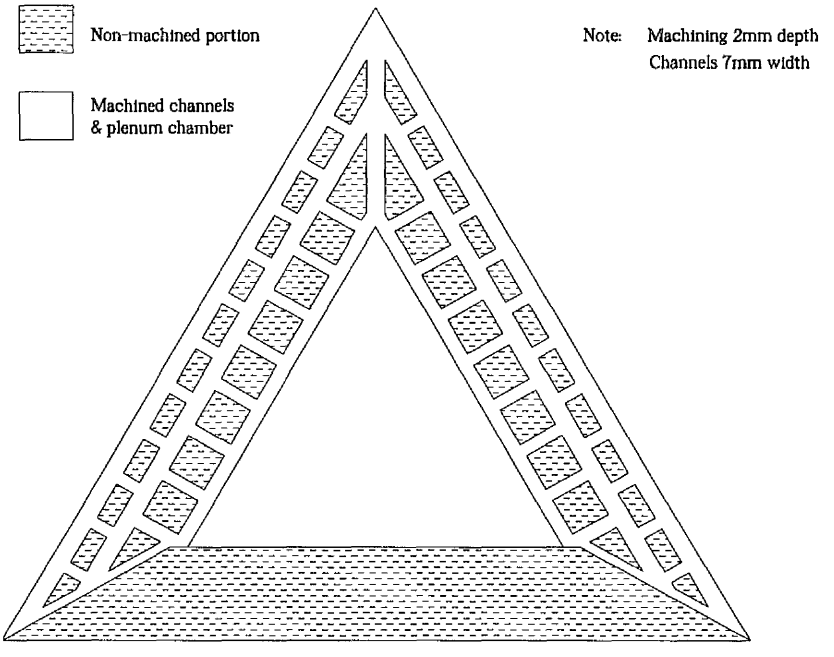

Figure 2.7 - A diagram of the machined pathways providing smoke egress along both leading-edges.

2.2.2 *The flow visualisation facility.*

The flow visualisation facility is an open-return type wind-tunnel with a square working section of 0.9m x 0.9m. This gave a span to tunnel width ratio of 44.4% and a model blockage of 0.77% to 5.72% over the same incidence range as the pressure measurement tests. All tests were carried out at a mean free stream speed of 0.44ms^{-1} that gave a nominal Reynolds number of 10000 based on root chord. A schematic diagram of the smoke visualisation wind-tunnel facility is shown in Figure 2.8.

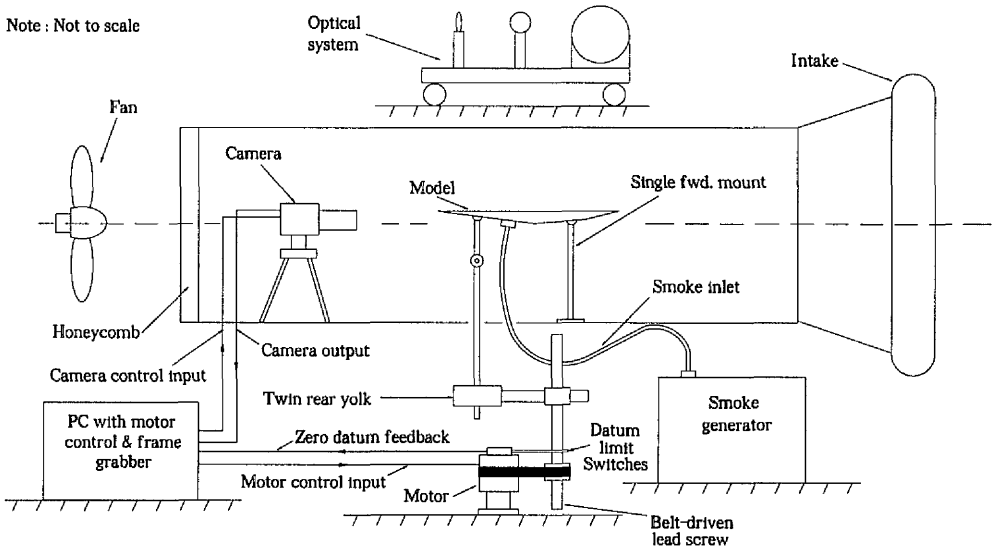

Figure 2.8 - A schematic diagram of the flow visualisation facility.

2.2.3 *The optical system.*

In the static case, illumination was provided by a Cyonics 0.5W Argon ion laser of 525nm-480nm wavelength located above the wind tunnel. Suitably arranged mirrors expanded the beam into a thin sheet, which shone down into the wind tunnel. The whole system was mounted on a trolley such that movement of the trolley along the length of the wind tunnel and adjustment of the optics allowed the light sheet to be positioned at any chosen chord station or at any lateral angle

relative to the trailing edge. For the pitching cases, the illumination was switched over to a Spectra Physics GCR-130-10 Nd:YAG laser located alongside the Argon ion laser. The laser had a maximum output energy of 250mJ at 532nm (green), the repetition rate was 10Hz and the pulse duration was 8ns. The optical set-up was similar to the static case. A schematic diagram is shown in Figure 2.9.

2.2.4 *Flow visualisation test procedure - static case.*

The static tests were carried out by positioning the laser light sheet parallel to the trailing edge at a chord position (x/c) of 0.95. The model was then placed at a starting incidence of 0° (accurate to within to ± 0.5°), and was then pitched up in increments of 0.5° until breakdown was observed to pass through x/c = 0.95. Then at each higher incidence the light sheet was positioned at the chord location where the vortex core was seen to fluctuate between breakdown and reformation. This chord position was recorded against incidence. Images were captured using a Kodak Megaplus ES1.0 digital video camera and Imaging Technology IC-PCI digital frame grabber.

2.2.5 *Flow visualisation test procedure - pitching cases.*

For each pitching case, a series of 'runs' were carried out. For each run the laser light sheet was positioned parallel to the trailing edge at a single chord position, starting at x/c = 0.9. In each successive run the laser sheet was moved towards the wing apex in 0.1c increments to x/c = 0.4. For each run in the pitch up cases, the model was placed at a starting incidence of 0° and then pitched up through an arc of 30°. In the pitch down cases, the model was placed at a starting incidence of 30° and then pitched down through an arc of 35°. Images were captured using the same equipment as the static case. However, model pitch control, and laser pulse to camera synchronisation were achieved via a 300MHz Pentium II PC fitted with a National Instruments PC-TIO-10 counter-timer card and

programmed using LabVIEW. Full details of the flow visualisation model, camera and laser control methodology are given in the work by Green (1998).

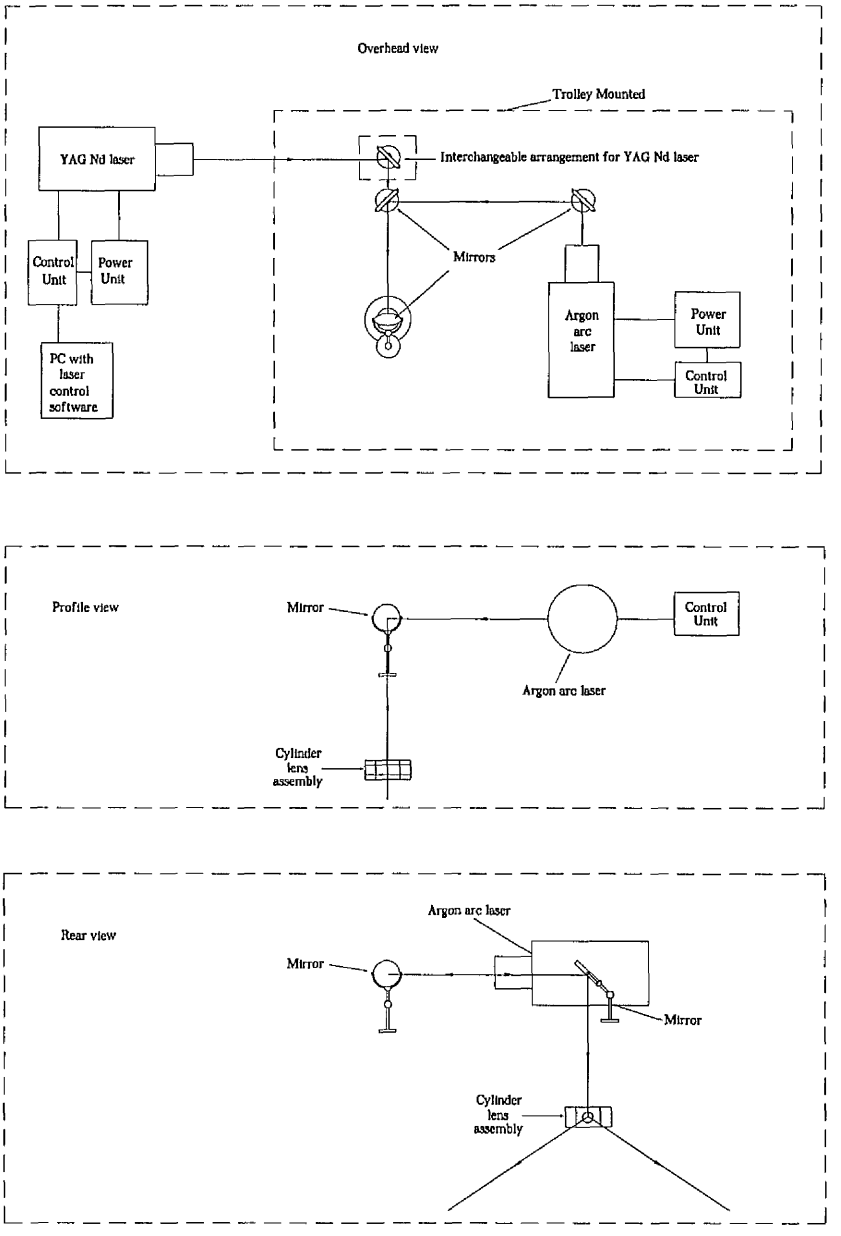

Figure 2.9 - A schematic diagram of the visualisation optics

Chapter 3

3. STATISTICAL ANALYSIS METHODS

The high spatial and temporal resolution of the pressure data allowed a detailed analysis to be carried out. Before this could commence, each 'raw' data set containing 192 channels of 32000 pressure transducer samples were non-dimensionalised to produce values of C_P. These were written to file and made up a 'reduced data' file measuring 192 x 16 x 2000 data values in the static case, (i.e. 2000 samples at 16 discrete incidence values from 192 transducers) or 192 x 4 x 8000 data values in each pitching case, (i.e. 8000 samples collected during 4 separate runs from 192 transducers). This manipulation of the data took place using bespoke code written in C. Each file was given a unique file number based on model configuration, motion type, run reference number and run version. The fourth identifier was added to allow the original run reference number to be used again. This was necessary in cases where an individual experimental run was repeated following data corruption during the original collection process. The use of an additional identifier made cataloguing much simpler. At the top of the file, a run information block (RIB) was added to log experimental variables such as flow speed, barometric/reference pressures, mean air temperature, sampling frequency and pitch rate. An example of the full data provided in a typical RIB is shown in Appendix A. At the bottom of the reduced data file, 8 rows of 32000 data samples (in either 16 x 2000 or 4 x 8000 format, depending on motion type) were added from the original raw data file. These extra rows were made up of temperature (Row 193), model acceleration x 3 (Rows 194 - 196), empty channels (i.e. zeros) x 2, (Rows 197 & 198), incidence (Row 199) and reference dynamic pressure (Row 200). A schematic diagram

showing the make-up of the reduced data file is shown in Figure 3.1. It was at this stage in the analysis process that the current study programme begins.

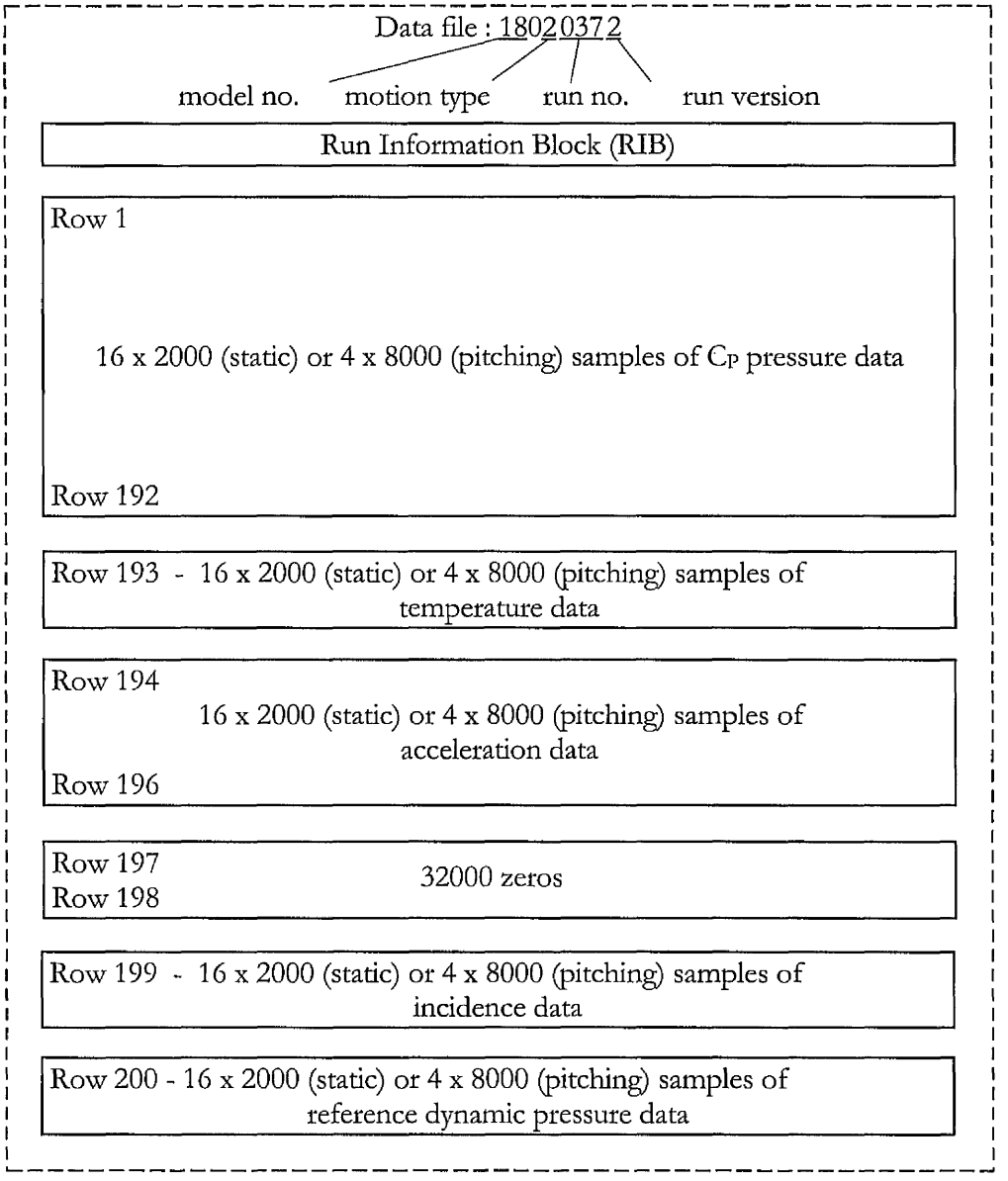

Figure 3.1 - Composition of C_P pressure data file.

Statistical methods were employed to measure the following five pressure signal properties: 1) The mean pressures (static case), the instantaneous pressures (pitching cases), and distributions. 2) The Root-Mean-Square (RMS) pressures and distributions. 3) The frequency content of the pressure signal. 4) The cumulative signal energy. (pitching cases only), and 5) The cross-spectral density function. These provided a basis for a quantitative comparison between: a) Two or more spatially distributed signals over a given time interval. b) Multiple time intervals at a given point location, or c) signals measured in tests carried out under differing experimental conditions. The following sections detail the methods used.

3.1 THE MEAN/INSTANTANEOUS PRESSURE DISTRIBUTION

3.1.1 *The mean/instantaneous pressure calculation*

To calculate mean or instantaneous pressure values, the reduced data file was manipulated using bespoke code named 'CPRMS versions 1 and 2', written in FORTRAN 77 for a UNIX platform. The first task of the CPRMS programme code in all cases was to read in the data into suitably configured arrays. The RIB information was fed into an single-dimension array for later output and the remainder was fed into a 3D array for calculation purposes.

The static case The next task of CPRMS1 (static cases) was to identify and segregate data collected at a given incidence. This was achieved in the static case by creating an array of 16 reference incidence values, which were fed, in turn, through a main loop whose task was to filter each row of data values. Each reference incidence array value was used as the test criterion used in an 'IF' statement to filter all data values, row by row, using the corresponding value of incidence found in Row 199 as the test subject. A sub-loop repeated the filter for each row of the data file (200 times) and employed an indexing counter to count the number of samples within each sub-loop. The integer value generated was

used later as the divisor in the averaging process. The filtering of each row was followed by a summation loop, after which the sum was divided by the sub-loop count value to produce 192 mean values of C_P, three acceleration values, and one value each of temperature, incidence and reference dynamic pressure. The main loop was repeated 16 times.

The pitching cases The process of identification and segregation of instantaneous C_P, acceleration, temperature, incidence and reference dynamic pressure values in the pitching cases using CPRMS2 was essentially similar to the mean calculations in the static case. However, the pitching case data sets were different from the static case, in that the values of C_P and other variables were collected continuously throughout the incidence range, rather than at discrete incidence values hence an average value was not applicable. In this analysis, for all pitching cases, the instantaneous pressure distributions were always indexed up (pitch up cases) or down (pitch down cases) in increments of 1°. Hence, for every pitching case, the reference incidence array filter contained 45 values and the main loop was repeated 45 times.

3.1.2 *The mean/instantaneous pressure surface distribution*

Having calculated the mean or instantaneous pressure values, subroutine 'CONPOINT' was called by CPRMS to generate a set of coordinate points for a right-angled-triangle-shaped grid system designed to represent the top surface of one half of a 60° delta wing. The grid contained 17 rows and 14 columns. Rows were numbered from the top, columns from the left. Row 1 represented the wing apex coordinates, Rows 2 - 16 represented the 15 rows of right-hand upper surface pressure transducer locations on the pressure test model (see Figure 2.2) and Row 17 represented the wing coordinates of the trailing-edge. Each row was vertically spaced according to the chordwise pitch of the transducer locations and the wing geometry of the pressure model, normalised by the root chord, (c).

Figure 2.2 reveals that the largest number of pressure transducers at a single chordwise location was thirteen. This occurred at x/c = 0.9, represented in this grid by Row 15. Hence, grid Columns 1 - 13 represented the spanwise locations of pressure transducers from the wing centreline towards the leading-edge, and included extra coordinate points in rows where transducers were absent. Column 14 represented the wing coordinates of the leading-edge. Each column was horizontally spaced according to the spanwise pitch of the transducer locations and the wing geometry of the pressure model, this time, normalised by the local semi-span, (s). The coordinate system for the sharp and round-nosed wing variants were similar for Rows 3 - 17, i.e. aft of the round-nosed radius centre at x/c = 0.125 shown in Figure 2.4. However, for the round-nosed wing grid, the column coordinate values in Rows 1 and 2 were revised to produce a rounded shape in common with the planform shape of the model.

Having generated the grid, extra C_P values were calculated using a sub-routine called 'CPCAL'. This was based on a three point Lagrangian extrapolation method which was developed for the previous research programme and was adapted for the delta wing data by Dr. Frank Coton of the Department. The C_P values generated included those where transducers were absent on the wing surface, those at the wing apex in its sharp and round-nosed forms and those at the wing leading and trailing-edges. When the subroutines were complete, the resulting full data set generated by CPRMS included three separate sub-sets: 1) x-coordinates (row position), 2) y-coordinates (column position), and 3) C_P values. All full data sets were written to file in a text format, allowing screen checking and use by another code format.

The full surface contour plots of the mean pressure distribution shown in Chapter 4 were produced using a programme named 'CPCON' written in Visual Numerics PV-Wave CL programming language. The 'CONTOUR' command

allowed a 3D image, (i.e. the 'out of page' direction represented in the diagram by colour or grey-scale contours), to be built using the three sub-sets of data produced by the CPRMS programme as the x, y and z variables of the contour plot. Using the CONTOUR command, the combination of setting upper and lower limits and the total number of contours in the z-direction, determined the C_P range assigned to each contour level. The results shown in Chapter 4 have the upper limit set at +1.0, the lower limit at -12.0 and contour levels at 150 per plot. Grey-scale levels were assigned to contour levels using the 'CONTOURFILL' command. The PV-Wave package has a grey-scale palette of 256 blacks, greys and whites each allocated a palette number, (i.e., very black = 0, very white = 256), which are recognised by the CONTOURFILL command. The specification of a particular grey-scale palette number to a given contour range was determined by a sub-routine in the code which allocated white and lighter shades of grey to high values of negative C_P, and darker shades of grey and black to lower negative values and positive values of C_P. The specification routine allowed a choice of minimum and maximum grey-scale numbers and incorporated a bias mechanism which added a weighting factor to lower palette numbers. This gave greater grey-scale resolution where C_P pressure gradients were lowest in order to highlight the limits of mean pressure flowfield features on the surface of the wing.

3.2 THE ROOT-MEAN-SQUARE PRESSURE DISTRIBUTION

3.2.1 *The Root-Mean-Square pressure calculation*

The calculation of Root-Mean-Square (RMS) pressure values was also carried out within the CPRMS programme, the reading-in and segregation of data values by incidence, being shared between the two calculation processes. The RMS pressure values are a measure of the statistical standard deviation of the signal and as such provide the magnitude of the fluctuating component of pressure around the mean value. The calculation of the RMS pressure values involved obtaining a trend line

by applying a linear best-fit through the data contained within a pre-determined 'incidence window'. The trend line was determined using the following formulae from Lapin (1993).

$$\acute{y} = a + bx \tag{3.1}$$

Where:

$$b = \frac{n\Sigma xy - \Sigma x\Sigma y}{n\Sigma x^2 - (\Sigma x)^2} \tag{3.2}$$

And:

$$a = y_{(mean)} - bx_{(mean)} \tag{3.3}$$

x = incidence values from Row 199. y = corresponding C_P values from Rows 1 - 192
$x_{(mean)} = \Sigma x/n$, $y_{(mean)} = \Sigma y/n$, n = number of data values within the incidence window.

Given that: $x_{(mean)} = \Sigma x/n$ and $y_{(mean)} = \Sigma y/n$, Formula 3.2 was simplified to:

$$b = \frac{\Sigma xy - n(x_{(mean)}\, y_{(mean)})}{\Sigma x^2 - n(x_{(mean)})^2} \tag{3.4}$$

The advantage of computing the calculation of b from Formula 3.4 is that each step involves computations with values of moderate size. Although this increases the danger of rounding errors, such errors are usually negligible (Lapin ibid.). The RMS values were then determined by the calculation of the standard deviation of pressure fluctuations about the trend line. The standard deviation was calculated using the following formula, also adapted from Lapin (ibid.)

$$\sigma = \sqrt{\left(\frac{\Sigma(y - y_{(trend)})^2}{n}\right)} \tag{3.5}$$

Where: $y_{(trend)}$ = the value of y on the trend line whose corresponding incidence value (x) is also that of the data value (y) under consideration.

The method of fitting a trend line and calculating RMS values was applied in pitching cases only. For the static case, there were problems in the trend line calculation. This was due, in some instances, to the calculation of the denominator in Equation 3.4 finding a value equal to zero. The result was a computed gradient of infinity for the subsequent trend line calculation. Therefore, calculations of the RMS pressures in the static case used $y_{(mean)}$ in a modified Equation 3.5 to replace the trend line value $y_{(trend)}$. $y_{(mean)}$ was taken as the mean value of all 2000 samples collected an incidence in question, where all 2000 values were included in the RMS calculation.

Due to the 'continuous' nature of the pitching case data collection process, the sample size for each pitching case calculation could be adjusted by nominating various upper and lower limits to create incidence 'windows' of different size, within which the corresponding values of C_P could have the RMS calculation performed on them. In this RMS analysis, the sample size was varied from approximately 300 data values using a 1° incidence 'window' in a 70°/s pitch up case, where each cycle was sampled at 5.18kHz (i.e. 75 values per cycle for each of the 4 cycles in the data set), to 1400 data values using a 4° incidence window in a 120°/s pitch up case, where each cycle was sampled at 10.38kHz (i.e. 4 cycles of 350 values per cycle). Having set the incidence window, it is clearly possible to nominate any value within its limits as the incidence under consideration. For this analysis, the incidences presented in Chapter 4 are those which sat centrally within the chosen incidence window limits and the calculation was performed in 1° incidence increments such that the calculation was repeated 45 times.

3.2.2 *The RMS pressure surface distribution*

The sub-routines CONPOINT and CPCAL were also employed in the RMS pressure surface distribution calculation to generate sub-sets of wing x-coordinates and y-coordinates, and to carry an interpolation routine to generate extra RMS values in the absence of transducer locations. The output of CPRMS consisted of three sub-sets of 3D arrays. The first and second subsets contained x-coordinates and y-coordinates respectively, and the third contained alternate rows of C_P and RMS data values.

The PV-Wave code used to generate images of RMS pressure contours called 'RMSCON' was developed from the CPCON programme for C_P pressure cases. The range of RMS value magnitudes were clearly different and always positive. Hence, the code required adjustment to suit. The upper and lower limits of z-variable range were reduced and narrowed to +0.12 and 0.0 respectively, although the number of contours remained at 150. The grey-scale specification routine was adjusted to allocate white and lighter shades of grey to higher values of RMS pressure and darker grey and black shades to RMS values approaching zero. The bias was also adjusted to give a weighting towards higher palette numbers to give greater grey-scale resolution where RMS pressure gradients were highest to give definition between closely-spaced but distinct unsteady flowfield features on the surface of the wing.

3.3 SIGNAL ENERGY

The advantage of using a cumulative pressure signal energy analysis over the RMS pressure analysis method in the detection and tracking of vortex flow surface features in pitching cases, is that frequency resolution problems and complicated choices of optimum incidence window size cease to be an issue. The rationale behind this analysis, however, is similar to the previous two analyses where large

increases in the magnitude of pressure fluctuations were seen to appear in the data when the instantaneous incidence under consideration was increased to, and beyond, the point where vortex breakdown was known to be present over the surface of the wing. Hence, it was thought that a cumulative summation of the pressure signal energy should be able to detect any non-linear rise in the magnitude of pressure fluctuations.

The energy content of the fluctuating pressure signal generated by each upper surface pressure transducer was calculated using a programme called 'ENERGY' written in FORTRAN 77. For this analysis, each of the four cycles contained in the reduced data file was treated separately, hence the first task of ENERGY was to read in 200 rows of 8000 samples of C_P pressure data. The energy or average power of a signal is given by (adapted from Lynn (1982)):

$$\text{average power} = \int_b^a p(y) \cdot y^2 \, dt \qquad (3.6)$$

Where: a = Incidence (Row 199) upper limit of 40°, b = Incidence (Row 199) lower limit of 0°, and p(y) = an amplitude probability density function.

The procedure involved a calculation of the square of the magnitude of pressure fluctuations either side of a mean value, and a summation of those fluctuations across an incidence range of 0° to 39° inclusive. The main loop of the programme was designed to segregate C_P pressure data using a nominal incidence window of 1°, and obtain a trend line by applying a linear best-fit through the segregated values in a similar manner to the CPRMS programme in the RMS analysis. This was not a requirement of the calculation, but provided a simple means of identification in terms of incidence for the plotting programme. The incidence window was carefully set such that there was no overlap of samples, or missed samples, from one window to the next. Having calculated the trend line, the

signal was processed to remove the d.c. component and the result squared prior to integration. The integration process, for each iteration of the main programme loop, involved the use of a simple summation sub-loop resulting in an output value to fill an array of 40 values per row to be written to file. The output value of the first iteration of the main loop served as the input value for the second iteration, and so on, hence, the output array was, in effect, a series of 40 snapshots taken during the summation process each identifiable with a value of incidence.

The output array was written to file in a text format for use in a PV-Wave image creation programme called 'EPLOT versions 1 to 3'. Each version of EPLOT used the PV-Wave PLOT command, as described in Section 3.3, to create the signal energy image. The x-axis values were created simply using an indexing loop to create an array of 40 values from 0 to 39. The y-axis values in EPLOT1 were input from ENERGY. Figure 3.2, plot a) shows one set of 8000 data samples taken from transducer T47 located at $x/c = 0.6$, $y/s = 0.6$ measured during a pitch up cycle at a reduced pitch rate, $k = 0.015$. What is clear from the plot is the steady increase in suction as the first 2400 samples of pressure data were collected during the early stages of the ramp manoeuvre. This was followed by a sudden increase in pressure fluctuations during the middle of the cycle for a duration of approximately 2800 samples (0.27 seconds of sampling duration at 10.38kHz, or 16.9 convective time units), and then a reduction in activity and suction as the wing approaches very high incidence and behaves more like a bluff body. Plot b) shows that, by inspection, this increase in signal energy as occurring somewhere in the incidence range 14° to 20°, and is indeed not so sudden as first impressions might suggest. Clearly, with these error limits, the measurement of signal energy alone did not provide an accurate method of tracking features such as vortex breakdown. Hence, a number techniques were applied to find a better method of pinpointing the breakpoint in the increase in signal energy, two of which are described here. The first was to increase the number of iterations in the

summation procedure to 80 and then 160. This produced no significant difference in signal energy output, but did serve as a useful validation exercise for

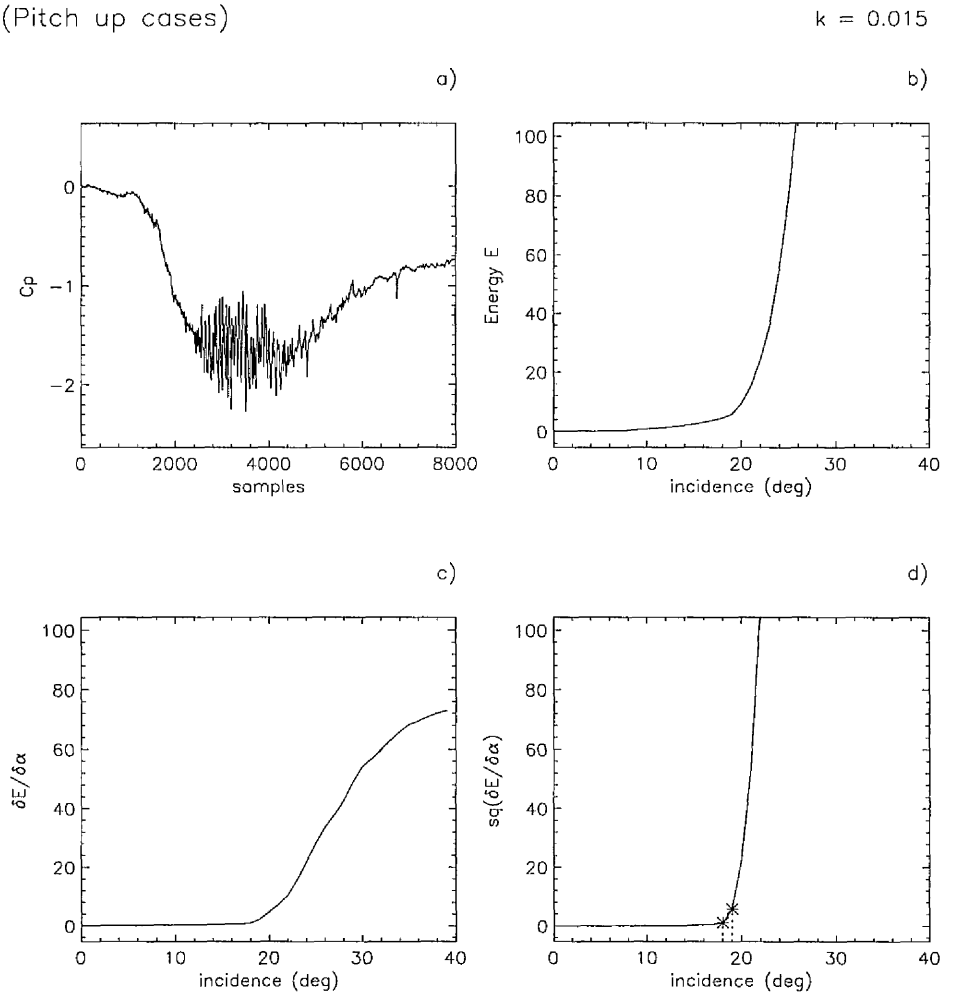

Figure 3.2 - Results from transducer T47, located at x/c = 0.6, y/s = 0.6 in a pitch up case, k = 0.015 showing a) the C_P pressure signal against sample count, b) the signal energy E, c) the first derivative of E wrt incidence, $\delta E/\delta\alpha$, and d) $(\delta E/\delta\alpha)^2$, each plotted against incidence. Note: plot d) includes Energy Data Reference Incidences, EDRI's (*).

the iteration method. The second method was to take the first derivative of the calculated signal energy values with respect to incidence. Plot c) shows that, by using the first derivative, the incidence corresponding to the breakpoint can be narrowed to the range 18° to 20°. The breakpoint could be sharpened further still by squaring the result to produce $(\delta E/\delta\alpha)^2$ and this is shown in Plot d). Two incidence values were plotted: 1) the incidence at which $(\delta E/\delta\alpha)^2$ first reached an arbitrary value of 2.0, as incidence was increased from 0° to 40°, where the signal energy had started to increase in a non-linear manner, and 2) at a value of 10.0, where the violent increase in signal energy could be said to be well under way. This provided a valid comparison between the range of potential breakpoint incidence values from one transducer to the next. Hence, the breakpoint in the increase in pressure signal energy could be said to lie within a narrow 'corridor' of Energy Data Reference Incidence (EDRI) limits that could then be plotted for a series of transducer locations against chordwise distance from the wing apex, (x/c), and compared with vortex breakdown locations determined by visualisation methods. The results of this analysis are presented in Chapter 4.

3.4 FREQUENCY SPECTRA

A series of FORTRAN 77 and PV-Wave CL code programmes were used in two separate exercises designed to calculate the frequency power spectra of pressure fluctuations for a range of transducer locations on the leeward side of the pressure test model. The first exercise was primarily concerned with the analysis of vortex breakdown buffet frequency calculations. This exercise required only frequency content and magnitude output and so made use of a Fast Fourier Transform (FFT) library routine within PV-Wave. The second exercise was concerned with the analysis of the cross-spectral density function of two pressure signals and therefore additionally required phase measurements which the PV-Wave routine

was unable to supply. This problem was solved by employing a series of FORTRAN library routines which were able to output both the magnitude and phase of frequency spectra. The second exercise will be discussed in Section 3.5, where in addition, the two methods will be compared.

The subject of this section concerns the calculation of vortex breakdown buffet frequencies using a PV-Wave programme called 'SPECMP versions 1 to 3'. Before input into the programme, the reduced data files were manipulated using FORTRAN code 'SPECTRUM' which was developed from the earlier CPRMS programme. It was designed to separate the RIB from the reduced data file and output selected sets of data, each defined by incidence criteria, (i.e. one incidence value in the static case, or an incidence window in the pitching cases) using the same methods employed in the pre-calculation stages of CPRMS. The RIB data was output as an unformatted ASCII file and the C_P data output was written in a text format for input into the subsequent PV-Wave code.

Static cases The calculation of frequency spectra in the static case was carried out by SPECMP1. This used a PV-Wave library function 'FFT' which employed the Cooley-Tukey algorithm to calculate the single-sided Fourier transform of a scaled-time function, defined as:

$$H(f) = \int_0^\infty h(t)e^{-j\omega t}\,dt \qquad (3.7)$$

Where: f relates to the frequency domain, and t relates to the time (space) domain

The input to the FFT calculation was processed to remove the d.c. content from the C_P pressure signal. The output of the FFT function returned an array of complex values, the real part described by the output data and the imaginary part set to zero. Hence, the inability of the FFT function to contribute to the

calculation of phase values. The one-sided output function calculated by the FFT command had frequency limits of $0 \leq f < \infty$, (a two-sided output function would have limits of $-\infty < f < \infty$), and the output array had the same number and size of dimensions as the input. The magnitude of the output values, called the one-sided Power Spectral Density or PSD, was normalised by a factor of 1/n, where n was the number of data values in the input array, to produce the one-sided PSD per unit time.

The plotting routine for the calculated frequency data was also included in SPECMP1. Images were constructed using the 'PLOT" command, (the 2D version of CONTOUR) which required the input of x and y variables. In this case, the y-variable was the calculated PSD data, and the x-variable was an floating-type array generated by a programme sub-loop. This sub-loop generated a set of array values by indexing from 0 to (n-1) and multiplying the index value by f_s/n, where f_s equals the data sampling frequency (1.0kHz in the static case). The sampling frequency information was input into the programme from the RIB data extracted from the reduced data file by the SPECTRUM programme.

Pitching cases The calculation and presentation of the frequency spectra in the pitching cases was carried out using the SPECMP2 programme. The FFT calculation and the presentation of results were carried out in a similar manner to the static cases, however, the pitching motion of the wing presented additional factors that had to be considered. For example, a data sample extracted from a pitching wing full data set over any given 1° incidence window having a linear pitch rate of 120°/s, would have a sample period of 1/120 second. A frequency analysis would be unable to successfully resolve frequencies whose period was greater than half the sample period, i.e. 1/240 second, which would fail to meet the Nyquist criterion. Hence, for a 1° incidence window, frequencies of less than

240 Hz cannot be resolved. To solve this problem, a high-pass filter was employed in the SPECMP2 programme to remove the frequencies below the critical frequency, prior to the FFT calculation.

The PV-Wave 'DIGITAL_FILTER' and 'CONVOL' library functions were used in series to construct a Finite Impulse Response (FIR) digital filter. The DIGITAL_FILTER function returned the coefficients of a convolution kernel which were then passed through the CONVOL function to apply the filter to the signal. The array size of the kernel was equal to (2 x NTERM) - 1, where NTERM was the number of terms in the filter formula and determined the order of the filter. NTERM was one of five input parameters that could be independently controlled by the user. The remainder were: 'FLOW' - the value of the low-pass frequency of the filter, 'FHIGH' - the value of the high-pass frequency of the filter, these were both expressed as a fraction of the upper Nyquist frequency, 'GIBBS' - the size of the Gibbs Phenomenon variations, expressed in decibels (-dB), and 'CENTRE' - the ability to undo the phase shift imparted on the output signal by linear-phase delay, a feature of the FIR filtering process. Thus, 'CENTRE = 1' switches phase centering on and 'CENTRE = 0' leaves phase centering switched off. The Gibbs Phenomenon variations are oscillations which result from the abrupt truncation of the infinite Fourier series (Lynn (1982)). The PV-Wave user notes warned that setting GIBBS too high or low may produce unacceptable results. It recommended a value of 50 -dB for most applications, and this, together with a FHIGH value of 1.0 and phase centering, was used for all calculations whose results are shown in Chapter 5. The parameters FLOW and NTERM were tested to assess their effect on a given signal prior to their application to 'real' data. To assess the effect on filter efficiency and to promote correct usage, a series of tests were performed using a much simpler signal waveform. A third filtering programme was written and called 'SPECMP3'. This programme used a sine wave to test the effects of input

parameter variations and also the effect of filtered sample size with respect to the FFT calculation input sample size. This was important due to the transient start up characteristics of the filter. The recurrence formula, which relates input and output sample values of the digital filter, takes the general form (Lynn (1982)):

$$y(n) = a_1 y(n-1) + a_2 \cdot y(n-2) + \ldots + b_0 x(n) + b_1 \cdot x(n-1) + b_2 \cdot x(n-2) + \ldots \quad (3.8)$$

The first non-zero output value occurs when the first non-zero data value is delivered to the filter's input. Hence, the first non-zero output is b_0 times the first non-zero input. As more non-zero inputs are applied to the filter, then more terms in the recurrence formula take on finite values, until finally all terms are taken into account. This means that if a steady level input, or a sinusoidal input is applied to the filter, then a number of sampling periods will elapse before the output reaches its 'steady-state' response, i.e. the filter exhibits a start up transient. This characteristic means to get a valid output from the final FFT calculation, it is necessary to filter more data samples than are actually passed through the FFT calculation stage. Section 3.1.1 revealed that, in the instantaneous pressure analysis, up to 1400 values made up a sample of data in a 4° incidence window at a linear pitch rate of 120°/s. Hence, in a similar analysis of the frequency content of pressure fluctuations, the same number of values may pass through the final FFT calculation. Therefore, a series of sine waves, each with the formula: $y = \sin x + \sin 10x$, was tested. The resolution the data that made up each sine wave was one data value per degree of sine wave, hence 360 data values made up one sine wave cycle and the effective sampling rate was 360Hz. Thus, the Nyquist sampling cut-off frequency in this case was 180Hz. The purpose of the tests was to filter out the 1Hz sine wave cycle frequency component (i.e. sin x) and leave the 10Hz frequency component (sin 10x) unaffected. Hence, the low-pass

frequency was set at 2Hz by setting FLOW to a value of 2/180 = 0.0111. Three tests of sample size were carried out, such that 1400, 2800, and 5600 data values were filtered. For each test, 1400 filtered values were passed through the final FFT calculation. Similarly, the effect of variations in the NTERM parameter were tested using the following values: 1, 10, 100, 200 and 400. The summary of these test results are shown in Figures 3.3 to 3.9. Figure 3.3 shows a signal of 1400 data samples and its frequency spectrum in unfiltered/filtered format where all 1400 samples were passed into the FFT calculation. In this case, NTERM =1 and shows that the filter in this format has no effect on the input waveform. Figure 3.4 shows the same signal, but for this test, NTERM = 10. Already, the effects of the start up transient are evident in the filtered signal resulting in a undesirable reduced magnitude of the 10Hz spike shown in the filtered frequency spectrum. If NTERM is increased to 100, as shown in Figure 3.5, the 1Hz spike is being filtered out but the 10Hz spike is worse affected. If the filtered sample set is increased to 2800 values, and values 721 to 2120 inc. are passed through the FFT calculation, then the effects of the start up transient on the FFT output are negated. Figure 3.6 shows a restored 10Hz spike and the partial suppression of the 1Hz frequency content. By increasing NTERM to 200, as shown in Figure 3.7, the 1Hz frequency content is further reduced with no transient interference and is suppressed completely when NTERM = 400 (Figure 3.8). A further increase in the filtered sample size to 5600, where values 2161 to 3560 were passed though the FFT calculation, revealed no increased benefit (Figure 3.9). Finally, Figure 3.10 shows the application of these results to a 'real' pitch up case, (k = 0.015), where the linear pitch rate =120°/s, sampling frequency = 10.38kHz, and incidence window = 2°. The lower cut-off frequency = 120Hz and the upper Nyquist frequency = 5.19kHz, hence FLOW = 120/5190 = 0.0231. Figure 3.10 shows the successful suppression of the frequencies below 120Hz, without detrimentally affecting higher frequencies of interest.

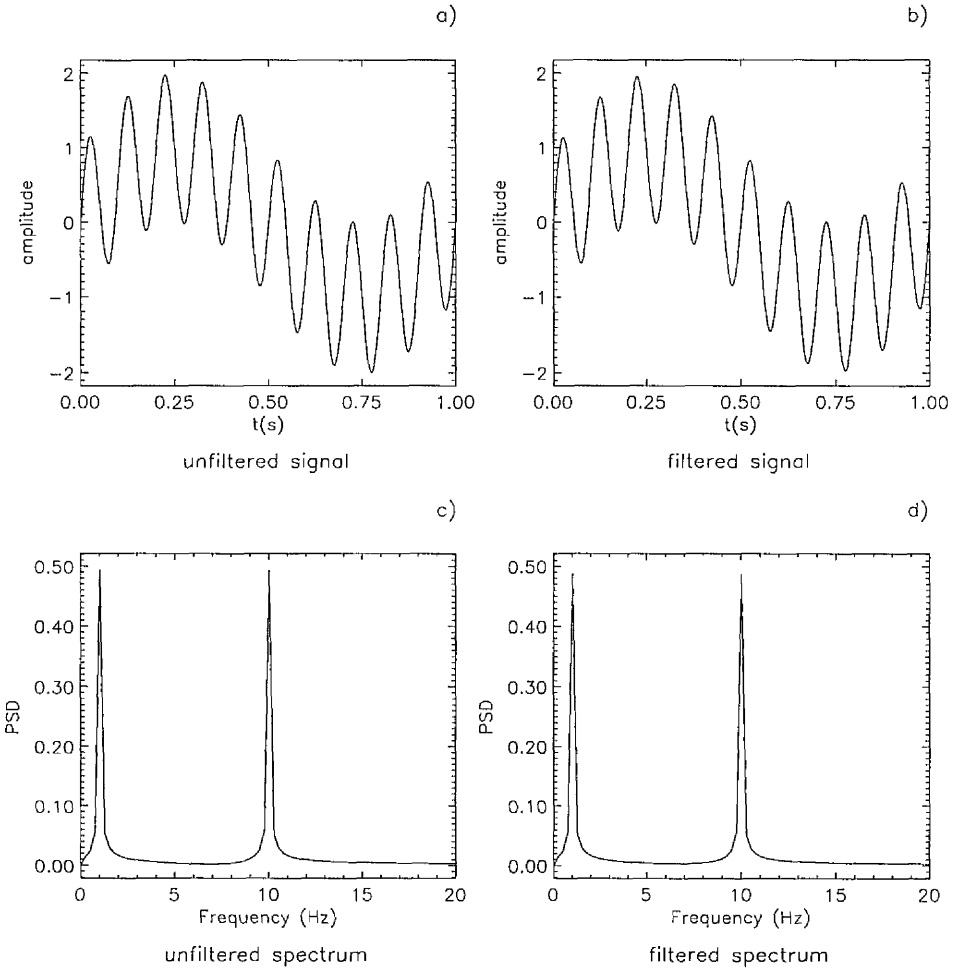

Figure 3.3 - Results of filtering tests on a y = sin x + sin 10x waveform. Showing signal and frequency spectrum in both unfiltered and filtered formats. 1400 filtered samples, 1400 samples input to FFT calculation, FHIGH = 1.0, FLOW = 0.0111, GIBBS = 50, NTERM = 1.

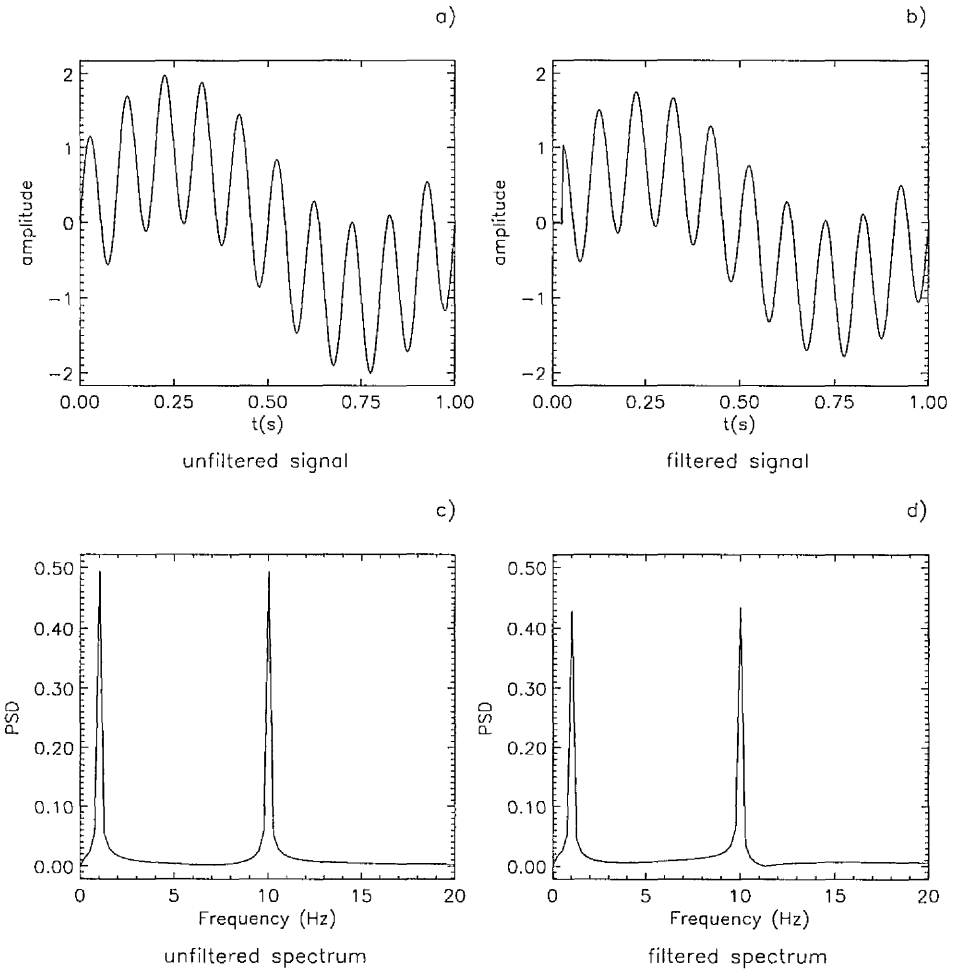

Figure 3.4 - Results of filtering tests on a y = sin x + sin 10x waveform. Showing signal and frequency spectrum in both unfiltered and filtered formats. 1400 filtered samples, 1400 samples input to FFT calculation, FHIGH = 1.0, FLOW = 0.0111, GIBBS = 50, **NTERM = 10.**

Note: **bold** type denotes change of parameter from previous figure.

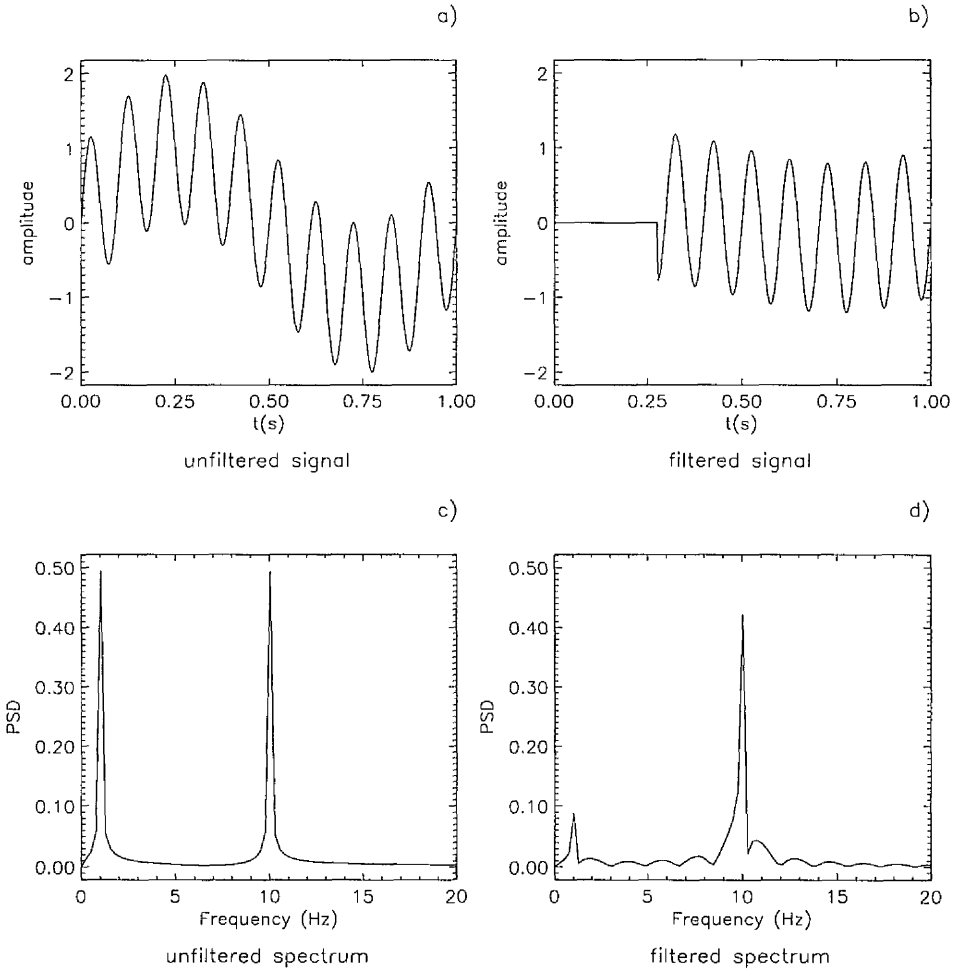

Figure 3.5 - Results of filtering tests on a y = sin x + sin 10x waveform. Showing signal and frequency spectrum in both unfiltered and filtered formats. 1400 filtered samples, 1400 samples input to FFT calculation, FHIGH = 1.0, FLOW = 0.0111, GIBBS = 50, **NTERM = 100**.

Note: **bold** type denotes change of parameter from previous figure.

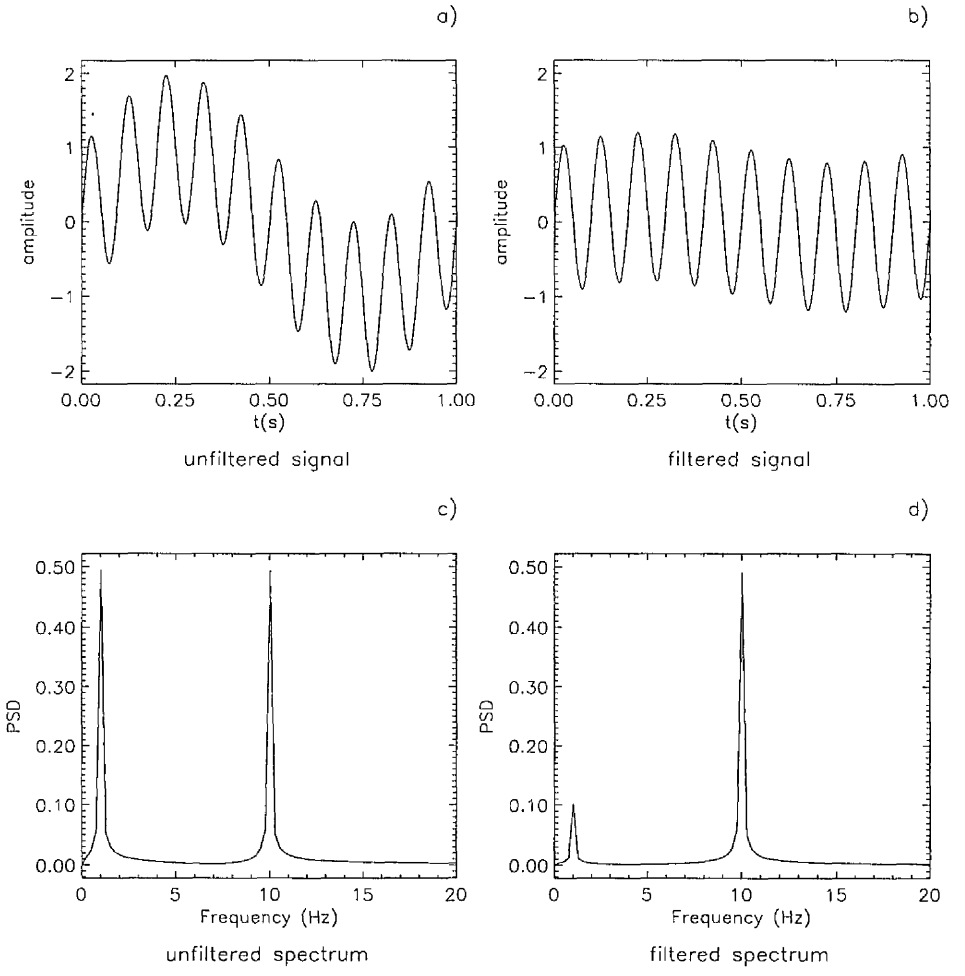

Figure 3.6 - Results of filtering tests on a y = sin x + sin 10x waveform. Showing signal and frequency spectrum in both unfiltered and filtered formats. **2800 filtered samples**, 1400 samples input to FFT calculation, FHIGH = 1.0, FLOW = 0.0111, GIBBS = 50, NTERM = 100.

Note: **bold** type denotes change of parameter from previous figure.

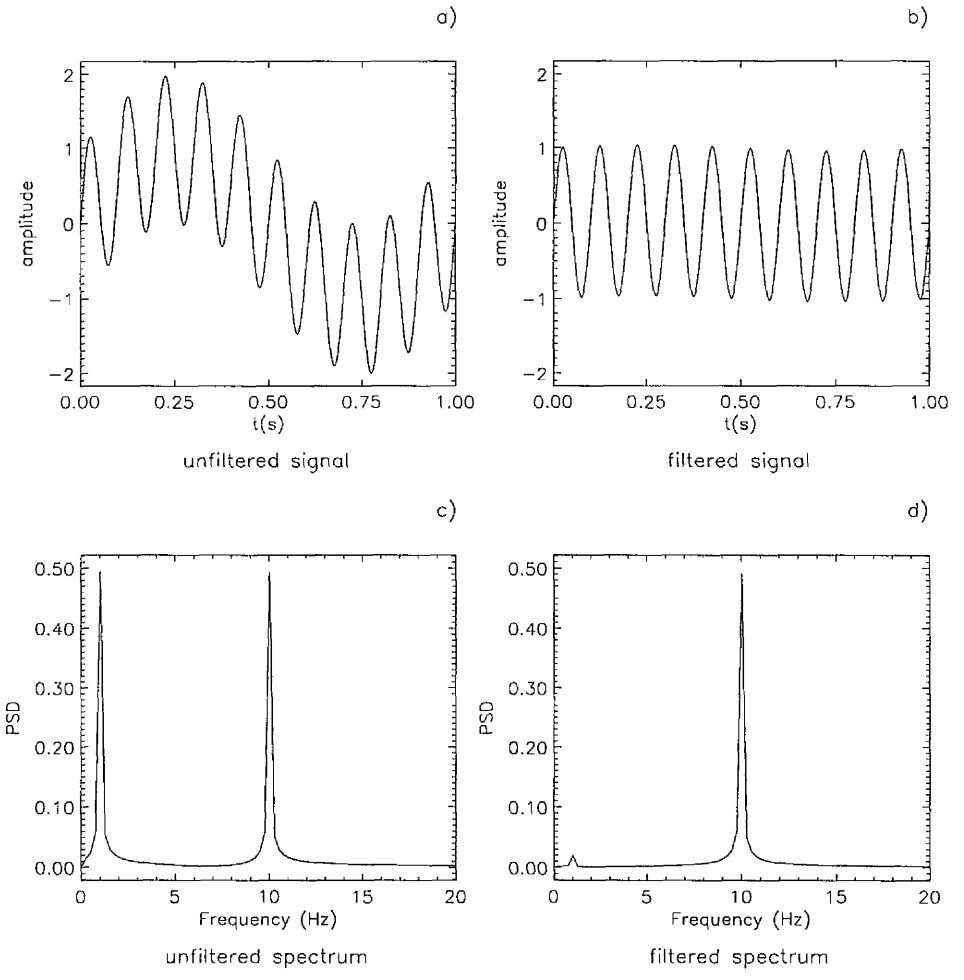

Figure 3.7 - Results of filtering tests on a y = sin x + sin 10x waveform. Showing signal and frequency spectrum in both unfiltered and filtered formats. 2800 filtered samples, 1400 samples input to FFT calculation, FHIGH = 1.0, FLOW = 0.0111, GIBBS = 50, **NTERM = 200**.

Note: **bold** type denotes change of parameter from previous figure.

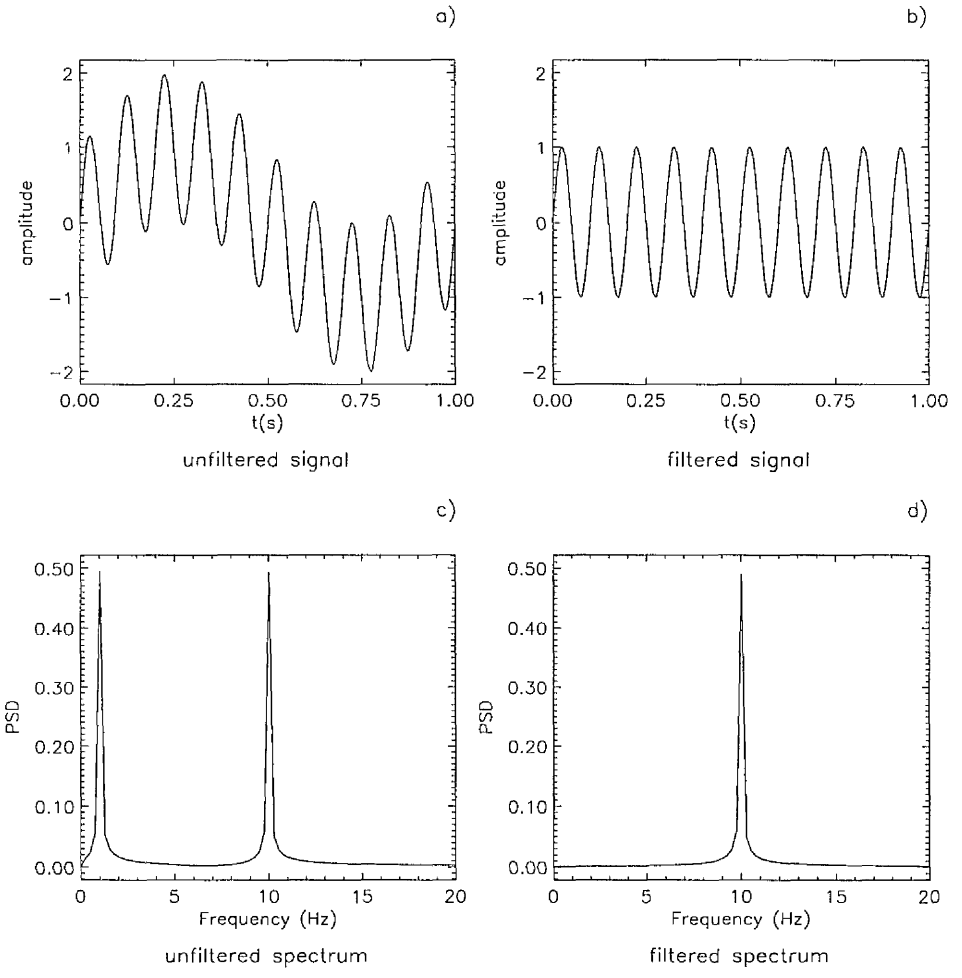

Figure 3.8 - Results of filtering tests on a y = sin x + sin 10x waveform. Showing signal and frequency spectrum in both unfiltered and filtered formats. 2800 filtered samples, 1400 samples input to FFT calculation, FHIGH = 1.0, FLOW = 0.0111, GIBBS = 50, **NTERM = 400**.

Note: **bold** type denotes change of parameter from previous figure.

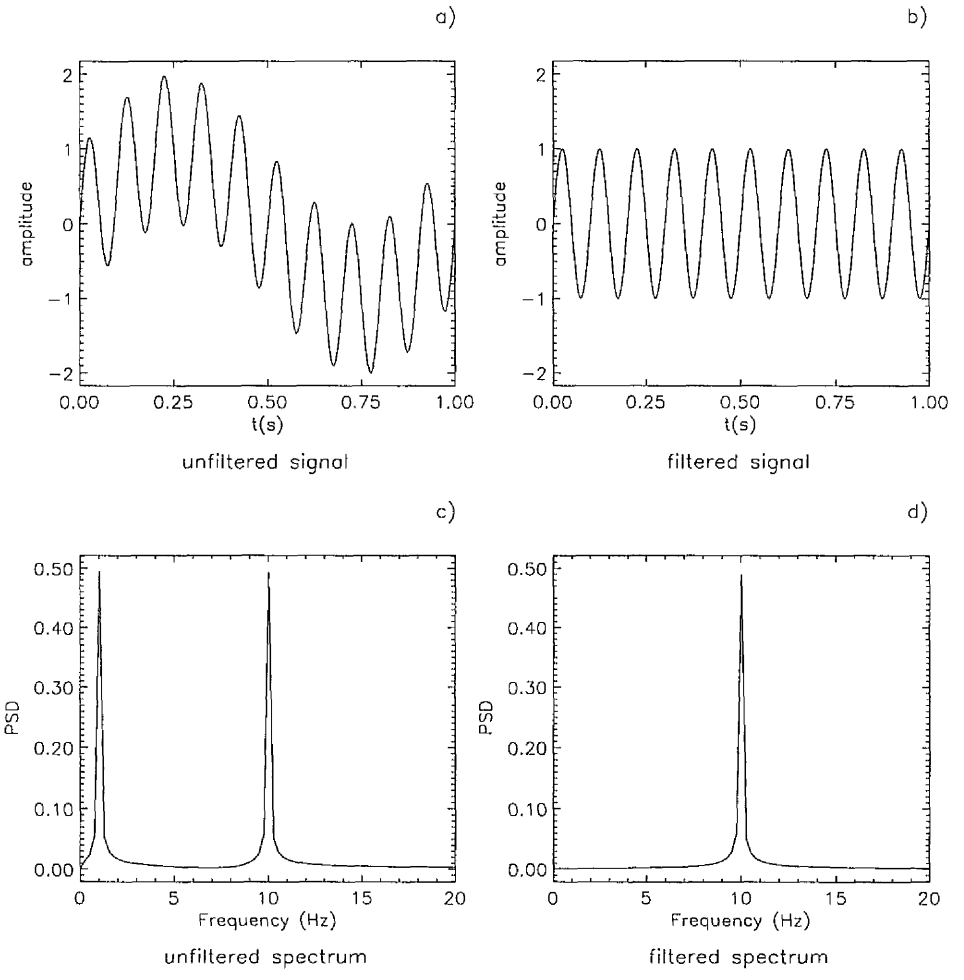

Figure 3.9 - Results of filtering tests on a y = sin x + sin 10x waveform. Showing signal and frequency spectrum in both unfiltered and filtered formats. **5600 filtered samples**, 1400 samples input to FFT calculation, FHIGH = 1.0, FLOW = 0.0111, GIBBS = 50, NTERM = 400.

Note: **bold** type denotes change of parameter from previous figure.

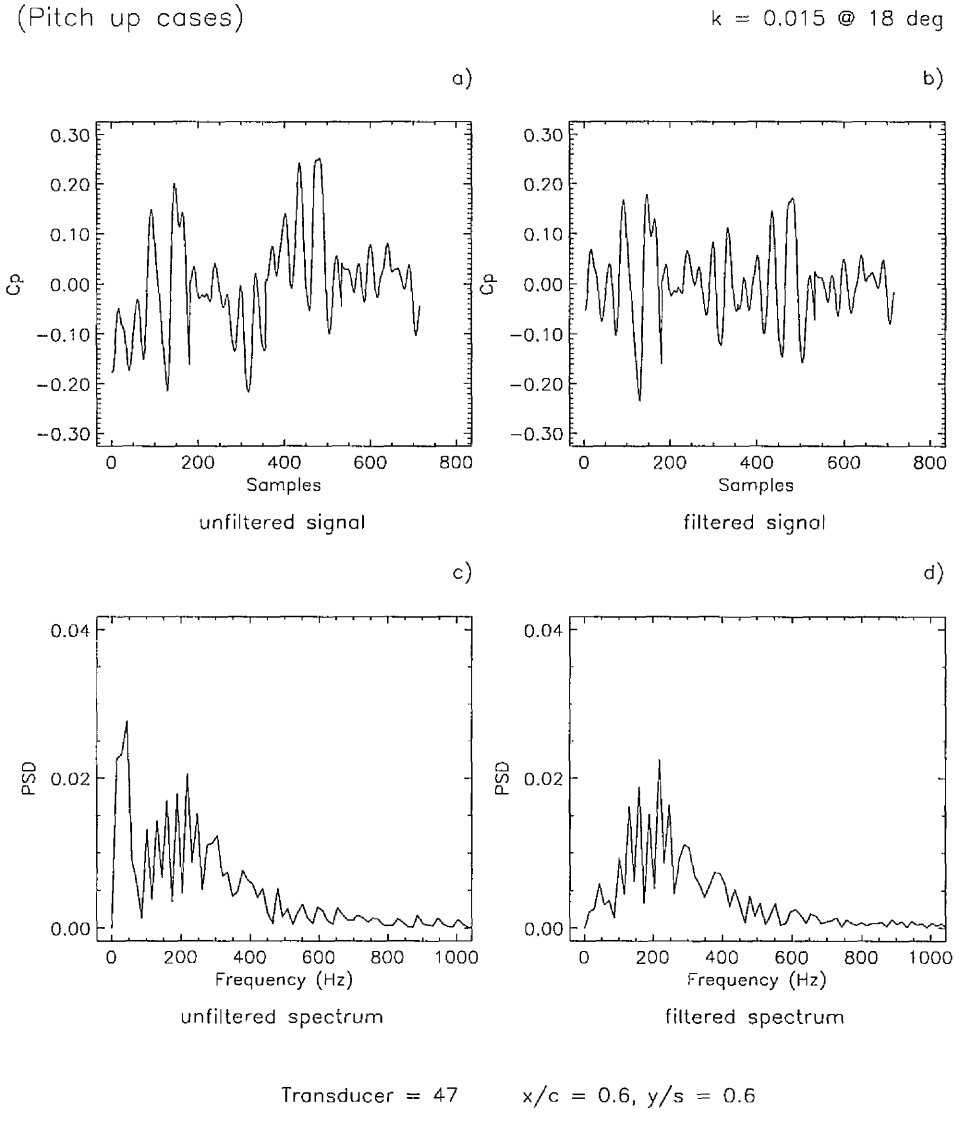

Figure 3.10 - Results of filtering tests on a 'real' data waveform from a pitch up case, k = 0.015 @ 18° instantaneous incidence, using a 2° incidence window. Showing signal and frequency spectrum in both unfiltered and filtered formats. **1500 filtered samples, 724 samples** input to FFT calculation, FHIGH = 1.0, **FLOW = 0.0231**, GIBBS = 50, NTERM = 400.

Note: **bold** type denotes change of parameter from previous figure.

3.5 CROSS-SPECTRAL DENSITY FUNCTION

The cross-spectral density relationship of magnitude and phase between the output of two pressure transducers can provide valuable insights into the behaviour of the flowfield just above the surface of the wing, (Gursul 1994). The measures of statistical properties so far described have been used primarily as a basis for a subjective comparison between two or more pressure signals. However, it is also possible to calculate a quantitative value of the shared signal frequency content of two signals and so establish their relationship in terms of shared frequency components. This frequency relationship between two transducer signals, measured at various positions on the surface of the wing can, under certain circumstances, provide information regarding the direction of movement of disturbances in the vortex flowfield.

The relationship of two signals in terms of the cross-spectral density function in the frequency domain may be expressed as (Lynn 1982):

$$P_{xy}(\omega) = \int_{-\infty}^{\infty} r_{xy}(\tau) \cdot e^{-j\omega t} \cdot d\tau \qquad (3.9)$$

Where $r_{xy}(\tau)$ = the cross correlation function in the time domain expressed as:

$$r_{xy}(\tau) = \int_{-\infty}^{\infty} f_1(t) \cdot f_2(t + \tau) \cdot dt \qquad (3.10)$$

Where f_1 and f_2 are the two signals under consideration and τ is an imposed time shift.

It is convenient to split the cross-spectrum function $P_{xy}(\omega)$ into its real and imaginary parts, hence:

$$P_{xy}(\omega) = C_{xy}(\omega) + jQ_{xy}(\omega) \tag{3.11}$$

Where $C_{xy}(\omega)$ is called the 'co-spectrum' and $Q_{xy}(\omega)$ the 'quadrature-spectrum'.

Therefore:

$$| P_{xy}(\omega) | = (C_{xy}^2(\omega) + Q_{xy}^2(\omega))^{1/2} \tag{3.12}$$

and:

$$\phi_{xy}(\omega) = \tan^{-1} \left[\frac{Q_{xy}(\omega)}{C_{xy}(\omega)} \right] \tag{3.13}$$

Where $\phi_{xy}(\omega)$ = the phase difference between components in the two signals at a given frequency ω.

Data to be analysed were first segregated by incidence and transducer value using PV-Wave programmes called 'DATASET versions 1 and 2'. The output file from DATASET supplied one set of data for a given transducer taken over a pre-determined incidence window, preceded by an index value stating the number of subsequent data values contained therein. DATASET2 was modified to include a filtering routine for pitching case data similar to that found in the SPECMP2 programme for frequency analysis. The data files created by DATASET where then input into a FORTRAN programme called 'FOURIER' which was designed to calculate the discrete Fourier transform of the data set using the NAG library routine 'C06EAF'. This provided an opportunity to compare the FFT output of the PV-Wave and NAG library routines. The NAG library routine differs from

the PV-Wave routine in that the output was normalised by a factor of $1/(n)^{1/2}$ (as opposed to $1/n$), where n was the number of data values in the input array, to produce the one-sided PSD per unit time. Hence, to obtain comparable values, the NAG output was multiplied by a factor of $1/(n)^{1/2}$. The output from FOURIER was in the form of the co-spectrum and its corresponding quadrature-spectrum as shown by Formula 3.11, therefore another FORTRAN programme called 'PHASE' was written to calculate the PSD magnitude and phase angle using Formulas 3.12 and 3.13. Shown in Figure 3.11, for a single transducer located at $x/c = 0.6$, $y/s = 0.6$, at an incidence of 18° in the $k = 0.015$ pitch up case, are: plot a) - the NAG output magnitude, plot b) - the PV-Wave output magnitude, plot c) - the NAG output phase and plot d) - the filtered sample under consideration. Comparison of the two magnitude plots by inspection showed no significant differences in the output spectra produced by the two routines.

The data files created by DATASET were also input into FORTRAN programmes called 'CROSS versions 1 and 2', designed to calculate the cross-spectral density function of two data sets of equal length, for static and pitching cases respectively. This was achieved using NAG library routine G13CCF which was capable of calculating the smoothed cross-spectrum using one of four possible smoothing methods - Rectangular, Bartlett, Tukey or Parzen. Each method was tested to assess the effect on two data sets of 2000 and 714 values from the static and $k = 0.015$ pitch up cases respectively, at an instantaneous incidence of 18°. There appeared, by inspection, to be no significant differences in the output of each calculation, although the rectangular window is generally regarded as being the least satisfactory and the Parzen window the most adaptable for the analysis of random signals (Lynn 1982), hence, for all cross-spectral density results shown in Chapter 5, the Parzen smoothing window was the one used. The biggest problem in applying the cross-spectrum calculation routine to

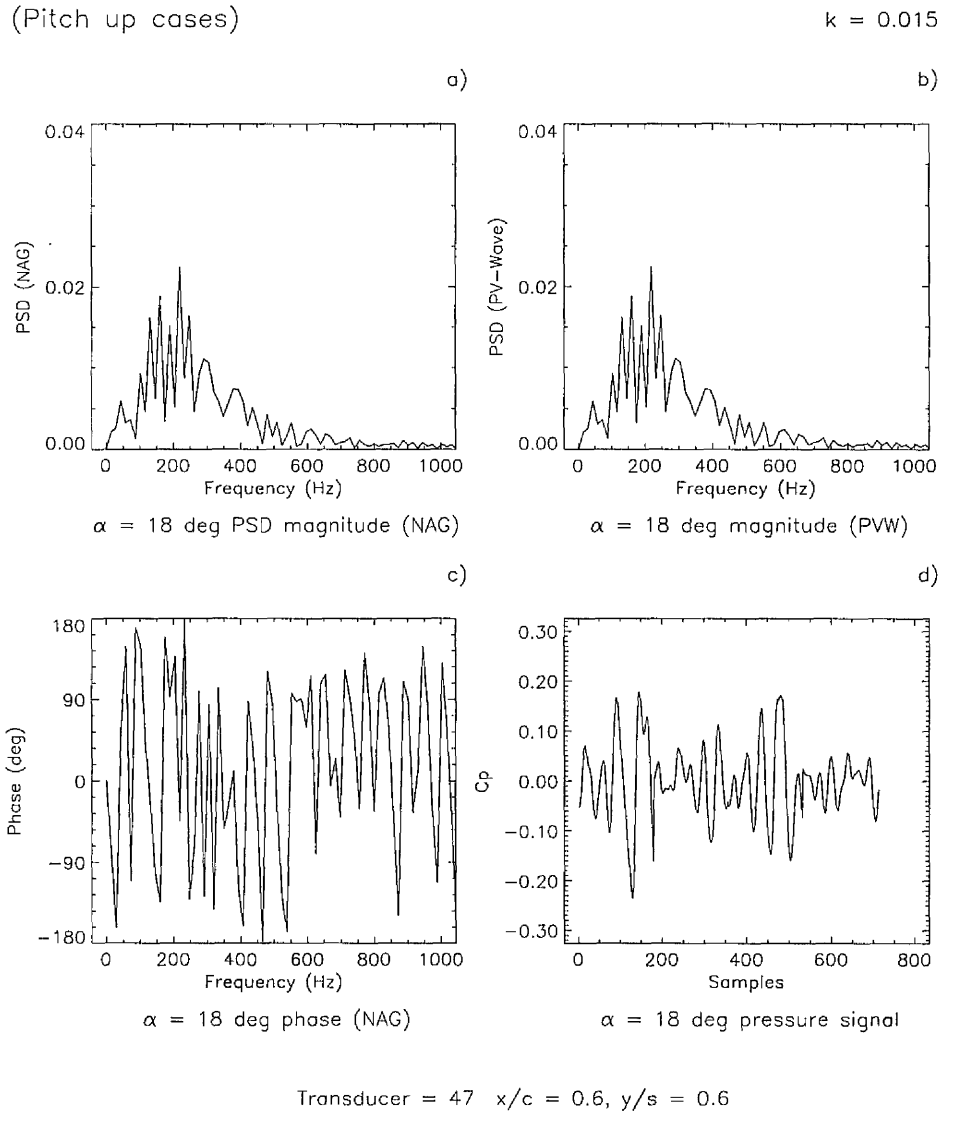

Figure 3.11 - Results from transducer T47, located at x/c = 0.6, y/s = 0.6 in a pitch up case, k = 0.015 showing a) the NAG output frequency spectrum magnitude b) the PV-Wave output frequency spectrum magnitude c) the NAG output frequency spectrum and d) the data set under consideration.

the pressure data signal concerned the number of data samples entered. The library routine would flag up an error message if a prime factor of the number n (of data samples) was greater than 19, or indeed, if the prime factors exceeded 19 in number. For speed of calculation the ideal number of input values would be of the form 2^n, although, for small numbers of prime factors (less than 6) the improvement in calculation speed wasn't significant. In the static case, where n = 2000 for all data sets passed through the calculation, this was never an issue, however, for the pitching cases using a variety of incidence window sizes from 300 to 1400 samples, this became a persistent problem. A solution to the problem required the implementation of a processing loop in CROSS2 which took account of the index value of data set size taken from the output of DATASET. The processing loop was designed to test the index value for compliance with the prime factor criterion. Upon completion of the processing loop routine, extra values were added, if required, to the input data set as zeros at the end of the file which did not affect the final outcome of the calculation (Lynn 1982). Shown in Figure 3.12 is an example of the cross-spectrum results discussed in Chapter 4. Shown, are the frequency spectra for two transducers T45 and T47 both located at chord station x/c = 0.6. Their spanwise locations were: T45 @ y/s = 0.4875 shown in plot a) and T47 @ y/s = 0.6, shown in plot b). Both plots show the k = 0.015 pitch up case at an instantaneous incidence of 18°. Plot c) shows the cross-spectrum PSD against frequency and plot d) shows the corresponding phase relationship.

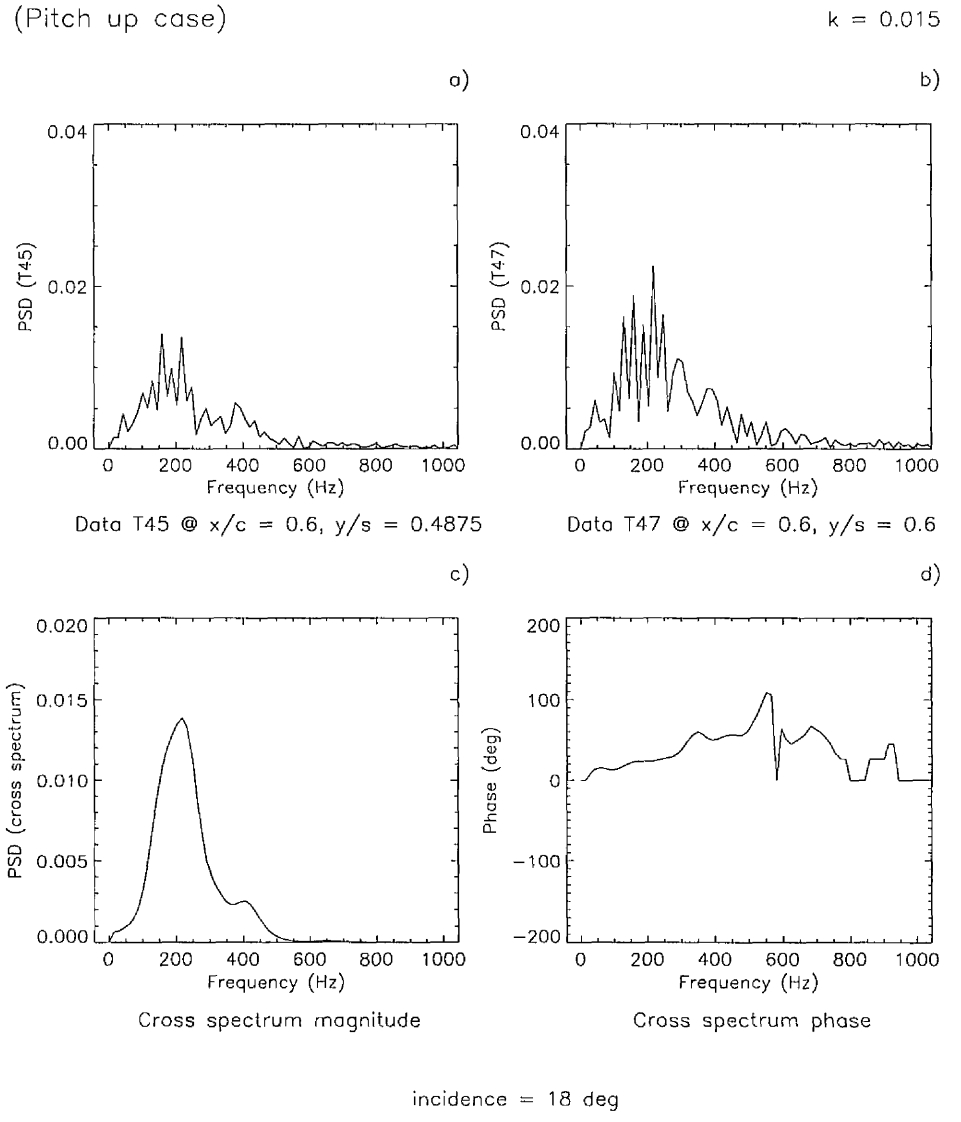

Figure 3.12 - Results from two transducers both located at x/c = 0.6, with spanwise locations of y/s = 0.4875 (T45) and y/s = 0.6 (T47), in the pitch up case, k = 0.015 at an incidence of 18°, showing a) the NAG frequency spectrum magnitude of T45, b) the NAG frequency spectrum magnitude of T47, c) the cross-spectrum magnitude and d) the cross-spectrum phase relationship.

Chapter 4

4. RESULTS - VORTEX BREAKDOWN DETECTION METHODS

The presentation of vortex breakdown detection method results is divided into four separate study areas. These are: 1) Flow visualisation, 2) Mean and instantaneous pressure measurements, 3) RMS pressure measurements, and 4) Pressure signal energy. It will also be shown later, that pressure signal frequency spectral analysis can also provide a method of vortex breakdown detection, however, these results are presented in Chapter 5 entitled, 'Results 2 - Analysis of vortex breakdown buffet frequency spectra.'

4.1 VISUALISATION

The advantage of conducting smoke flow visualisation tests at low Reynolds numbers is that important features of the flow structure can be clearly seen. Figure 4.1 shows a photographic image of the vortex structure on the right-hand half of the leeward surface of the wing at a chord position of $x/c = 0.7$, at an incidence of 12° during a static test. Indicated on the image are the principle features of the vortex flow structure in the pre-vortex breakdown state. In this image, the position of the wing leading-edge is marked by the limit of the wing surface laser light sheet illumination at the right-hand side of the picture. The figure is a close up of a photograph, which in its entirety, also showed the position of the wing centreline. Hence, the local semi-span (s) could be determined and used as a reference length in positional measurement. The position of the primary

vortex core is indicated by a region of the flow, approximately 2.5% of the wing semi-span in diameter, which is devoid of smoke at the centre of the primary vortex spiral (Payne *et al* 1986). It has a lateral position of y/s = 0.48 and a vertical height above the wing surface, z/s = 0.125. Also seen is the secondary vortex structure centred at y/s = 0.76, z/s = 0.0625, and its separation point just above the wing surface at y/s = 0.61.

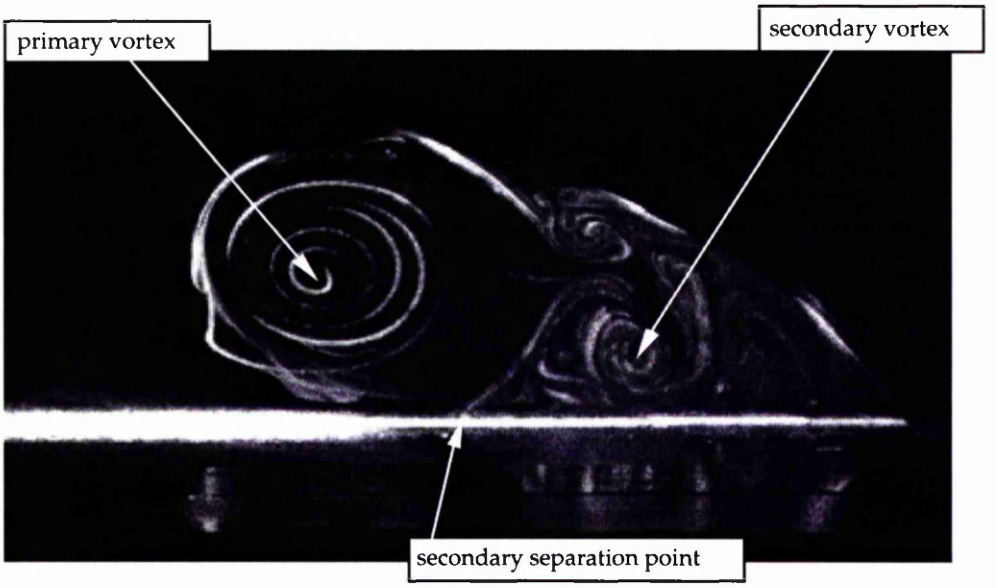

Figure 4.1 - Vortex flow structure above the leeward surface of the delta wing at x/c = 0.7, at 12° incidence during a static test Re = 10000.

Given that clarity of results can be obtained, is it possible to compare vortex breakdown location data between these tests and pressure measurement tests carried out at a Reynolds number of 2.7×10^6 ? The justification for carrying out these visualisation tests on scaled down models is based on the findings of a number of researchers. It was shown in Chapter 1, via the findings of Lambourne & Bryer (1961), Erickson (1982), Atta & Rockwell (1987) and others, that for

static wings, the chordwise position of vortex breakdown is largely unaffected by Reynolds number in the range $10000 \leq Re \leq 4.0x10^7$. More recently, Thompson & Nelson (1992) have suggested that, rather than an effect of Reynolds number, there may be a significant influence on the position of vortex breakdown due to the physical attributes of the wind-tunnel and the model. By increasing model size and peak frontal area blockage from 3.7% to 6.5% they noted a significant upstream shift in vortex breakdown location at a given model incidence by as much as 0.15c. Significantly, they also reported that increasing model size to give a peak frontal area blockage of 14.8% did not induce a significant further shift in vortex breakdown location. Lowson & Riley (1995) successfully reproduced results from a number of previous experiments, including Lambourne & Bryer, concluding that the detail geometry of the wings used was by far the most important factor in determining the position of vortex breakdown. Indeed, it was suggested that the up-wash effect caused by the proximity of the wing to the tunnel walls may influence breakdown. This effect had been previously investigated by Weinberg (1992) who found that by increasing the wing span to tunnel width ratio from 17.5% to 35% produced a downstream shift of up to 0.3c in the position of vortex breakdown, under otherwise similar test conditions, at a given model incidence. Weinberg concluded that the closer proximity of the tunnel walls in the test with the larger model, created an effectively cambered wing which tended to move the vortex breakdown location backward when compared with the smaller model. Finally, the excellent survey of experimental work and empirical methods carried out by Jobe (1998) also supported all of the above findings. Hence, geometrically similar models with the same span to tunnel width ratio were used in the present study to provide a basis for correlation between the pressure measurement and flow visualisation tests.

Previous work by Lowson (1991) has shown however that, unlike the position of vortex breakdown, the position of the main vortex core is significantly affected by

Reynolds number. Lowson displayed results from a number of tests involving delta wings. These were plotted as non-dimensional spanwise position against the ratio of incidence to semi-apex angle. It is clear from Lowson's results that the lateral position of the vortex core, at a given ratio of incidence to semi-apex angle, was further outboard for those tests at high Reynolds numbers, compared with those at low Reynolds numbers. Similarly, the vertical position of the vortex core for tests at high Reynolds numbers is closer to the surface of the wing than at lower Reynolds numbers although the effect is not so marked. It was suggested that the smaller turbulent secondary vortex structure which forms at high Reynolds numbers is not as effective in displacing the primary vortex as its larger laminar counterpart which exists at lower Reynolds numbers. In this respect, the results from the visualisation tests done as part of the present study show agreement with Lowson's findings.

4.1.1 *Visualisation - static tests*

During static tests at a Reynolds number of 10000 and at an incidence of 12°, the lateral position of the vortex core was found to oscillate very gently across the range, $y/s = 0.48$ to $y/s = 0.52$. Shown in Figure 4.2 are three images of the vortex flow at $x/c = 0.7$, at 12° incidence during a static test. The three images are captured at time intervals of 0.2s and together make up approximately one cycle of oscillation. Shown in image a), captured at $t = 0$, a concentrated region of vorticity is apparent to the right of the primary vortex. This feature, marked as 'A', has a similar structure to one previously reported by Gad-el-Hak & Blackwelder (1985) which was then thought to be the result of a Kelvin-Helmholtz instability. However, unlike the previous structure which moved towards the primary vortex, image b) at $t = 0.2s$ shows that vortex A has moved to the right and downward towards the wing surface and another vortex 'B' is beginning to form to the top-right of the primary vortex. In the meantime, vortex A is apparently extracting vorticity from the secondary vortex which, at this stage, is very weak or diffuse and is barely rotating. The reduction in size and strength of the secondary vortex

allows the primary vortex to take up a more outboard position by as much as 0.025s. In image c), at t = 0.4, vortex A is close to the wing surface and, due to its proximity, will be quickly drawn into the region of slow moving fluid near the leading-edge (Doligalski 1994). This is followed by the reinstatement of the primary vortex position due to an increase in size and strength of the secondary vortex whose revitalised vorticity content is the product of the adverse pressure gradient under the primary core in the direction of the leading-edge.

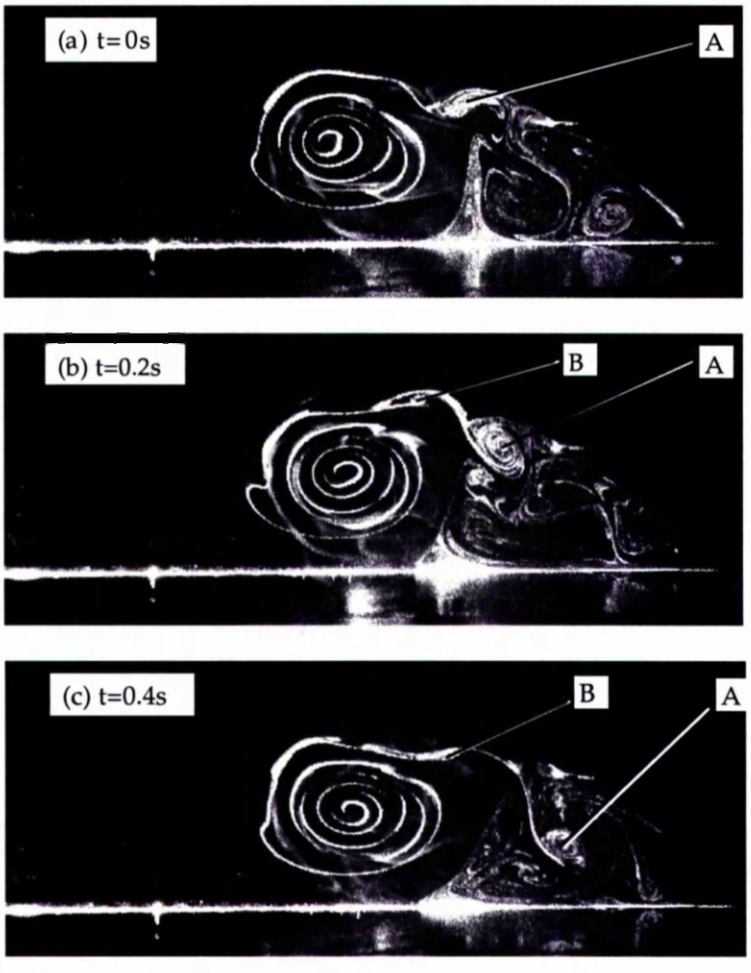

Figure 4.2 - The vortex flow structure above the leeward surface of the wing at x/c = 0.7, at 12° incidence during a static test. Captured over three 0.2s time steps. Re = 10000

The mean lateral position of the primary vortex core at approximately y/s = 0.5 did not compare well with the findings of the pressure data at a Reynolds number of 2.7×10^6 which placed the centre of the vortex at y/s = 0.7. For both cases, there were slight variations in lateral core position at different chordwise locations but these did not follow any particular pattern. It is thought that the unusual shape of the windward surface of the wing may have an effect on vortex core position but this has not been positively determined.

In the flow visualisation study, vortex breakdown was first observed on the wing at x/c = 0.9 at an incidence of 11°. It was seen to progress steadily up the wing until the observations were concluded at an incidence of 19° when the breakdown position had reached x/c = 0.35. Shown in Figures 4.3 and 4.4 are four images at a chord position x/c = 0.8, at four incidences of 8°, 10°, 12° and 14° in the static case. In Figure 4.3, image a) at 8°, the vortex is a tightly formed steady structure. In this image the smoke has not become entrained underneath and outboard of the main vortex structure and as such the secondary vortex is not visible. Smoke is however, entrained in the feeding sheet emanating from the leading-edge to the right of the image and a discrete vortex that maintains its position in the separated shear layer is visible. Figure 4.3, image b) shows a photograph taken at 10° incidence. In this image, the secondary vortex structure is clearly visible and the discrete vortex structure in the separated shear layer previously described, is moving towards the wing surface and leading-edge. This will be shed and replaced by another discrete vortex at an increasingly greater frequency with increasing incidence. In Figure 4.4, image a) at 12°, the secondary vortex structure is barely rotating indicating that it is very weak or diffuse and the primary vortex core is just at the point of expansion. At a given incidence where vortex breakdown was observed on the wing, the point of expansion of the vortex core was seen to gently oscillate along the vortex centreline. The amplitude

of the oscillation was approximately 0.05c. Therefore, at this chord location and incidence the primary vortex core is fluctuating between a tightly rotating structure and an expanded, incoherent mass of fluid. The first appearance of the expanded core, fluctuating or not, is the criterion used to decide whether vortex breakdown has reached this particular chord location. Finally, Figure 4.4, image b) at 14° shows the fully broken down structure.

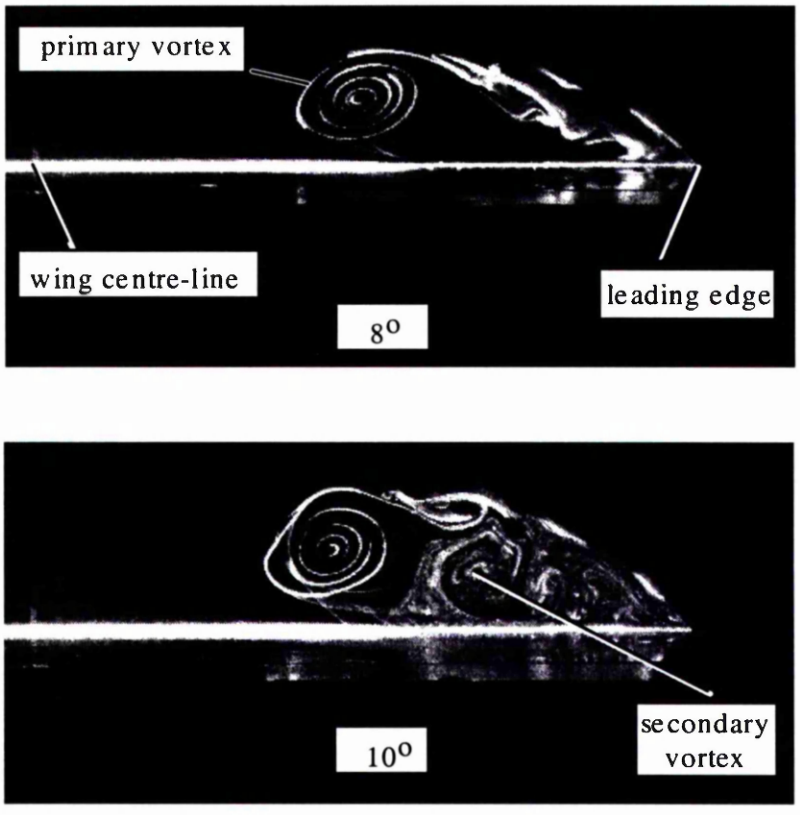

Figure 4.3 - Vortex flow structure above the leeward surface of the delta wing at x/c = 0.8, at incidences of 8° and 10° during a static test. Re = 10000.

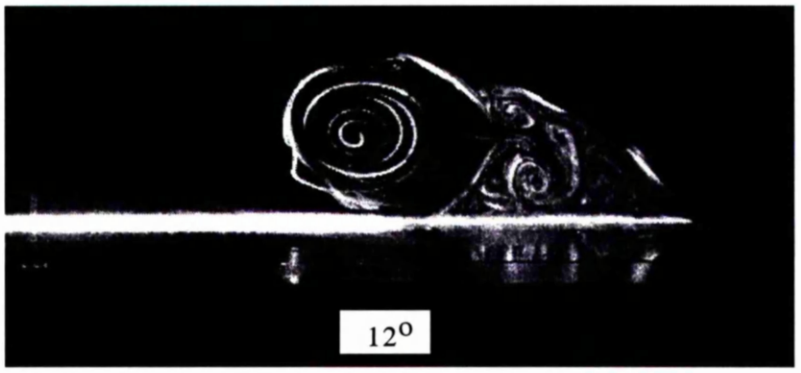

a)

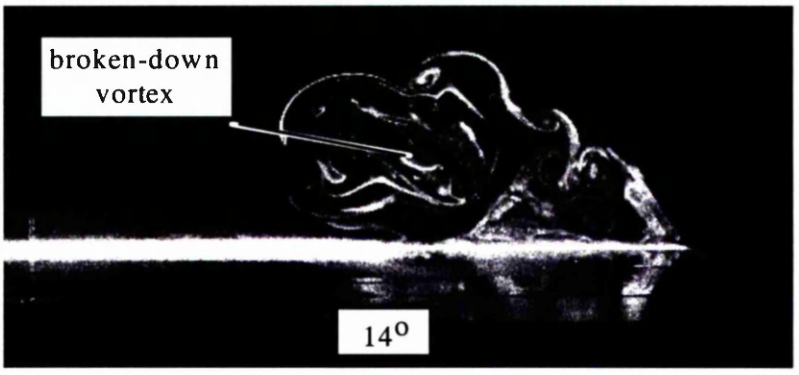

b)

Figure 4.4 - Vortex flow structure above the leeward surface of the delta wing at x/c = 0.8, at incidences of **12°** and **14°** during a static test. Re = 10000.

Note: **bold** type denotes change of parameter from previous figure.

The observed location of vortex breakdown at a given incidence in the static case is shown in Figure 4.5. The plot shows that the progression of vortex breakdown with an increase in incidence from x/c = 0.9 to x/c = 0.35 is almost linear. There are two deviations from linearity. The first occurs very close to the trailing-edge, where vortex breakdown was observed to 'jump' onto the wing at x/c = 0.9 as incidence was increased to 11°, rather than move onto the wing from the wake at

the trailing-edge. The second deviation occurs around x/c = 0.62, where vortex breakdown occurs slightly rearward of the expected breakdown location. This may be explained by experimental error or may be due to the shape of the windward surface (Figure 2.1) which changes direction abruptly at x/c = 0.58 and may influence the feeding shear layer immediately downstream.

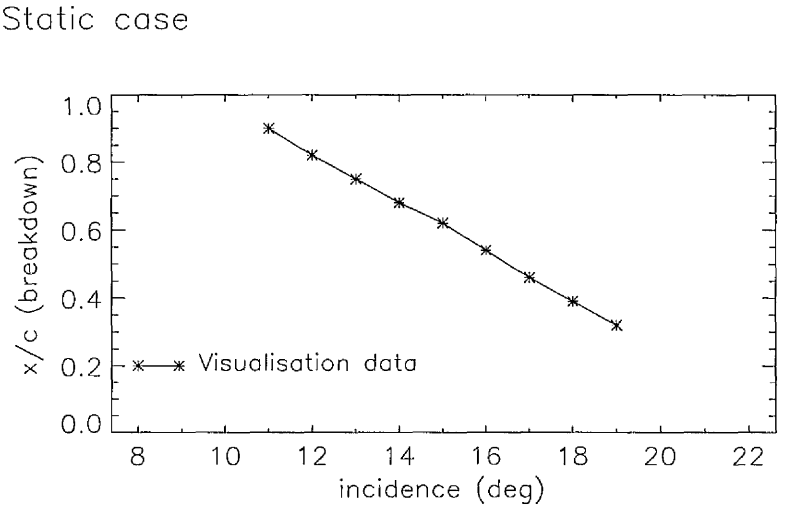

Figure 4.5 - The chordwise location of vortex breakdown as a function of incidence in the static case. Measured during flow visualisation experiments. Re = 10000

4.1.2 *Visualisation - pitch up tests*

In the pitch up cases, the determination of the point of vortex breakdown is more difficult than in the static case. Figure 4.6 shows photographic images of the vortex structure on the right-hand half of the leeward surface of the wing at a chord position of x/c = 0.8 at three instantaneous incidences (12°, 14° and 16°) and a pitch rate of k = 0.015. Plot a) at 12° shows a coherent primary vortex structure with a weak or diffuse secondary vortex. By 14° in plot b), the periphery of the main vortex has become very unsteady. A series of discrete vortices can be

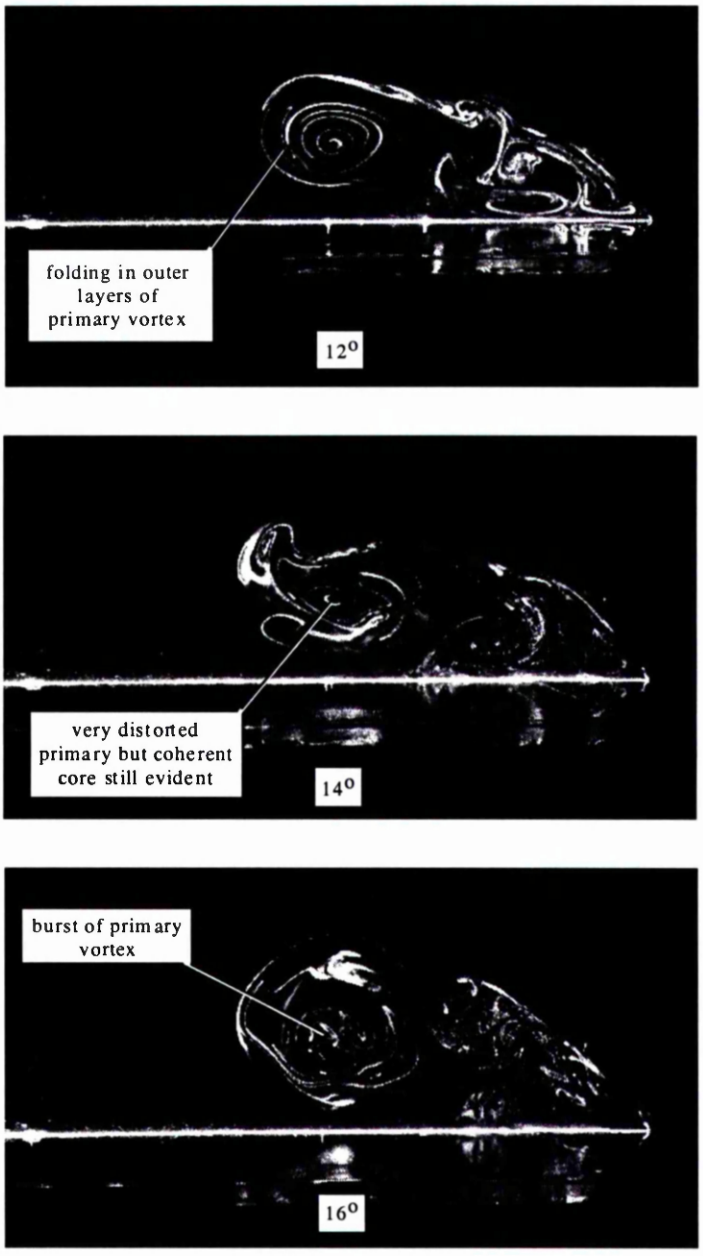

Figure 4.6 - Vortex flow structure above the leeward surface of the delta wing at x/c = 0.8, at incidences of 12°, 14° and 16° and k = 0.015 during a pitch up test. Re = 10000.

seen moving around the vortex core in the same direction as the free shear layer, becoming entrained into the main core with increasing frequency as incidence is increased. In this case however, the centre of the primary vortex core is still tightly formed and rotating, and as such has not yet broken down. By 16° in plot c), the primary vortex core has broken down. The manner of breakdown is different to that in the static case. In the pitch up case, there is no chordwise oscillation of the breakdown point, it merely moves steadily upstream with increased incidence. Similarly, there is no expansion and diffusion of the vortex core, indeed, the core was seen to apparently disintegrate in a relatively violent manner. This disintegration takes place over a small incidence range, beginning with a 'buckling' of the core centre (not shown) and ending with the core being ripped apart from the inside out. The disintegration process occupies a greater incidence range as the pitch rate is increased.

The observed chordwise progression of vortex breakdown for two pitch up cases ($k = 0.007$ and $k = 0.015$) is presented in Figure 4.7. By comparing these two plots with that of the static case, it is clear that that the appearance of vortex breakdown on the wing (at $x/c = 0.8$ and 15.5°, for $k = 0.007$ and at $x/c = 0.9$ and 14°, for $k = 0.015$) and its subsequent progression upstream towards the wing apex were subject to an increasing delay or lag with increase in pitch rate. The sudden appearance of vortex breakdown at $x/c = 0.8$ in the $k = 0.007$ case is an anomaly that is as yet unexplained. It is particularly puzzling when seen alongside the $k = 0.015$ case where vortex breakdown was observed on the wing at $x/c = 0.9$ as per the static case. The speed of vortex breakdown progression for the two pitch up cases as a function of non-dimensional pitch rate magnitude is shown in Figure 4.8. These data are taken from a larger data set which includes progression rates for higher pitch rate cases shown by Green (1998). Taken as a whole, there is an indication that the acceleration of vortex breakdown upstream

progression which would be expected with an increase in non-dimensional pitch rate is much reduced.

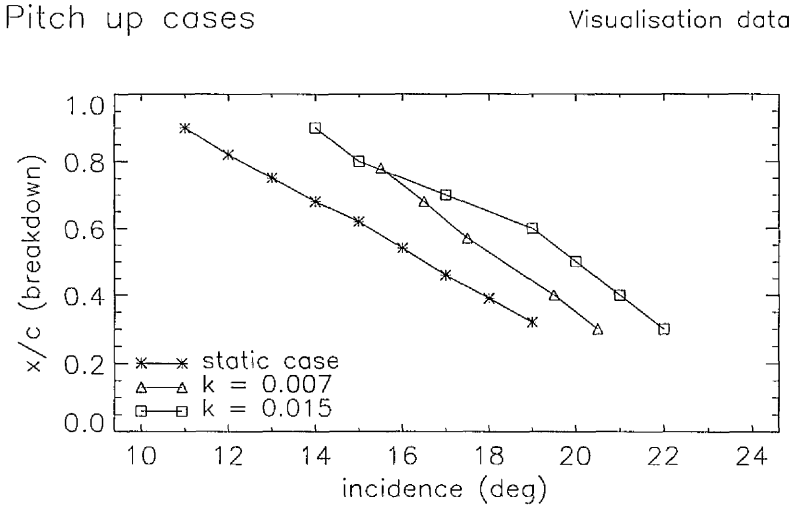

Figure 4.7 - The chordwise location of vortex breakdown as a function of incidence in the static and two pitch up cases (k = 0.007 & 0.015). Measured during flow visualisation experiments. Re = 10000

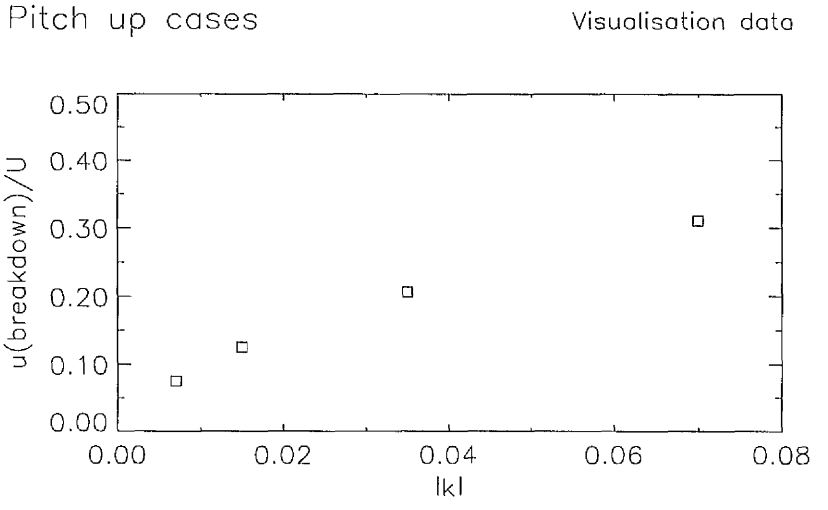

Figure 4.8 - The speed of upstream progression of vortex breakdown as a function of pitch rate in four pitch up cases (k = 0.007, 0.015, 0.035 & 0.07). Measured during flow visualisation experiments. Re = 10000. Taken from Green (1998).

4.1.3 *Visualisation - pitch down tests*

In the pitch down cases, the determination of the point of vortex breakdown is again more difficult than in the static case. Figure 4.9 shows photographic images of the vortex structure at x/c = 0.8 on the right-hand half of the leeward surface of the wing at three incidences (10.0°, 8.4° and 7.6° respectively) for the reduced pitch rate k = -0.017. Plot a) at 10° shows that the primary vortex core is in a pre-reformation state. The outer core is rotating slowly, but the inner core has no coherent structure. By 8.4° in plot b), the periphery of the main vortex core is now rotating with greater energy and the inner core is beginning to reform. Note the lack of discrete vortices either surrounding the main vortex core (a feature of the pitch up cases), or in the separated shear layer (a feature of the static case). It is at this stage that the vortex is said to be on the 'point' of reformation, although it should be noted that this reformation process takes place over a finite range of incidence that increases with increasing pitch rate magnitude. By 7° in plot c), a coherent primary vortex structure has reformed with a weak or diffuse secondary vortex. The manner of reformation in the pitch down cases would appear to be different from the breakdown phenomenon in either the pitch up or static case. In the pitch down case, the main vortex core reforms from the outside towards the centre and does so over a relatively long incidence range when compared to breakdown during a pitch up case with a comparable pitch rate magnitude.

The observed chordwise progression of vortex reformation for two pitch down cases (k = -0.007 and k = -0.017) is presented in Figure 4.10. Comparison with the progression of breakdown in the static case shows that during pitch down, the reformation of the main vortex at the apex of the wing and its subsequent progression downstream towards the wing trailing edge occurs later in the pitch down motion with an increase in pitch rate magnitude.

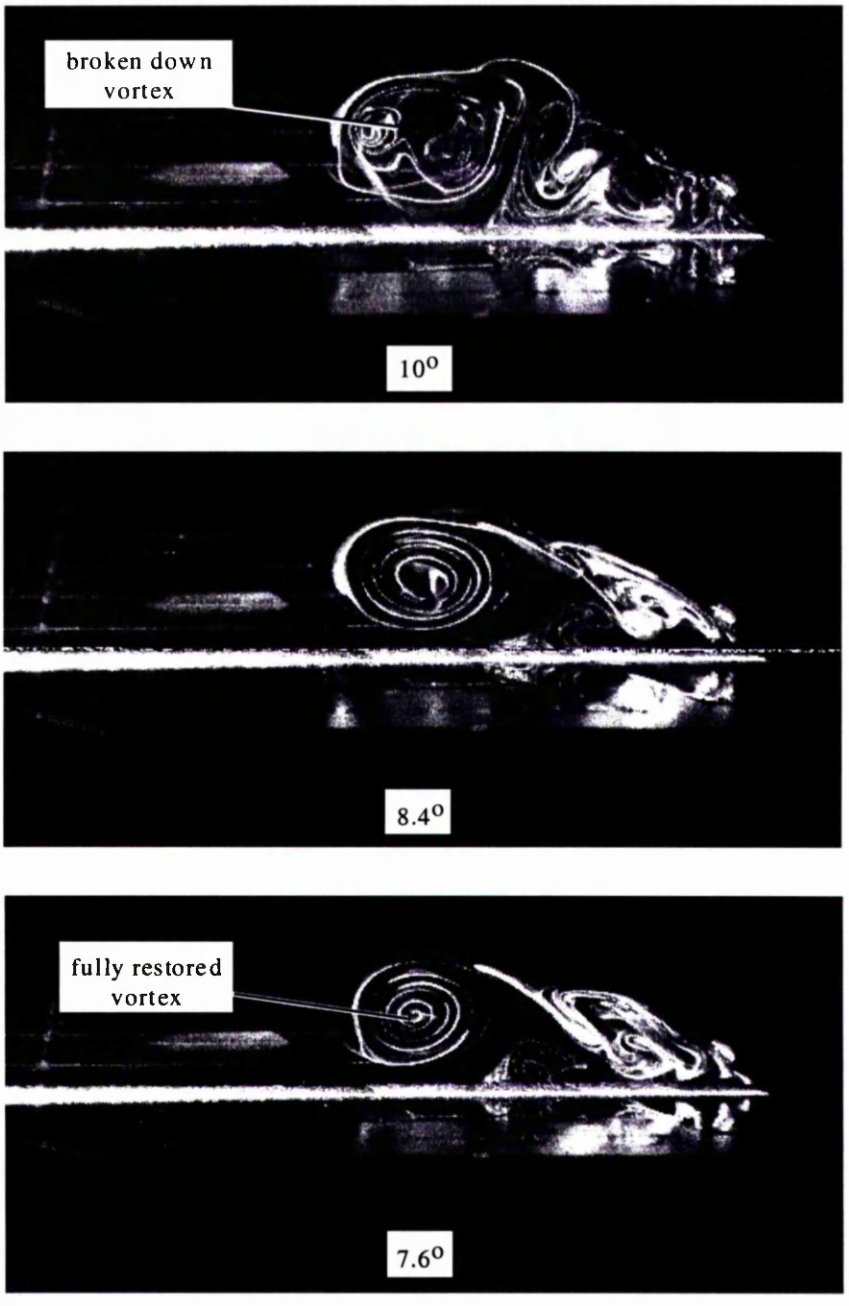

Figure 4.9 - Vortex flow structure above the leeward surface of the delta wing at x/c = 0.8, at incidences of 10.0°, 8.4° and 7.6° and k = -0.017 during a pitch down test. Re = 10000.

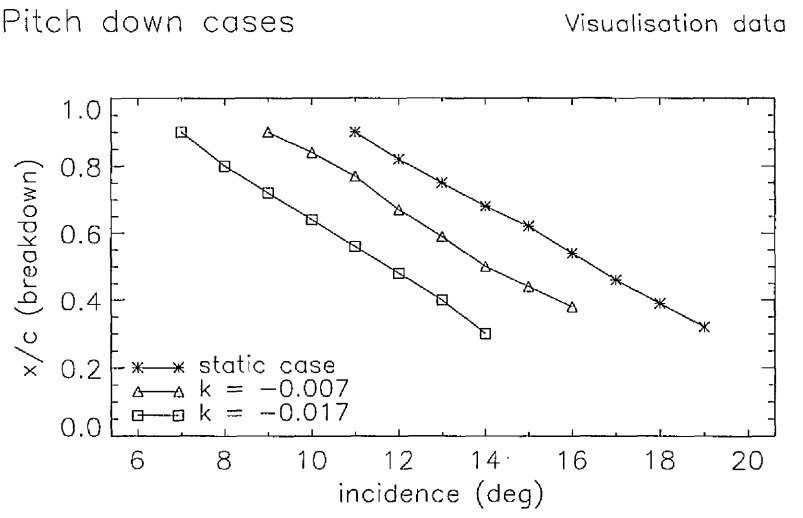

Figure 4.10 - The chordwise location of vortex breakdown as a function of incidence in the static and two pitch down cases (k = -0.007 & -0.017). Measured during flow visualisation experiments. Re = 10000

The speed of vortex core reformation downstream progression for the two pitch down cases as a function of non-dimensional pitch rate magnitude is shown in Figure 4.11, plot b). This is also taken from a larger data set of pitch down cases (Green ibid.). The larger data set indicates a progressively reduced acceleration in vortex reformation with increase in non-dimensional pitch rate magnitude, however this is not as pronounced as that found in the pitch up cases. The pitch down case with a non-dimensional pitch rate magnitude of $|k| = 0.007$ reveals a vortex reformation speed of $u_{(b/d)}/U = 0.06$. The corresponding pitch up case reproduced in plot a) has a 25% higher vortex breakdown progression speed measured as $u_{(b/d)}/U = 0.075$. In the two higher pitch rate cases, the pitch rate magnitudes are different, which makes comparison difficult. However, if the ratio of progression speeds of pitch up and pitch down cases were maintained at 1.25:1

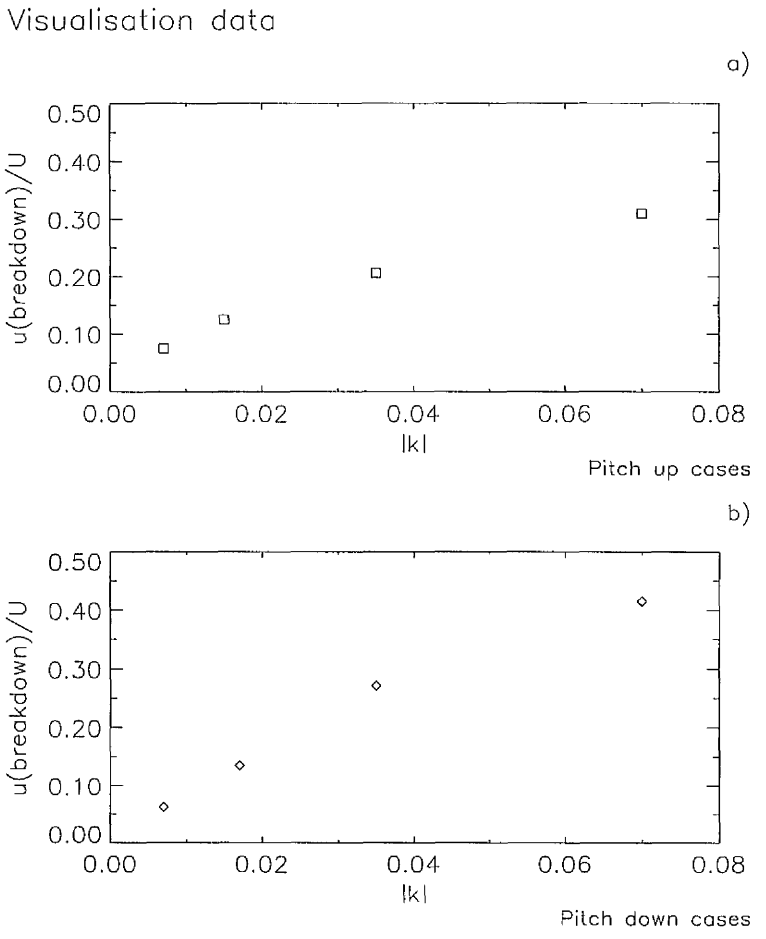

Figure 4.11 - The speed of upstream progression of vortex breakdown as a function of pitch rate in four pitch up cases (k = 0.007, 0.015, 0.035 & 0.07) and four pitch down cases (k = -0.007, -0.017, -0.035 & -0.07). Measured during flow visualisation experiments. Re = 10000. Taken from Green (1998).

at the higher pitch rates where, in the k = 0.015 case, $u_{(b/d)}/U = 0.125$ and using a crude linear scaling over the range $0.015 \leq |k| \leq 0.017$, it would be reasonable to expect the pitch down case of k = -0.017 to indicate a vortex reformation speed of:

$$u_{(b/d)}/U = (0.125/1.25) \times (0.017/0.015) = \mathbf{0.113} \qquad (4.1)$$

However, the k = -0.017 case actually reveals a vortex reformation speed of $u_{(b/d)}/U = 0.135$, a 19% increase on the expected figure. Even allowing for the linear scaling method used in the estimation, this indicates that the pitch down cases are subject to a reduced delay in the acceleration of vortex reformation with an increase in pitch rate magnitude. This is in agreement with the findings of Miau *et al* (1992), who identified two delays in the progression of vortex breakdown/reformation in pitching cases. The first delay, equally applicable to pitch up and pitch down cases, was caused by the underdevelopment of the primary vortex when compared with the static case. The second delay, a feature of pitch up cases only, was caused by the suppression of the primary vortex by the secondary separation immediately after the initiation of the pitching motion.

4.1.4 *Visualisation - changes in apex geometry*

The vortex flow features over the leeward surface of the round-nosed wing were essentially similar to those of its sharp-nosed counterpart during static tests. Indeed they were so similar that it is felt that the inclusion of photographic images in this section comparing the features of sharp and round-nosed cases would not prove worthwhile. However, the principal difference between the two wing planforms was in the chordwise location of vortex breakdown at a given incidence. Figure 4.12 shows the location of vortex breakdown as a function of incidence for the sharp and round-nosed wings during static tests. This diagram shows that vortex breakdown appears on the surface of the round-nosed wing at an incidence of 10°, compared to 11° for the sharp-nosed case. Similarly, for a given incidence, vortex breakdown occurs further upstream on the round-nosed wing. The difference in breakdown position is 0.08c towards the trailing-edge at 11° incidence increasing to 0.14c above the wing mid-section at 15°. Given that the expetimental conditions were similar, it must be concluded that these variations are due to the shape of the wing apex.

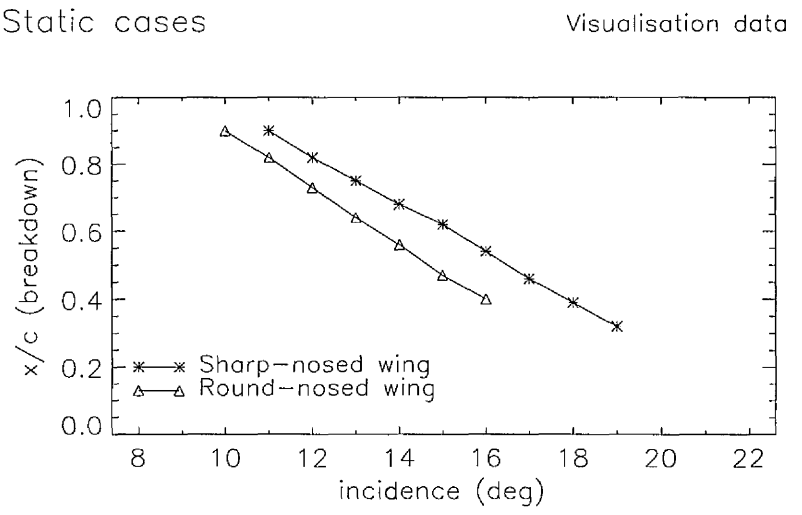

Figure 4.12 - The chordwise location of vortex breakdown as a function of incidence in the sharp and round-nosed wing static cases. Measured during flow visualisation experiments. Re = 10000

4.2 PRESSURE MEASUREMENTS

4.2.1 *Static tests*

For a given transducer in the static test case, the pressure data at each angle of incidence were non-dimensionalised and averaged to produce values of mean C_P. The uncertainty in the pressure coefficient values obtained in this way was± 0.5%. The mean C_P distribution was found to be dominated by a localised suction ridge on the leeward surface of the wing originating at the apex and extending towards the trailing-edge. Figure 4.13, shows a series of contour plots indicating the mean C_P distribution on the leeward surface of the wing at incidences of 0°, 1°, 2°, 4°, 6° and 8°. The contour plots chart the formation and growth of the suction ridge from its origins as a region of low suction at the leading- edge of the wing just downstream of the apex to a fully formed vortex originating at the wing apex and

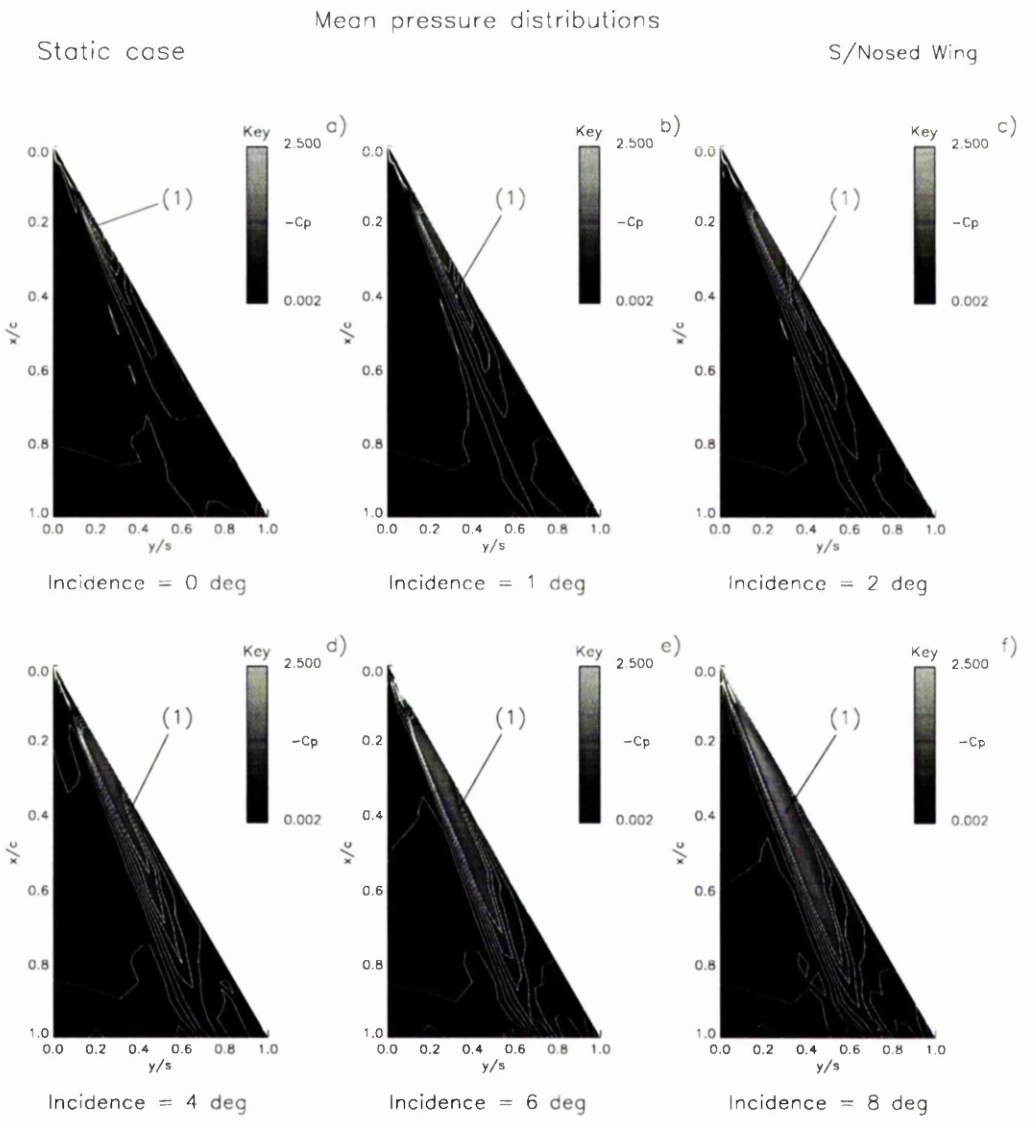

Figure 4.13 - Contour plots of mean C_P pressure distributions at 0°, 1°, 2°, 4°, 6° and 8° incidences during static pressure measurement tests. Re = 2.7×10^6

Key: Suction pressure ridge labelled as (1)

extending along a ray at a span station of y/s = 0.7. In plot a) at an incidence of 0°, a suction region can be seen on the leading-edge of the wing at x/c = 0.2, indicated by the area marked as (1). In plot b) at an incidence of 1°, this region began to form a ridge extending towards the trailing-edge along a ray at y/s = 0.8. By 2° incidence in plot c), the ridge had increased in size and magnitude. At 4° incidence (plot d), and again at 6° (plot e), the origin of the suction ridge had moved progressively towards the wing apex, such that by 8° incidence shown in plot f), the origin had reached the apex and the ridge had begun to move inboard towards a 'stable' spanwise location. This stable spanwise location is defined as the established position of the primary vortex core which was largely fixed over a range of incidence after vortex formation, during vortex breakdown and before vortex collapse in an inboard direction towards the wing centreline. Figure 4.13 is indicative of a general trend. That is, for all angles of incidence the magnitude and localisation of the suction ridge were at a maximum at the apex of the wing, with a decrease in magnitude towards the trailing edge. Similarly, the ridge increased in magnitude and tended to move inboard as the wing incidence was increased. This behaviour is consistent with the observations of Parker (1977) that the ridge is indicative of both the position and, to some extent, the condition of the leading-edge vortex. For the final incidence case shown in Figure 4.13, the vortex is fully developed and the path of the centreline of the vortex core can be clearly seen as indicated by the region marked as (1).

Figure 4.14 is a continuation of the previous diagram showing contour plots of the mean C_P pressure distributions at incidences of 10°, 14°, 18°, 24°, 30° and 36°. In plot a) at 10° incidence, the suction ridge, labelled as (1), began to broaden across the wing rather than extend any further towards the trailing-edge. At 14°, shown in plot b), it had widened further and had found its stable spanwise position of y/s = 0.7. By 18° incidence shown in plot c), the peak magnitude of

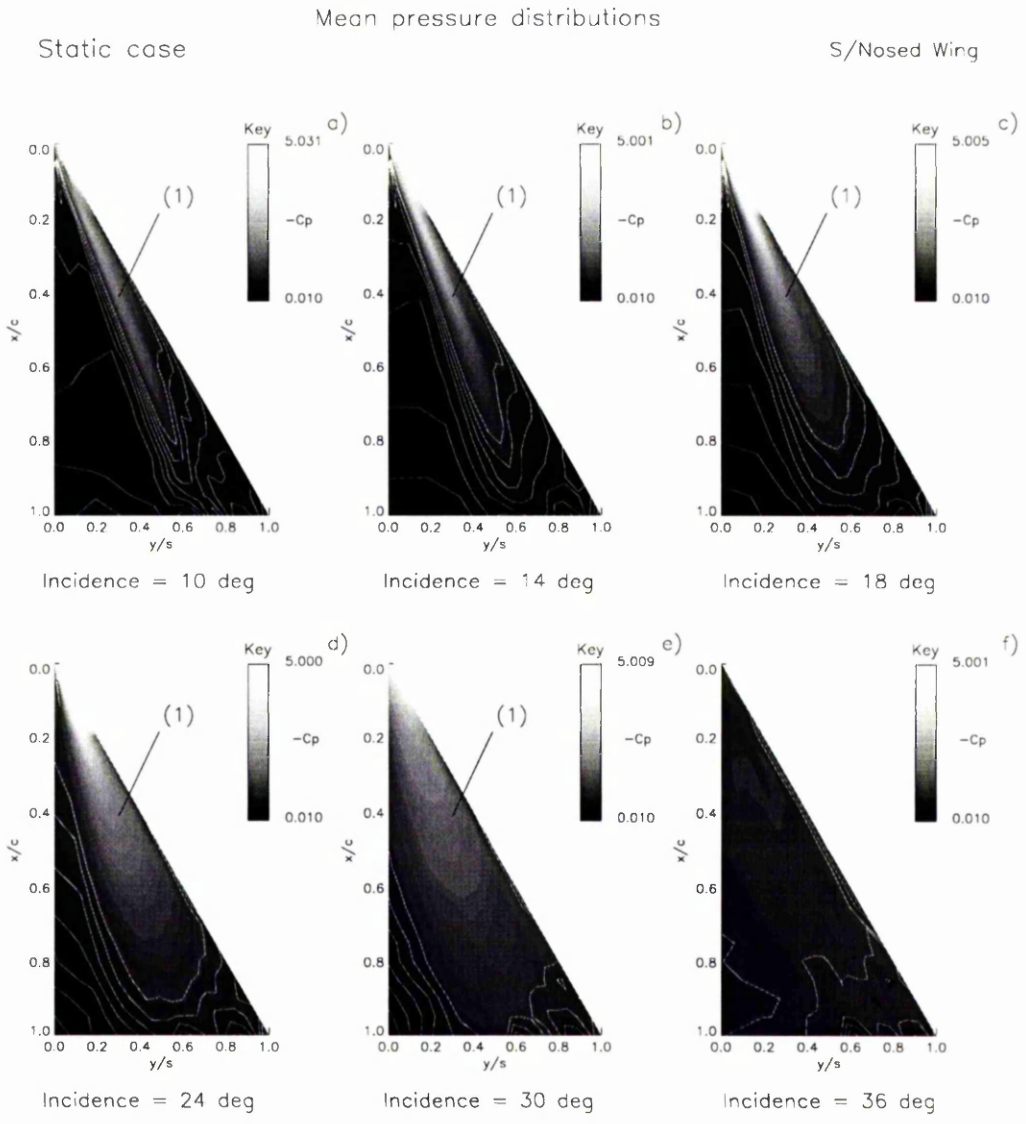

Figure 4.14 - Contour plots of mean C_P pressure distributions at **10°, 14°, 18°, 24°, 30°** and **36°** incidences during static pressure measurement tests. Re = 2.7×10^6.

Key: Suction pressure ridge labelled as (1)

Note: **bold** type denotes change of parameter from previous figure.

the suction ridge located between x/c = 0.2 and x/c = 0.125 had reached its maximum value. However, spanwise peak suction values at chord stations to the rear of x/c = 0.2 were beginning to decline. At an incidence of 24°, illustrated in plot d), the peak suction magnitude had fallen, although the general form of the suction ridge was still apparent. However, at this incidence, the suction ridge (1) had begun to move inboard towards the wing centreline. By 30° shown in plot e), the suction ridge had moved further inboard and the peak suction magnitude had fallen to approximately half of its value at 18° incidence. At 36° in plot f), the pressure distribution over the wing surface is almost uniform and the wing resembles a bluff body.

The rise and fall of mean C_P pressure at a given chordwise location can also be illustrated using line plots. Figure 4.15 shows the mean spanwise C_P pressure distributions at x/c = 0.3875 for three sets of four incidences. Plot a) shows the increase in the peak suction at this chord station as incidence is increased from 0° to 4°, and plot b) clearly shows the inboard movement of the suction ridge over an incidence range from 6° to 14°. Plot c) on the other hand, illustrates the decline and levelling off of peak suction at x/c = 0.3875 and downstream, from a high at 16° incidence.

Figure 4.16 shows three sets of maximum spanwise suction values measured over the chord range, x/c = 0.2 to x/c = 0.95, each set measured over four incidences. Like the previous diagram, plot a) charts the increase in the chordwise pressure gradient over the incidence range 0° to 4° and plot b) illustrates a sharp rise in the chordwise pressure gradient as the suction ridge found its stable lateral position at 14°. Plot c) shows the peak suction magnitude at 18° incidence and thereafter a decline until the uniform pressure state is reached at an incidence of 36°.

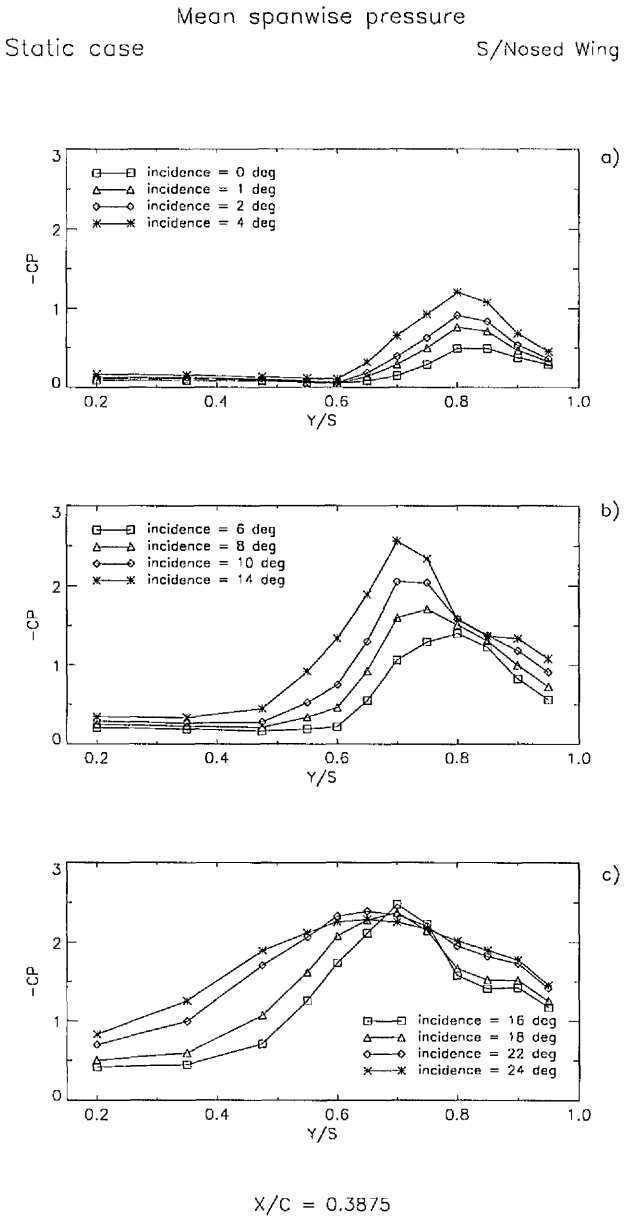

Figure 4.15 - Line plots of mean spanwise C_P pressure distributions at x/c = 0.3875 for 0°, 1°, 2°, 4°, 6°, 8°, 10°, 14°, 16°, 18°, 22° and 24° incidences. Data collected during static pressure measurement tests. Re = 2.7×10^6

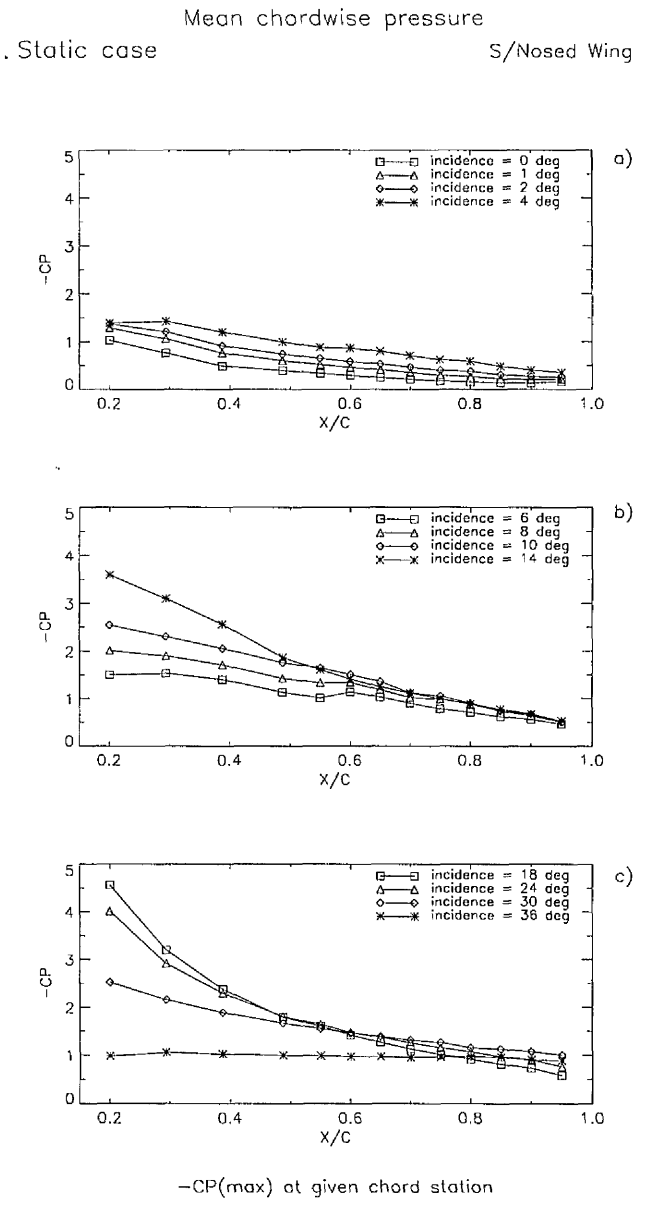

Figure 4.16 - Line plots of maximum spanwise mean C_P pressure values at chord stations from x/c = 0.2 to x/c = 0.95 for incidences of 0°, 1°, 2°, 4°, 6°, 8°, 10°, 14°, 18°, 24°, 30° and 36° data collected during static pressure measurement tests. Re = 2.7×10^6

4.2.2 *Pressure measurements - pitch up tests*

For the pitching cases, the pressure data collected at each transducer location were non-dimensionalised to produce values of instantaneous C_P. Once again, these data were characterised by the growth of a localised suction ridge on the leeward surface of the wing. Like the static case, the suction ridge on the wing in each pitch up case originated in a region on the leading-edge just downstream of the apex at an incidence 1°. Figures 4.17, 4.18 and 4.19 show contour plots of instantaneous C_P pressure distributions on the leeward surface of the wing for static and two pitch up cases ($k = 0.007$ and $k = 0.015$).

Figure 4.17 shows, that at an incidence of 2° for the pitch up cases (plots b and c), a suction ridge (1) was forming and extending towards the trailing-edge in a similar manner to the static case reproduced in plot a). It is apparent however, that with increase in pitch rate magnitude (as illustrated in the $k = 0.015$ case), this downstream extension is subject to a delay. At an incidence of 4°, shown in plots d) to f), the origin of the suction ridge in all cases began to move upstream towards the wing apex. Figure 4.18 reveals however, that at 8° incidence, in both pitch up cases (plots b and c), the origin of the suction ridge (1) had yet to reach the wing apex contrary to the static case (plot a). At 14° incidence, indicated in Figure 4.18, plots d) to f), the origin had reached the wing apex in all cases, and the suction ridge has reached its stable spanwise location at $y/s = 0.7$.

Figure 4.19 shows that at 24° incidence, the downstream extremity of the suction ridge (1) in the pitch up cases (plots b and c), is more pronounced than the static case shown in plot a) and at 30°, shown in Figure 4.19, plots e) and f), there is a progressive delay in the inboard movement of the suction ridge towards the wing centreline when compared with the static case shown in Figure 4.19, plot d). Also, the peak suction near the wing apex increased with increasing pitch rate.

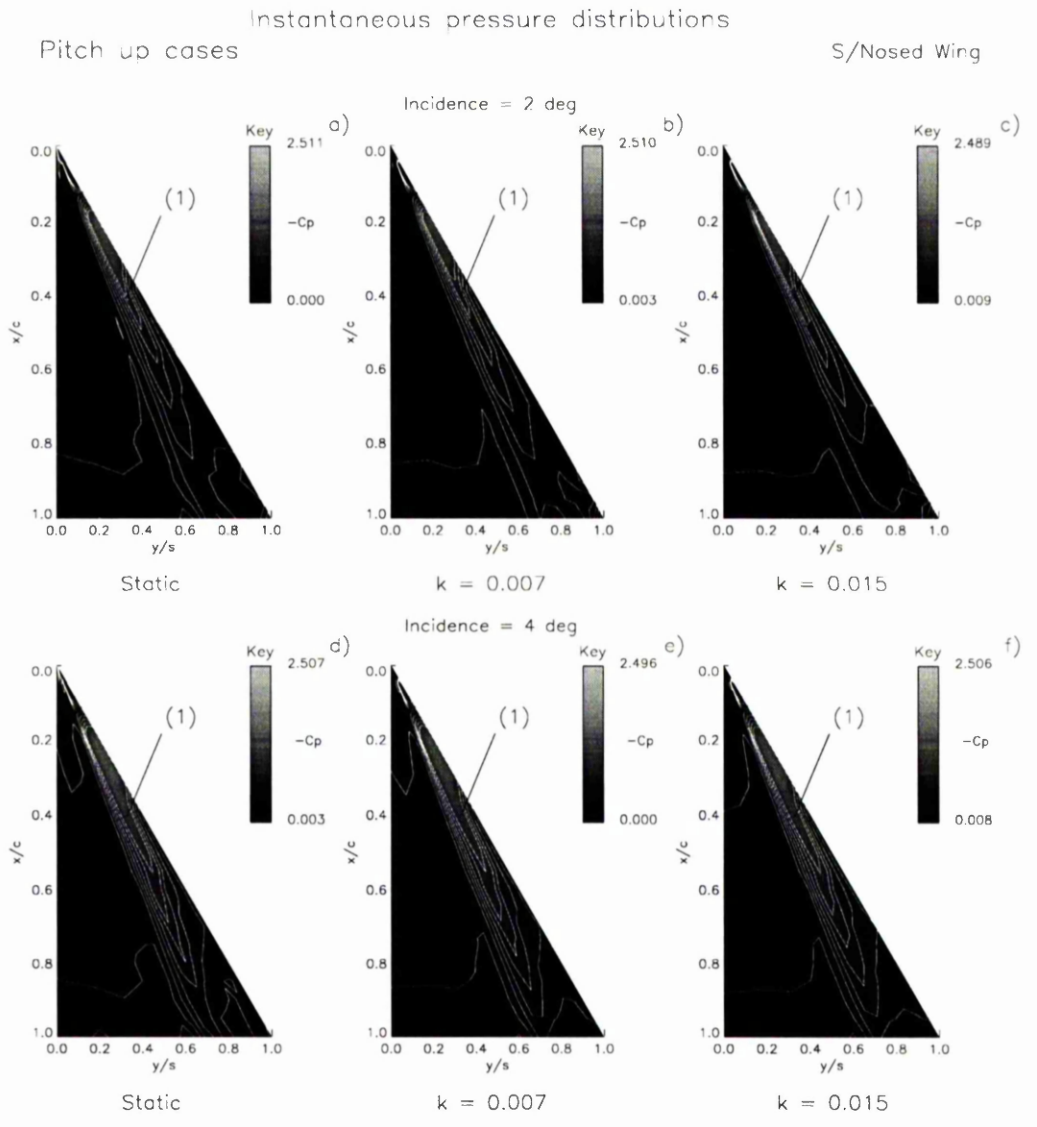

Figure 4.17 - Contour plots of mean & instantaneous C_P pressure distributions at 2° and 4° incidences for static, k = 0.007 and k = 0.015 cases. Data collected during pressure measurement tests. Re = 2.7×10^6.

Key: Suction pressure ridge labelled as (1)

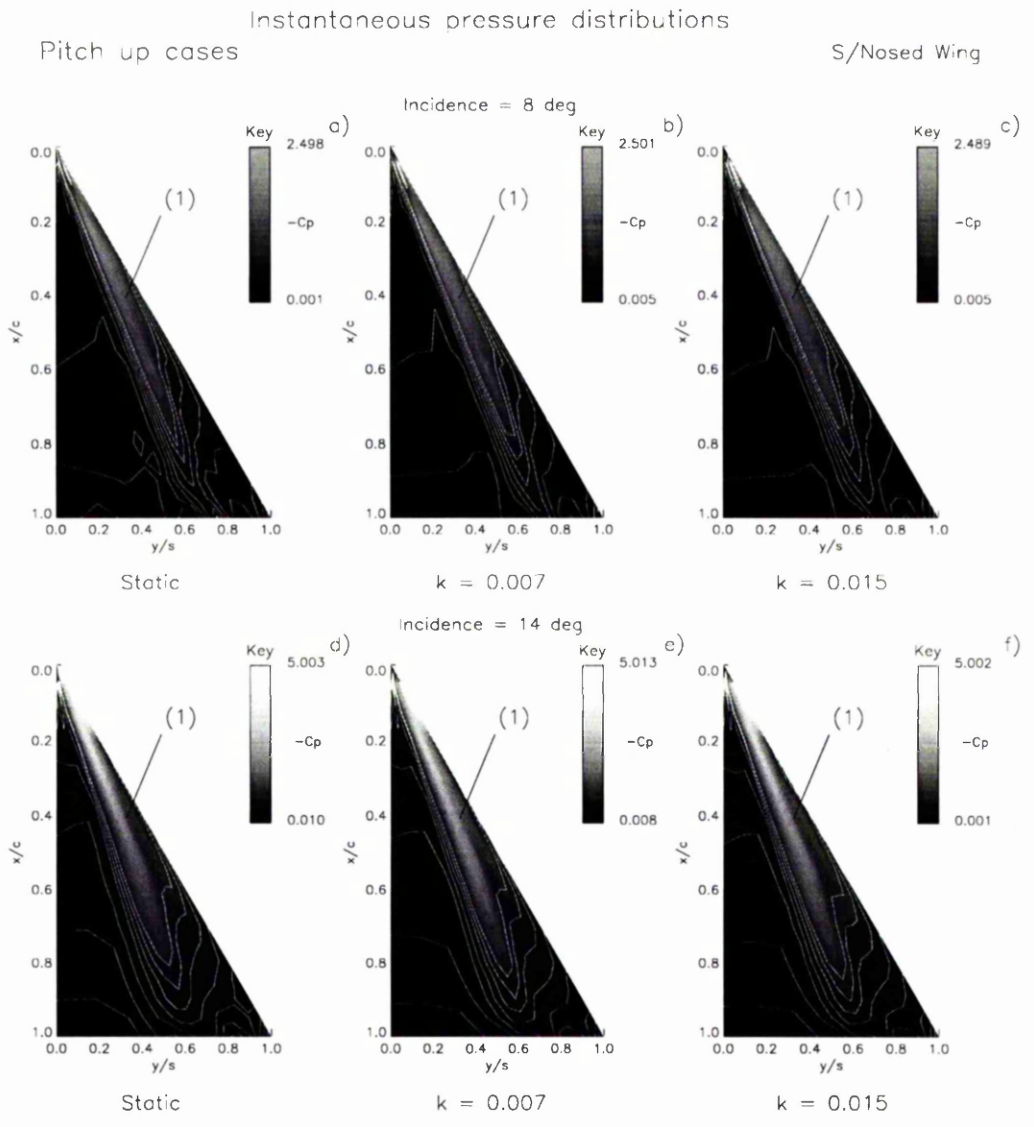

Figure 4.18 - Contour plots of mean & instantaneous C_P pressure distributions at **8°** and **14°** incidences for static, k = 0.007 and k = 0.015 cases. Data collected during pressure measurement tests. Re = 2.7×10^6.

Key: Suction pressure ridge labelled as (1)

Note: **bold** type denotes change of parameter from previous figure.

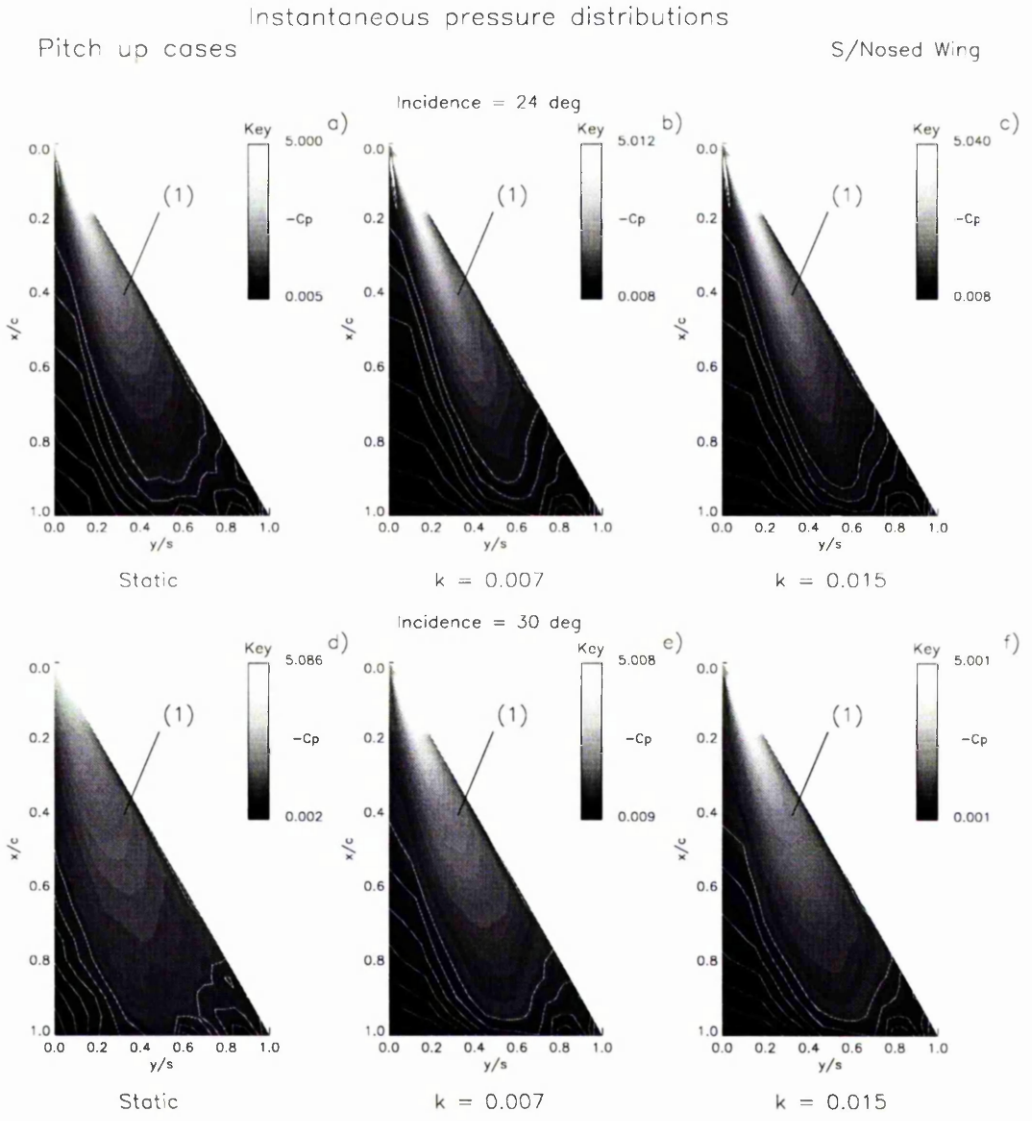

Figure 4.19 - Contour plots of mean & instantaneous C_P pressure distributions at **24°** and **30°** incidences for static, k = 0.007 and k = 0.015 cases. Data collected during pressure measurement tests. Re = 2.7×10^6.

Key: Suction pressure ridge labelled as (1)

Note: **bold** type denotes change of parameter from previous figure.

Figure 4.20 shows the distribution of -C_P across the span of the wing for the same three pitch rates at chord station x/c = 0.3875 at incidences of 2°, 4° and 8°. At an incidence of 2° in plot a), all three spanwise suction peaks were located at y/s = 0.8 with the two pitching cases slightly lagging the static case in terms of peak magnitude. At 4° shown in plot b), there is very little difference in the magnitude of each suction peak, but it is at this incidence that the suction peak origin in all cases began its upstream movement towards the wing apex and the ridge itself began its inboard movement towards its stable spanwise position and subsequently demonstrated a progressive lag in both phenomena with an increase in pitch rate magnitude. At 8° indicated by plot c), the lead in terms of inboard movement and peak magnitude of the static over the pitching cases is quite clear.

Figure 4.21 presents the spanwise pressure distributions for the same three cases at incidences of 14°, 24° and 30°. At 14° incidence shown in plot a), all three suction ridges have reached their stable spanwise position at x/c = 0.7 and the suction peak magnitudes are very similar. By 24° indicated in plot b), the static case spanwise peak suction is declining and the k = 0.007 case has reached its maximum value. The k = 0.015 case will reach its maximum at 26°. At 30° incidence shown in plot c), static case suction has declined considerably and is clearly moving towards the wing centreline, whereas the pitching cases exhibit a higher level of suction and a position which lies further outboard.

4.2.3 *Pressure measurements - pitch down tests*

For the pitch down cases, the instantaneous C_P distributions revealed similar features and characteristics to the static and pitch up cases. The suction ridge first became apparent at an incidence of 21° along a ray at a span station of y/s = 0.5. Figures 4.22, 4.23 and 4.24 present a series of contour plots of the static case mean pressure and instantaneous pressure distributions for two pitch down cases

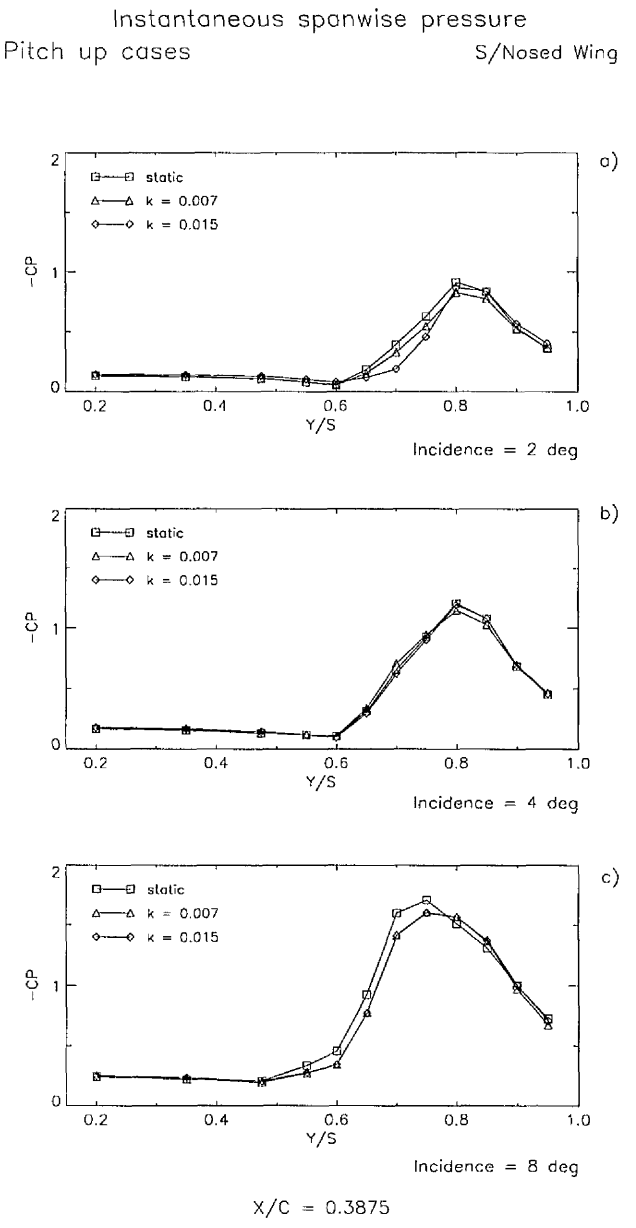

Figure 4.20 - Line plots of spanwise mean and instantaneous Cp pressure distributions at x/c = 0.3875 for static, k = 0.007 and k = 0.015 cases at 2°, 4°and 8° incidences. Data collected during pressure measurement tests. Re = 2.7×10^6

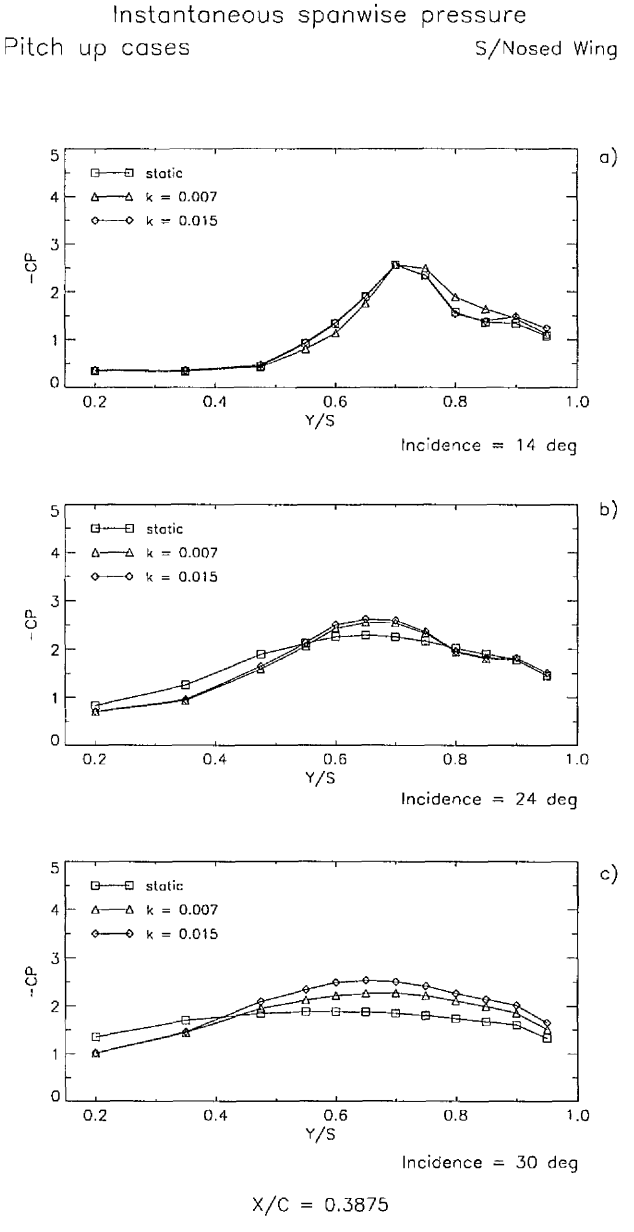

Figure 4.21 - Line plots of spanwise mean and instantaneous C_P pressure distributions at x/c = 0.3875 for static, k = 0.007 and k = 0.015 cases at **14°**, **24°**and **30°** incidences. Data collected during pressure measurement tests. Re = 2.7×10^6

Note: **bold** type denotes change of parameter from previous figure.

(k = -0.007 & k = -0.017) on the leeward surface of the wing at incidences of 18°, 14°, 10°, 8°, 4° and 0°. At 18° incidence shown in Figure 4.22, plots a) to c), indeed at all incidences where the suction ridge was present on the wing, there appeared to be a progressive lag in its growth, and in the progression of the ridge towards the trailing-edge with an increase in pitch rate magnitude. By 14°, the suction ridge (1) in the k = -0.007 case, indicated in Figure 4.22, plot e) had extended further downstream and has reached its stable spanwise location. The suction ridge in the k = -0.017 case, shown in plot f), lags its lower pitch rate counterpart in terms of downstream progression and spanwise movement, not reaching its stable spanwise location until an incidence of 12°.

By 10° indicated in Figure 4.23, plots a) to c), the suction ridge (1) was more defined in each case although the progression towards the trailing-edge was still less advanced with an increase in the pitch rate magnitude. At 8° incidence, shown in Figure 4.23, plots d) to f), the suction ridge in the pitch down cases still advanced towards the trailing-edge, however in all cases, the ridge began to narrow. At an incidence of 4°, presented in Figure 4.24, the static case suction ridge origin, shown in plot a), has yet to advance upstream towards the wing apex from a position on the leading-edge at x/c = 0.2. However, in both pitch down cases, shown in plots b) and c), the origin has only receded as far as x/c = 0.125. Similarly, the static case suction ridge, having taken up a spanwise location of y/s = 0.8, leads the two pitch down cases, where spanwise location of the suction ridge was positioned at y/s = 0.75. At 0°, the origin of the suction ridge in both pitch down cases has finally receded to x/c = 0.2 and the downstream extent of the ridge, particularly the k = -0.007 case, is greater than the for the static wing.

Figures 4.25 and 4.26 show a series of line plots of the spanwise mean and instantaneous C_P distributions at a chord station of x/c = 0.3875, for the static

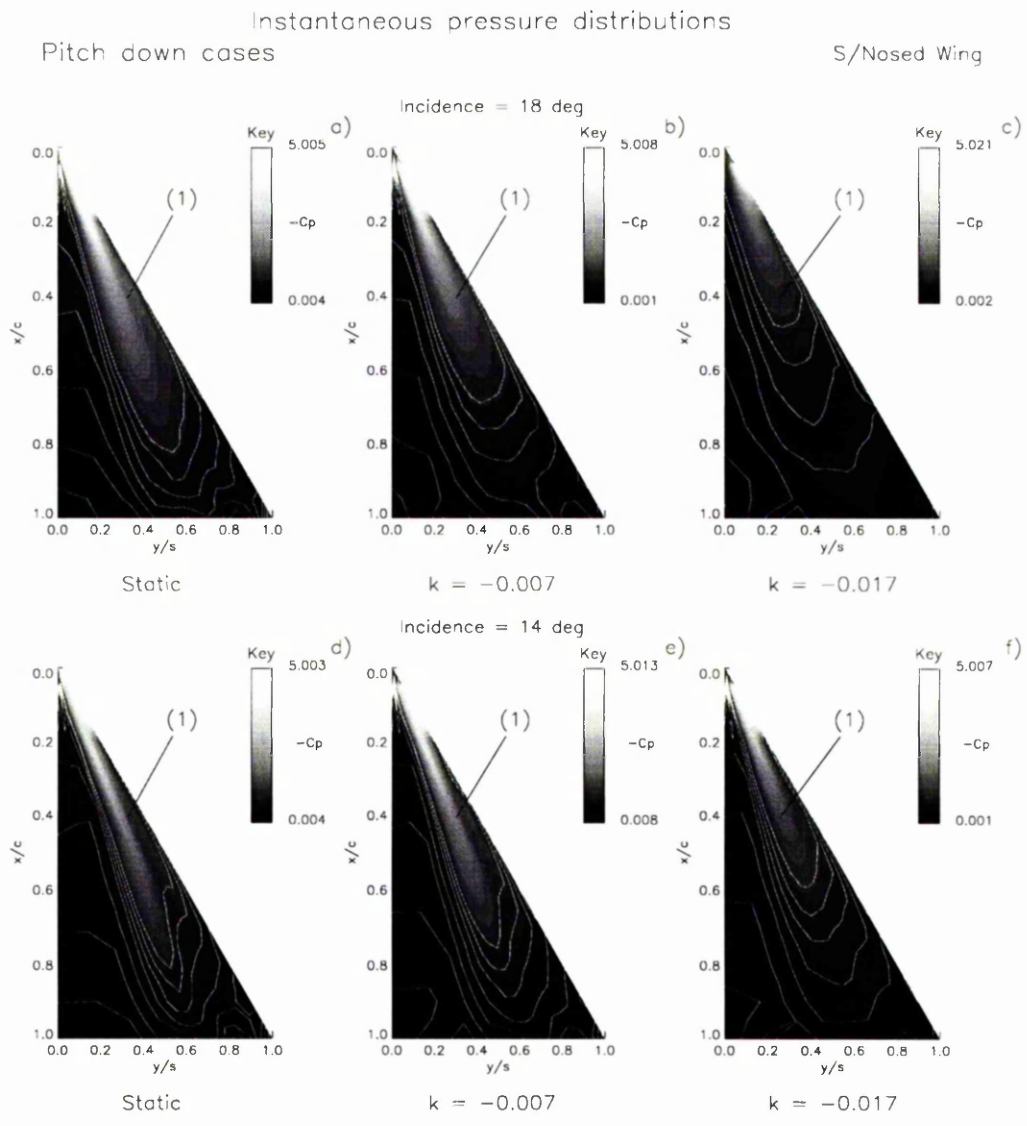

Figure 4.22 - Contour plots of mean & instantaneous C_P pressure distributions at 18° and 14° incidences for static, k = -0.007 and k = -0.017 cases. Data collected during pressure measurement tests. Re = 2.7×10^6.

Key: Suction pressure ridge labelled as (1)

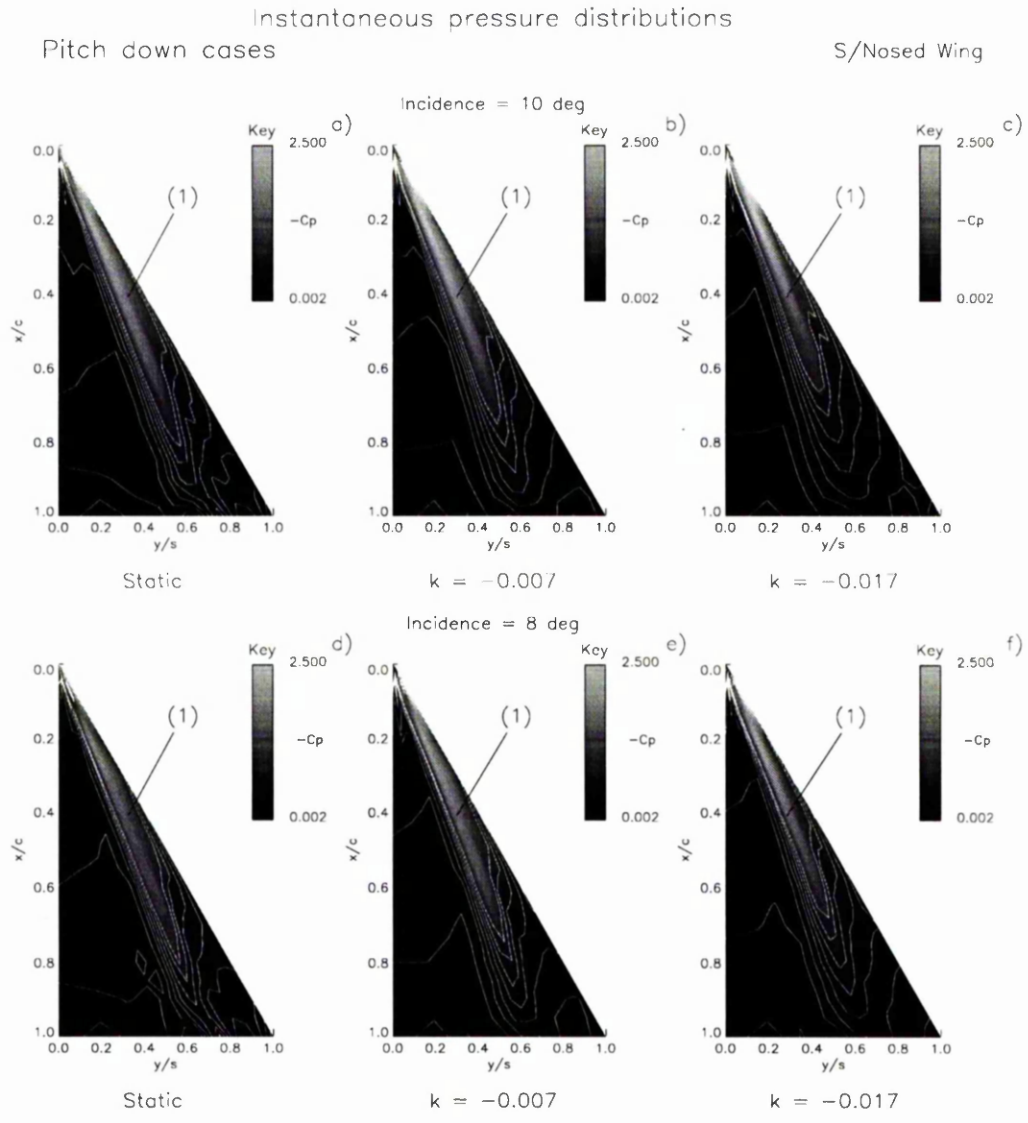

Figure 4.23 - Contour plots of mean & instantaneous Cp pressure distributions at **10°** and **8°** incidences for static, k = -0.007 and k = -0.017 cases. Data collected during pressure measurement tests. Re = 2.7×10^6.

Key: Suction pressure ridge labelled as (1)

Note: **bold** type denotes change of parameter from previous figure.

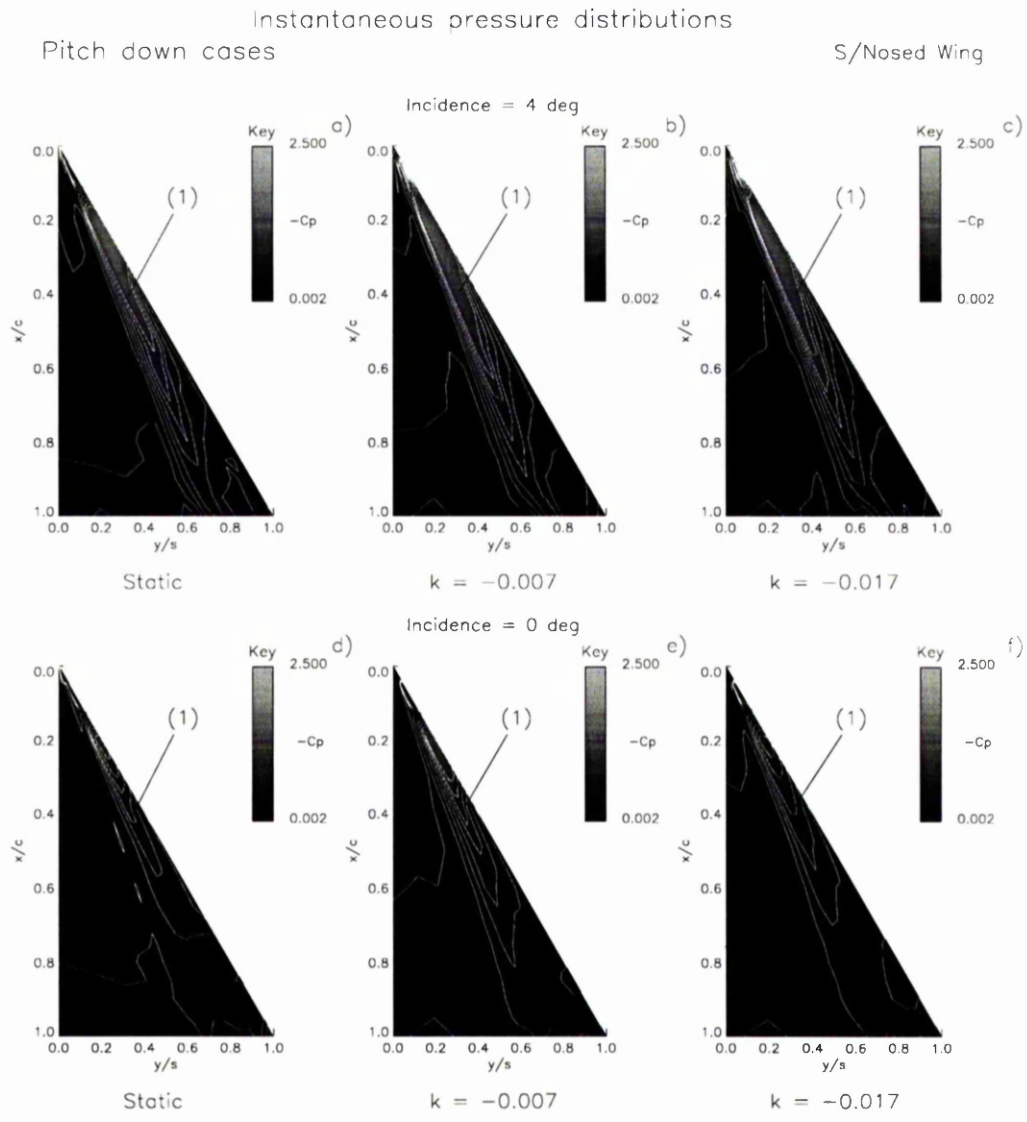

Figure 4.24 - Contour plots of mean & instantaneous Cp pressure distributions at **4°** and **0°** incidences for static, k = -0.007 and k = -0.017 cases. Data collected during pressure measurement tests. Re = 2.7×10^6.

Key: Suction pressure ridge labelled as (1)

Note: **bold** type denotes change of parameter from previous figure.

and two pitch down cases. Figure 4.25, plot a) shows the spanwise distributions at 18° incidence where the progressive lag in peak suction with increase in pitch rate magnitude, can be clearly seen. At 14° incidence, shown in Figure 4.25, plot b), the lag in peak pressure magnitude was still apparent and it is clear that, in the k = -0.017 case, the suction peak had yet to reach its stable spanwise location. By 10° incidence shown in Figure 4.25, plot c), the peak spanwise suction on the static wing now lagged the k = -0.007 peak magnitude and is fast being approached by the peak suction magnitude in the k = -0.017 case, which, at this chord station and incidence is reaching its maximum value. At this incidence, the three suction ridges were located at a span position of y/s = 0.7. At an incidence of 8°, shown in Figure 4.26, plot a), the static case now displays the lowest peak suction magnitude of the three cases and is taking up a span station of y/s = 0.75. By 4° incidence, shown in Figure 4.26, plot b), it is clear that in the two pitch down cases, the suction peaks have just started their outboard movement towards the leading-edge in a similar fashion to the initial formation of the static case but tended to lag the static case at this incidence. Finally, by 0° incidence shown in Figure 4.26, plot c), the suction ridge in the k = -0.007 case was still discernible at a span station of y/s = 0.8 and the higher rate pitch down case of k = -0.017 shows, surprisingly, a lower peak magnitude centred around y/s = 0.75.

4.2.4 *Pressure measurements - changes in apex geometry*

For the round-nosed wing during static tests, the formation and development of the leeward surface suction ridge was essentially similar to that of its sharp-nosed counterpart, however, subtle key differences were observed throughout the incidence range. Figures 4.27 and 4.28 show contour plots of the mean pressure distributions in the sharp and round-nosed static cases at incidences of 2°, 6°, 10°, 16°, 24° and 30°. Figure 4.27, plots a) and d) show, for the sharp and round

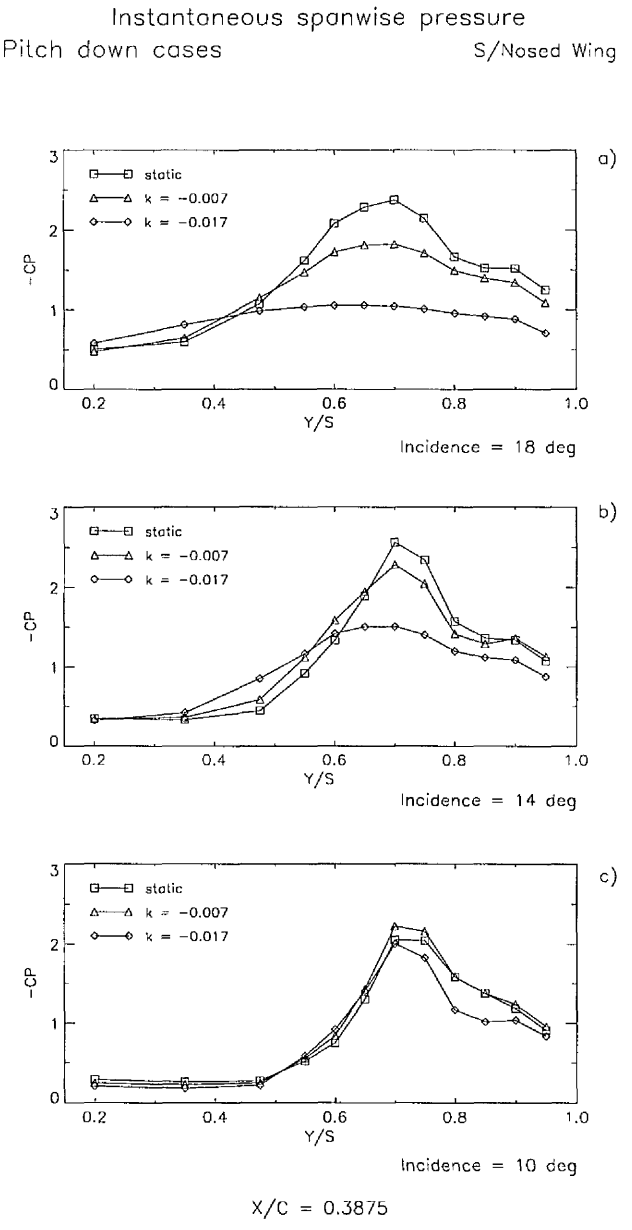

Figure 4.25 - Line plots of spanwise mean and instantaneous C_P pressure distributions at x/c = 0.3875 for static, k = -0.007 and k = -0.017 cases at 18°, 14°and 10° incidences. Data collected during pressure measurement tests. Re = 2.7×10^6

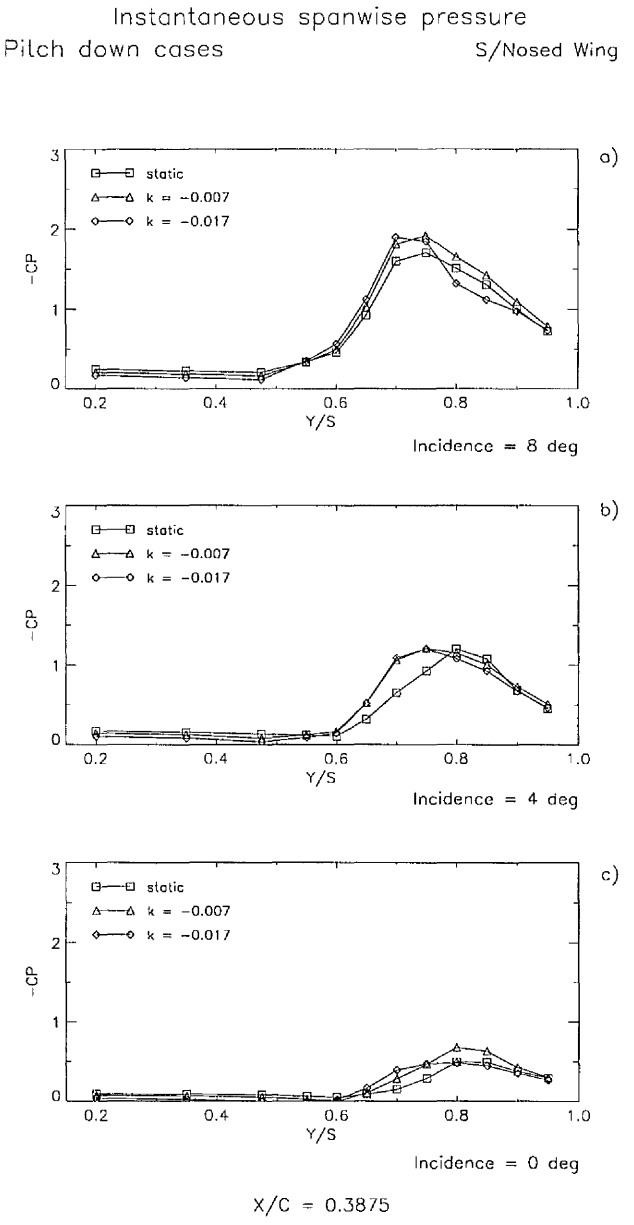

Figure 4.26 - Line plots of spanwise mean and instantaneous C_P pressure distributions at x/c = 0.3875 for static, k = -0.007 and k = -0.017 cases at **8°, 4°**and **0°** incidences. Data collected during pressure measurement tests. Re = 2.7×10^6

Note: **bold** type denotes change of parameter from previous figure.

nosed wings respectively, that at 2° incidence, both suction ridges originated at the leading-edge at a chord station of $x/c = 0.2$ and extended towards the trailing-edge along a ray at $y/s = 0.8$. It was apparent that the downstream extent of the suction in the round-nosed case lagged that of the sharp-nosed case at this incidence. At an incidence of 6°, the general form of the suction ridge was similar for the two wings. However, in the sharp-nosed case, shown in plot b) the origin of the suction ridge was moving towards the wing apex, whereas the round-nosed case ridge (plot e) apparently remained stationary at $x/c = 0.2$. At 10° incidence, shown in plots c) and f), the origin of the suction ridge had reached the wing apex in the sharp-nosed case (plot c) whereas the ridge origin in the round-nosed case (plot f), had moved upstream only as far as $x/c = 0.13$. However, the round-nosed case indicates a higher suction pressure at a chord position of $x/c = 0.2$ than is evident in the sharp-nosed case. By 16° incidence for the round-nosed case, as indicated in Figure 4.28, plot d) the origin of the suction ridge has yet to reach the apex of the wing, although the form of the suction ridge is similar to the sharp-nosed case shown in plot a). By 24° and again at 30° incidence, as shown in plots b) & e) and c) & f) respectively, the differences between the two mean C_P distributions are minimal.

It is clear from the previously described contour plots of the mean C_P distributions that the most significant differences between the sharp and round nosed cases occur during the initial formation and development of the suction ridge at incidences of 10° or less. Figure 4.29 shows the spanwise mean C_P distributions for the sharp and round-nosed cases at a chord position of $x/c = 0.3875$, at incidences of 2°, 6° and 10°. At 2° incidence shown in plot a), where the origin of the two suction ridges were similarly located at $x/c = 0.2$, the magnitude and spanwise position of the two ridges was also similar. At 6°

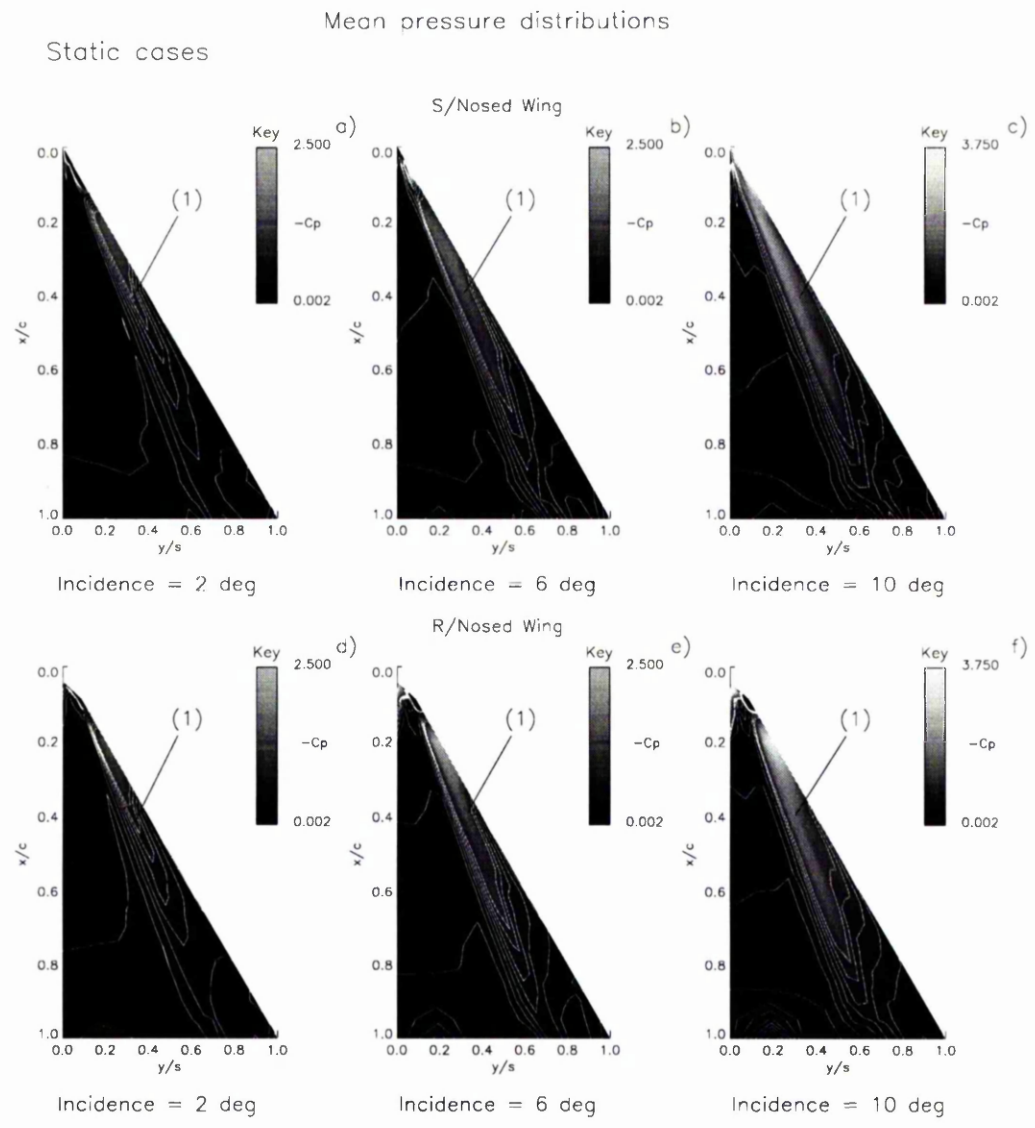

Figure 4.27 - Contour plots of mean C_P pressure distributions on sharp and round-nosed wings at 2° 6° and 10° incidences for static cases. Data collected during pressure measurement tests. Re = 2.7×10^6.

Key: Suction pressure ridge labelled as (1)

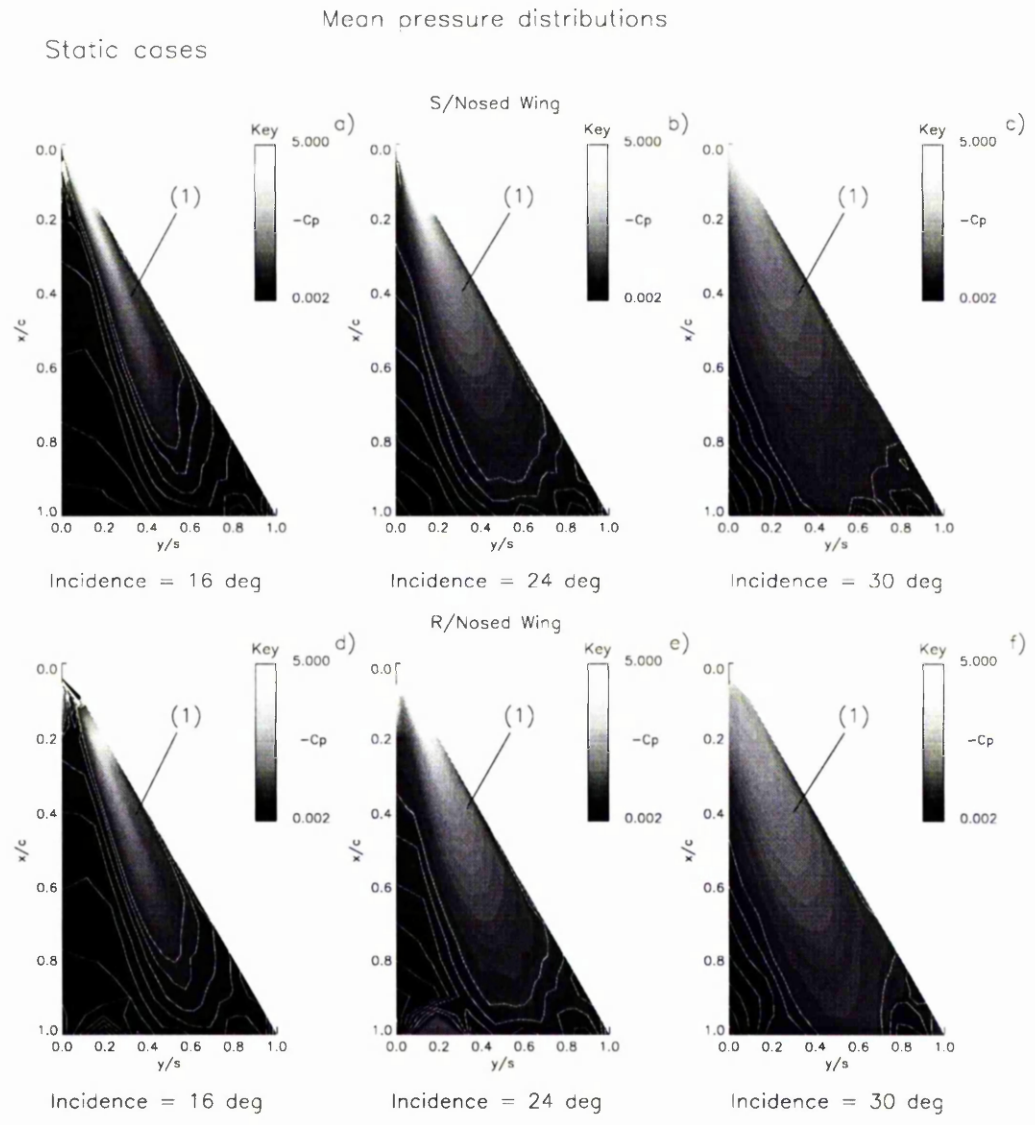

Figure 4.28 - Contour plots of mean C_P pressure distributions on sharp and round-nosed wings at **16°**, **24°** and **30°** incidences for static cases. Data collected during pressure measurement tests. Re = 2.7×10^6.

Key: Suction pressure ridge labelled as (1)

Note: **bold** type denotes change of parameter from previous figure.

incidence, shown in plot b), where the origin of the suction ridge in the sharp-nosed case was moving towards the wing apex and where it was still stationary in the round-nosed case, there was little difference in the magnitude of the peak suction pressure, however, the sharp-nosed case ridge was beginning to show an inboard movement towards its stable position and the round-nosed case was starting to lag behind. By 10° incidence shown in plot c), the difference in spanwise position was still evident and the magnitude of the peak suction pressure at this chord position was significantly higher in the sharp-nosed case than for its round-nosed counterpart at the same incidence. This corresponds to the arrival of the suction ridge origin at the wing apex in the sharp-nosed case and the delay in upstream movement of the origin on the round-nosed wing. At subsequent incidences (not shown) the magnitude and position of the suction ridge in the round-nosed case caught up with the sharp-nosed wing, until at 19°, where the round-nosed suction ridge origin finally reached the wing apex, the differences in the two pressure distributions became negligible. Figure 4.30 shows the maximum spanwise suction pressure at each chord station from $x/c = 0.2$ to $x/c = 0.95$ for the sharp and round-nosed cases at incidences of 2°, 6° and 10°. This diagram charts the increase in chordwise pressure gradient between the sharp and round-nosed wings as incidence was increased, where the origin of the suction ridge in the round nosed case remained at $x/c = 0.2$, whilst its counterpart advanced upstream towards its sharp-nosed wing apex. This difference in chordwise pressure gradients and their effect on the arrival and upstream progression of vortex breakdown is discussed in Chapter 6.

In summary, the analysis of the mean and instantaneous pressure distributions provide useful information regarding the formation and development of vortices above the leeward surface of delta wings with changes in incidence and pitch rate magnitude. At very low incidences, these vortices above the wing produce suction

ridges on the surface of the wing which have their origins at some point on the leading-edge and extend towards the trailing-edge. In all static and pitch up cases, at some incidence, the origin of each suction ridge moves to the apex of the wing and the vortex takes up a spanwise location inboard of its original starting point. An increase in pitch rate magnitude reveals a progressively increased lag in such movement and a subsequent delay in the increase in peak suction magnitude. Peak suction increases until, at some incidence, it declines again under the influence of vortex breakdown. An increased overshoot in terms of incidence and a delay in the reduction of peak suction, are observed with increasing pitch rate magnitude. Eventually, at a given incidence, the suction ridge moves towards the wing centreline, where the probable interaction of the two primary vortices on the wing results in a rapid decline in peak suction. At very high incidence, the wing behaves like a bluff body.

Similarly, in pitch down cases, the initial appearance of the suction ridge occurs during vortex restoration inboard of its steady state position and moves outboard with decreasing incidence showing a progressively increased lag in ridge movement and peak suction increase with an increase in pitch rate magnitude. At incidences of 8° or less, the pitch down cases exhibit peak suction levels above that of the static case at a comparable incidence and still maintain a coherent suction ridge at incidences as low as 0°.

Despite this detailed information, the analysis of the mean and instantaneous pressure distributions was unable to accurately track the progress of vortex breakdown or restoration over the wing surface. The only clues apparent in the data were the decline in suction values at high incidences, but these occurred long after the arrival of vortex breakdown at the trailing-edge of the wing. Hence, further investigation methods were examined.

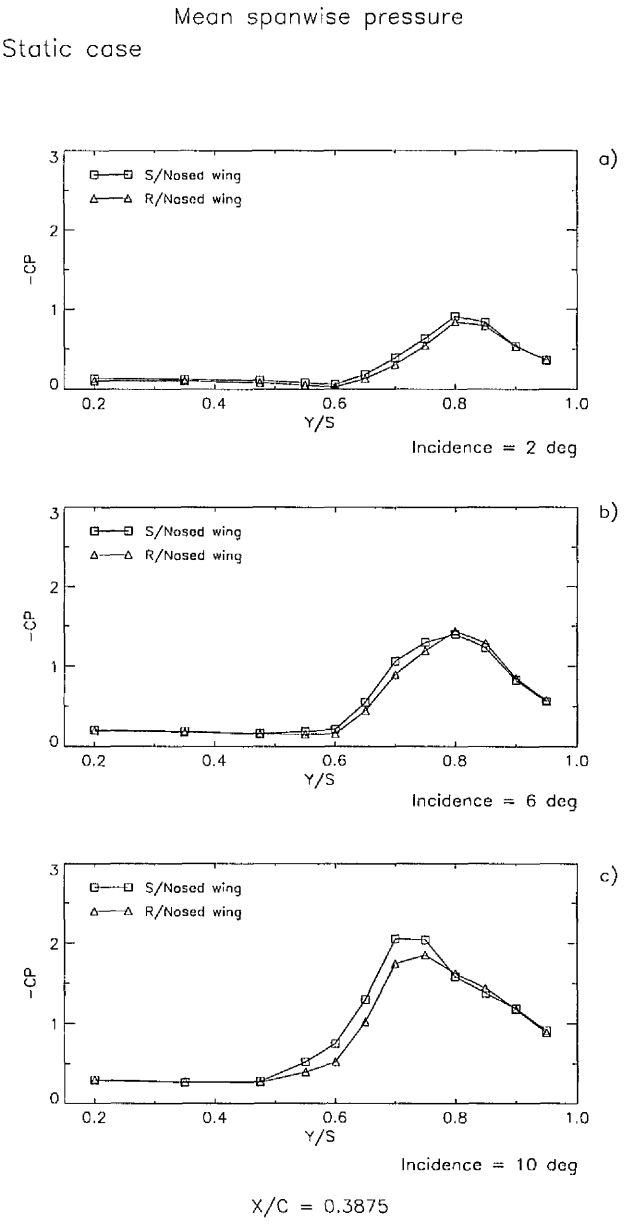

Figure 4.29 - Line plots of spanwise mean C_P pressure distributions at x/c = 0.3875 on sharp and round-nosed wings for static cases at 2°, 6°and 10° incidences. Data collected during pressure measurement tests. Re = 2.7×10^6

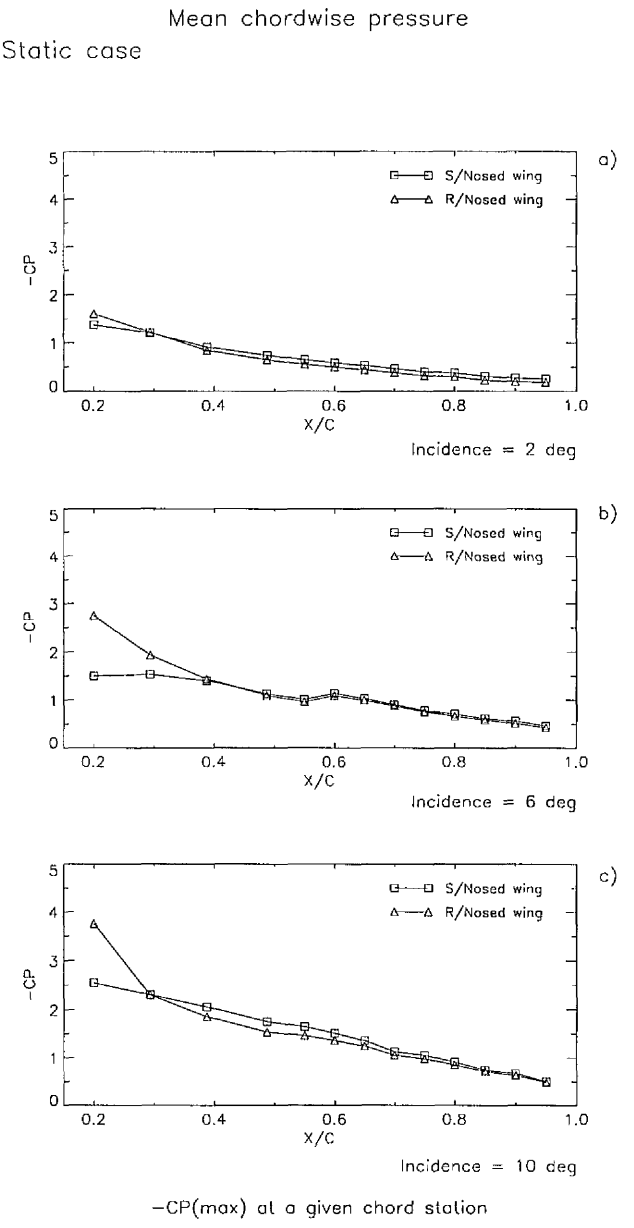

Figure 4.30 - Line plots of maximum spanwise mean suction pressure at chord positions from x/c = 0.2 to x/c = 0.95 on sharp and round-nosed wings for static cases at 2°, 6°and 10° incidences. Data collected during pressure measurement tests. Re = 2.7×10^6

4.3 ANALYSIS OF THE ROOT-MEAN-SQUARE PRESSURE DISTRIBUTION

4.3.1 *Static tests*

In addition to the study of the mean C_P distribution, the RMS pressure fluctuations around the mean were examined for static test data at each angle of incidence. Figure 4.31 shows a series of contour plots of the RMS pressure distribution on the leeward surface of the wing at incidences of 0°, 1°, 2°, 4°, 8° and 10°. Examination of the distribution at 0° incidence in plot a) shows the growth of a region of high RMS pressure, labelled as (2), in the form of a ridge located along a ray from a region on the leading-edge towards the trailing edge of the wing. Like its counterpart in the mean C_P distribution, the region of high RMS grew in strength with an increase in incidence, but unlike the suction ridge its strength did not diminish with distance from the wing apex. As the incidence was increased to 1°, as shown in plot b), the tail of the region of high RMS began to split into two at a chord station of $x/c = 0.72$. By 2° incidence, (plot c), the fork-tailed region of high RMS pressure (2) had grown in magnitude and the division point had moved upstream to $x/c = 0.6$. At an incidence of 4° shown in plot d) a further change in the structure of the region of high RMS pressure takes place. The 'split' region of high RMS pressure was composed of two distinct ridge-like structures. The 'primary' region (2) extends from the apex towards the trailing edge whereas the 'secondary' region (3) is seen as a branch of the primary emanating from some point downstream of the apex and terminating near of the trailing edge. At 8° incidence (plot e), the distinct nature of the two regions of high RMS pressure was more apparent and the primary structure (2) had reached the trailing-edge of the wing. By 10° incidence, as clearly illustrated by plot f), the two regions of high RMS pressure have separated completely such that the secondary region (3) appears to have an origin at $x/c = 0.25$ on the leading-edge of the wing.

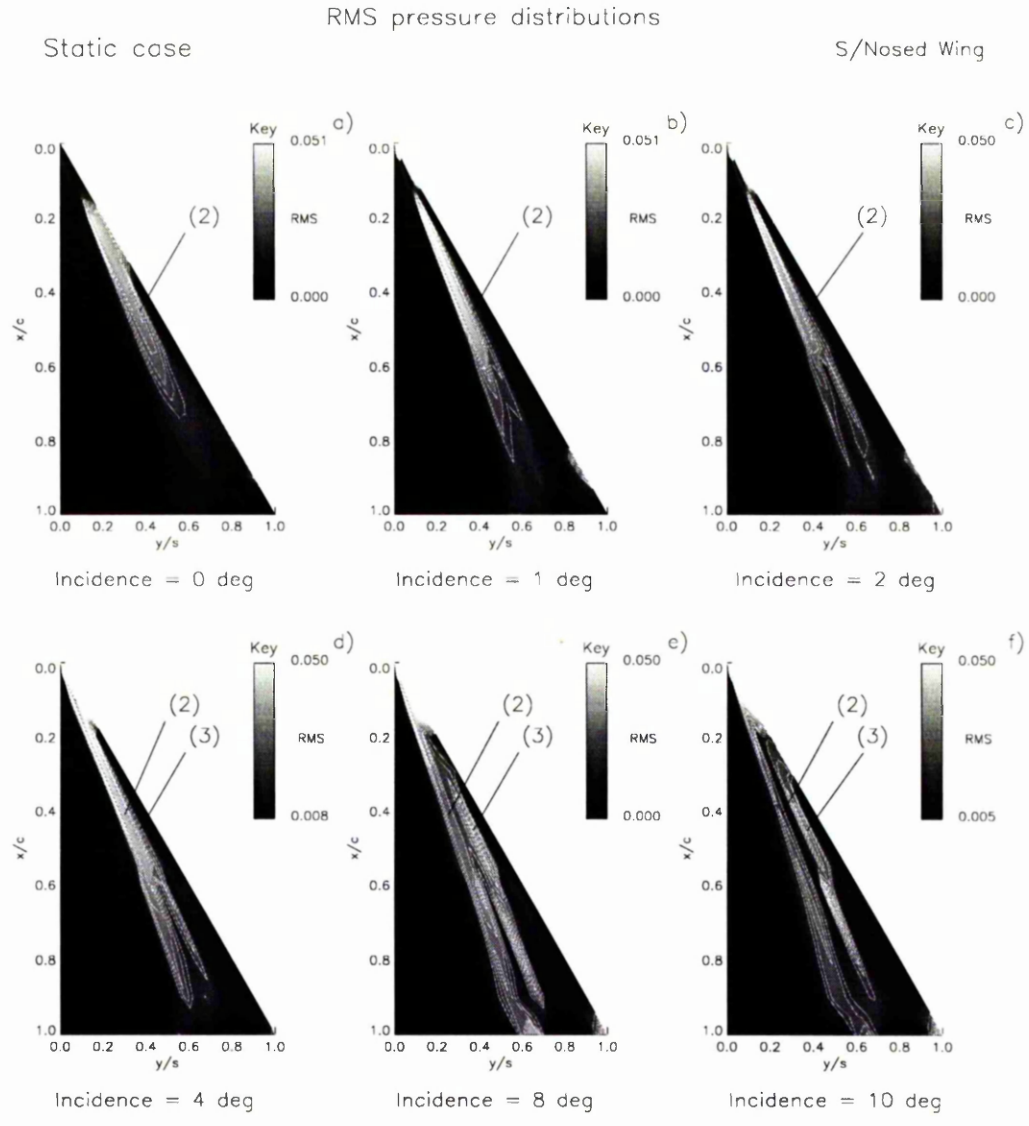

Figure 4.31 - Contour plots of RMS pressure distributions at 0°, 1°, 2°, 4°, 8° and 10° incidences during static pressure measurement tests. Re = 2.7×10^6

Key: Primary RMS region labelled as (2)
Secondary RMS region labelled as (3)

Figure 4.32 shows the RMS pressure distribution across the span of the wing at chord station x/c = 0.6 at an incidence of 10°. Also plotted is the corresponding mean -C_P distribution. It is clear from both plots that the primary region of high RMS pressure lies inboard of the centreline of the primary vortex core. The secondary RMS pressure region, when apparent, lies outboard of the core. These plots are typical of the RMS pressure distribution over the incidence range corresponding to post-vortex formation and pre-vortex breakdown. The presence of a high RMS pressure region inboard of the vortex core was also observed by Woods and Wood (1996) in their work on novel planforms.

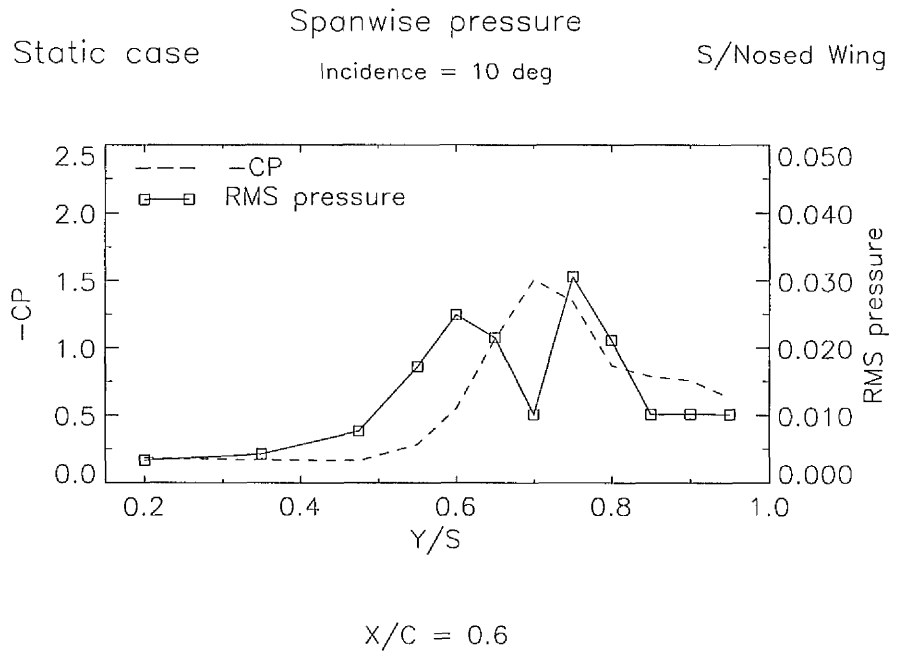

Figure 4.32 - Spanwise distributions of mean suction and RMS pressure in the static case at x/c = 0.6 and 10° incidence. Data collected during pressure tests. Re = 2.7x10^6

A further series of contour plots of the RMS pressure distribution on the leeward surface of the wing for six angles of incidence (12°, 14°, 18°, 24°, 30° and 36°) are

shown in Figure 4.33. At 12° incidence shown in plot a), it can be seen that the secondary branch of high RMS pressure (3) first shown in Figure 4.31 was still apparent, although it had begun to fragment. More significantly, an additional peak of high RMS pressure (4) is forming on the ridge of the primary region (2) at a point close to the trailing edge. Careful scrutiny of all contour plots revealed that this additional peak first appeared at this location on the wing at an incidence of 11° (not shown). The significant features accompanying the appearance of the additional peak were a 'waisting' of the above-described ridge upstream of the peak centre followed by a significant expansion towards the peak. At 14° incidence in plot b), the secondary region of high RMS pressure was still apparent, but had significantly reduced in length. Meanwhile, the additional peak of high RMS pressure (4) had increased in size and the waist had progressed upstream along the primary region (2) towards the wing apex. As the incidence was increased to 18°, (plot c), the secondary region of high RMS pressure was no longer apparent. The additional peak of high RMS pressure (4) had expanded in all directions and the waist (5) had moved further upstream to $x/c = 0.4$. At this incidence it is possible to detect the beginning of the upstream movement of the centre of the peak, but this occurs much more slowly than either the expansion of the high RMS pressure peak or the movement of the waist. By 24°, shown in plot d), the waist (5) upstream of the additional peak of high RMS pressure had reached $x/c = 0.2$ and the additional peak itself (4) had begun to move inboard towards the wing centreline in a similar manner to the mean pressure distribution suction ridge described in Section 4.2.1. By 30° incidence (plot e), the waist in the RMS pressure contours had reached the apex of the wing and the additional peak of high RMS pressure (4) was very close to the wing centreline, and by 36° the RMS pressure distribution was almost uniform with a low magnitude across the wing surface.

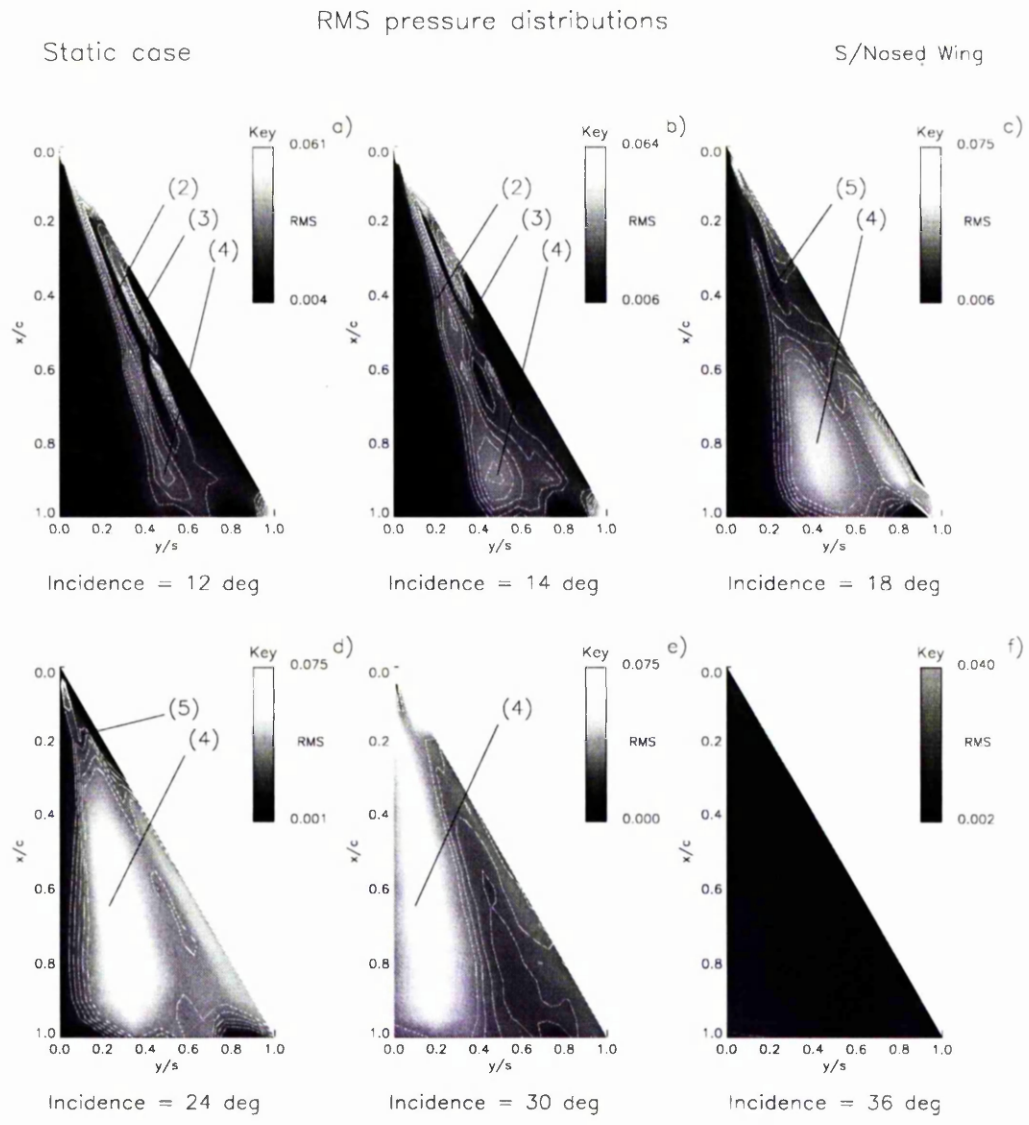

Figure 4.33 - Contour plots of RMS pressure distributions at 12°, 14°, 18°, 24°, 30° and 36° incidences during static pressure measurement tests. Re = 2.7×10^6

Key: Primary RMS region labelled as (2)
Secondary RMS region labelled as (3)
Additional peak of high RMS pressure, labelled as (4)
'Waisting' of RMS pressure contours, labelled as (5)

The upstream progression of the waisted region of RMS pressure contours, labelled in Figure 4.33 as (5) can be observed in some detail by plotting the chordwise distribution of RMS pressure. Figure 4.34 presents the maximum spanwise RMS pressure value at chordwise locations from $x/c = 0.2$ to $x/c = 0.95$ at incidences of 14°, 16°, 18°, 20°, 22° and 24°. Indicated on plots a), b) and c) is the chordwise location of the narrowest part of the waist in the contours of the primary region of high RMS pressure, labelled as (5) in each incidence case. It is clear from these plots, that the waist corresponded to the minimum in a small localised trough of RMS pressure which occurs before a rapid increase towards the peak. The plots as a whole show two general trends as incidence was increased. Firstly, the additional peak of high RMS pressure increased in magnitude, and secondly, the localised trough of RMS pressure, and hence the waist, moved upstream towards the apex of the wing. It can also be clearly seen that at incidences of 18° and higher, the centre of the additional peak moved upstream, but at a much slower velocity than the movement of the waist or the expansion of the peak.

Figure 4.35 shows the chordwise position of the waisted region or localised trough of RMS pressure as a function of incidence in the static case. Also reproduced on this plot is the chordwise location of vortex breakdown as indicated by the flow visualisation tests, whose results were described in Section 4.1. This diagram shows that there is a good agreement between the vortex breakdown position, as determined by the flow visualisation experiments, and the location of the waist or localised trough of RMS pressure immediately upstream of the additional peak of high RMS pressure.

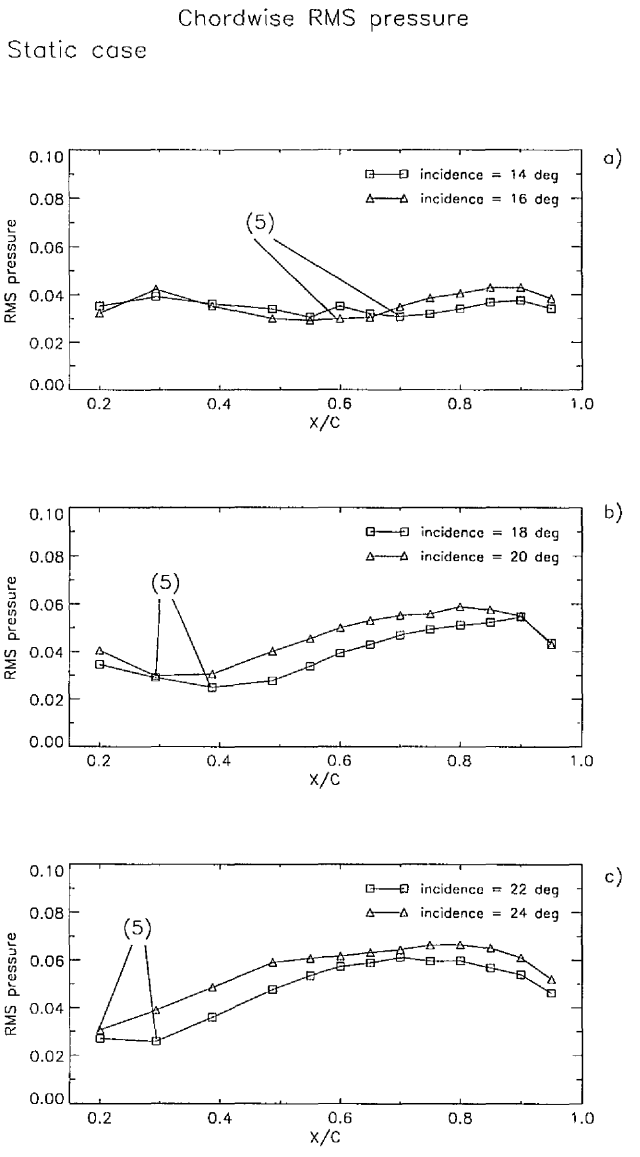

Figure 4.34 - Line plots of maximum spanwise RMS pressure values at chord stations from x/c = 0.2 to x/c = 0.95 for incidences of 14°, 16°, 18°, 20°, 22° and 24° data collected during static pressure measurement tests. Re = 2.7×10^6

Key: 'Waisting' of RMS pressure contours, labelled as (5)

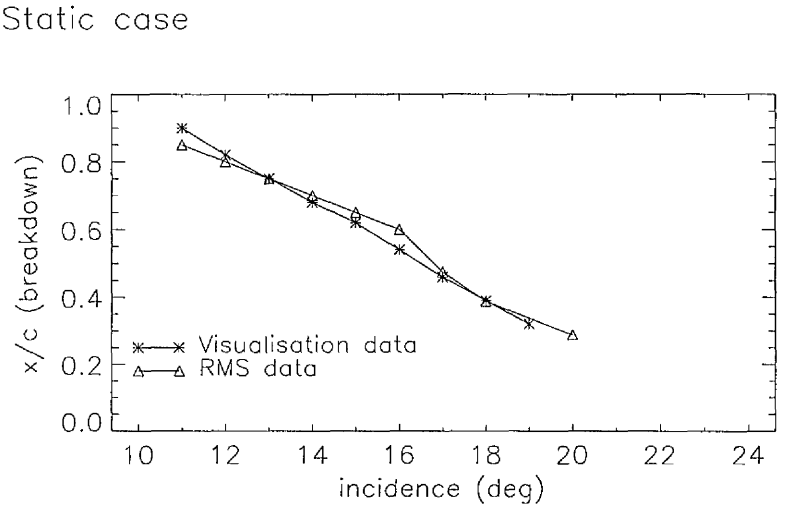

Figure 4.35 - The chordwise location of the waist or localised trough of RMS pressure compared with the chordwise location of vortex breakdown as functions of incidence in the static case. Data collected during pressure measurement tests & flow visualisation experiments. Re = 2.7×10^6 and 10000 respectively.

4.3.2 *RMS analysis - pitch up tests*

The high temporal resolution of the data provided the opportunity to study the RMS pressure distribution in a range of pitching cases. As described previously, this involved obtaining a trend line by applying a linear best-fit through the data signal for a given transducer over a pre-determined incidence range or 'window'. In order to minimise 'smearing' of physical effects across an incidence range, that is to say, mixing pre and post breakdown data, the incidence window had to be kept as small as possible. There was however, a limit to the size to which a given incidence window could be minimised. This was determined by the pitch rate and the pressure fluctuation frequency of interest. Clearly, the higher the pitch rate, the smaller the time period spanning a given incidence range. Therefore, increasing the pitch rate increases the lower limit of frequency of pressure fluctuations that satisfy the Nyquist criterion. Examination of the frequency

power spectrum of pressure fluctuations on the pitching wing at reduced pitch rates of k = 0.007 (54°/s) and k = 0.015 (115°/s) revealed a band of frequencies, whose appearance and dominance in the static case, had been shown by Gursul (1994), Woods & Wood (1996) and Mabey (1996) to be associated with the onset and progression of vortex breakdown. In order to capture these frequencies in their entirety, it will be shown later in this section that it was necessary to set the incidence windows to 1.5 deg. and 2.0 deg. respectively.

Figure 4.36 shows a series of contour plots of the RMS pressure distribution on the leeward surface of the wing for three pitch rates, (static, k = 0.007 and k = 0.015) at incidences of 2° and 4°. Like the static case, the distribution in each pitch up case is dominated by two ridges of high RMS pressure located along a ray from the apex towards the trailing edge. The initial appearance of the primary ridge in each case occurred at an incidence of 1°. At 2° incidence, shown in plots a) to c), there was clearly a lag in the formation and division of the primary region of high RMS pressure (2) with an increase in pitch rate magnitude. This trend was continued at an incidence of 4°, where the separate nature of the secondary ridge of high RMS pressure (3) was apparent in the static case (plot d), however, for the two pitching cases, (plots e and f), the single primary region of high RMS pressure (2) was in a progressively earlier stage of development and division as pitch rate magnitude was increased.

Figure 4.37 is a continuation of the previous diagram presenting the RMS pressure distributions of the same static and pitch up cases at incidences of 8° and 14°. By the time the wing incidence reaches 8° in each case, the secondary ridge of high RMS pressure (3) is formed, however in the two pitch up cases, shown in plots b) and c), the division of the two regions of high RMS pressure is not as well defined as in the static case, shown in plot a). In plots d) to f) at 14° incidence, the

secondary region of high RMS pressure (3) is still apparent in all three pitch rate cases, however, in the k = 0.007 case (plot e), the region has receded upstream to a lesser extent than the static case shown in plot d). The same feature in the higher pitch rate case k = 0.015 (plot f), has surprisingly all but disappeared. The additional peak of high RMS pressure (4) is also apparent and was centred at x/c = 0.9, for all three cases. This first appeared on the wing in the k = 0.007 case at 13°, and in the k = 0.015 case at 15°. However, the chordwise position of the waist in the contours of RMS pressure, clearly indicated at x/c = 0.7 on the static wing, is not so obvious in the k = 0.007 case. On the other hand, for the higher pitch rate of k = 0.015, the waist is again apparent, this time at x/c = 0.8.

Figure 4.38 shows the RMS pressure distribution across the span of the wing in the static and two pitch up cases, k = 0.007 and k = 0.015, at a chord station of x/c = 0.6 and an incidence of 10°. Also plotted is the corresponding instantaneous negative C_P distribution. It is clear from Figure 4.38 that in the pitch up cases (plots b and c respectively), the locations of the primary and secondary ridges of high RMS pressure in relation to the primary vortex core are similar to their static counterparts reproduced in plot a).

Figure 4.39 shows contour plots of the RMS pressure distribution for same three pitch rates at an incidences of 24° and 30°. In each case at 24°, (plots a to c), the secondary ridge of high RMS pressure has disappeared and the additional peak of high RMS pressure (4), together with the upstream waisting of the primary ridge contours (5), is present. The major difference between each case is a lag in the growth of the additional peak on the primary ridge, its upstream movement and the upstream movement of the waist as the pitch rate is increased. Similarly, plots d) to f), presenting results at 30° incidence, show for each case, the progressive lag in inboard movement of the additional peak of RMS pressure (4) that accompanies the inboard movement of the vortex suction ridge at this incidence.

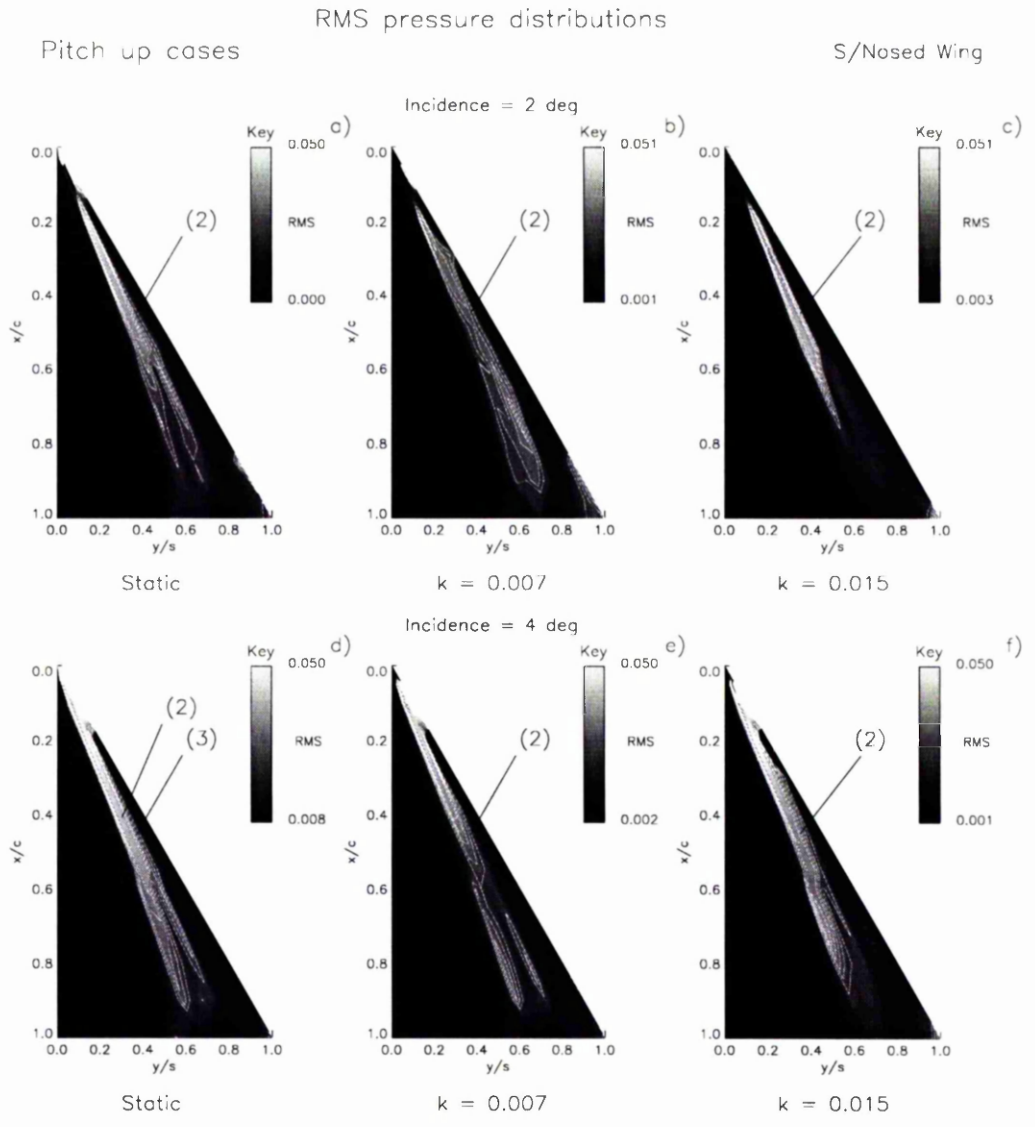

Figure 4.36 - Contour plots of RMS pressure distributions for static and two pitch up cases (k = 0.007 & k = 0.015) at incidences of 2° and 4°. Data collected during pressure measurement tests. Re = 2.7×10^6

Key: Primary RMS region labelled as (2)
Secondary RMS region labelled as (3)

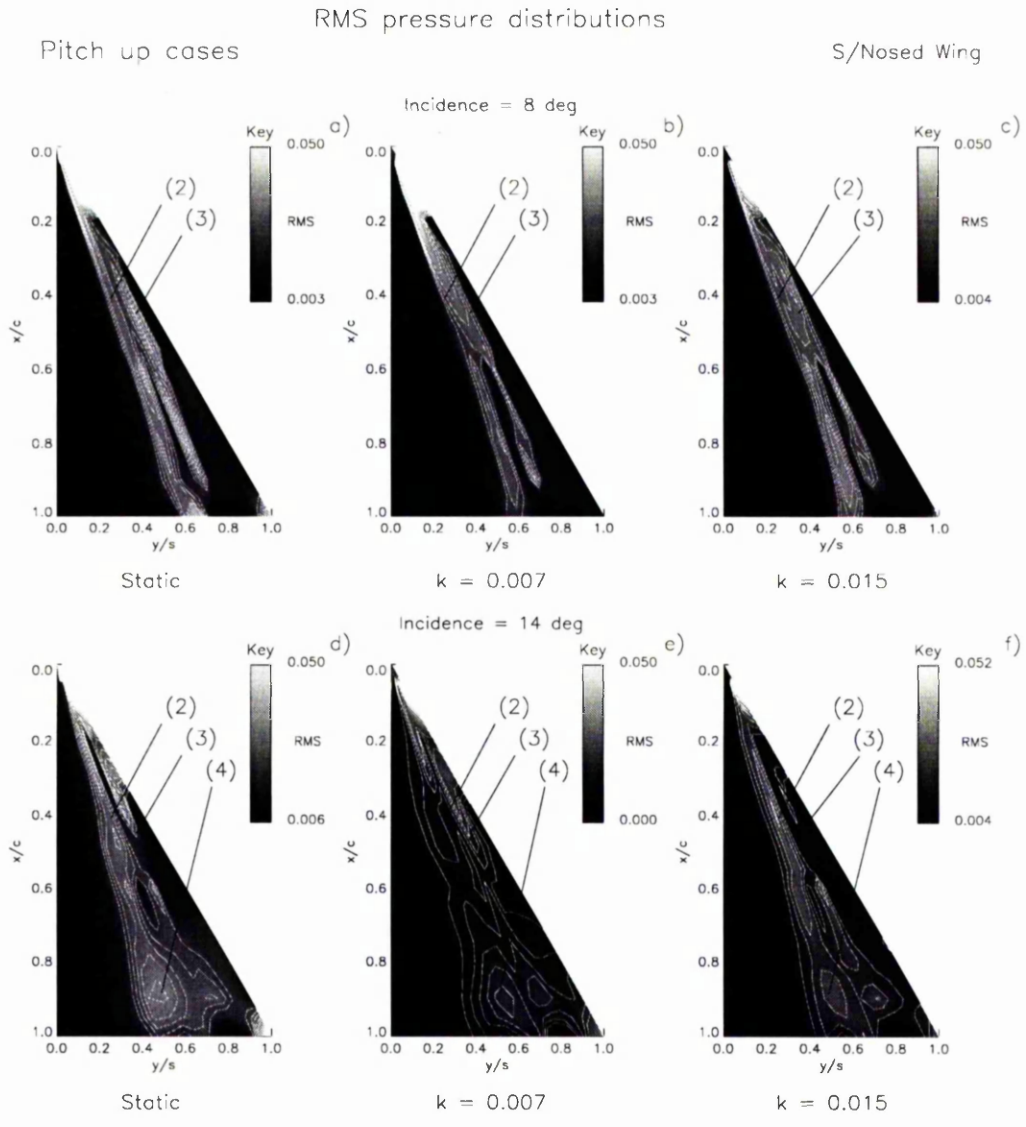

Figure 4.37 - Contour plots of RMS pressure distributions for static and two pitch up cases (k = 0.007 & k = 0.015) at incidences of **8°** and **14°**. Data collected during pressure measurement tests. Re = 2.7×10^6

Key: Primary RMS region labelled as (2)
Secondary RMS region labelled as (3)
Additional peak of high RMS pressure, labelled as (4)

Note: **bold** type denotes change of parameter from previous figure.

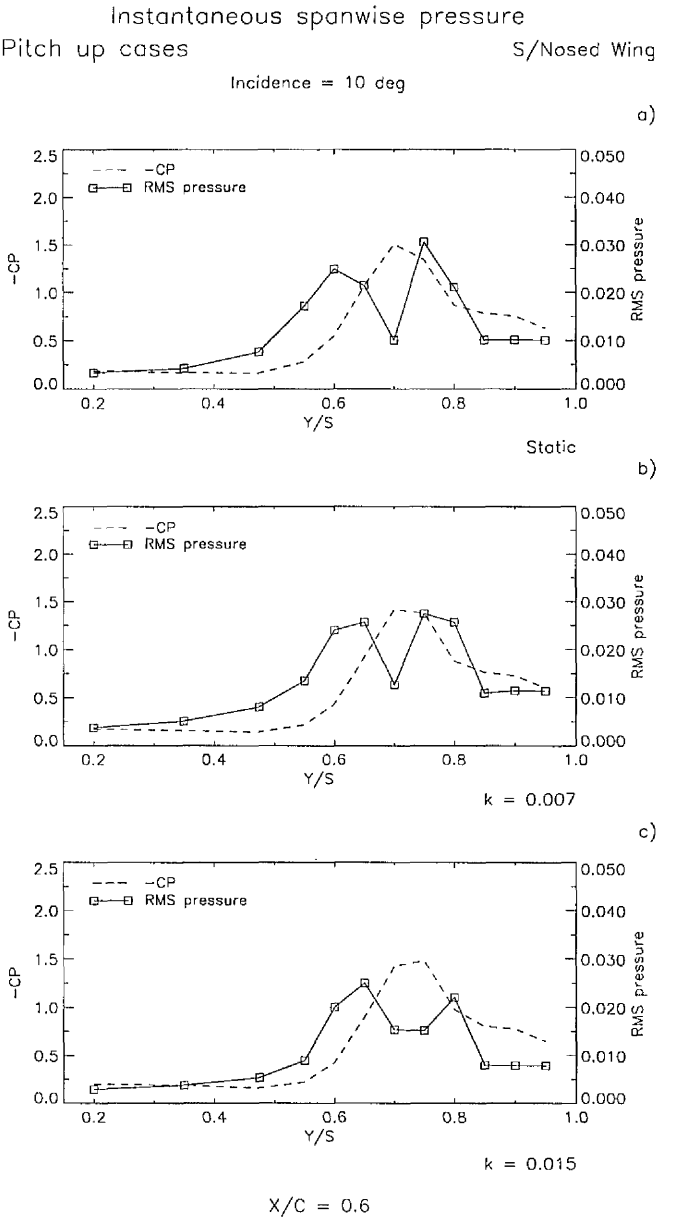

Figure 4.38 - Spanwise distributions of mean suction and RMS pressure in the static and two pitch up cases (k = 0.007 & k = 0.015) at x/c = 0.6 and 10° incidence. Data collected during pressure tests. Re = 2.7×10^6

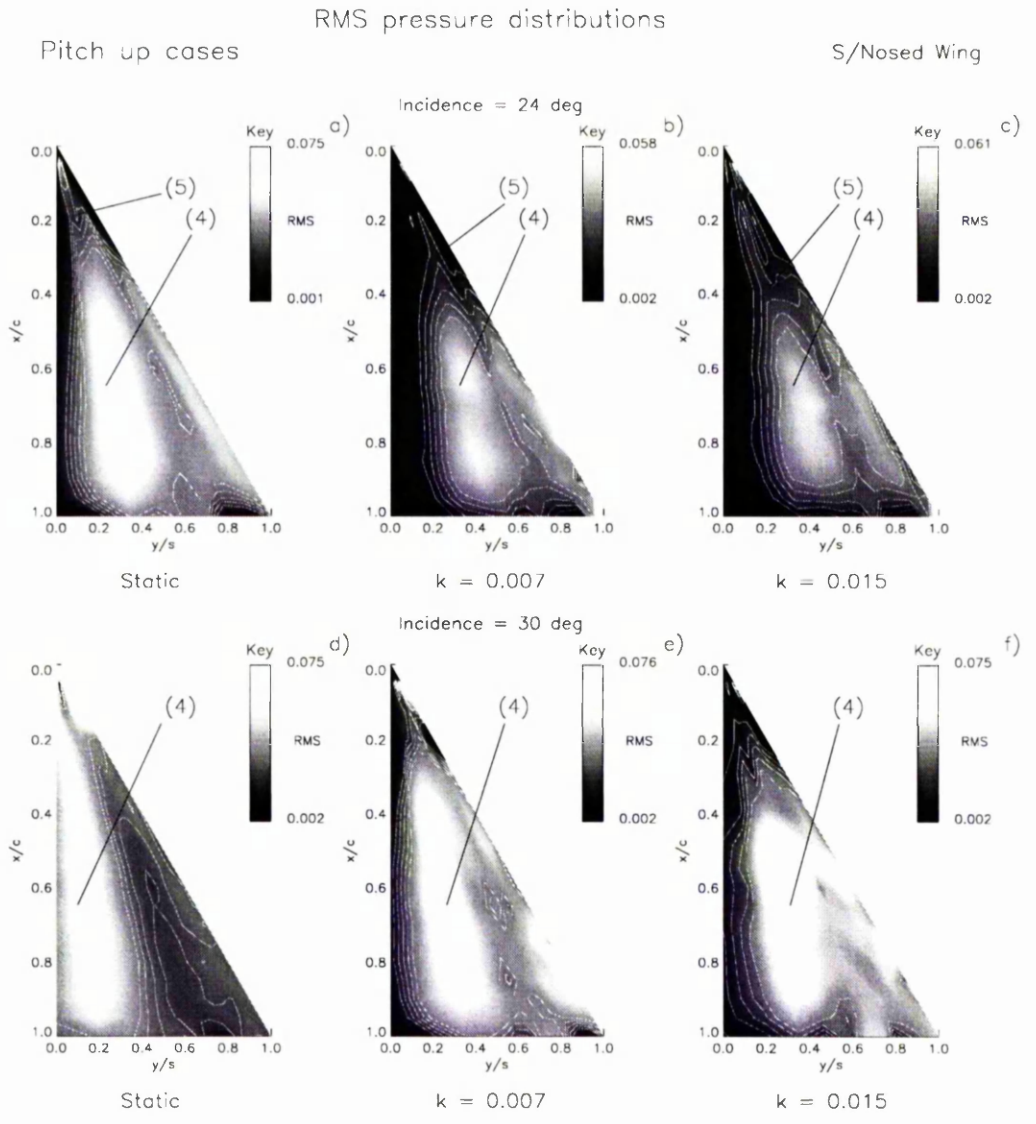

Figure 4.39 - Contour plots of RMS pressure distributions for static and two pitch up cases (k = 0.007 & k = 0.015) at incidences of **24°** and **30°**. Data collected during pressure measurement tests. Re = 2.7×10^6

Key: Additional peak of high RMS pressure, labelled as (4)
'Waisting' of RMS pressure contours, labelled as (5)

Note: **bold** type denotes change of parameter from Figure 4.37.

The upstream progression of the waisted region of RMS pressure contours, labelled in Figure 4.39 as (5) is presented in Figures 4.40 and 4.41, which show the maximum spanwise RMS pressure value at chordwise locations for the static and two pitch up cases ($k = 0.007$ and $k = 0.015$) from $x/c = 0.2$ to $x/c = 0.95$ at incidences of 14°, 16° and 18° (Figure 4.40) and 20°, 22° and 24° (Figure 4.41). Like the static case, the chordwise location of the narrowest part of the waist in the contours of the primary region of high RMS pressure, are labelled as (5) in each case and incidence. The plots as a whole show two general trends for all cases as incidence was increased. Firstly, the additional peak of high RMS pressure increased in magnitude, and secondly, the localised trough of RMS pressure, and hence the waist, moved upstream towards the apex of the wing. With an increase in pitch rate magnitude there is a trend indicating a lag in the upstream movement of the waist. Again it can be seen that at incidences of 18° and higher in all cases, the centre of the additional peak moved upstream, but at a much slower velocity than the movement of the waist or the expansion of the peak.

Figure 4.42 shows the chordwise position of the waisted region or localised trough of RMS pressure as a function of incidence in the static (plot a), $k = 0.007$ (plot b) and $k = 0.015$ (plot c) cases. Also reproduced on each plot are the corresponding chordwise locations of vortex breakdown as indicated by the flow visualisation tests, whose results were described in Section 4.1. This diagram shows that for static and pitch up cases there is a good agreement between the vortex breakdown position, as determined by the flow visualisation experiments, and the location of the waist or localised trough of RMS pressure immediately upstream of the additional peak of high RMS pressure.

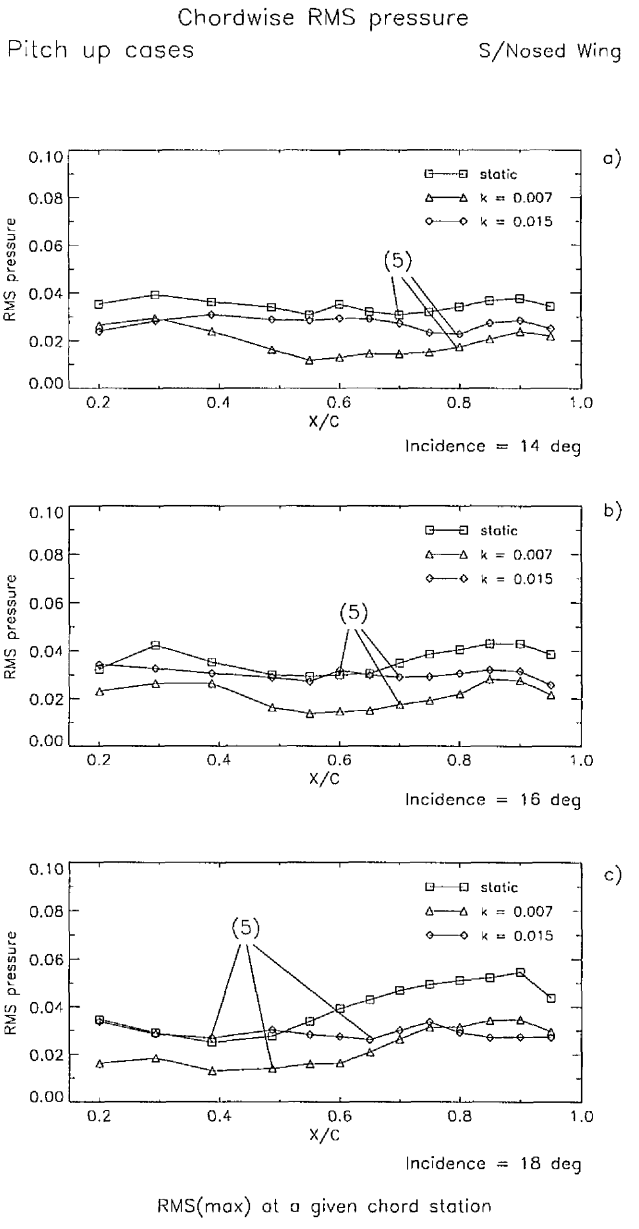

Figure 4.40 - Line plots of maximum spanwise RMS pressures for static and pitch up cases ($k = 0.007$ & $k = 0.015$) at chord stations $x/c = 0.2$ to $x/c = 0.95$ for incidences of 14°, 16° and 18°. Data collected during static pressure measurement tests. $Re = 2.7 \times 10^6$

Key: 'Waisting' of RMS pressure contours, labelled as (5)

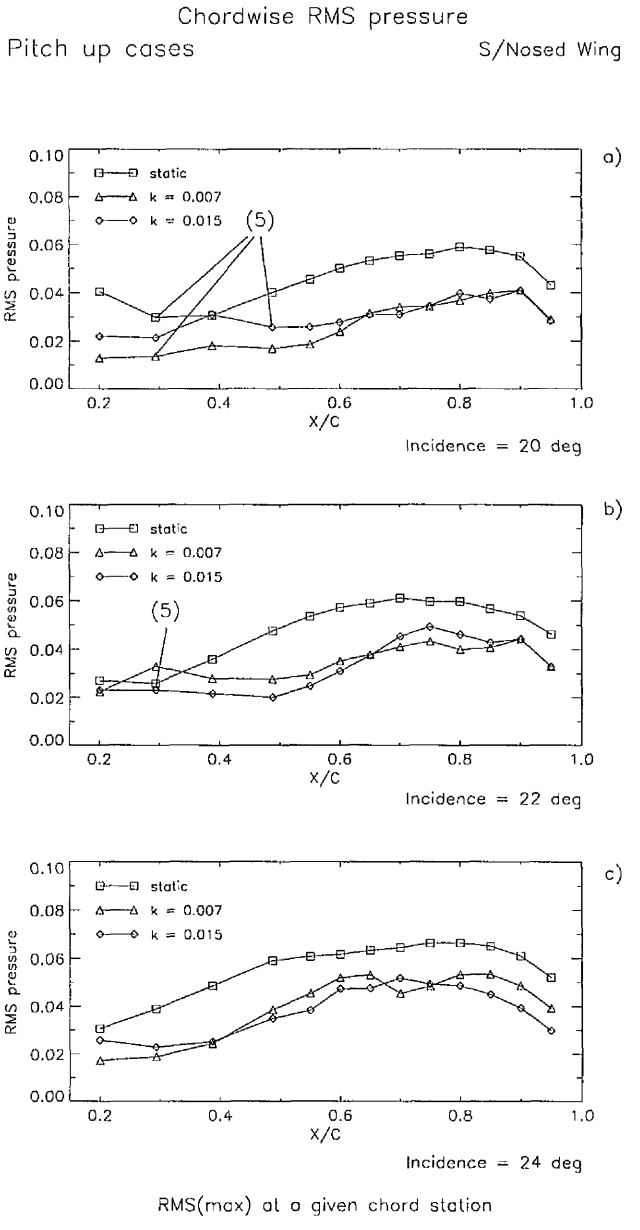

Figure 4.41 - Line plots of maximum spanwise RMS pressures for static and pitch up cases (k = 0.007 & k = 0.015) at chord stations x/c = 0.2 to x/c = 0.95 for incidences of **20°**, **22°** and **24°**. Data collected during pressure measurement tests. Re = 2.7×10^6

Key: 'Waisting' of RMS pressure contours, labelled as (5)

Note: **bold** type denotes change of parameter from previous figure.

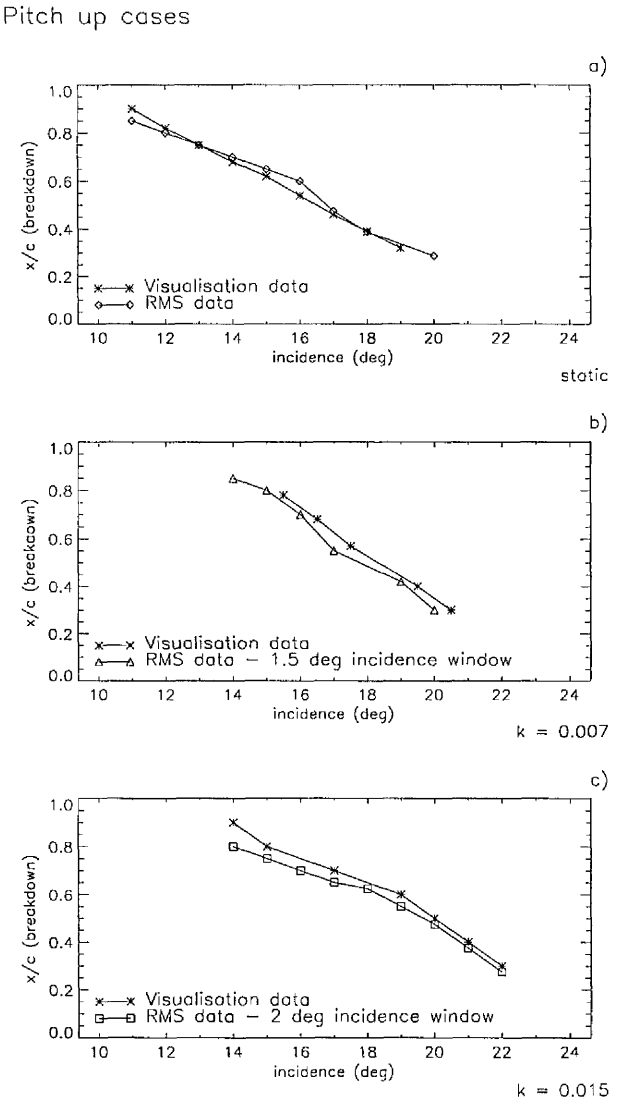

Figure 4.42 - The chordwise location of the waist or localised trough of RMS pressure compared with the chordwise location of vortex breakdown as functions of incidence in the static, k = 0.007 and k = 0.015 cases. Data collected during pressure measurement tests & flow visualisation experiments. Re = 2.7×10^6 and 10000 respectively.

4.3.3 *RMS analysis - pitch down tests*

The technique used to determine the RMS pressure distribution in the pitch down cases was identical to that used for the pitch up cases. The incidence windows chosen at each pitch rate were similar to those pitch up cases of similar magnitude. Figures 4.43 and 4.44 show a series of contour plots of the RMS pressure distribution on the leeward surface of the wing for static and two pitch down cases ($k = -0.007$ and $k = -0.017$), at incidences of 18° and 14° (Figure 4.43), and 10° and 8° (Figure 4.44). In Figure 4.43, plot c), an expanded region of high RMS pressure (4) which corresponds to that seen in the static and pitch up cases, is seen moving outboard after initially forming along the wing centreline. As either incidence or pitch rate is decreased, this region of high RMS pressure moves further outboard and a waist forms on the RMS pressure contours upstream of the peak of the high RMS region (5) near the wing apex. As the wing incidence is decreased further, the lateral position of the expanded region of high RMS pressure stabilises and the expanded peak of high RMS pressure recedes downstream towards the wing trailing-edge. For the pitch down cases, Figure 4.43 and subsequently Figure 4.44 clearly shows the recession of the expanded region of high RMS pressure, the formation of the primary (2) and secondary (3) regions of high RMS pressure previously described in the static and pitch up cases, and the delay or lag in the recession process as the magnitude of the pitch rate is increased.

Figure 4.45 shows the RMS pressure distribution across the span of the wing in the static and pitch down cases, $k = -0.007$ and $k = -0.017$, at a chord station of $x/c = 0.6$ and an incidence of 8°. Also plotted is the corresponding mean negative C_P distribution. Clearly, the relative lateral position of the two ridges of high RMS pressure to the main vortex core is similar in pitch down to that in the static and pitch up cases.

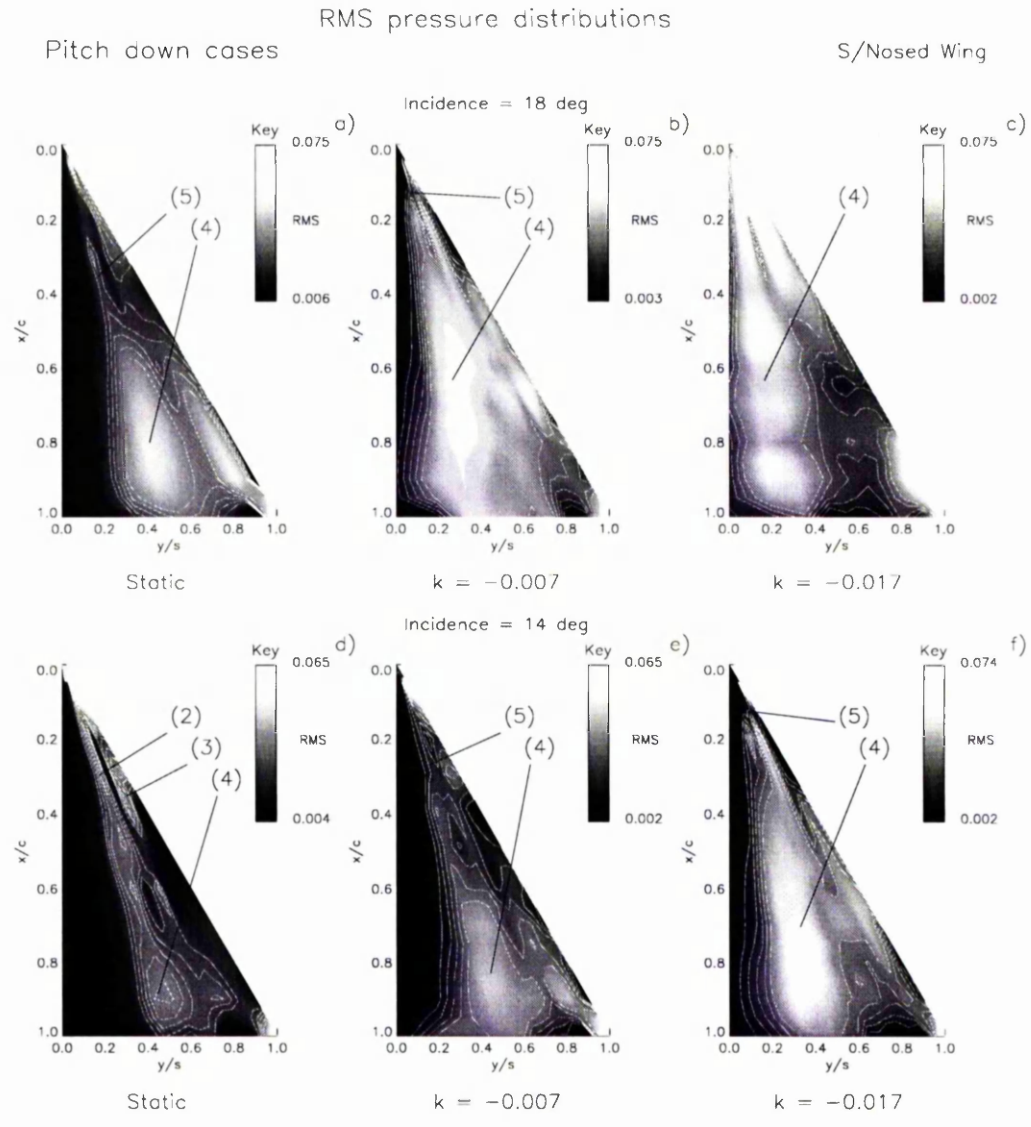

Figure 4.43 - Contour plots of RMS pressure distributions for static and two pitch down cases (k = -0.007 & k = -0.017) at incidences of 18° and 14°. Data collected during pressure measurement tests. Re = 2.7×10^6

Key: Primary RMS region labelled as (2)
Secondary RMS region labelled as (3)
Additional peak of high RMS pressure, labelled as (4)
'Waisting' of RMS pressure contours, labelled as (5)

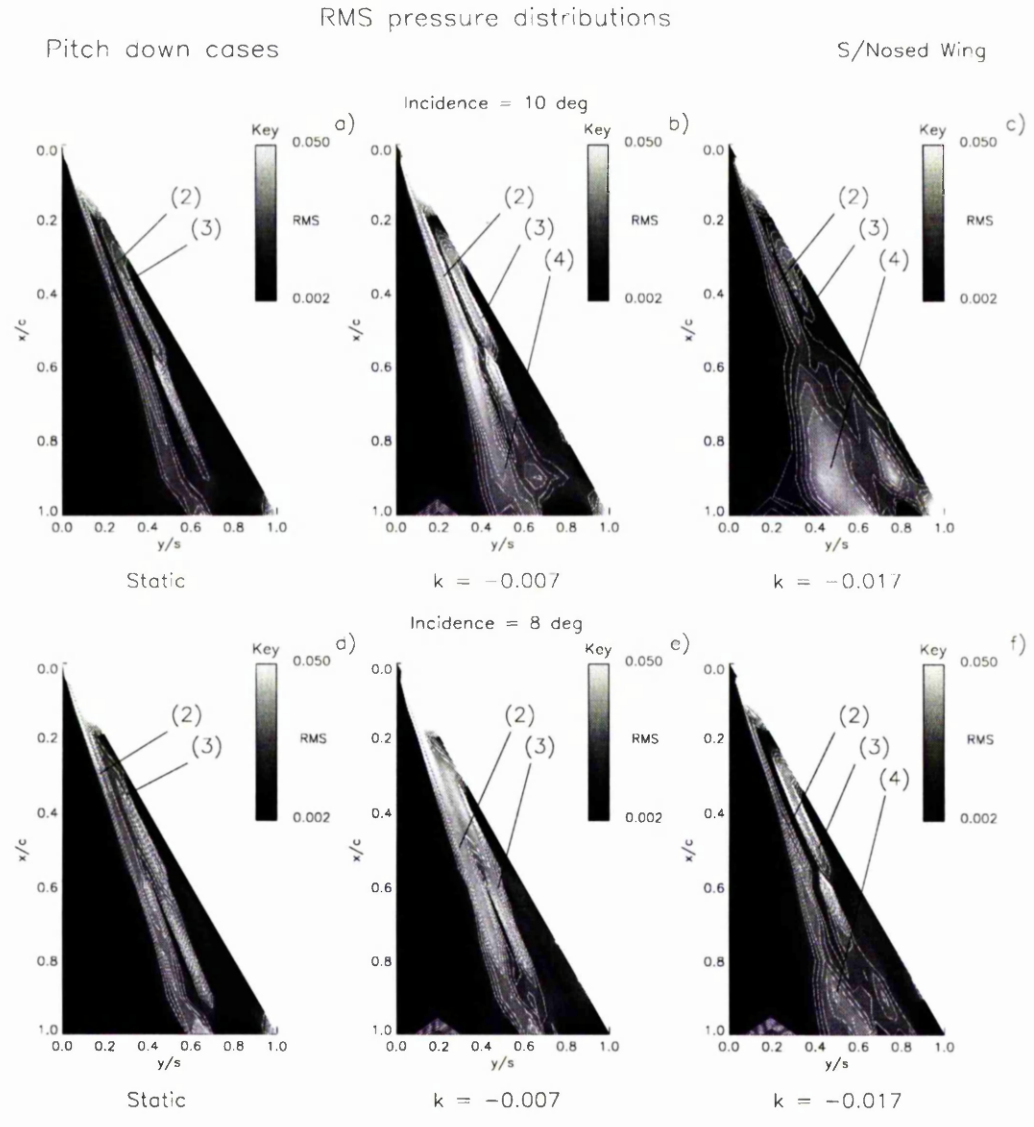

Figure 4.44 - Contour plots of RMS pressure distributions for static and two pitch down cases (k = -0.007 & k = -0.017) at incidences of **10°** and **8°**. Data collected during pressure measurement tests. Re = 2.7×10^6

Key: Primary RMS region labelled as (2)
Secondary RMS region labelled as (3)
Additional peak of high RMS pressure, labelled as (4)

Note: **bold** type denotes change of parameter from previous figure.

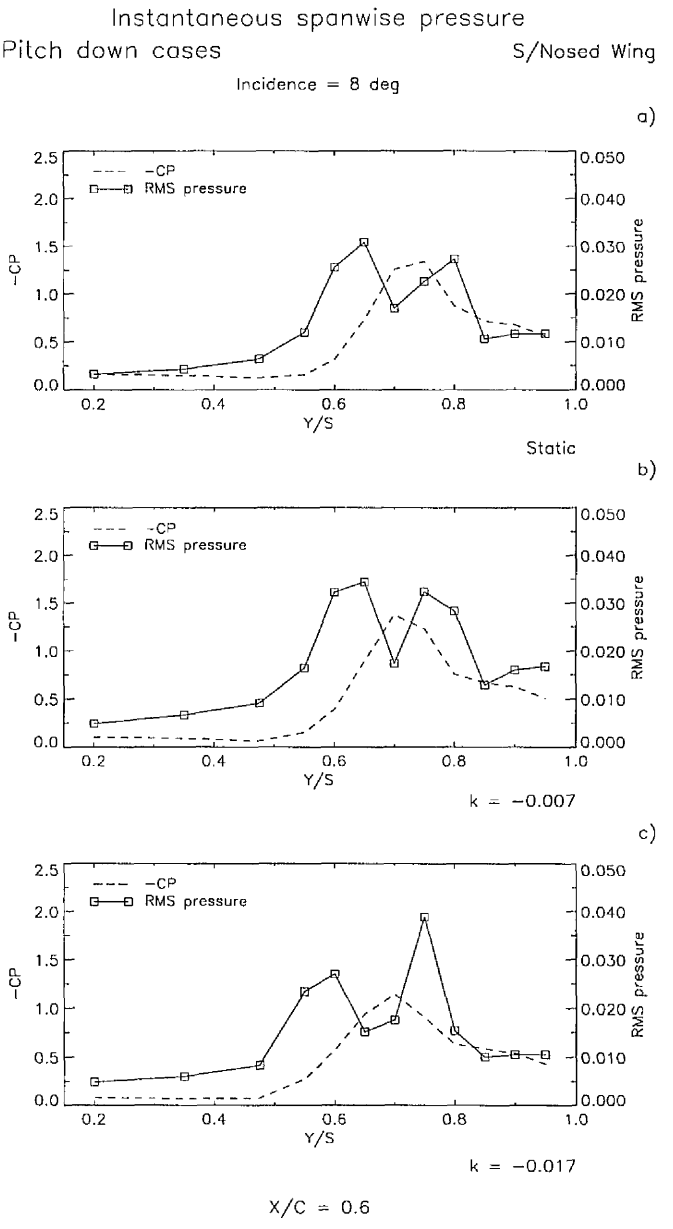

Figure 4.45 - Spanwise distributions of mean suction and RMS pressure in the static and two pitch down cases (k = -0.007 & k = -0.017) at x/c = 0.6 and 8° incidence. Data collected during pressure tests. Re = 2.7×10^6

Figure 4.46 shows a series of contour plots of the RMS pressure distribution on the leeward surface of the wing for the static and two pitch down cases ($k = -0.007$ and $k = -0.017$) at incidences of 4° and 0°. Like the static case, the distribution in each pitch down case is dominated by two ridges of high RMS pressure located along a ray from the apex towards the trailing edge. At an incidence of 4°, plots a) to c) reveal a trend. That is, there was a lag in the recombination of the primary (2) and the secondary (3) regions of high RMS pressure with an increase in pitch rate magnitude. This trend was continued at an incidence of 0°, where the lag was seen in the recession of the primary region towards the wing apex, such that the single primary region of high RMS pressure (2) remained in a progressively more advanced stage of development and division as pitch rate magnitude was increased.

Similarly, the downstream recession of the waisted region of RMS pressure contours, labelled in Figure 4.43 as (5) is presented in Figure 4.47, which shows the maximum spanwise RMS pressure value for the same pitch rate cases, at chordwise locations from $x/c = 0.2$ to $x/c = 0.95$, and incidences of 14°, 12° and 10°. Like the static and pitch up cases, the chordwise location of the narrowest part of the waist in the contours of the primary region of high RMS pressure, are again labelled as (5) for each case at a given incidence. The plots as a whole show two general trends for all cases as incidence was decreased. Firstly, the additional peak of high RMS pressure decreased in magnitude, and secondly, the localised trough of RMS pressure, and hence the waist, moved downstream towards the trailing-edge of the wing. With an increase in pitch rate magnitude there is a trend indicating a lag in the downstream movement of the waist, such that the additional region of high RMS pressure remains on the wing surface at progressively lower incidences.

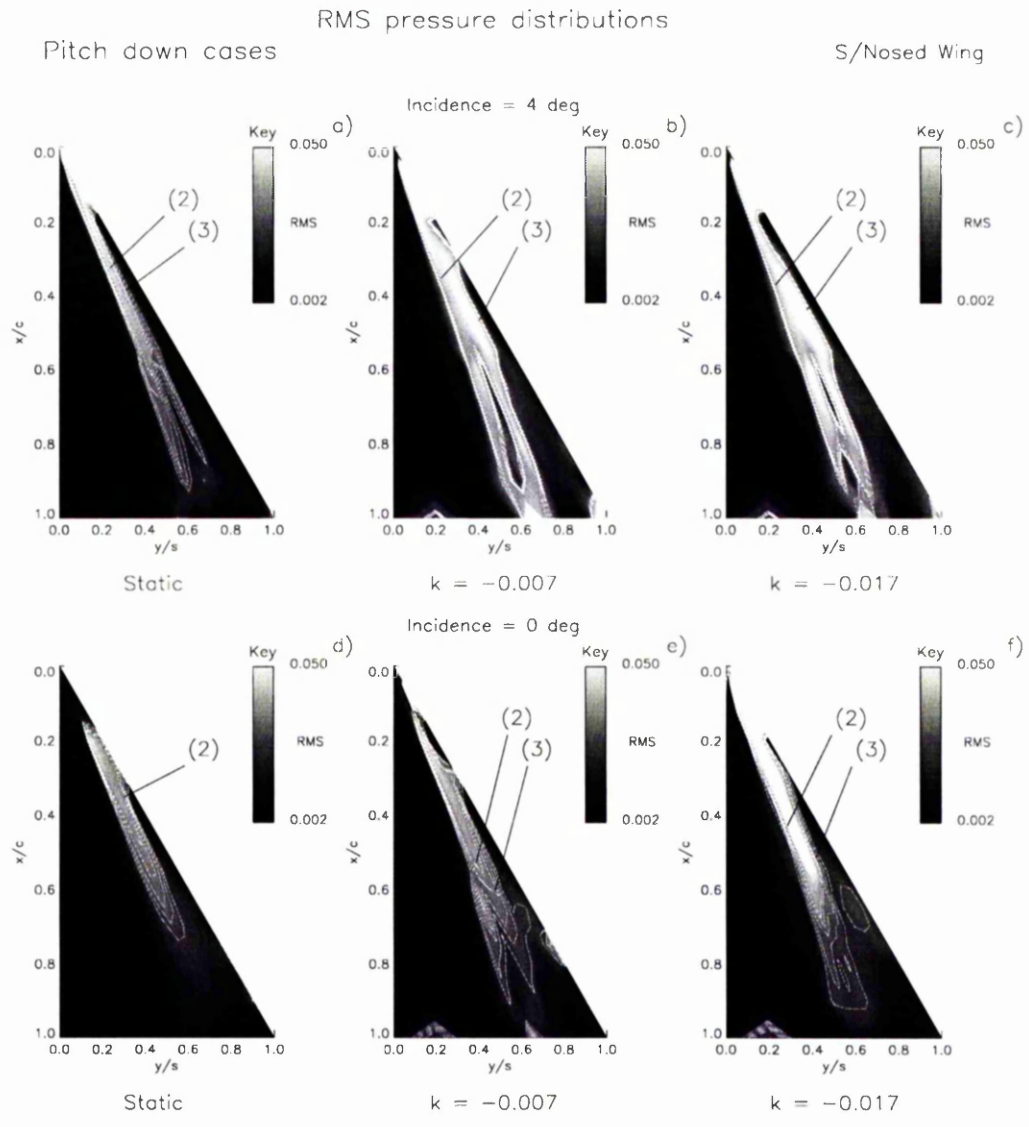

Figure 4.46 - Contour plots of RMS pressure distributions for static and two pitch down cases (k = -0.007 & k = -0.017) at incidences of **4°** and **0°**. Data collected during pressure measurement tests. Re = 2.7×10^6

Key: Primary RMS region labelled as (2)
Secondary RMS region labelled as (3)

Note: **bold** type denotes change of parameter from Figure 4.44

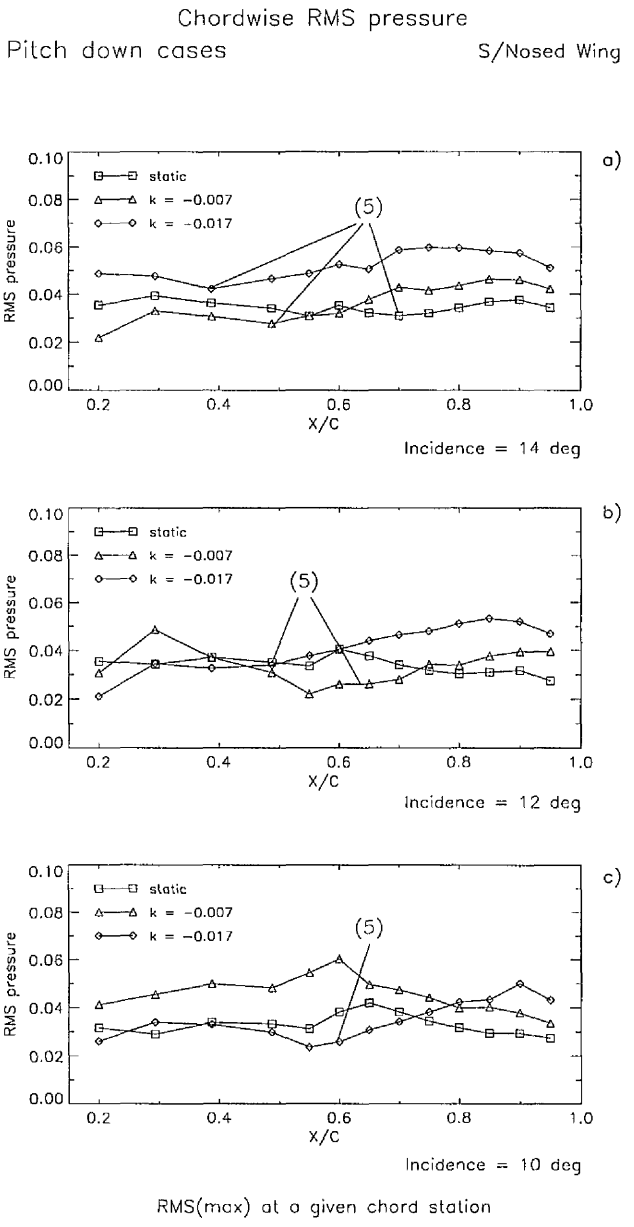

Figure 4.47 - Line plots of maximum spanwise RMS pressures for static and pitch down cases (k = -0.007 & k = -0.017) at chord stations x/c = 0.2 to x/c = 0.95 for incidences of 14°, 12° and 10°. Data collected during pressure measurement tests. Re = 2.7×10^6

Key: 'Waisting' of RMS pressure contours, labelled as (5)

Figure 4.48 shows the chordwise position of the waisted region or localised trough of RMS pressure as a function of incidence in the static (plot a), k = -0.007 (plot b) and k = -0.017 (plot c) cases. Also reproduced on each plot are the corresponding chordwise locations of vortex breakdown/restoration as indicated by the flow visualisation tests. This diagram shows that for pitch down cases there is again a good agreement between the vortex restoration point, as determined by the flow visualisation experiments, and the location of the waist or localised trough of RMS pressure immediately upstream of the additional peak of high RMS pressure.

4.3.4 *RMS analysis - changes in sample window size*

Throughout this presentation of the RMS pressure analysis for pitch up and pitch down cases, the pressure sample window sizes, to which the RMS calculation was applied, remained constant at 1.5° for a pitch rate magnitude $|k| = 0.007$ and 2° for the pitch rate magnitudes of $|k| = 0.015$ and $|k| = 0.017$. The optimum size of the sample windows was determined in each case by the pitch rate magnitude and a pressure fluctuation frequency of interest. The frequency of interest was itself determined by reference to the frequency spectra analysis that is presented in some detail in the following chapter. The findings of the spectral analysis can be briefly summarised by saying that, at incidences where vortex breakdown/restoration was observed over the wing between the apex and trailing-edge, the frequency spectra of pressure fluctuations were characterised by a bandwidth of dominant frequencies. At a given chordwise location downstream of the vortex breakdown/restoration point, the characteristic dominant frequency band was detected across a range of spanwise locations on the wing surface. The area of greatest spanwise fluctuation activity was found to be in the region identified in this RMS analysis as the primary region of high RMS pressure inboard of the path of the main vortex core, labelled in the contour plots as (2).

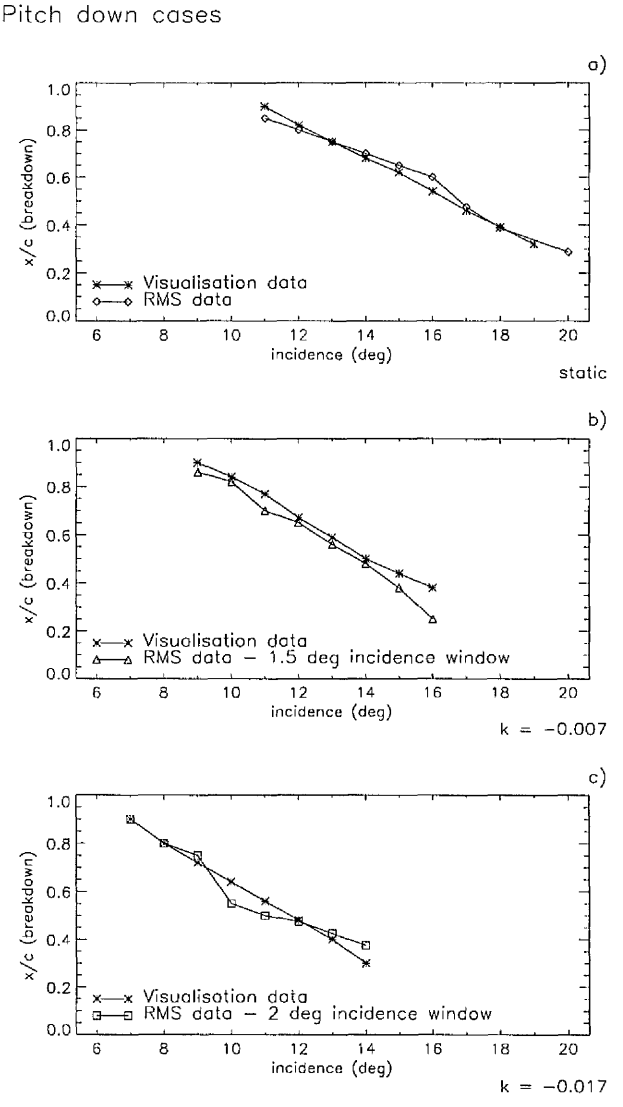

Figure 4.48 - The chordwise location of the waist or localised trough of RMS pressure compared with the chordwise location of vortex breakdown as functions of incidence in the static, k = -0.007 and k = -0.017 cases. Data collected during pressure measurement tests & flow visualisation experiments. Re = 2.7×10^6 and 10000 respectively.

In order to resolve these dominant frequencies in the RMS analysis at a given pitch rate magnitude, it was generally necessary to increase the sample window size to a value greater than a nominal 1°, in order to increase the sample time period, so that the dominant frequency in question would fall into the frequency range that satisfied the Nyquist criterion at the lower end of the frequency spectrum as previously described in Section 3.3. The size of the increase in the sample window was determined by the pitch rate magnitude, i.e., the higher the pitch rate, the smaller the time period spanning a given incidence range. Therefore, a greater increase in the sample window size was required, to lower the limit of frequency of pressure fluctuations that satisfy the Nyquist criterion, in order to accommodate the frequency of interest.

Figure 4.49 shows contour plots of the RMS pressure distributions for the two pitch up cases, k = 0.007 and k = 0.015 at an incidence of 24° using incidence windows of 1°, 1.5° and 2° in the k = 0.007 case, and 1°, 2° and 4° in the k = 0.015 case. The diagram shows the variations in magnitude and extent of the additional region of high RMS pressure (4) and variations in the chordwise location of the waist (5) across the range of window sizes for each pitching case. Figures 4.50 and 4.51 show the chordwise position of the waist as a function of incidence for the k = 0.007 and k = 0.015 cases respectively, using the sample window sizes illustrated in Figure 4.49. Also plotted in each case is the observed position of vortex breakdown seen during the flow visualisation tests. For the k = 0.007 case, shown in Figure 4.50, the effect of increasing the sample window size from 1° (plot a) to 1.5° (plot b) was to advance the indicated chordwise position of the waist in the RMS contours by as much as 4° incidence at the trailing-edge of the wing and show better agreement with flow visualisation results. Using a 2° incidence window, (plot c), the effects of smearing can be seen, where pre and post vortex breakdown data were included in the RMS calculation.

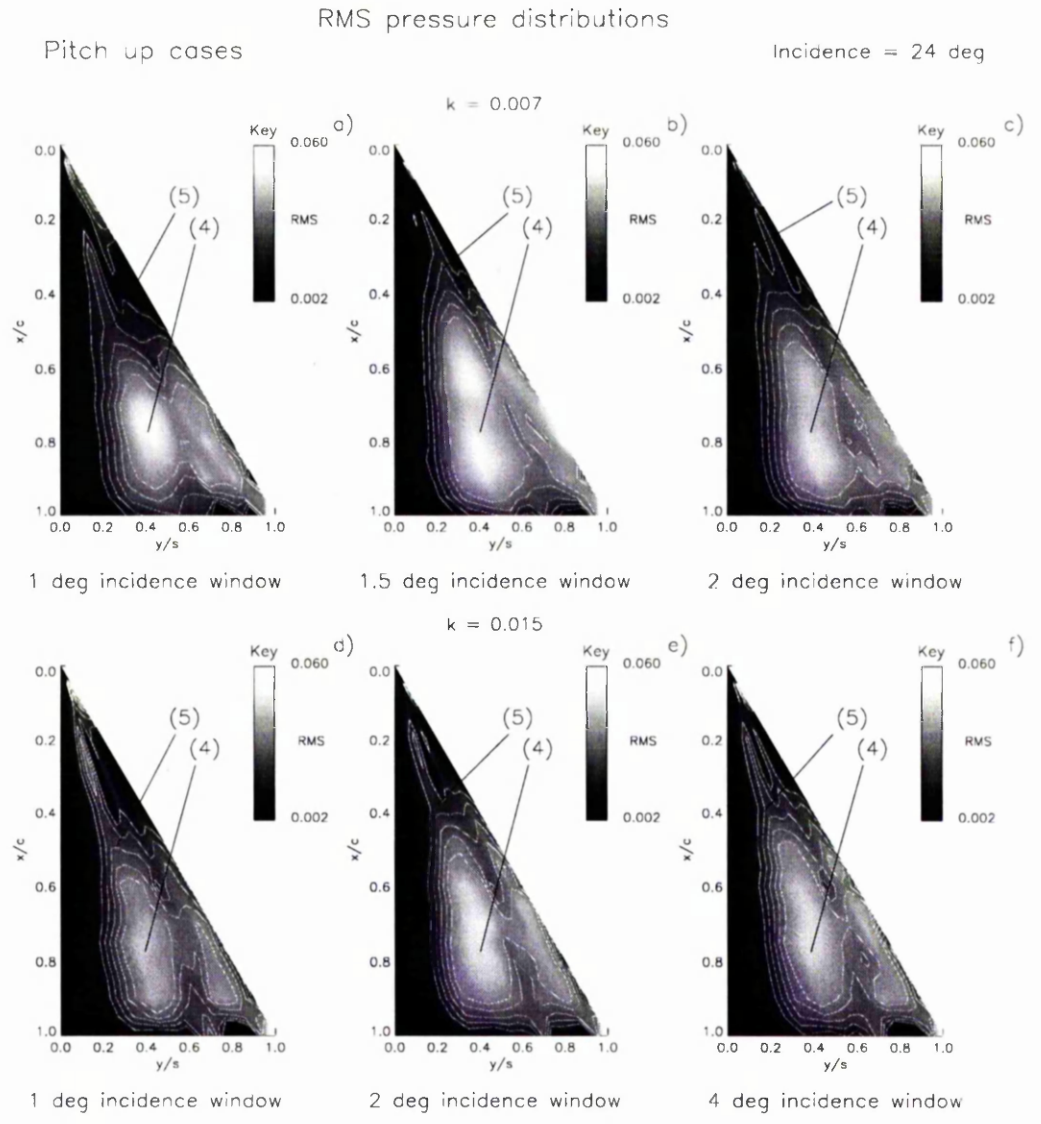

Figure 4.49 - Contour plots of RMS pressure distributions for two pitch up cases at an incidence of 24° using sample windows of 1°, 1.5° & 2° (k = 0.007 case) and 1°, 2° & 4° (k = 0.015 case). Data collected during pressure measurement tests. Re = 2.7×10^6

Key: Additional peak of high RMS pressure, labelled as (4)
'Waisting' of RMS pressure contours, labelled as (5)

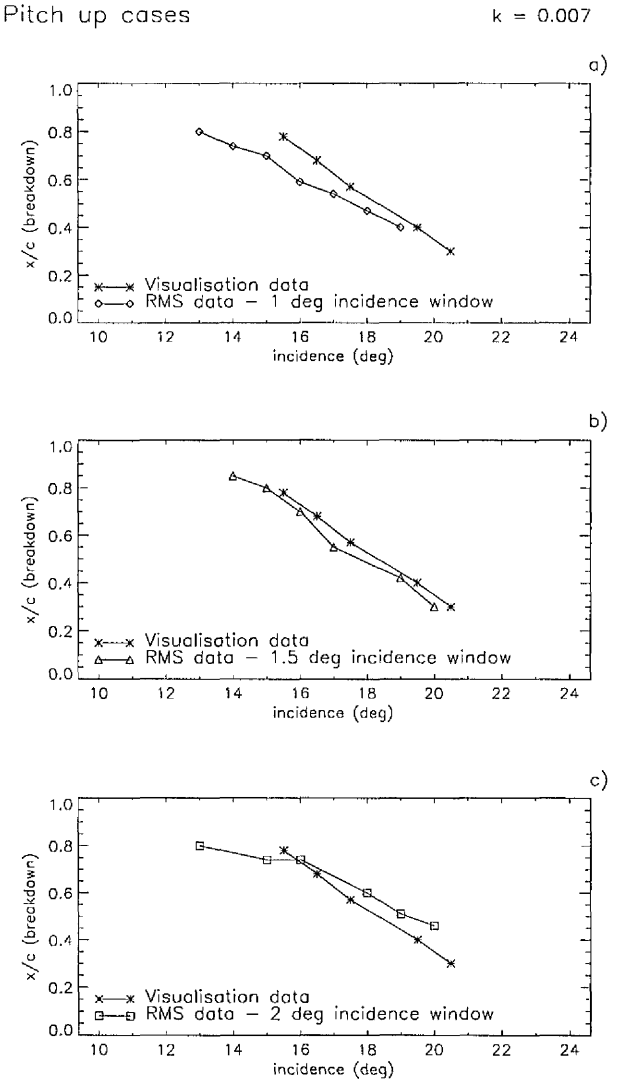

Figure 4.50 - The chordwise location of the waist in the RMS pressure contours compared with the chordwise location of vortex breakdown as functions of incidence in the k = 0.007 case using sample window sizes of 1°, 1.5° & 2°. Data collected during pressure measurement tests & flow visualisation experiments. Re = 2.7×10^6 and 10000 respectively

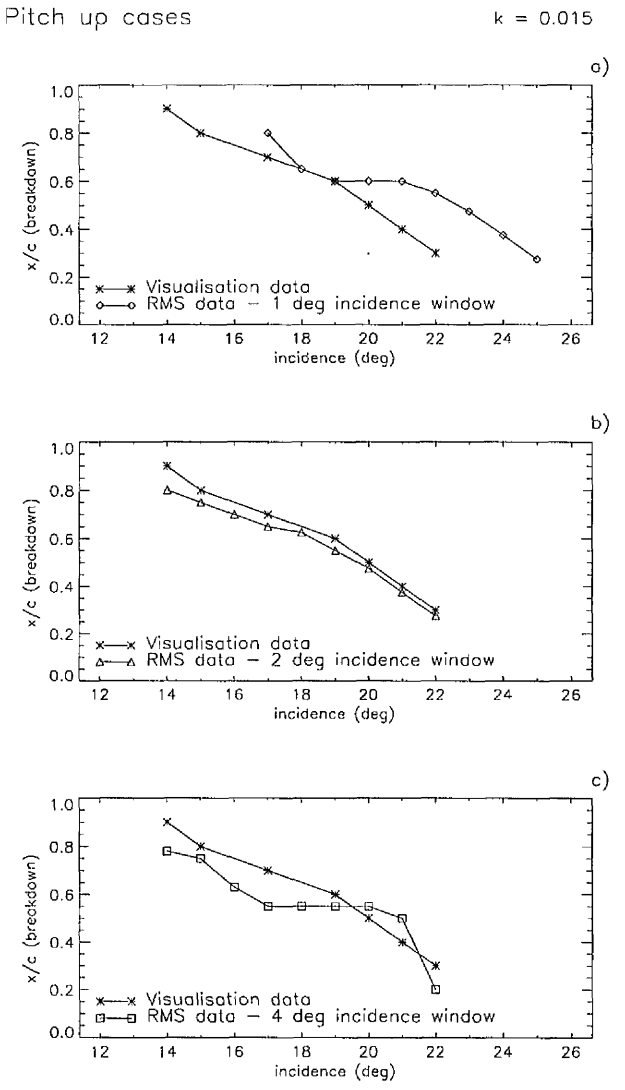

Figure 4.51 - The chordwise location of the waist in the RMS pressure contours compared with the chordwise location of vortex breakdown as functions of incidence in the **k = 0.015** case using sample window sizes of **1°, 2° & 4°**. Data collected during pressure measurement tests & flow visualisation experiments. Re = 2.7×10^6 and 10000 respectively.

Note: **bold** type denotes change of parameter from the previous figure

Similarly, for the k = 0.015 case shown in Figure 4.51, a 1° sample window (plot a) produces a RMS data plot showing very poor agreement with the corresponding visualisation test result. This was undoubtedly due to the inability of the RMS calculation to resolve the entire dominant frequency band, some of which lies outside the Nyquist frequency range. However, using a 2° sample window (plot b), where the vital excitation frequencies identified in the frequency analysis are satisfactorily resolved during the RMS calculation, the RMS data result shows much better agreement with the visualisation results. Plot c) shows, for a 4° sample window, the effect of an incidence window that is too large, i.e. where there is a significant mixing pre and post vortex breakdown data.

The same sample window size analysis can be applied in the same way to pitch down cases. Figure 4.52 shows contour plots of the pitch down cases k = -0.007 and k = -0.017 at an incidence of 12° using the same sample window sizes as the pitch up cases of similar pitch rate magnitude. Again there are variations in the extent of the additional peak of RMS pressure (4) and in the chordwise position of the waist in the RMS pressure contours (5). In a similar manner to the pitch up cases, Figures 4.53 and 4.54 show the chordwise position of the waist as a function of incidence for the k = -0.007 and k = -0.017 cases respectively, using the same sample window sizes illustrated in Figure 4.52. Also plotted in each case is the observed position of vortex reformation seen during the flow visualisation tests. The effect of aliasing is not as significant as those shown for the pitch up cases, possibly due to the increased frequency of pressure fluctuations observed in both pitch down cases when compared with their pitch up counterparts at equivalent positions on the wing and at similar incidences. However, to capture the full range of dominant frequencies that may influence the RMS pressure distributions, incidence windows were used in the pitch down analyses which were similar to those at corresponding pitch rate magnitudes in pitch up.

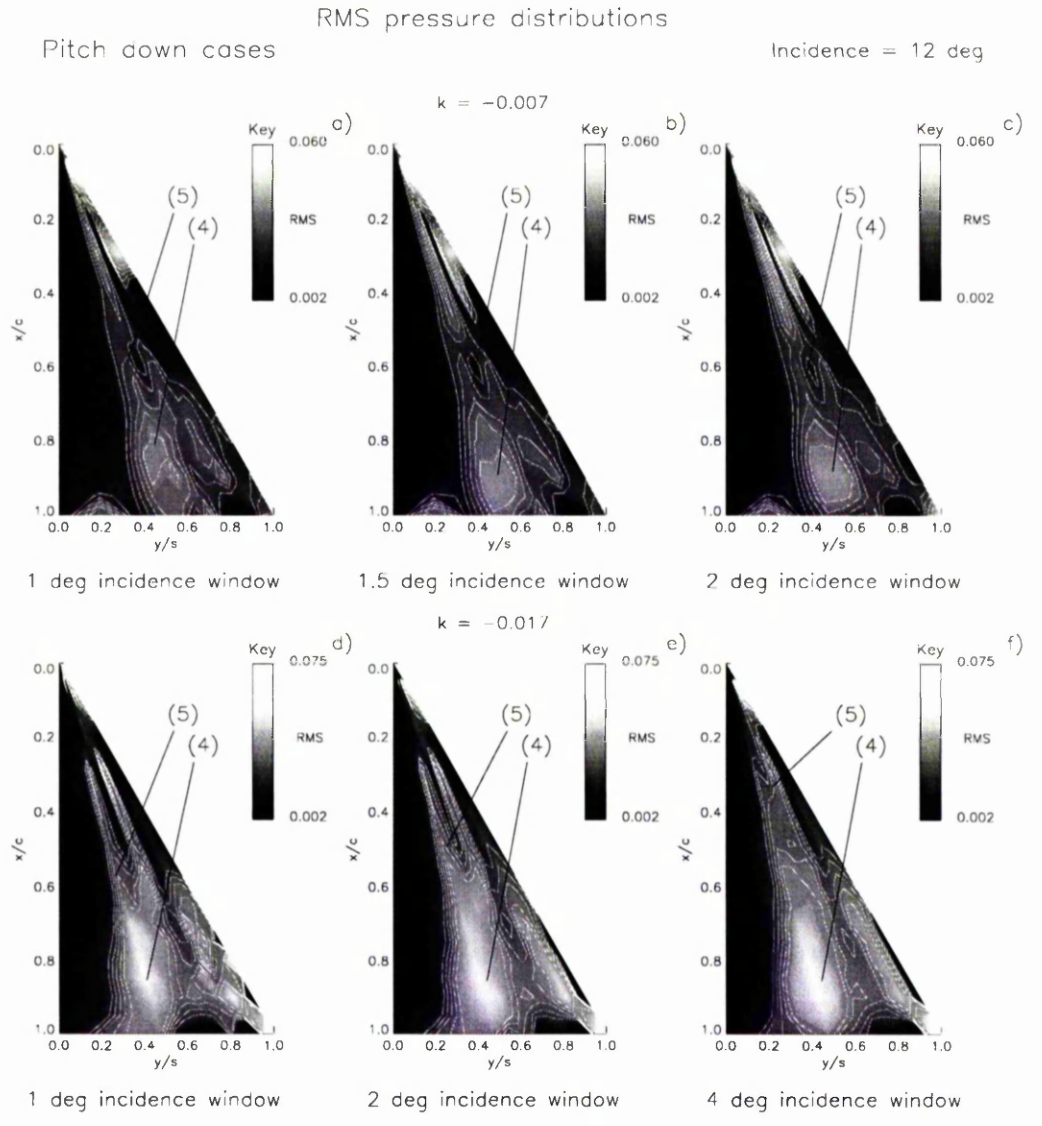

Figure 4.52 - Contour plots of RMS pressure distributions for two pitch down cases at an incidence of 12° using sample windows of 1°, 1.5° & 2° (k = -0.007 case) and 1°, 2° & 4° (k = -0.017 case). Data collected during pressure measurement tests. Re = 2.7×10^6

Key: Additional peak of high RMS pressure, labelled as (4)
'Waisting' of RMS pressure contours, labelled as (5)

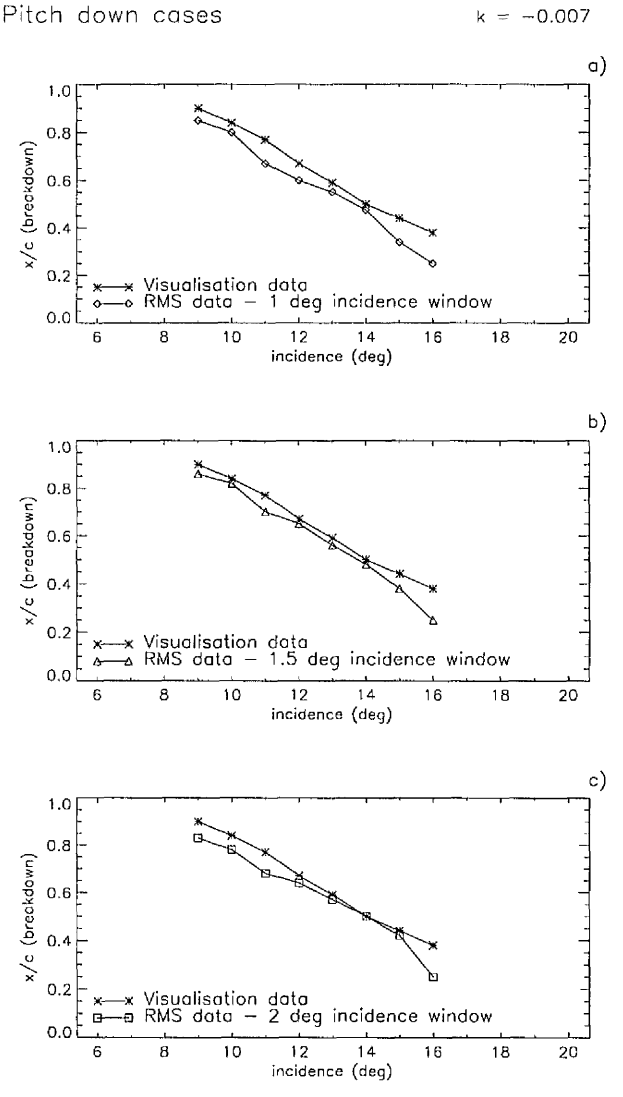

Figure 4.53 - The chordwise location of the waist in the RMS pressure contours compared with the chordwise location of vortex breakdown as functions of incidence in the k = -0.007 case using sample window sizes of 1°, 1.5° & 2°. Data collected during pressure measurement tests & flow visualisation experiments. Re = 2.7×10^6 and 10000 respectively.

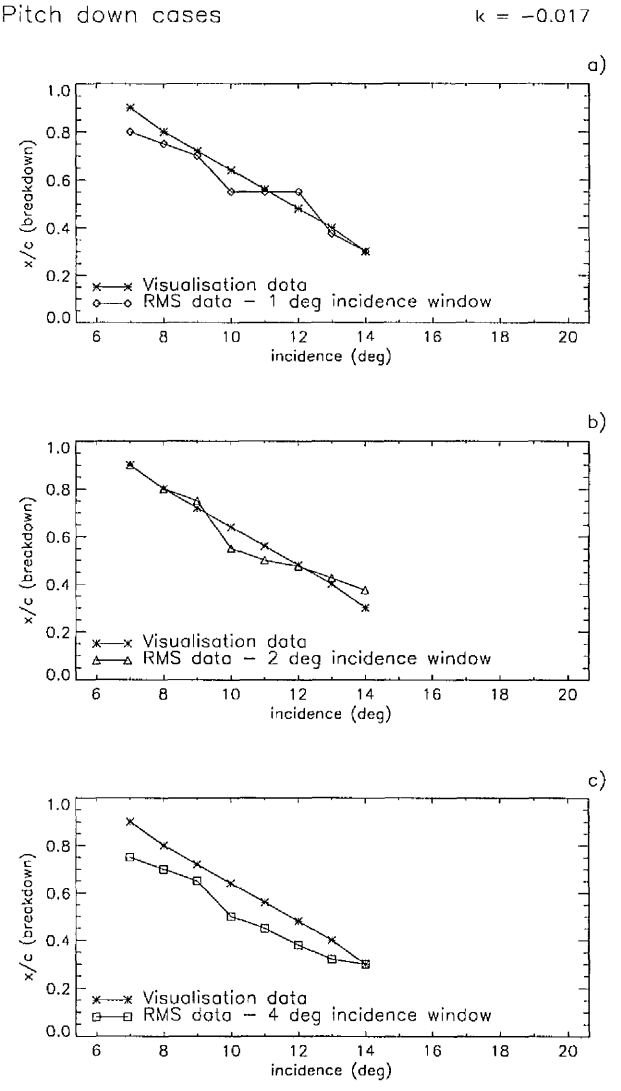

Figure 4.54 - The chordwise location of the waist in the RMS pressure contours compared with the chordwise location of vortex breakdown as functions of incidence in the **k = -0.017** case using sample window sizes of **1°**, **2°** & **4°**. Data collected during pressure measurement tests & flow visualisation experiments. Re = 2.7×10^6 and 10000 respectively.

Note: **bold** type denotes change of parameter from the previous figure

4.3.5 *RMS analysis - changes in apex geometry*

The formation and development of the leeward surface RMS pressure distribution on the round-nosed wing was essentially similar to that of its sharp-nosed counterpart, however, a number of differences were observed throughout the incidence range. Figures 4.55 and 4.56 show contour plots of the RMS pressure distributions in the sharp and round-nosed static cases at incidences of 2°, 6°, 10°, 16°, 24° and 30°. Figure 4.55, plot d) shows that at 2° incidence, there is a lag in the formation and division of the primary region of high RMS pressure (2) for the round-nosed wing when compared with the sharp-nosed case (plot a) and that its origin is located on the leading-edge of the wing at $x/c = 0.2$. By 6° incidence, the general form of the primary (2) and secondary (3) regions of high RMS pressure was similar for the two wings (plots b and e), and in the round-nosed case, shown in plot e) the division point of the two regions has caught up with its sharp-nosed counterpart. At 10° incidence in the round-nosed case, shown in plot f), the secondary region of high RMS pressure (3) had already begun to fragment and an additional peak of high RMS pressure (4) had appeared on the primary ridge near the trailing-edge of the wing at $x/c = 0.9$. Meanwhile, in the sharp-nosed case, the secondary region of high RMS pressure (3) was seen to be intact and no additional peak was present.

At subsequent incidences as shown in Figure 4.56, the trend in the data observed at 10°, was seen to continue. Plots a) and d) at 16° incidence show that the growth of the additional peak of high RMS pressure (4) and the upstream progression of the waist in the RMS contours ahead of the peak (5) are more advanced in the round-nosed case (plot d). However, at 24° and subsequently 30° incidence, shown in plots b) & e) and c) & f) respectively, the final movement of the peak towards the wing centreline was seen to occur at roughly the same incidence on the round-nosed wing as for the sharp nosed case.

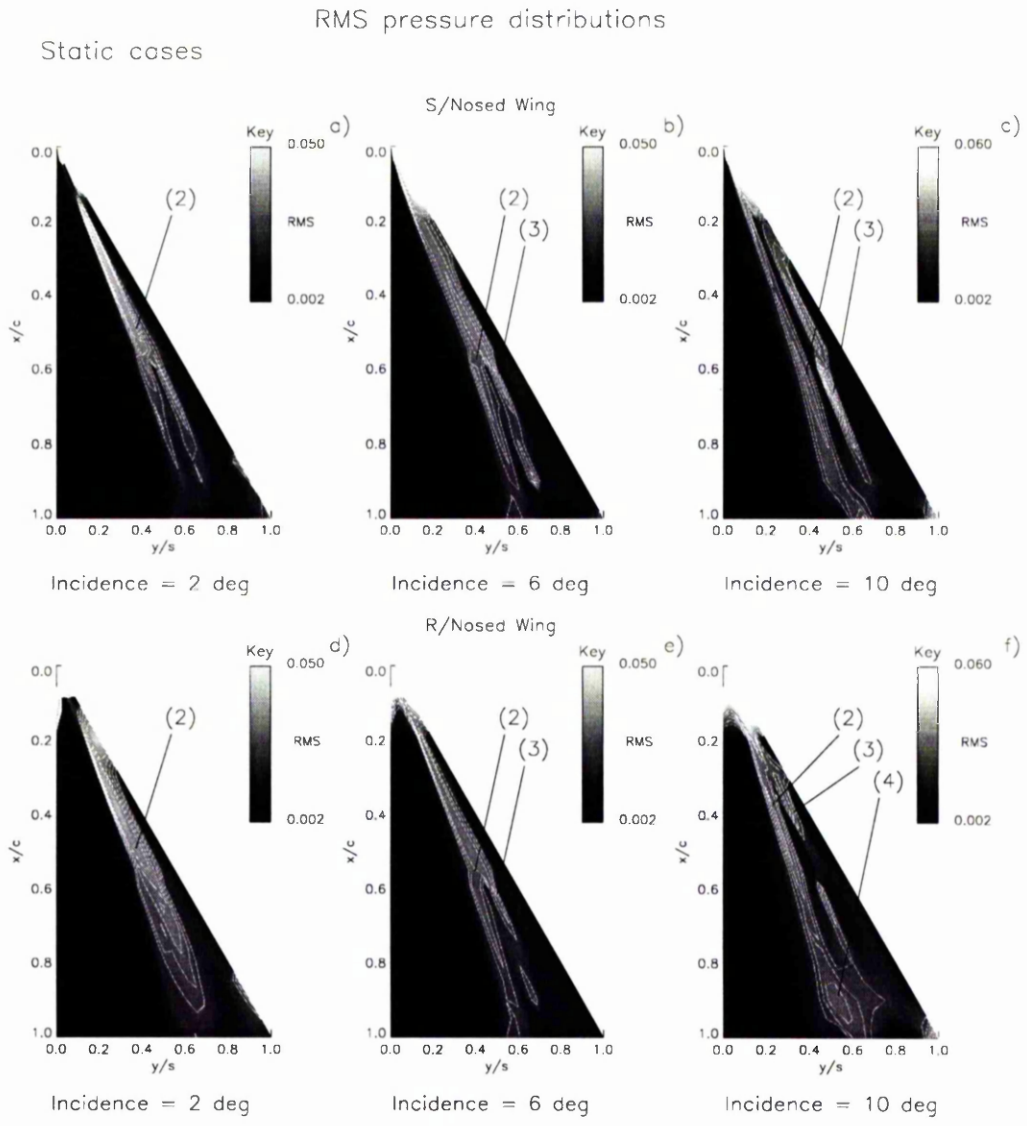

Figure 4.55 - Contour plots of RMS pressure distributions for sharp and round-nosed static cases at incidences of 2°, 6° and 10°. Data collected during pressure measurement tests. Re = 2.7×10^6

Key: Primary RMS region labelled as (2)
Secondary RMS region labelled as (3)

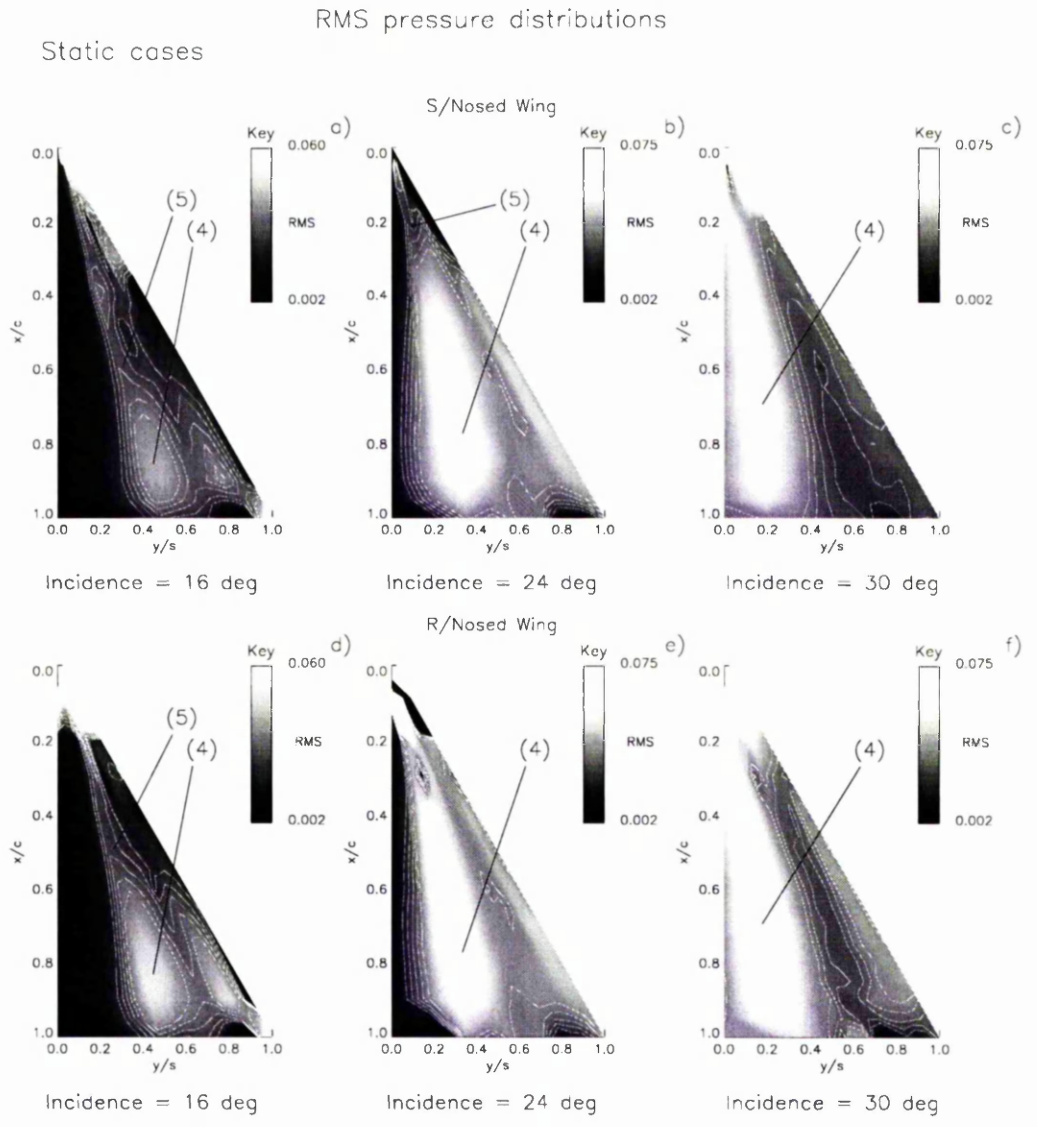

Figure 4.56 - Contour plots of RMS pressure distributions for sharp and round-nosed static cases at incidences of **16°**, **24°** and **30°**. Data collected during pressure measurement tests. Re = 2.7×10^6

Key: Additional peak of high RMS pressure, labelled as (4)
'Waisting' of RMS pressure contours, labelled as (5)

Note: **bold** type denotes change of parameter from previous figure.

It is clear from the previously described contour plots of the RMS pressure distributions that the most significant differences between the sharp and round nosed cases occur after the appearance of the additional peak of high RMS pressure at incidences of 10° or more. Figure 4.57 shows the maximum spanwise RMS pressure values at each chord station from $x/c = 0.2$ to $x/c = 0.95$, for the sharp and round-nosed cases at incidences of 14°, 16° and 18°. The plots as a whole show two general trends for the two cases as incidence was increased. Firstly, the additional peak of high RMS pressure increased in magnitude, and secondly, the localised trough of RMS pressure, and hence the waist, moved upstream towards the apex of the wing. It can also be seen that at incidences of 18° and higher in both cases, the centre of the additional peak moved upstream, but at a much slower velocity than the movement of the waist or the expansion of the peak. The differences between the sharp and round-nosed wings are twofold. In the sharp-nosed case, there is a lag in the upstream movement of the waist, and a lag in the magnitude of maximum spanwise RMS pressure downstream of the waist, when measured at a given chord station, compared with the round-nosed wing.

Figure 4.58 shows the chordwise position of the waisted region or localised trough of RMS pressure as a function of incidence in the sharp-nosed static (plot a) and the round-nosed static (plot b) cases. Also reproduced on each plot are the corresponding chordwise locations of vortex breakdown as indicated by the flow visualisation tests, whose results were described in Section 4.1. This diagram shows that for the round-nosed static case there is a good agreement between the vortex breakdown position, as determined by the flow visualisation experiments, and the location of the waist or localised trough of RMS pressure immediately upstream of the additional peak of high RMS pressure.

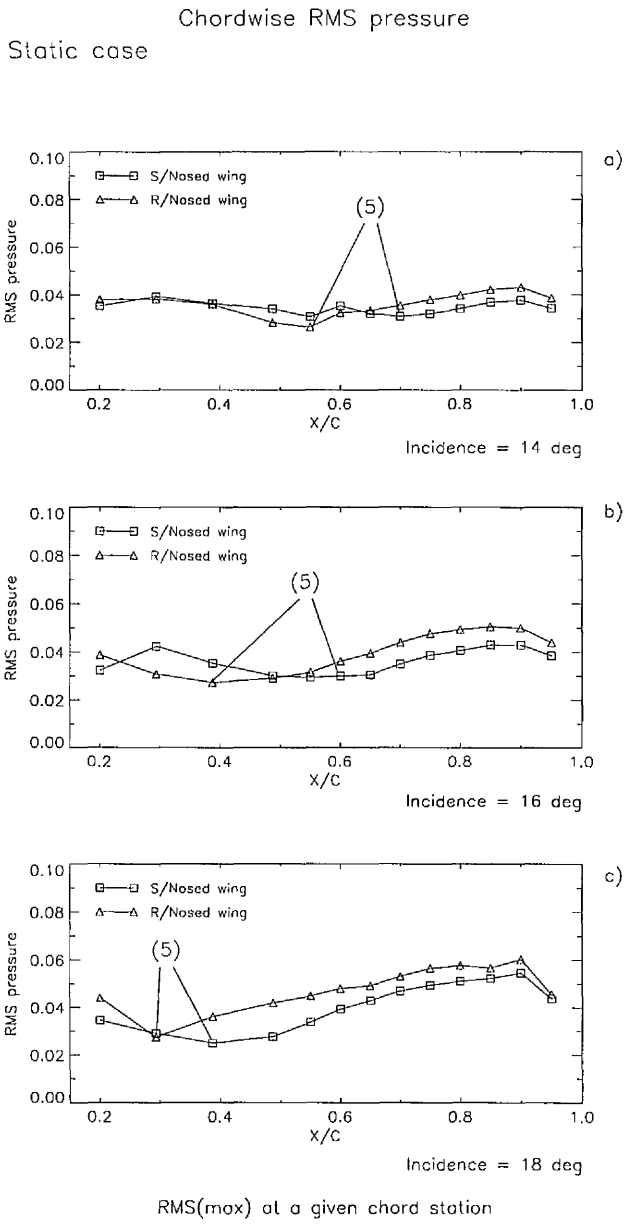

Figure 4.57 - Line plots of maximum spanwise RMS pressures for sharp and round-nosed static cases at chord stations x/c = 0.2 to x/c = 0.95 for incidences of 14°, 16° and 18°. Data collected during pressure measurement tests. Re = 2.7×10^6

Key: 'Waisting' of RMS pressure contours, labelled as (5)

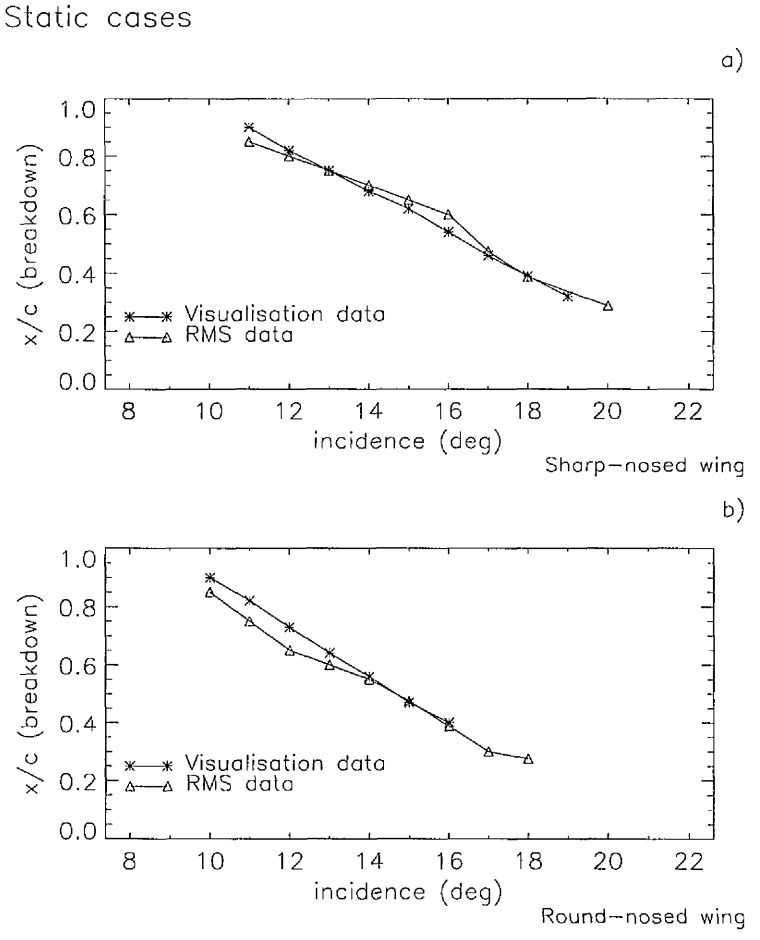

Figure 4.58 - The chordwise location of the waist or localised trough of RMS pressure compared with the chordwise location of vortex breakdown as functions of incidence in the sharp and round-nosed static cases. Data collected during pressure measurement tests & flow visualisation experiments. Re = 2.7×10^6 and 10000 respectively.

4.4 ANALYSIS OF PRESSURE DATA SIGNAL POWER

The pressure signal energy analysis method uses a simple numerical summation to perform an integration of the square of each discrete RMS pressure value from a given transducer during the pitching motions over a range of incidence from 0° to 39°.

4.4.1 *Pitch up tests*

Figure 4.59 and 4.60 show plots of $(\delta E/\delta\alpha)^2$ against incidence for the pitch up cases k = 0.007 and k = 0.015 respectively. The four transducers chosen for this illustration were those mounted on the wing at span station y/s = 0.6, with chord locations of x/c = 0.4875 (Plot a), x/c = 0.6 (plot b), x/c = 0.7 (plot c) and x/c = 0.8 (plot d). These were identified during the RMS analysis as being within the primary region of high RMS pressure inboard of the vortex core suction region. What is clear from each result is that the integrated signal energy is nearly constant with an increase in incidence, i.e. $(\delta E/\delta\alpha)^2 \cong 0$, over the early part of the incidence range. However, at some point, the value of $(\delta E/\delta\alpha)^2$ shows a rapid increase in value, where the rate of increase tends to infinity over a short incidence range. In order to compare results from transducer to transducer, arbitrary values of $(\delta E/\delta\alpha)^2$ were chosen as references. Indicated by two dotted lines on each plot, are the incidences at which $(\delta E/\delta\alpha)^2$ exceed values of 2.0 and 10.0. The lower value was chosen to represent the initial deviation of signal energy away from the constant value of $(\delta E/\delta\alpha)^2$ associated with an increase in incidence and acts as a potential lower limit of vortex breakdown activity, whilst the higher value was chosen to suggest a suitable upper limit. The resulting incidence values provided by each energy limit will be referred to as the 'Energy Data Reference Incidences' (EDRI).

The trend apparent in each of the Figures 4.59 and 4.60, is that the upper and lower EDRI values each tend to occur at a lower incidence as the transducer chosen for analysis is positioned closer to the trailing-edge of the wing. Comparing one pitch up case with the other reveals no trend in the EDRI values.

4.4.2 *Signal power - pitch down tests*

The format of the line plots that illustrate the pressure signal energy for the pitch down cases is similar to the pitch up results. However, their interpretation should be rather different. The summation process for the pitch down data is carried out in the same way to the pitch up cases, i.e. starting at 0°. Hence, the calculation of signal energy is carried out in the opposite sense, in terms of incidence, to the direction of motion of the wing during the test. Therefore, Figures 4.61 and 4.62, which show plots of $(\delta E/\delta\alpha)^2$ against incidence for the same four transducers illustrated in the pitch up cases, but here for pitch down cases k = -0.007 and k = -0.017 respectively, should be read from right to left, such that the energy was seen to decline from an incidence of 39°. Both figures illustrate a general trend. The pressure signal energy falls to a level, i.e., $(\delta E/\delta\alpha)^2$ approaches zero, at a lower incidence at successive chord stations in the direction of the trailing-edge of the wing. Comparison of the two pitch down cases shows that upper and lower EDRI values tend to occur at a lower incidence with an increase in pitch rate.

Shown in Figures 4.63 and 4.64 for the pitch up, (k = 0.007 & k = 0.015) and pitch down, (k = -0.007 & k = -0.017) cases respectively, are the variations in upper and lower EDRI values for the transducers that lie within the primary region of high RMS pressure as indicated in Figures 4.38 and 4.45. Also plotted for each case, is the vortex breakdown location indicated by the visualisation data previously shown in Section 4.1. For each pitching case, it can be seen that the EDRI limits form a corridor of approximately 2° of incidence that successfully bounds the observed vortex breakdown location.

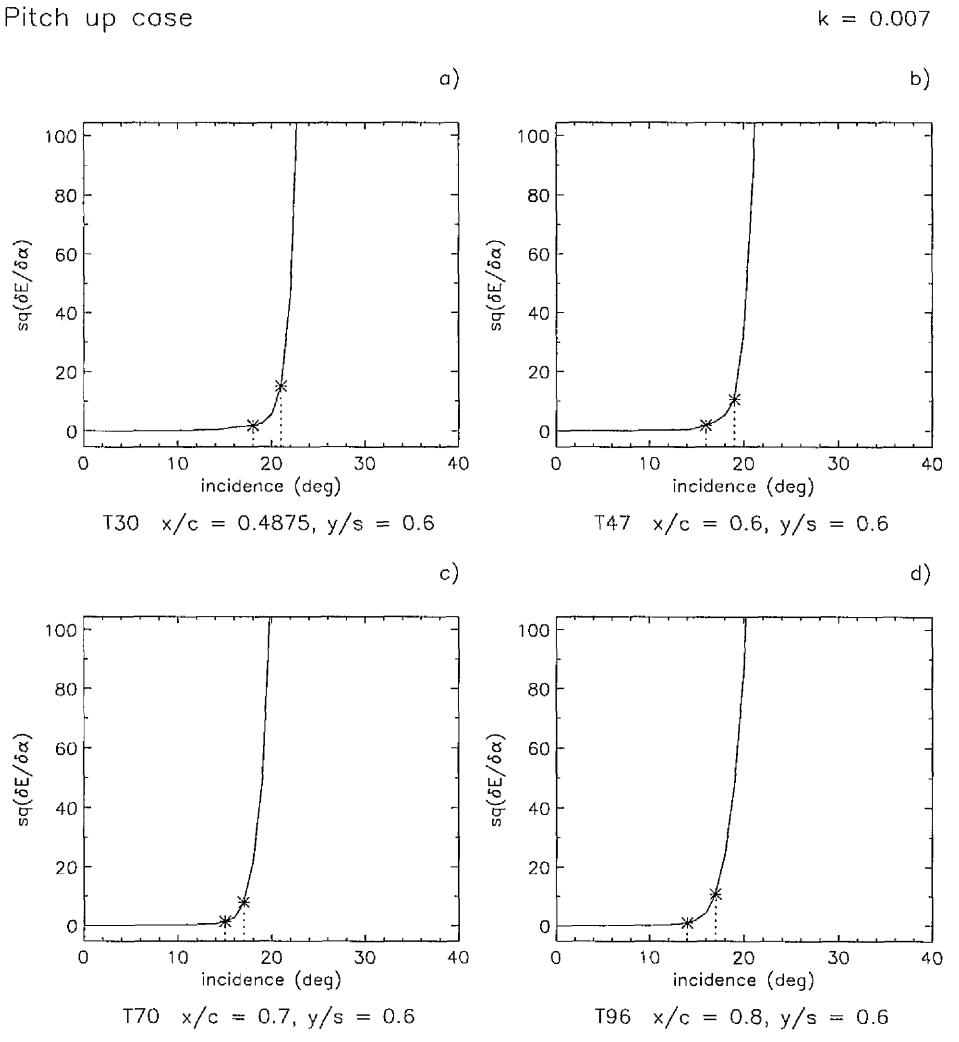

Figure 4.59 - Measurements of the square of the first derivative of signal energy E wrt incidence, $(\delta E/\delta\alpha)^2$, over the incidence range 0° to 39° inclusive, in the pitch up case, k = 0.007. Transducers positioned at y/s = 0.6, with chord locations of x/c = 0.4875, 0.6, 0.7 and 0.8

Each plot includes Energy Data Reference Incidences, EDRI's (*).

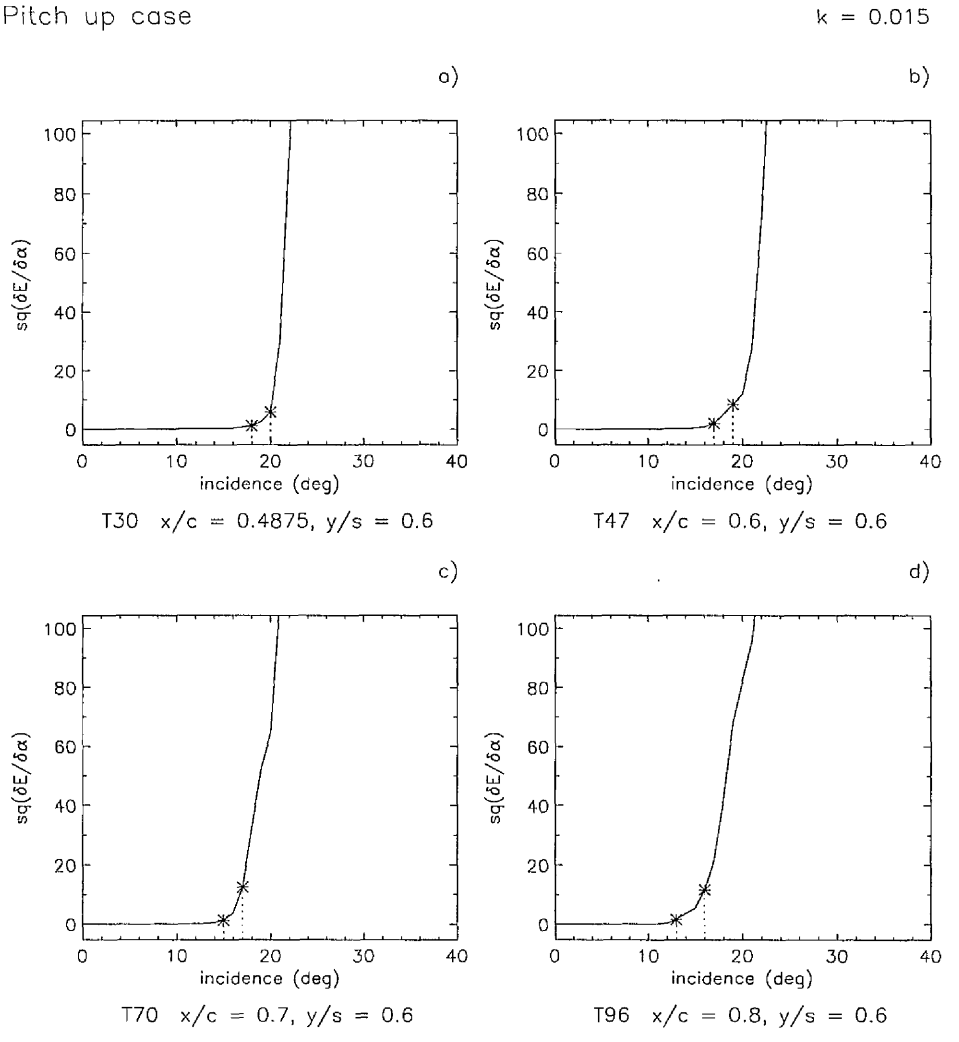

Figure 4.60 - Measurements of the square of the first derivative of signal energy E wrt incidence, $(\delta E/\delta\alpha)^2$, over the incidence range 0° to 39° inclusive, in the pitch up case, **k = 0.015**. Transducers positioned at y/s = 0.6, with chord locations of x/c = 0.4875, 0.6, 0.7 and 0.8

Each plot includes Energy Data Reference Incidences, EDRI's (*).

Note: **bold** type denotes change of parameter from previous figure.

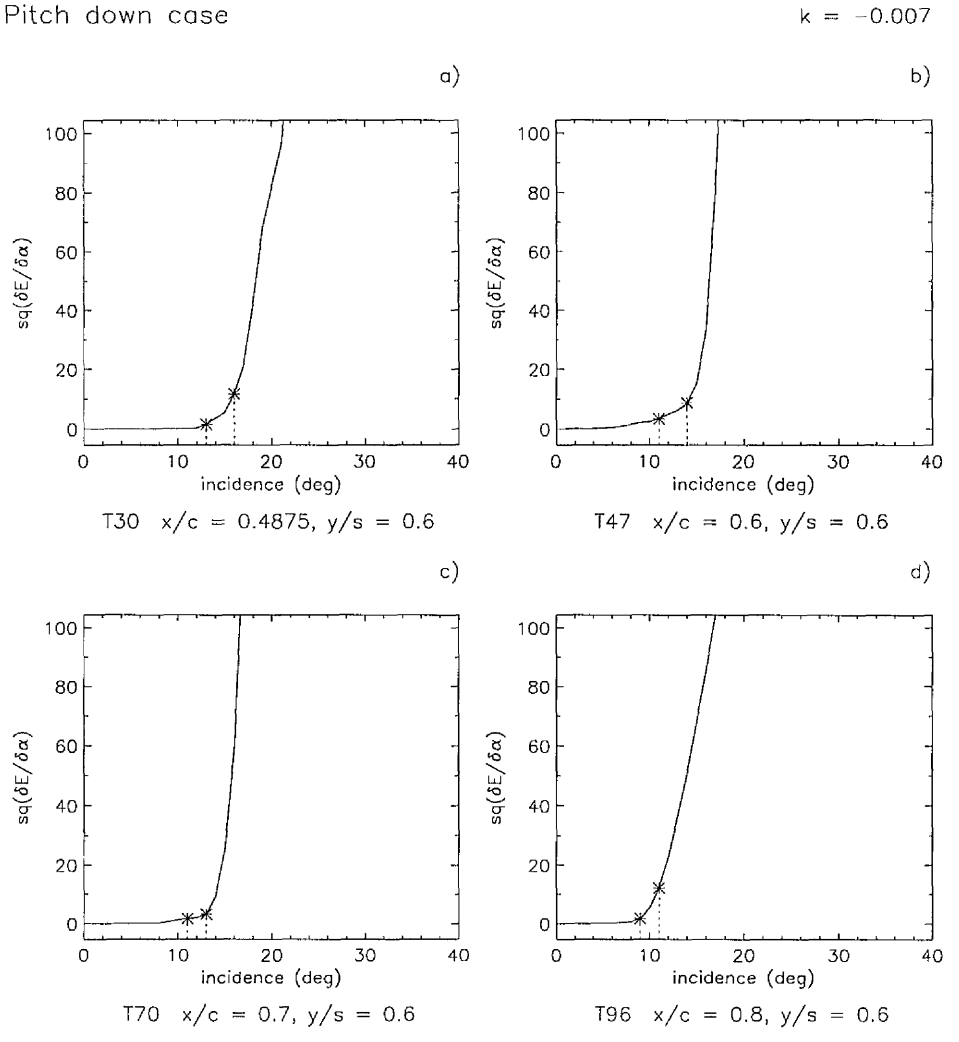

Figure 4.61 - Measurements of the square of the first derivative of signal energy E wrt incidence, $(\delta E/\delta\alpha)^2$, over the incidence range 0° to 39° inclusive, in the **pitch down** case, **k = -0.007**. Transducers positioned at y/s = 0.6, with chord locations of x/c = 0.4875, 0.6, 0.7 and 0.8

Each plot includes Energy Data Reference Incidences, EDRI's (*).

Note: **bold** type denotes change of parameter from previous figure.

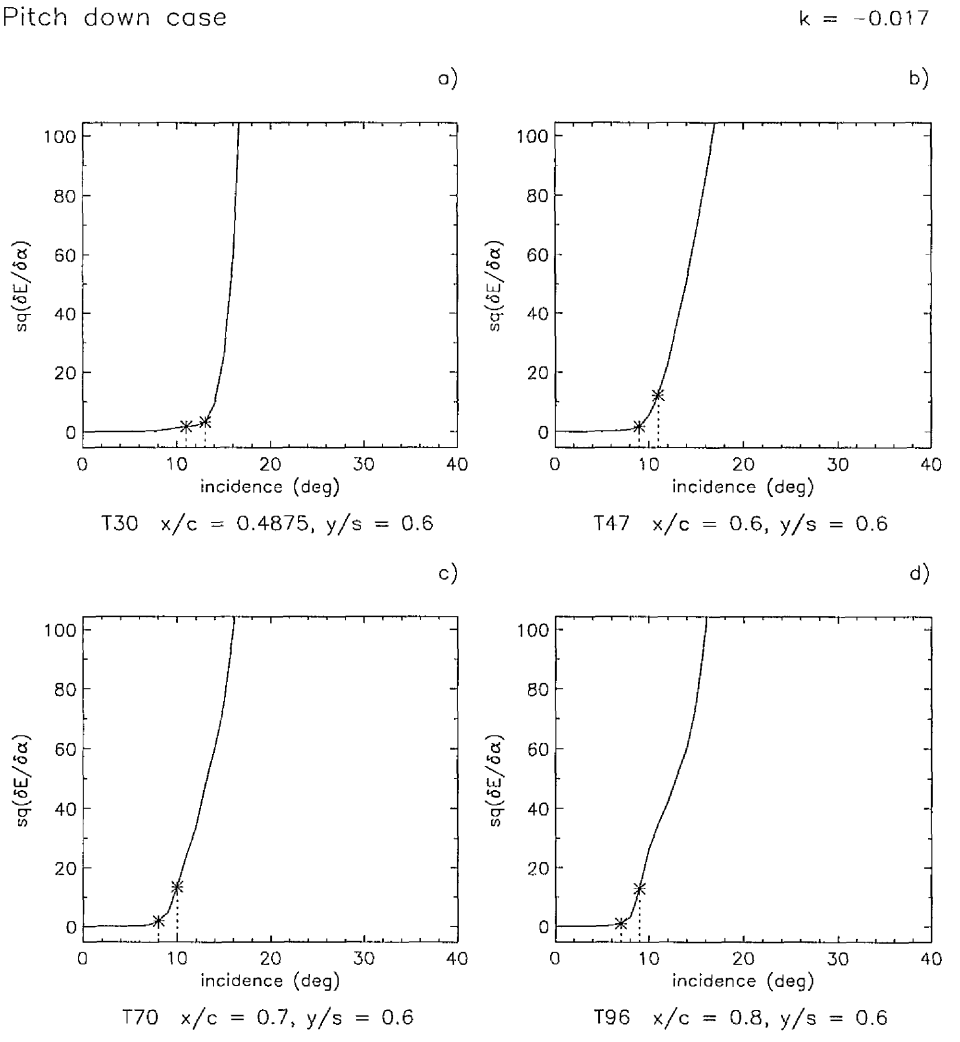

Figure 4.62 - Measurements of the square of the first derivative of signal energy E wrt incidence, $(\delta E/\delta\alpha)^2$, over the incidence range 0° to 39° inclusive, in the pitch down case, **k = -0.017**. Transducers positioned at y/s = 0.6, with chord locations of x/c = 0.4875, 0.6, 0.7 and 0.8

Each plot includes Energy Data Reference Incidences, EDRI's (*).

Note: **bold** type denotes change of parameter from previous figure.

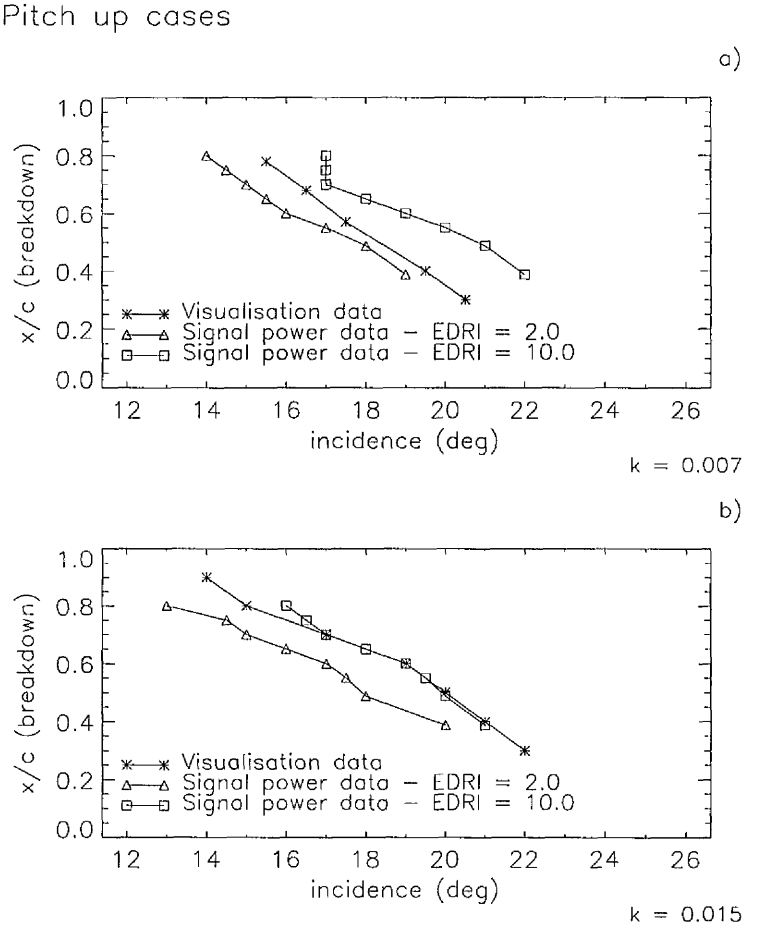

Figure 4.63 - The chordwise location of the upper and lower EDRI values compared with the chordwise location of vortex breakdown, each as functions of incidence in the pitch up cases k = 0.007 and k = 0.015. Data collected during pressure measurement tests & flow visualisation experiments. Re = 2.7×10^6 and 10000 respectively.

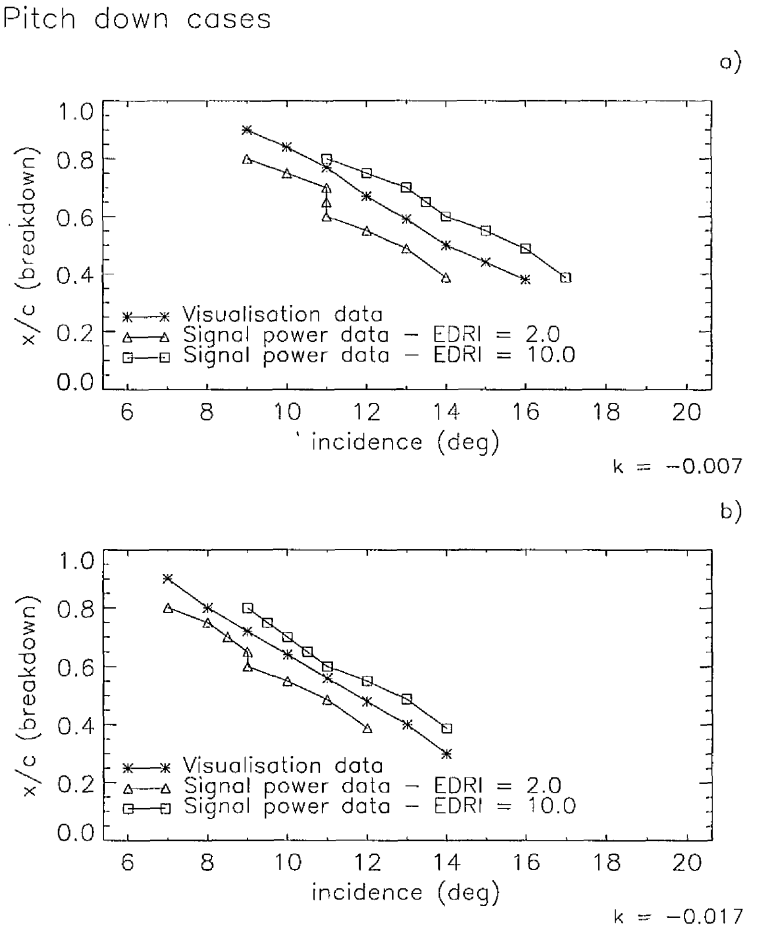

Figure 4.63 - The chordwise location of the upper and lower EDRI values compared with the chordwise location of vortex breakdown, each as functions of incidence in the **pitch down** cases **k = -0.007** and **k = -0.017**. Data collected during pressure measurement tests & flow visualisation experiments. Re = 2.7×10^6 and 10000 respectively.

Note: **bold** type denotes change of parameter from previous figure.

Chapter 5

5. RESULTS - ANALYSIS OF VORTEX BREAKDOWN BUFFET FREQUENCY SPECTRA

5.1 ANALYSIS OF SINGLE POINT FREQUENCY SPECTRA

The power spectra of the sampled pressure data obtained during static and pitching tests were calculated for a number of transducers in each case. The transducers chosen were those identified by the RMS analyses as being located under the path of the vortex core centreline and in the region of high RMS pressure inboard of the vortex core.

5.1.1 *Static tests*

For all frequency spectra examined in the static case, all data collected at a given incidence (2000 samples for a given transducer at each incidence) were processed to remove the d.c. component prior to input into the FFT calculation. No other filtering was applied. A series of power spectra are shown in Figure 5.1 for one chosen transducer located at x/c = 0.6 , y/s = 0.6 for four angles of incidence (12°, 14°, 16° and 18°). At an incidence of 12° (plot a) and again at 14° (plot b), there is a low frequency component of around 5Hz that dominates the spectrum. The exact nature and cause of this component is as yet unclear. It is noted that this phenomenon has not been described elsewhere and the results of the visualisation tests in the present study do not permit any detailed conclusions to be drawn. However, it first appears in the spectrum of each analysed transducer at an incidence of 2°, which coincides with the first appearance of the ridge of high

negative C_P in the pressure data. Further analysis reveals three spatial and temporal trends regarding the behaviour of the magnitude and bandwidth of the low frequency component. Firstly, they both increase towards the apex of the wing. Secondly, they are at a maximum underneath and immediately inboard of the path of the vortex core and decrease dramatically towards the wing centreline. Thirdly, they appear to be independent of incidence between post-vortex-formation and pre-vortex breakdown. In plot c) at 16° incidence, the magnitude of the low frequency component, which has remained roughly constant since its first appearance, has dropped to about half of its previous value at 14°. In addition, another band of higher frequencies centred in the region of 180Hz - 200Hz makes its appearance at this incidence. This behaviour is typical of the transducers analysed, although the sudden drop in magnitude of the low frequency component occurs at a higher incidence towards the apex of the wing. Similarly, the higher frequency band appears later, closer to the apex. Note that whatever the chordwise location, the initial appearance of the higher frequency signals always occurs before the fall in magnitude of the low frequency component. In Figure 5.1, plot d) at 18°, this higher excitation frequency band has come to dominate the frequency spectrum.

Previous work by Gursul (1994), described a series of experiments on various delta wing planforms. For each planform, Gursul identified a dominant frequency in the coherent pressure fluctuations observed downstream of vortex breakdown. It was thought that this frequency was associated with the helical mode instability of the vortex breakdown flow field. Figure 5.2 charts the appearance of the excitation frequency in the frequency spectra of successive upstream chord stations on the wing with increasing incidence. Also plotted is the upstream progression of vortex breakdown with incidence as determined by the results of the flow visualisation tests presented in Chapter 4. This diagram shows that there

(Static case)

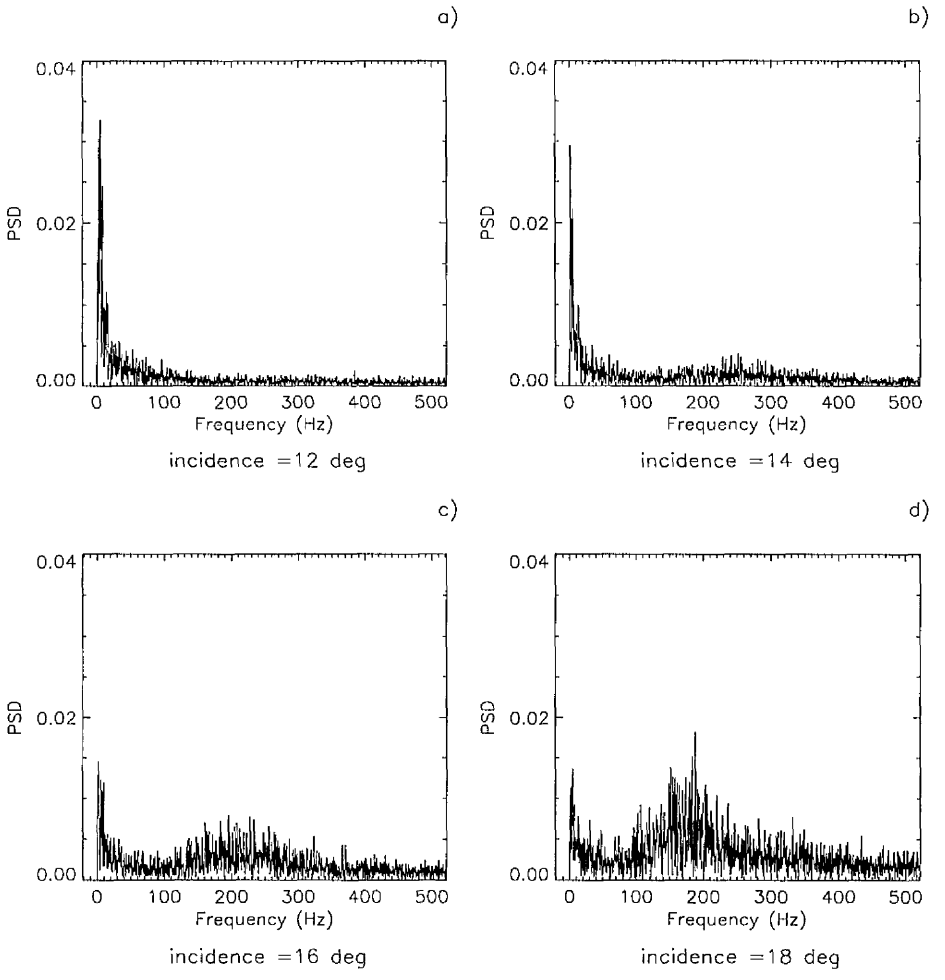

Figure 5.1 - Frequency spectra of pressure fluctuations for a single transducer located at x/c = 0.6, y/s = 0.6 at incidences of 12°, 14°, 16° and 18° in the static case. For each plot, 2000 samples of data collected during pressure measurement tests. Re = 2.7×10^6.

is a similar trend in the appearance of the excitation frequency and the arrival of vortex breakdown at a given chord station over the surface of the wing.

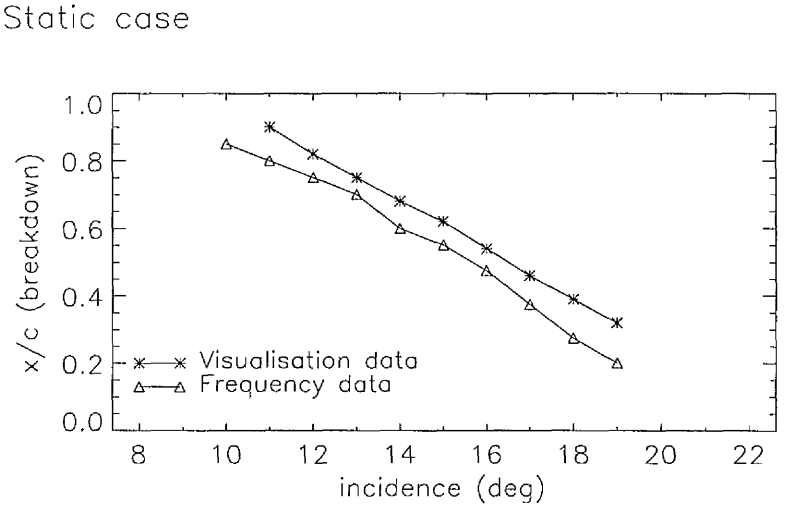

Figure 5.2 - The chordwise location of the appearance of the excitation frequency compared with the chordwise location of vortex breakdown as functions of incidence in the static case. Data collected during pressure measurement tests & flow visualisation experiments. Re = 2.7×10^6 and 10000 respectively.

Figure 5.3 shows another series of frequency spectra, this time at an incidence of 18°, for four transducers positioned across the semi-span of the wing at a chord station of x/c = 0.6. The span stations chosen were y/s = 0.4875 (plot a), y/s = 0.6 (plot b), y/s = 0.7 (plot c) and y/s = 0.8 (plot d). The plots as a whole show that the band of excitation frequencies have their greatest magnitude inboard of the vortex core (plots a and b) reaching a peak at a given incidence and chord station in the centre of the primary region of high RMS pressure, in this case at y/s = 0.6 (plot b). Conversely, under the vortex core at y/s = 0.7 (plot c),

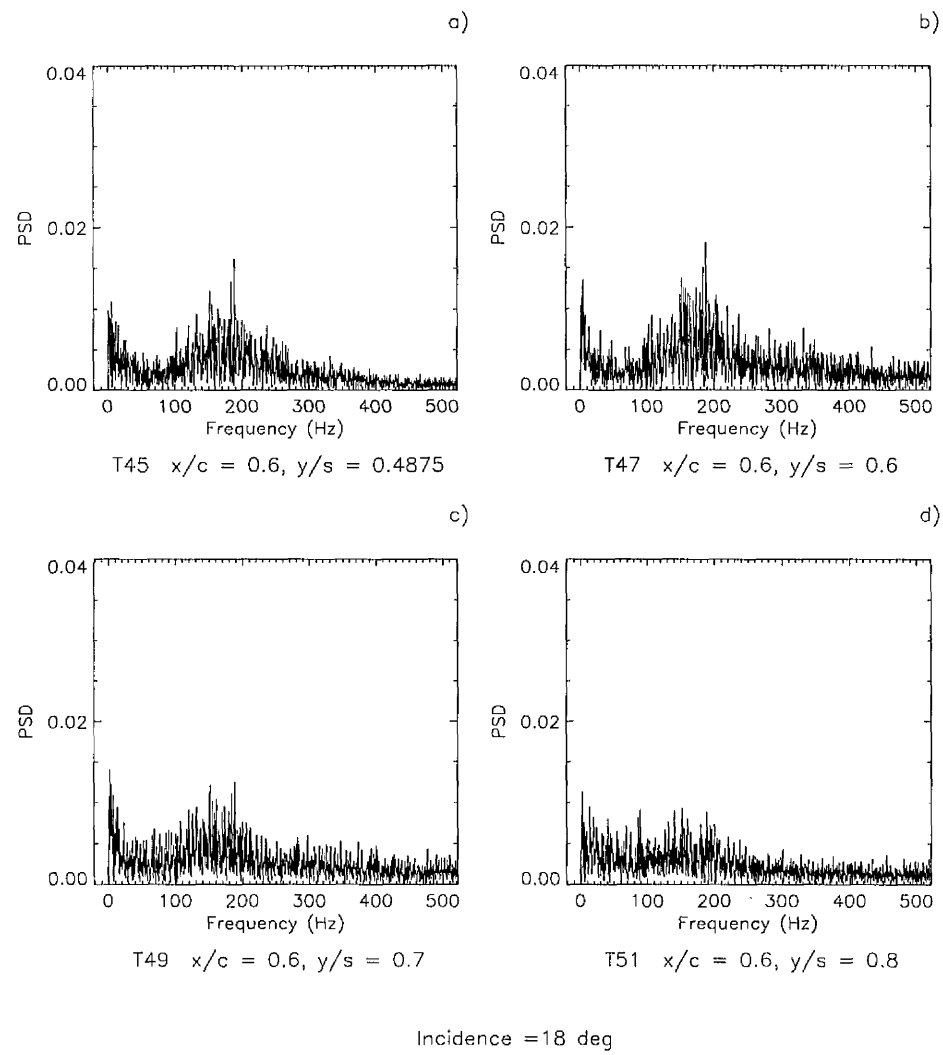

Figure 5.3 - Frequency spectra of pressure fluctuations at an incidence of 18° in the static case for four transducers located at chord station x/c = 0.6 and span stations, y/s = 0.4875, 0.6, 0.7 and 0.8. For each plot, 2000 samples of data collected during pressure measurement tests. Re = 2.7×10^6.

the magnitude of the excitation frequency is reduced. Outboard of the vortex core, at y/s = 0.8 (plot d), the magnitude is reduced further still. Careful examination of the data in these plots reveals a tendency for slightly higher excitation frequencies in the high RMS pressure region inboard of the vortex core at a given chordwise position and incidence. However, the data for this 60° delta wing do not reveal the much higher excitation frequencies that have been observed previously by Woods & Wood (1996) and Woods (1999) in the high RMS pressure region of a more complex wing planform.

Figure 5.4 shows a third series of frequency spectra, again at 18° incidence in the static case, but for four transducers located at span station y/s = 0.6, in the centre of the primary region of high RMS pressure inboard of the vortex core, at chord stations of x/c = 0.4875 (plot a), x/c = 0.6 (plot b), x/c = 0.7 (plot c) and x/c = 0.8 (plot d). Plot a) reveals the initial appearance of an excitation frequency at chord station x/c = 0.4875, centred in the region of 200Hz - 220Hz. This is higher than the more mature excitation frequency band at x/c = 0.6 (180Hz - 200Hz), reproduced in plot b). At subsequent chord stations of x/c = 0.7 (plot c) and x/c = 0.8 (plot d), the centre of the excitation frequency band had fallen to regions around 150Hz - 170Hz and 120Hz - 140Hz respectively. Clearly these plots reveal a trend. In the static case at a given incidence, the dominant excitation frequency of pressure fluctuations tended to decrease in terms of centre frequency value with distance from the apex of the wing. This is in agreement with the work of Gursul (ibid.), who found for each of his planforms, (with sweep angles of 60°, 65°, 70° and 75°), that the centre of the excitation frequency band occurred at a higher frequency towards the apex of the wing.

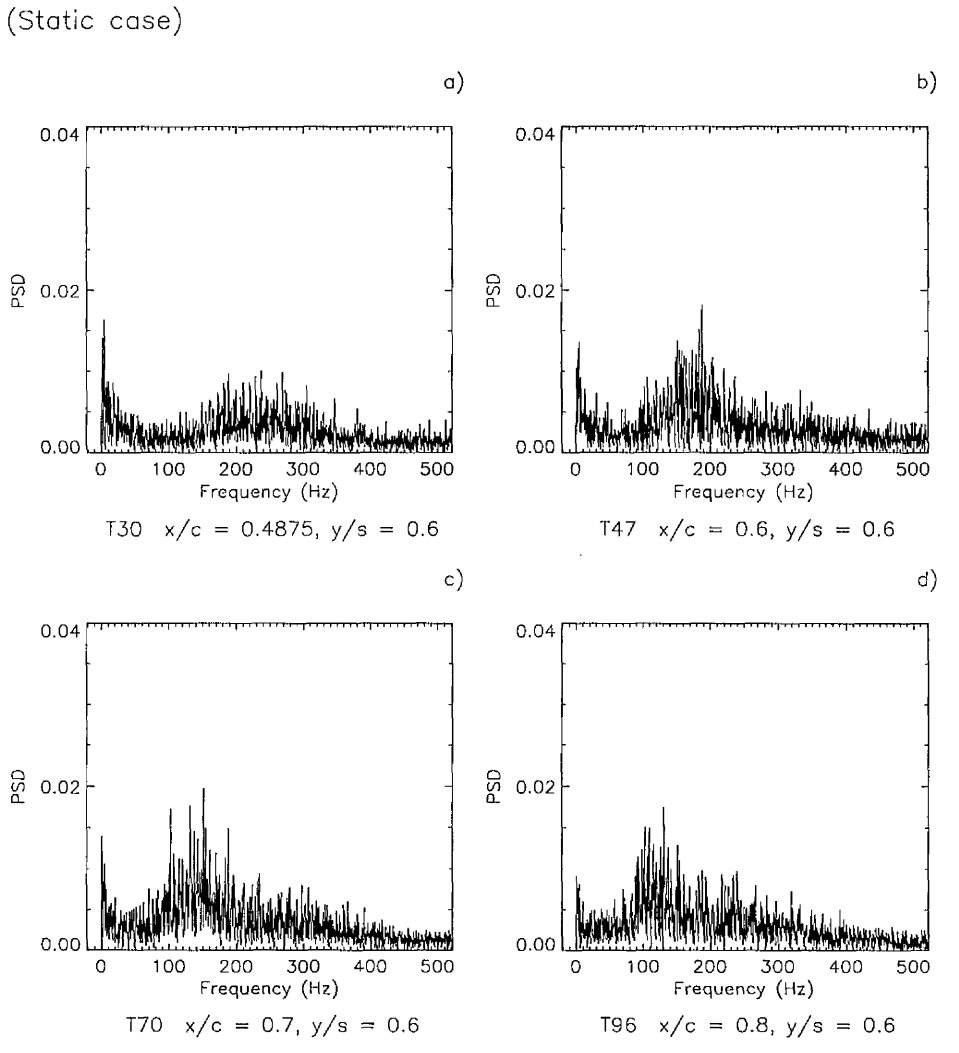

Figure 5.4 - Frequency spectra of pressure fluctuations at an incidence of 18° in the static case for four transducers located at span station **y/s = 0.6** and chord stations, **x/c = 0.4875, 0.6, 0.7** and **0.8**. For each plot, 2000 samples of data collected during pressure measurement tests. Re = 2.7×10^6.

Note: **bold** type denotes change of parameter from previous figure

Figure 5.5 illustrates two trends in the frequency data concerning this central frequency value. Plot a) shows the variation in central frequency as a function of chord wise position for five incidences (16°, 18°, 20°, 22° and 24°). The trend apparent in Figure 5.4 is confirmed over this range of incidence. However, what is

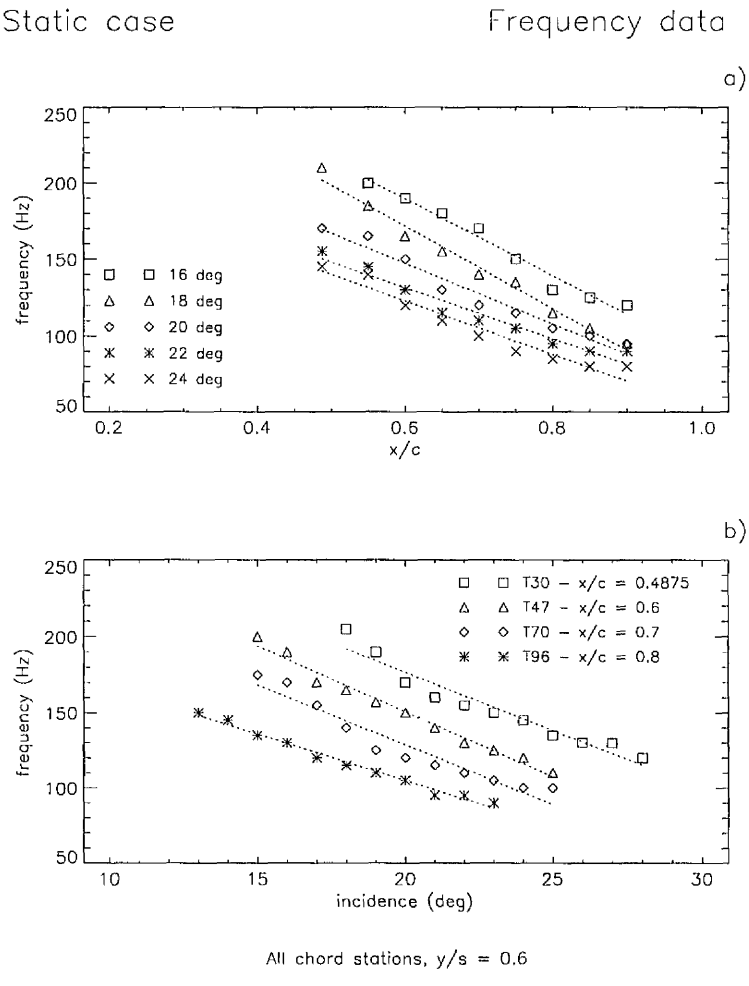

Figure 5.5 - Line plots showing the variation of central excitation frequency as:
a) a function of chord position for incidences of 16°, 18°, 20°, 22° and 24°
b) a function of incidence for chord stations x/c = 0.4875, 0.6, 0.7 and 0.8.
Data collected during pressure measurement tests. Re = 2.7×10^6

also apparent is the variation in central frequency at a given chord station with an increase in incidence. This second trend is better illustrated in plot b) which shows the variation in central frequency as a function of incidence for four chord stations. It is clear that for each chord station, the central excitation frequency of pressure fluctuations decreased with an increase in incidence. This is also in agreement with Gursul's findings who observed that, for all chordwise locations in each of his cases, an increase in incidence tended to decrease the central frequency of the high frequency band while the strength and bandwidth increased.

It has been shown by Mabey (1996) that this frequency can be expressed as a non-dimensional constant for a given geometry and angle of attack. Mabey suggested that this constant has a value of about 0.4 for delta wings with a sweep angle of 60°. Mabey (ibid.) has also suggested that a unique frequency parameter can be found for all delta wings which takes into account the sweep angle as well as angle of incidence. It was suggested that the value of this modified frequency parameter n_m is 0.25 ± 0.02. Jupp *et al* (1999) demonstrated that the excitation frequency signals identified above are consistent with these values.

5.1.2 *Frequency spectra - pitch up tests*

Despite the extensive analysis of post-breakdown dominant buffet frequencies on static wings carried out by Gursul (1994), Mabey (1996), Woods & Wood (1996) and Woods (1999), it is apparent that, until now, no data has been available regarding this dominant frequency in the pitching case. To satisfy the demand for pitch up and pitch down frequency data, the power spectra of the sampled pressure data were calculated for the same transducers that were highlighted in the static case analysis. Each calculation used the incidence window sizes determined by the RMS analysis. In each pitching case, the data had been filtered using a Finite Impulse Response (FIR) high-pass digital filter to remove spectrum

data below the pitch rate Nyquist cut-off frequency. The determination of the Nyquist frequency and the filtering process was described in some detail in Section 3.4.

A series of power spectra are shown in Figures 5.6 and 5.7 for one chosen transducer in pitch up cases located at x/c = 0.7 , y/s = 0.6 (k = 0.007) and x/c = 0.75, y/s = 0.6 (k = 0.015) respectively. Four angles of incidence are shown in each case (12°, 14°, 16° and 18°). At an incidence of 12°, shown in plot a), and again at 14° shown in plot b) of each diagram, there is very little activity in the power spectrum. In plot c) at 16° incidence in either case, a broad band of frequencies, this time centred in the range 150Hz - 250Hz, makes its appearance. In plot d) at 18°, this high frequency band now dominates the frequency spectrum. This result is indicative of the general behaviour of the high band of frequencies in the pitch up cases. The high frequency band showed similarity with its static counterpart but the observed changes in behaviour were delayed until a higher incidence with increasing pitch rate. Figure 5.8 reveals a series of line plots, showing the appearance of the excitation frequency in the frequency spectra of successive upstream chord stations on the wing with increasing incidence, in the static and pitch up cases (k = 0.007 and k = 0.015). Also plotted, is the corresponding upstream progression of vortex breakdown with incidence as determined by the results of the flow visualisation tests presented in Chapter 4. This diagram shows that there is again a similar trend in the appearance of the excitation frequency and the arrival of vortex breakdown at a given chord station on the wing, this time for the pitch up cases.

Following the pattern of illustration used in the static case, Figures 5.9 and 5.10 show series of frequency spectra, at an incidence of 18° in the k = 0.007 and k = 0.015 cases, for four transducers positioned across the semi-span of the wing

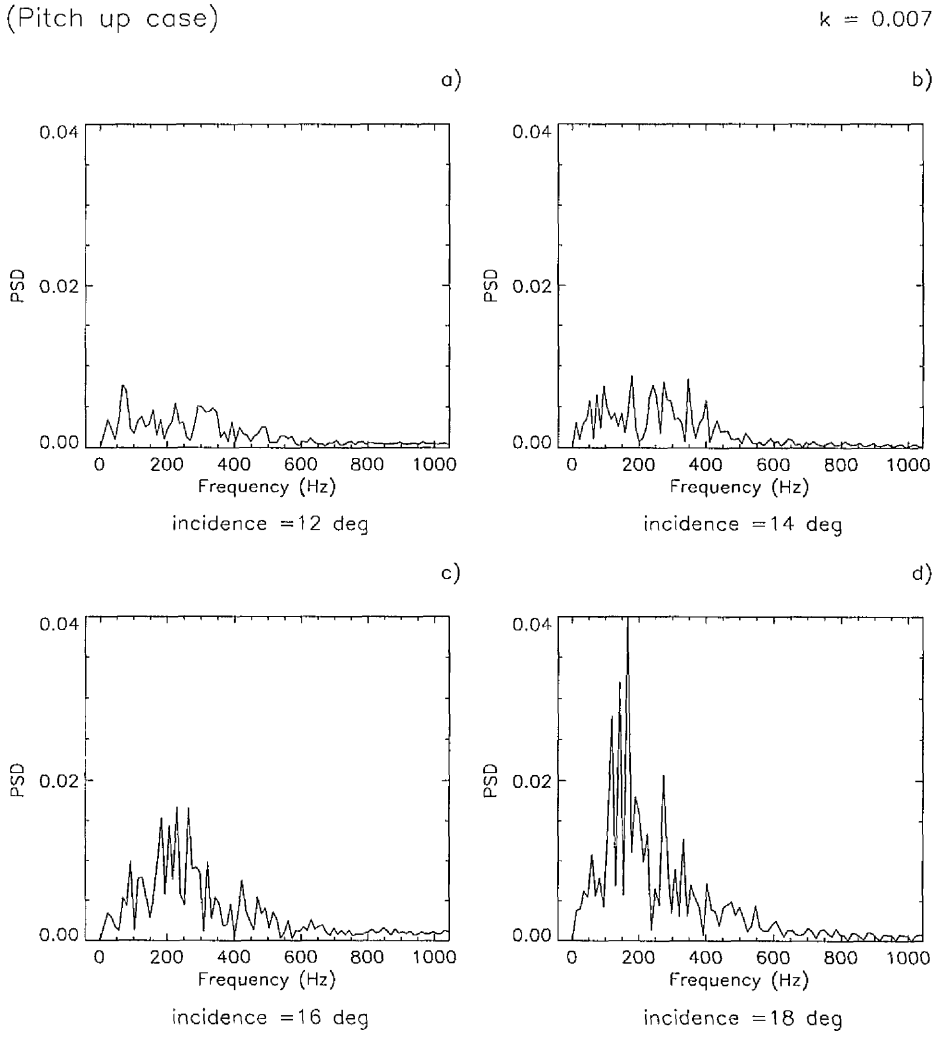

Figure 5.6 - Frequency spectra of pressure fluctuations for a single transducer located at x/c = 0.7, y/s = 0.6 at incidences of 12°, 14°, 16° and 18° in the pitch up case k = 0.007. For each plot, 471 samples of data collected during pressure measurement tests. Re = 2.7×10^6.

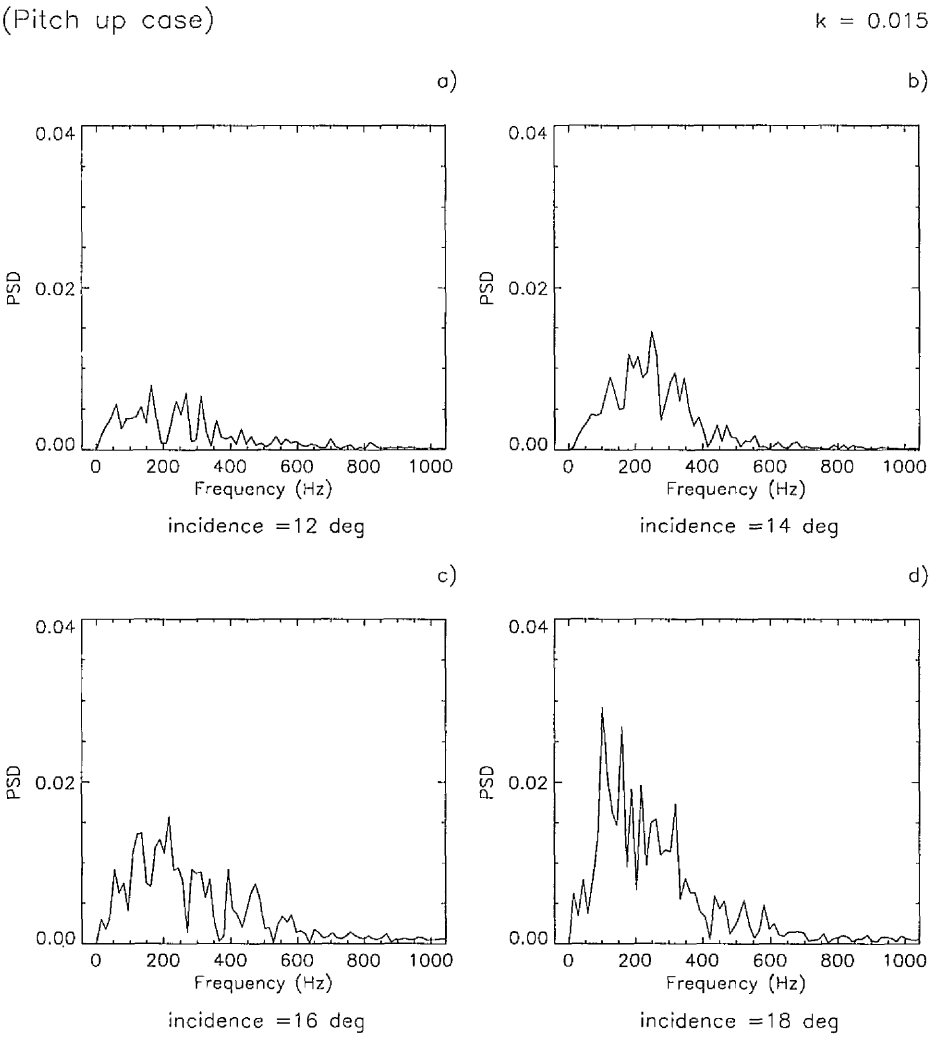

Figure 5.7 - Frequency spectra of pressure fluctuations for a single transducer located at **x/c = 0.75, y/s = 0.6** at incidences of 12°, 14°, 16° and 18° in the pitch up case **k = 0.015**. For each plot, **724** samples of data collected during pressure measurement tests. Re = 2.7×10^6.

Note: **bold** type denotes change of parameter from previous figure.

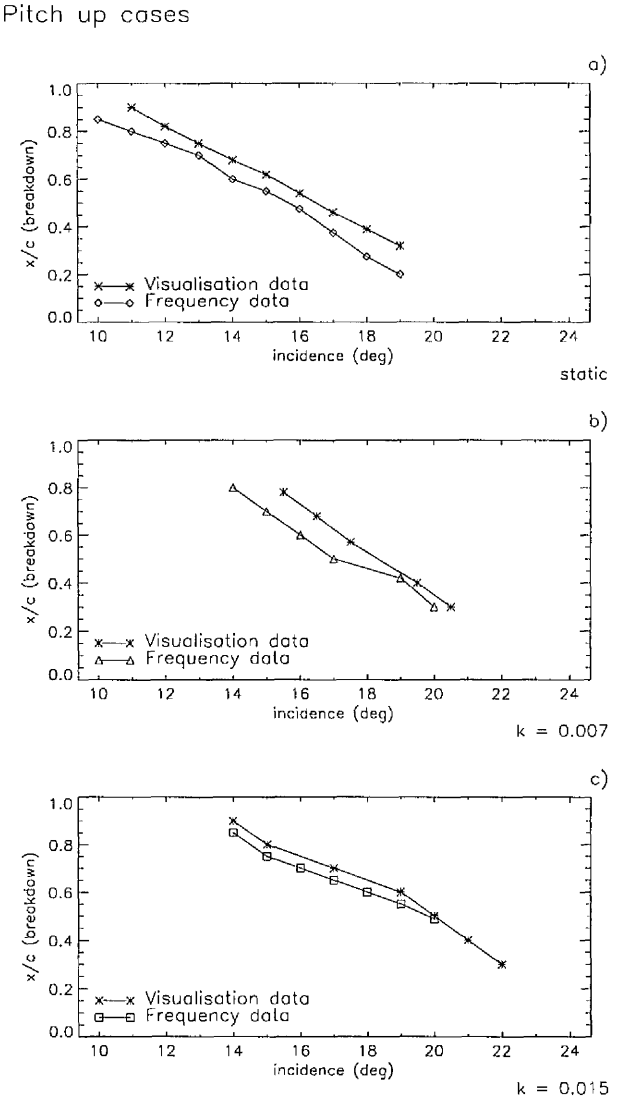

Figure 5.8 - The chordwise location of the appearance of the excitation frequency compared with the chordwise location of vortex breakdown as functions of incidence in the static and two pitch up cases (k = 0.007 & k = 0.015). Data collected during pressure measurement tests & flow visualisation experiments. Re = 2.7×10^6 and 10000 respectively.

at chord stations of x/c = 0.7 and x/c = 0.75 respectively. The span stations are the same as those detailed in the static case, and in both cases, show a similar trend in frequency behaviour patterns with increasing spanwise location, i.e., the band of excitation frequencies have their greatest magnitude inboard of the vortex core (plots a and b), reaching a peak at a given incidence and chord station in the centre of the primary region of high RMS pressure at y/s = 0.6 (plot b). Under the vortex core at y/s = 0.7 (plot c), the magnitude of the excitation frequency had again reduced and outboard of the vortex core, at y/s = 0.8 (plot d), the magnitude had reduced further still. Contrary to the static case, the data in either pitch up case reveals little or no change in the central excitation frequency across the wing at a given chordwise position and incidence.

Figures 5.11 and 5.12 show a third series of frequency spectra, again at 18° incidence in the k = 0.007 and k = 0.015 cases respectively, but for four transducers located at span station y/s = 0.6, in the centre of the primary region of high RMS pressure inboard of the vortex core, at similar chord stations to those shown in the static case. Figure 5.11, plot a) reveals for the k = 0.007 case, the initial appearance of an excitation frequency at chord station x/c = 0.6, centred in the region of 200Hz - 270Hz. This is again higher than the excitation frequency band at x/c = 0.7 (140Hz - 200Hz) and reproduced in plot b). At subsequent chord stations of x/c = 0.8 (plot c) and x/c = 0.9 (plot d), the centre of the excitation frequency band had fallen to regions around 130Hz -180Hz and 120Hz - 170Hz respectively. Figure 5.12 reveals a similar trend for the k = 0.015 case, however, these were measured at chord stations 0.05c further downstream from those examined in Figure 5.11, and therefore the frequencies measured cannot be directly compared with the lower pitch rate case.

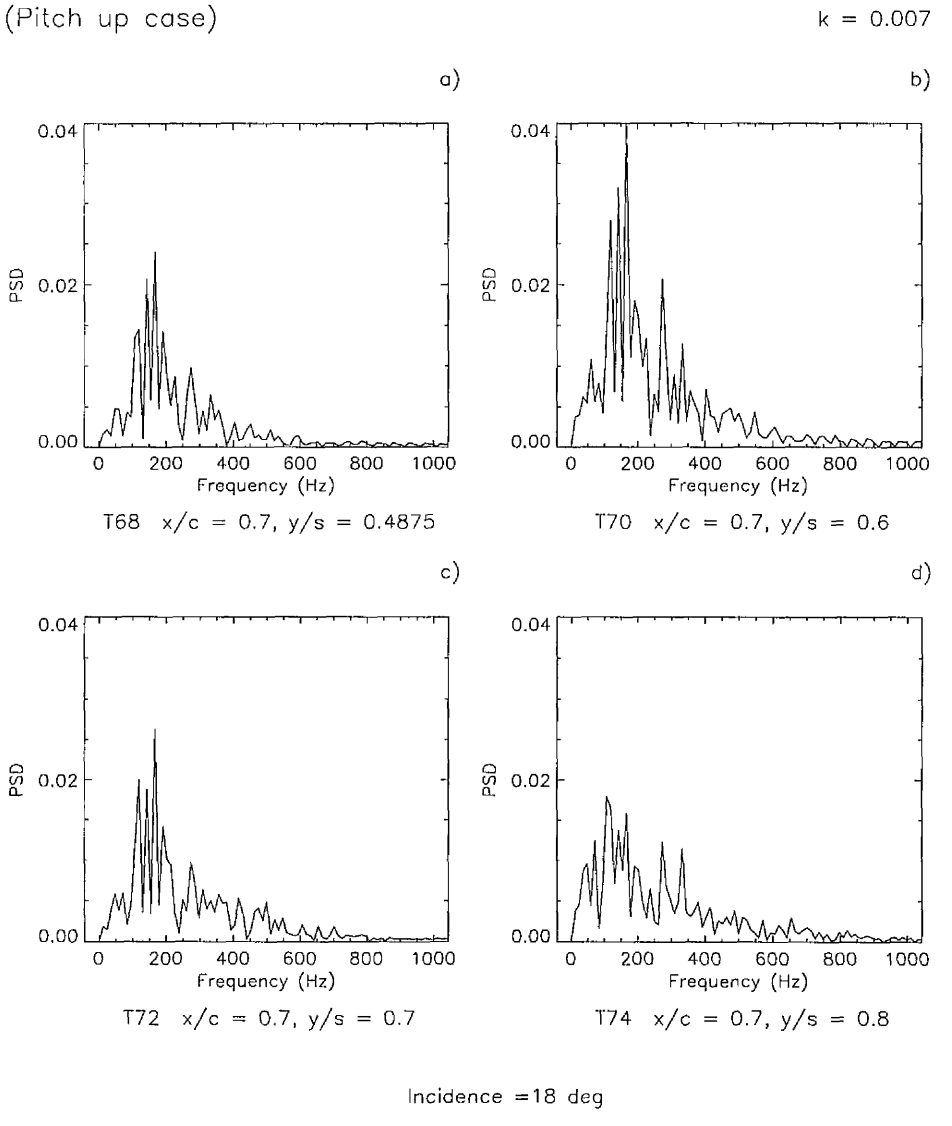

Figure 5.9 - Frequency spectra of pressure fluctuations at an incidence of 18° in the pitch up case k = 0.007 for four transducers located at chord station x/c = 0.7 and span stations, y/s = 0.4875, 0.6, 0.7 and 0.8. For each plot, 471 samples of data collected during pressure measurement tests. Re = 2.7×10^6.

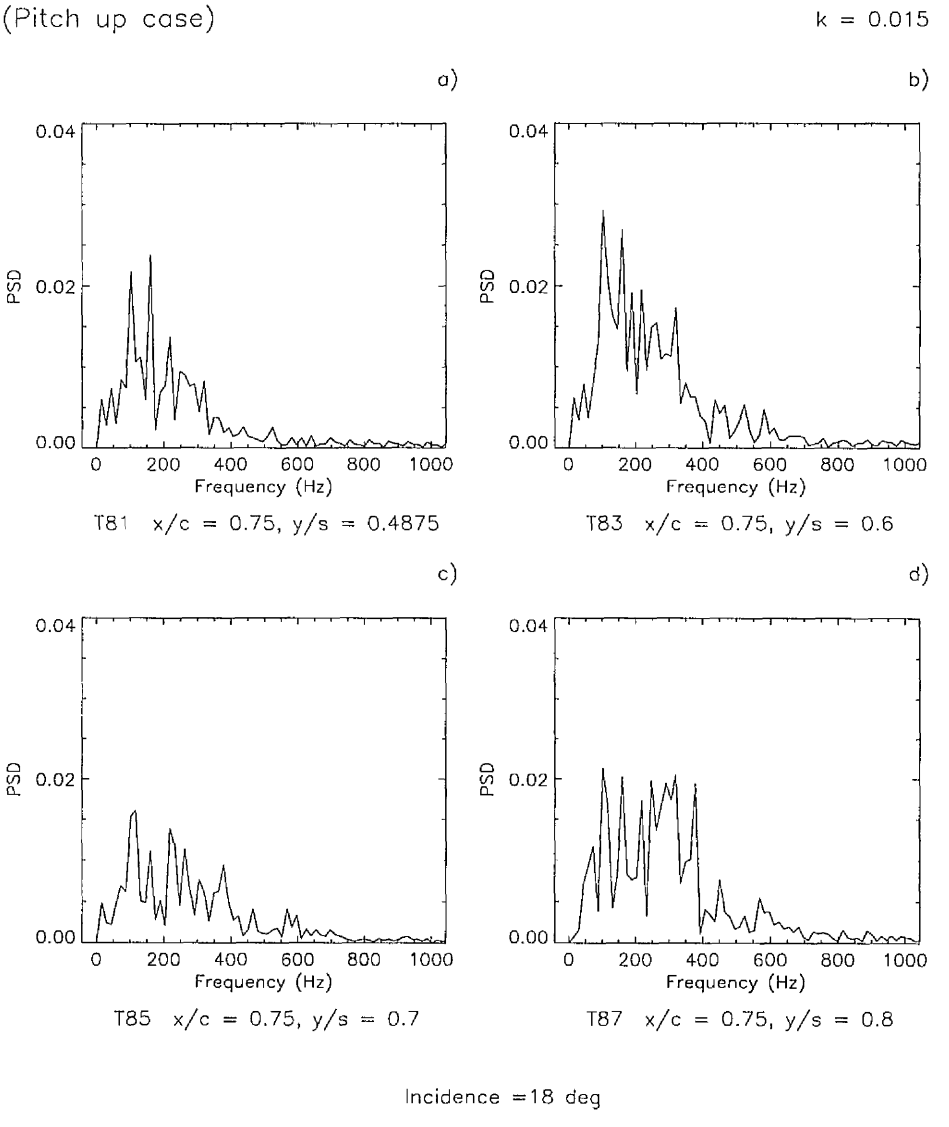

Figure 5.10 - Frequency spectra of pressure fluctuations at an incidence of 18° in the pitch up case **k = 0.015** for four transducers located at chord station **x/c = 0.75** and span stations, y/s = 0.4875, 0.6, 0.7 and 0.8. For each plot, **724** samples of data collected during pressure measurement tests. Re = 2.7×10^6.

Note: **bold** type denotes change of parameter from previous figure.

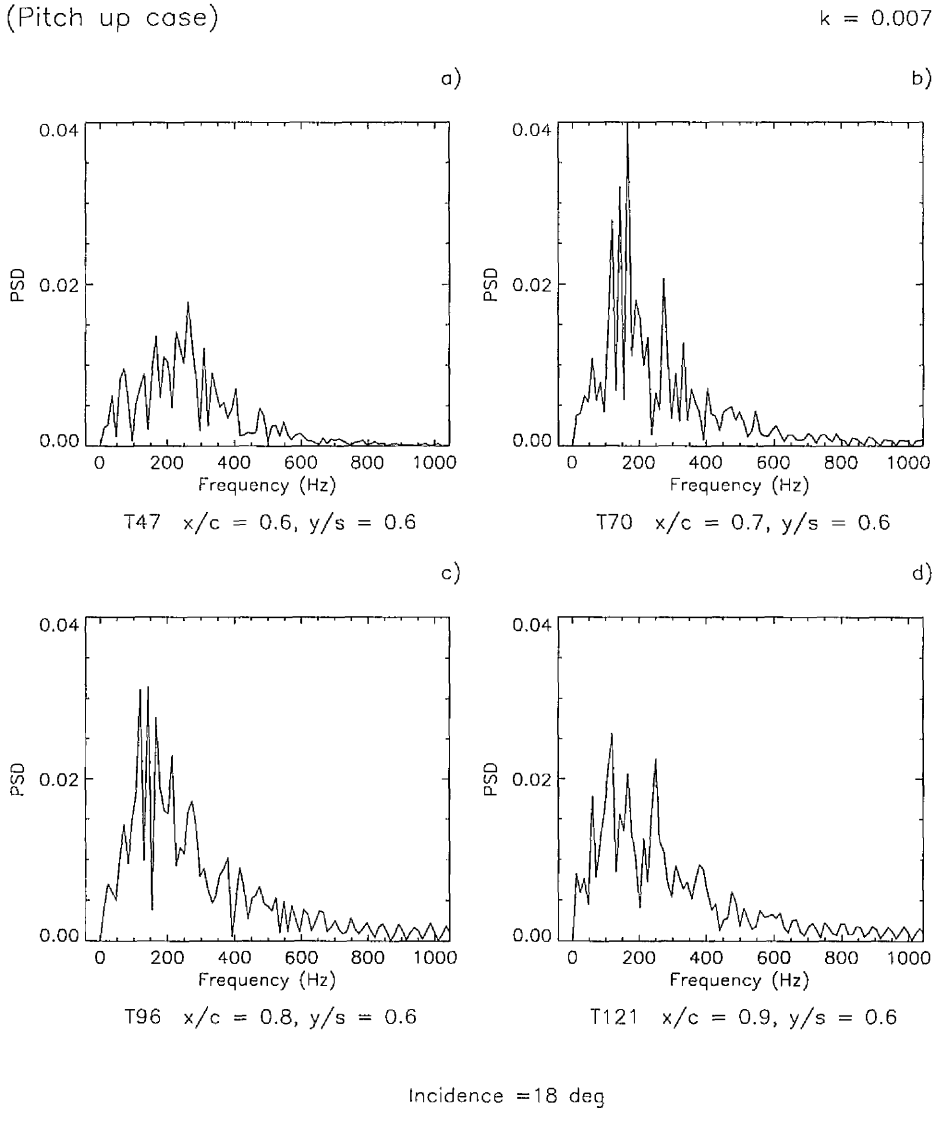

Figure 5.11 - Frequency spectra of pressure fluctuations at an incidence of 18° in the pitch up case **k = 0.007** for four transducers located at **span station y/s = 0.6** and **chord stations, x/c = 0.6, 0.7, 0.8** and **0.9**. For each plot, **471** samples of data collected during pressure measurement tests. Re = 2.7×10^6.

Note: **bold** type denotes change of parameter from previous figure.

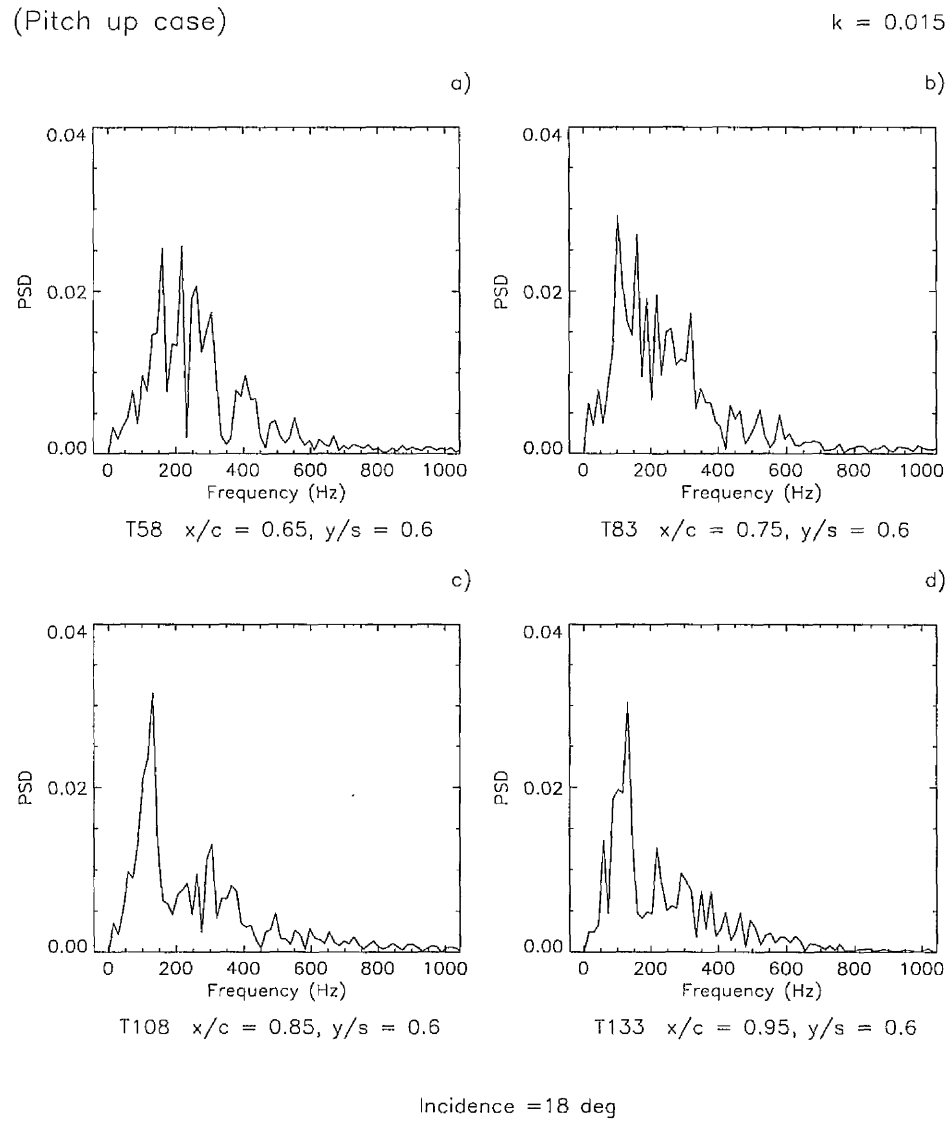

Figure 5.12 - Frequency spectra of pressure fluctuations at an incidence of 18° in the pitch up case **k = 0.015** for four transducers located at span station y/s = 0.6 and chord stations, **x/c = 0.65, 0.75, 0.85** and **0.95**. For each plot, **724** samples of data collected during pressure measurement tests. Re = 2.7×10^6.

Note: **bold** type denotes change of parameter from previous figure.

Figure 5.13, plot a) illustrates the variation in excitation frequency as a function of chordwise position in the static and pitch up cases at an incidence of 18°. Similarly, Figure 5.13, plot b) shows the same variation, but this time as a function of incidence at a chord location of x/c = 0.6.

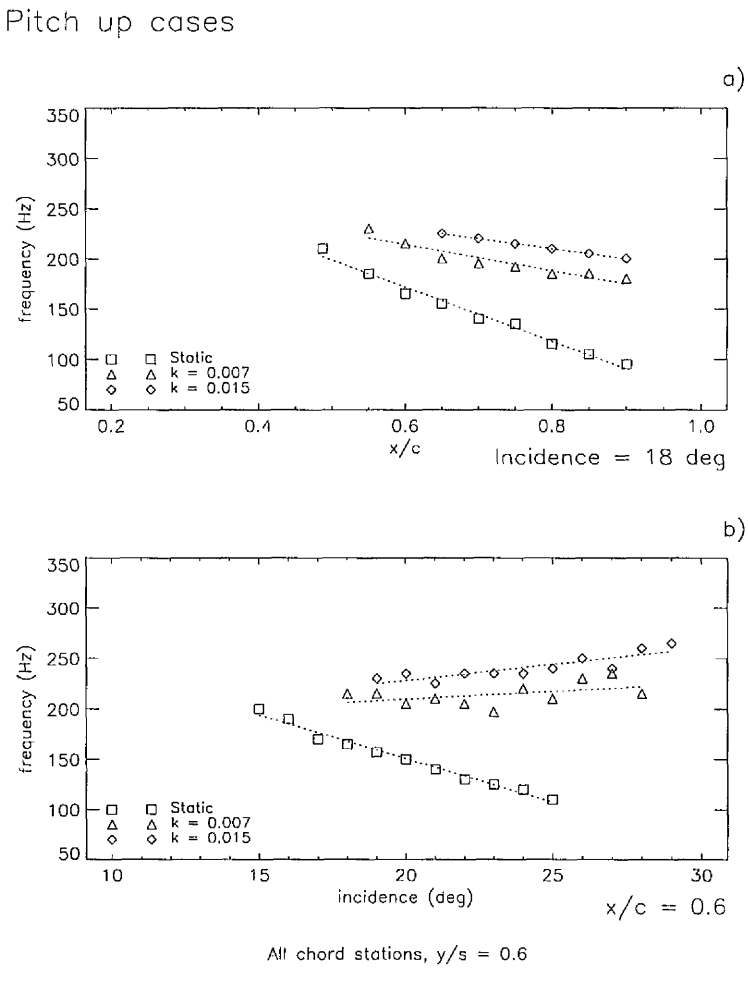

Figure 5.13 - Line plots showing the variation of central excitation frequency in static and two pitch up cases (k = 0.007 & k = 0.015) as: a) a function of chord position for an incidence of 18°. b) a function of incidence at chord station x/c = 0.6. Data collected during pressure measurement tests. Re = 2.7×10^6.

The spectrum in each pitch up case, with relatively fewer data samples and greater noise throughout the incidence range, made the measurement of the centre frequency more difficult than the static case and it should be noted that there may be some margin for error. However, given that two pitch up cases are presented, it is suggested that trends apparent in the data are genuine and representative. It was shown for static cases, that the centre of the excitation frequency band was found to occur at a higher frequency towards the apex of the wing. By determining the mean within a broad band of excitation frequencies, Figure 5.13, plot a) revealed that the pitch up cases would appear to show a similar trend. Similarly, it was also shown for the static case, that the central frequency of the higher frequency band would tend to decrease with an increase in incidence. Figure 5.13, plot b) clearly shows that in the pitch up cases, the excitation frequency band is largely insensitive to incidence.

5.1.3 *Frequency spectra - pitch down tests*

Figures 5.14 and 5.15 show the frequency spectra for a single transducer in two pitch down cases (k = -0.007 and k = -0.017 respectively) at four angles of incidence (26°, 18°, 16° and 14°). In the k = -0.007 case, the transducer was located at x/c = 0.4875, y/s = 0.4875 and in the k = -0.017 case, the transducer in question was positioned at the same span station (y/s = 0.4875) but at 0.1c further upstream at x/c = 0.3875. At 26° incidence in either figure (plot a), there is very little pressure fluctuation activity apparent in the data. At this incidence, RMS contour plots (not shown) revealed that, in either pitch rate case, the chordwise position of the waist in the RMS pressure contours, i.e., Figure 4.43, label (5), which in turn had been shown in Figure 4.48, plots b) and c) to be a good indicator of the location of vortex restoration in the pitch down cases, had yet to move downstream away from the apex of the wing. This finding is in agreement with the findings of Gursul (1994) who found that, for static cases, pressure fluctuation excitation frequency activity ceased when vortex breakdown

reached the apex of the wing. At 18° incidence in either case (plot b), a high frequency band, now centred in the frequency range 150Hz - 300Hz dominates the spectrum. The high frequency band first appears at incidences of 21° and 20° in the k = -0.007 and k = -0.017 cases respectively (not shown), and in each case coincides with the first indication of movement of the expanded region of high RMS pressure i.e., Figure 4.43, label (4), outboard from the wing centreline. At 16° incidence in the k = -0.007 case (Figure 5.14, plot c), the width and power of the high frequency band had diminished somewhat. However, in the k = -0.017 case at the same incidence (Figure 5.15, plot c), the same features of the excitation frequency band have reached a maximum. At an incidence of 14°, the dominant frequency in both cases (plot d) has all but disappeared. This general progression with incidence is typical for all transducers analysed.

Figure 5.16 plots b) and c) show line plots indicating the disappearance of the excitation frequency in the frequency spectra of successive downstream chord stations on the wing with decreasing incidence in the pitch down cases k = -0.007 and k = -0.017 respectively. Also plotted is the corresponding downstream progression of vortex restoration with decreasing incidence as determined by the results of the flow visualisation tests presented in Chapter 4. Figure 5.16, plot a) shows the equivalent data in the static case which details the appearance of the excitation frequency in the frequency spectra of successive upstream chord stations on the wing with increasing incidence and the upstream progression of vortex breakdown. This diagram shows that there is a similar trend in the subsidence of the excitation frequency and the arrival of vortex restoration at a given chord station on the wing for the pitch down cases.

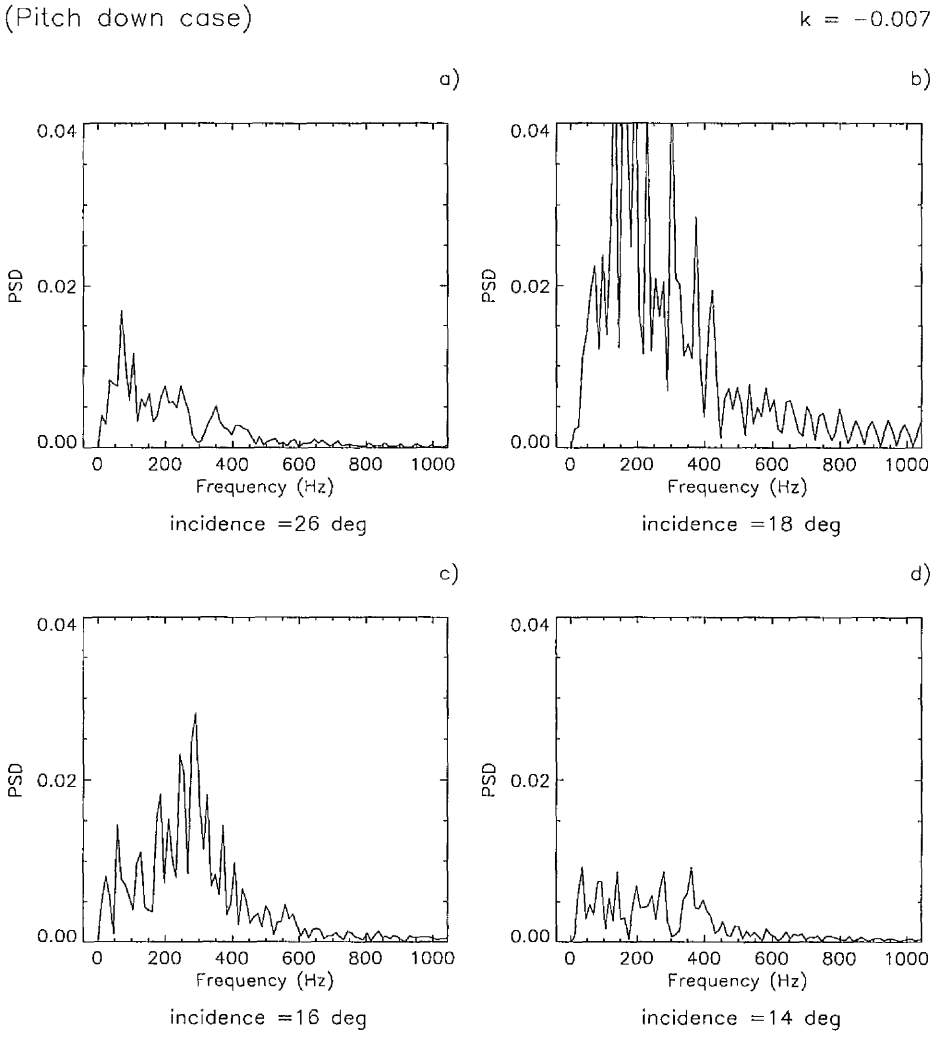

Figure 5.14 - Frequency spectra of pressure fluctuations for a single transducer located at x/c = 0.4875, y/s = 0.4875 at incidences of 26°, 18°, 16° and 14° in the pitch down case k = -0.007. For each plot, 445 samples of data collected during pressure measurement tests. Re = 2.7×10^6.

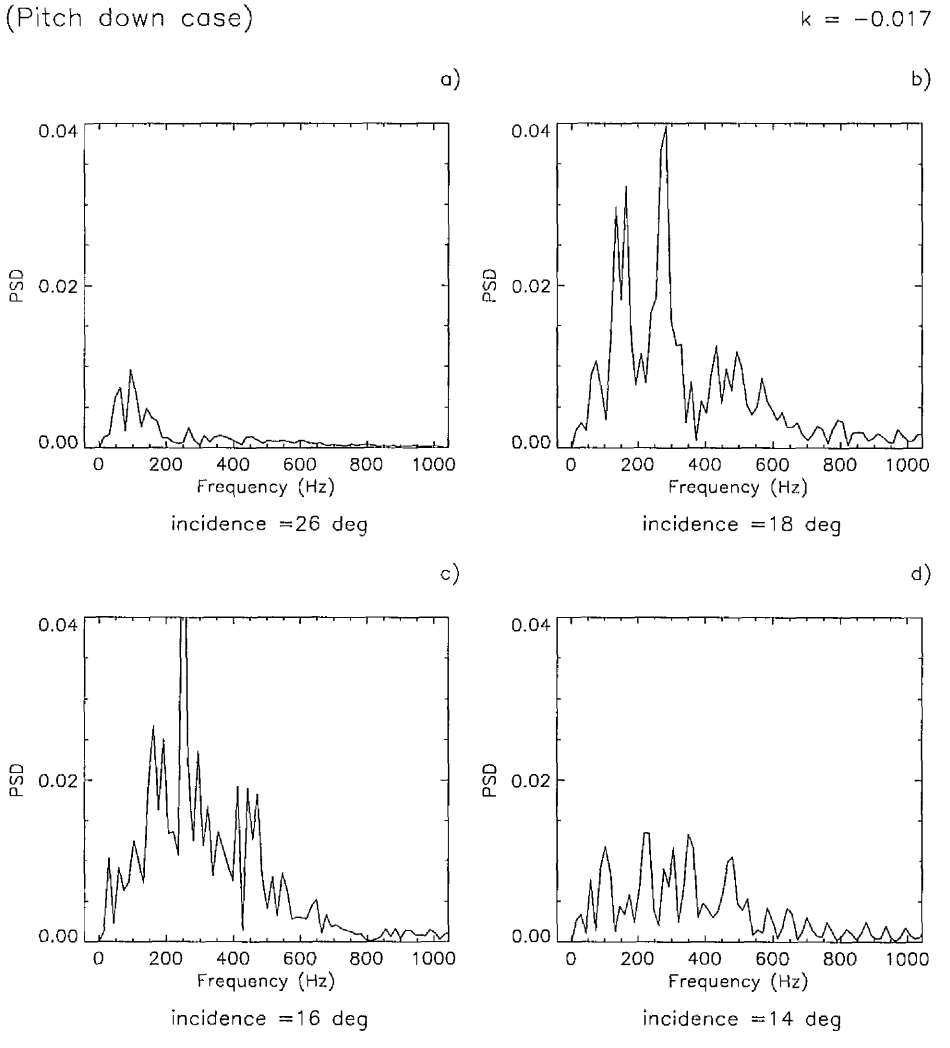

Figure 5.15 - Frequency spectra of pressure fluctuations for a single transducer located at **x/c = 0.3875**, y/s = 0.4875 at incidences of 26°, 18°, 16° and 14° in the pitch down case **k = -0.017**. For each plot, **692** samples of data collected during pressure measurement tests. Re = 2.7x10^6.

Note: **bold** type denotes change of parameter from previous figure.

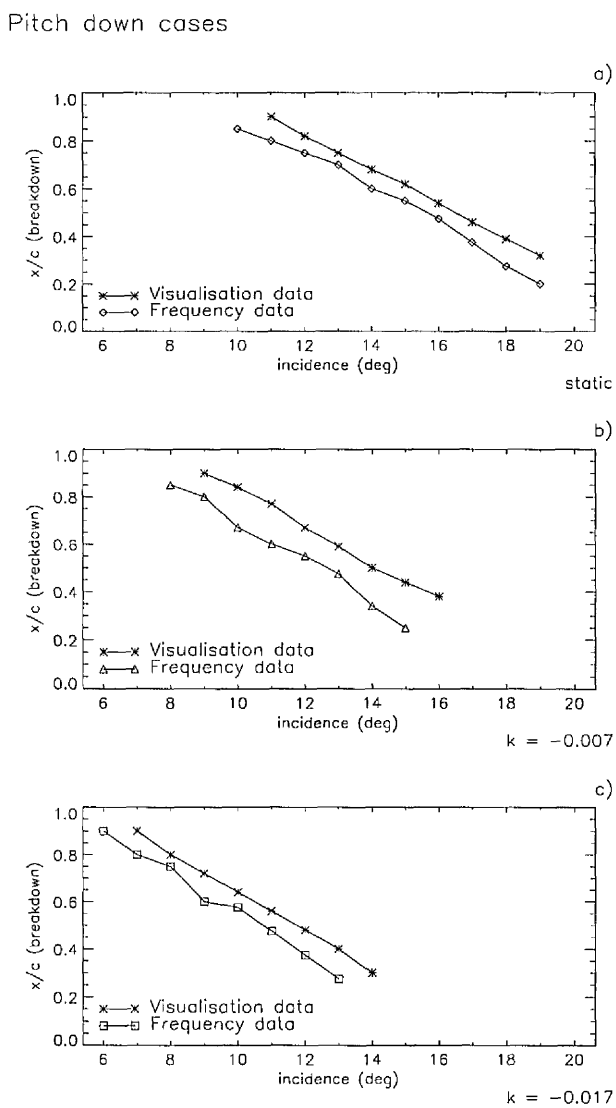

Figure 5.16 - The chordwise location of the appearance/disappearance of the excitation frequency compared with the chordwise location of vortex breakdown/restoration as functions of incidence in the static and two pitch down cases (k = -0.007 & k = -0.017). Data collected during pressure measurement tests & flow visualisation experiments. Re = 2.7×10^6 and 10000 respectively.

Figures 5.17 and 5.18 show series of frequency spectra, at an incidence of 18° in the k = -0.007 and k = -0.017 cases, for four transducers positioned across the semi-span of the wing at chord stations of x/c = 0.4875 and x/c = 0.3875 respectively. The span stations chosen were y/s = 0.3875 (plot a), y/s = 0.4875 (plot b), y/s = 0.6 (plot c) and y/s = 0.7 (plot d). As a group, these transducers are further inboard than those shown for the static and pitch up cases, reflecting the spanwise position of the region of high RMS pressure, Figure 4.43, label (4), which was observed at this incidence in the RMS pressure analysis. The plots as a whole showed a similar trend in frequency behaviour patterns with increasing spanwise location as those displayed for static and pitch up cases. For each pitch down case, the band of excitation frequencies have their greatest magnitude inboard of the vortex core at y/s = 0.4875 in the centre of the region of high RMS pressure, decreasing in width and magnitude in an outboard direction towards the wing leading-edge. In a similar manner to the pitch up cases, the data in both pitch down cases reveal little or no change in the central excitation frequency across the wing at a given chordwise position and incidence.

Figures 5.19 and 5.20 show another series of frequency spectra, again at 18° incidence in the k = -0.007 and k = -0.017 cases respectively, but for four transducers located at span station y/s = 0.4875, in the centre of the primary region of high RMS pressure inboard of the vortex core. Figure 5.19, plot a) reveals for the k = -0.007 case, the initial appearance of an excitation frequency at chord station x/c = 0.29375, in the region of 100Hz - 350Hz. This is similar to the excitation frequency band at x/c = 0.3875 shown in plot b), whose centre is located in the region 150Hz - 300Hz. At chord stations of x/c = 0.4875 (plot c) and x/c = 0.6 (plot d), the width of the excitation frequency band had increased, however, the centre had fallen into the regions 150Hz - 250Hz and 120Hz - 220Hz respectively. Figure 5.20 reveals a similar trend for the k = -0.017

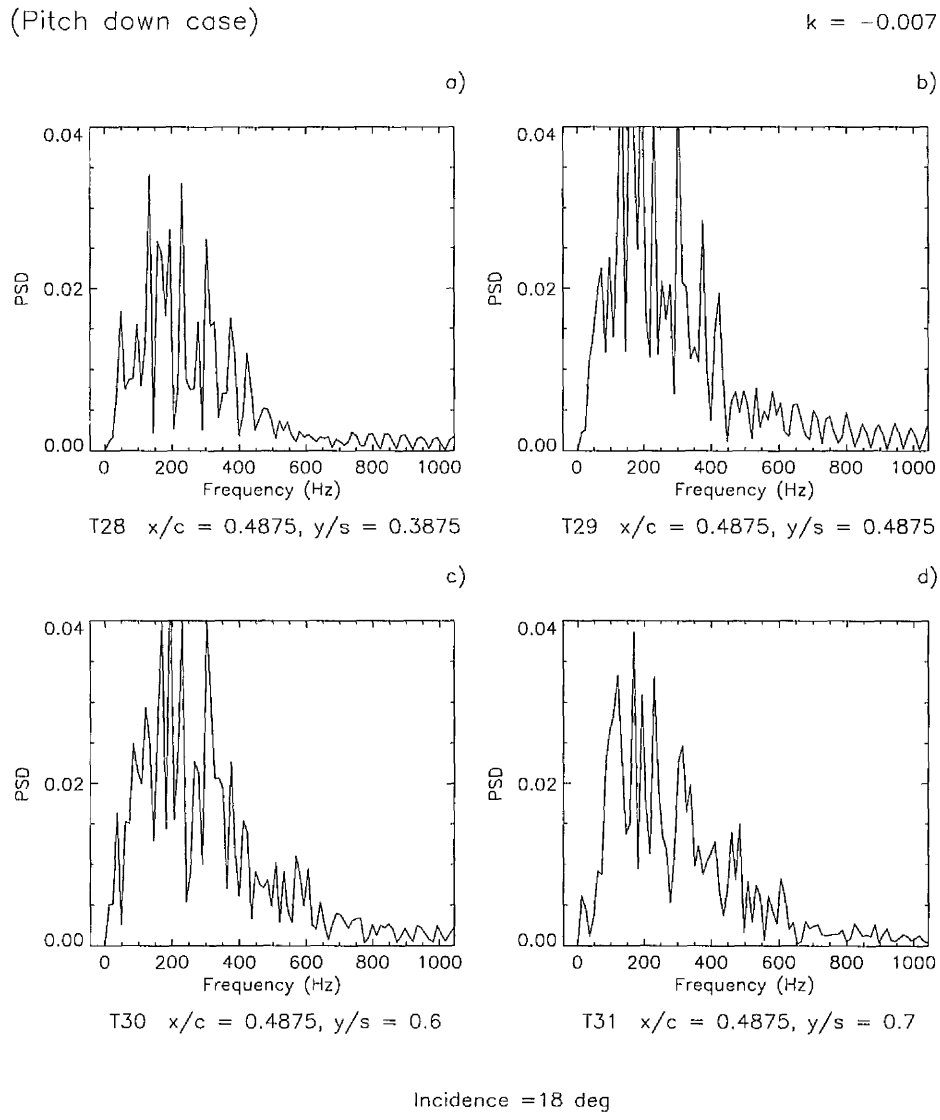

Figure 5.17 - Frequency spectra of pressure fluctuations at an incidence of 18° in the pitch down case k = -0.007 for four transducers located at chord station x/c = 0.4875 and span stations, y/s = 0.3875, 0.4875, 0.6 and 0.7. For each plot, 445 samples of data collected during pressure measurement tests. Re = 2.7×10^6.

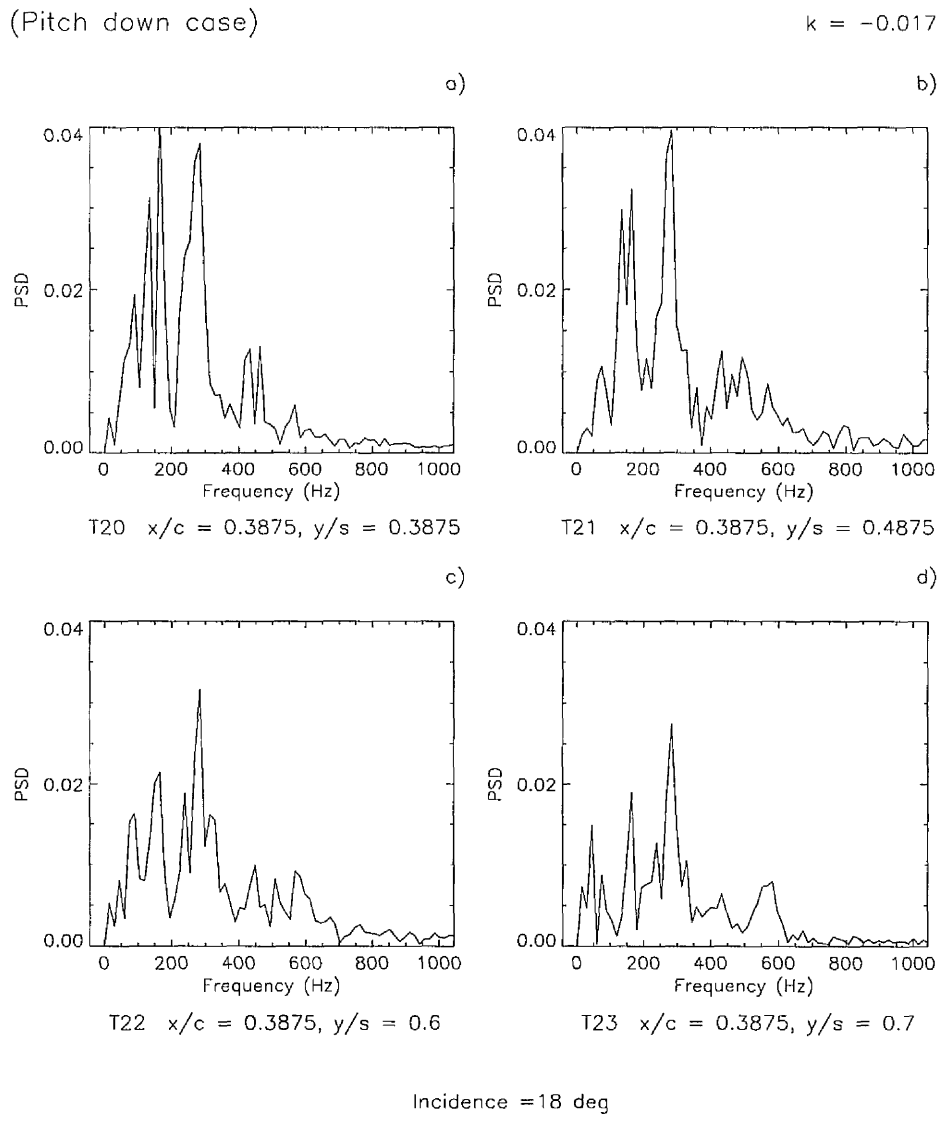

Figure 5.18 - Frequency spectra of pressure fluctuations at an incidence of 18° in the pitch down case **k = -0.017** for four transducers located at chord station **x/c = 0.3875** and span stations, y/s = 0.3875, 0.4875, 0.6 and 0.7. For each plot, **692** samples of data collected during pressure measurement tests. Re = 2.7×10^6.

Note: **bold** type denotes change of parameter from previous figure.

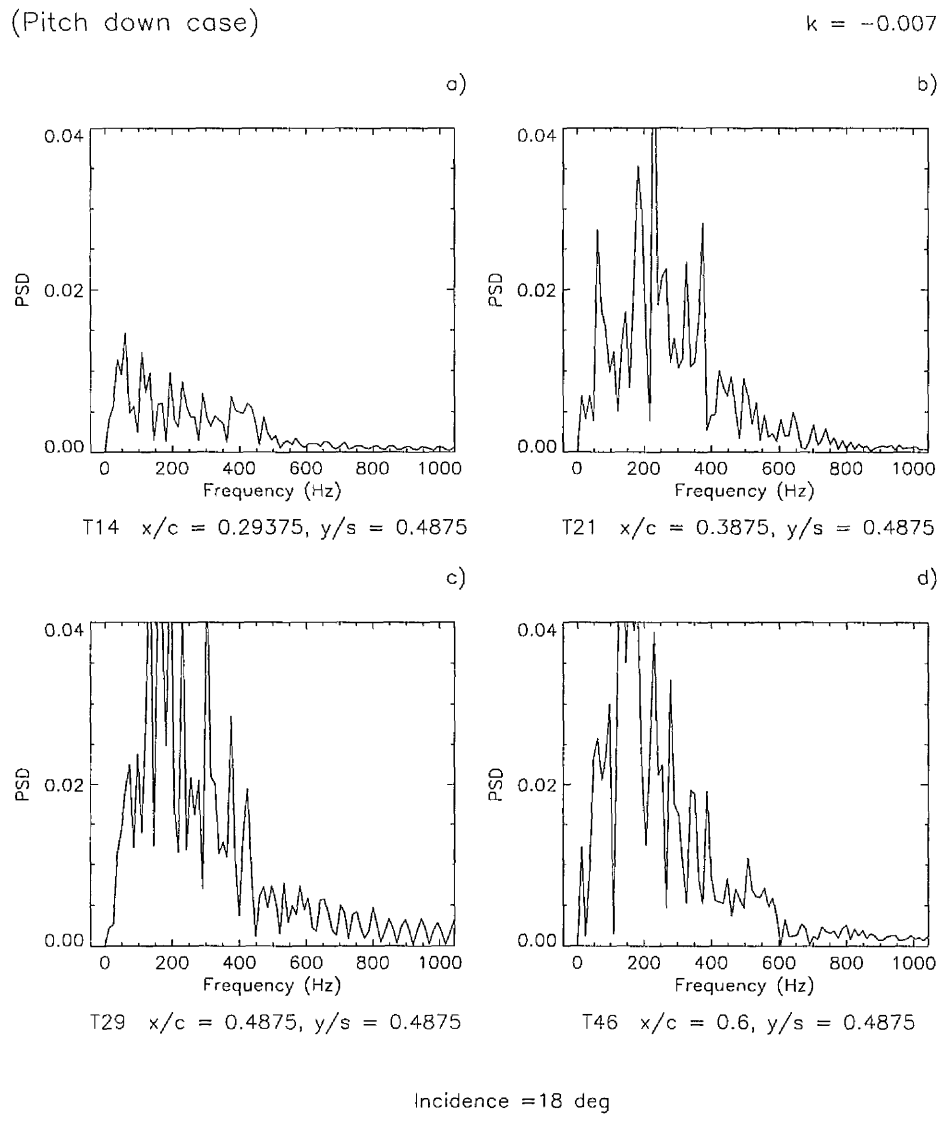

Figure 5.19 - Frequency spectra of pressure fluctuations at an incidence of 18° in the pitch down case **k = -0.007** for four transducers located at **span station y/s = 0.4875** and **chord stations, x/c = 0.29375, 0.3875, 0.4875** and **0.6**. For each plot, **445** samples of data collected during pressure measurement tests. Re = 2.7x10^6.

Note: **bold** type denotes change of parameter from previous figure.

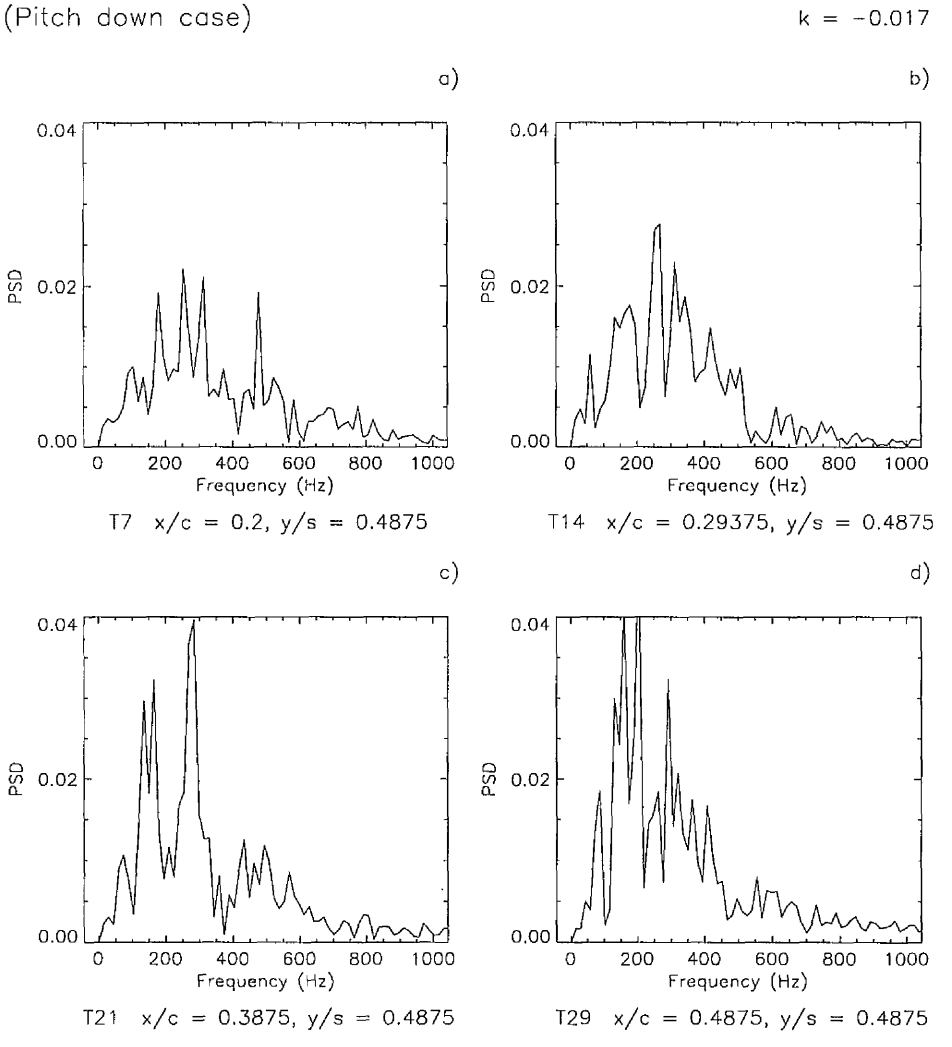

Figure 5.20 - Frequency spectra of pressure fluctuations at an incidence of 18° in the pitch down case **k = -0.017** for four transducers located at span station y/s = 0.4875 and chord stations, **x/c = 0.2, 0.29375, 0.3875** and **0.4875**. For each plot, **692** samples of data collected during pressure measurement tests. Re = 2.7×10^6.

Note: **bold** type denotes change of parameter from previous figure.

case, however, like the pitch up cases, these were measured at different chord stations from those examined in the previous figure, in this case, 0.1c further upstream, and therefore the frequencies measured cannot be directly compared with the lower magnitude pitch down case.

Like the pitch up cases, the centre of the high frequency band in the pitch down cases was found to be difficult to determine. However, results are presented for two pitch down cases which suggests that trends apparent in the data can be taken again as genuine and representative. A mean frequency value was chosen from a broad band of excitation frequencies and plotted against chord position and incidence. Figure 5.21, plot a) shows these mean frequency values in the pitch down cases as a function of chordwise position at an incidence of 18°. These are displayed together with the results from the static and pitch up cases previously shown in Figure 5.13, plot a). Figure 5.21, plot b) shows the mean frequency values for the same five cases, measured at a chord position of $x/c = 0.6$, plotted as a function of incidence. Figure 5.21 plot a) shows that for the pitch down cases, the centre of the excitation frequency band was found again to occur at a higher frequency towards the apex of the wing. The plot also shows that this frequency is generally much higher in the pitch down cases than either the static or pitch up cases. Figure 21, plot b) reveals that the value of the central excitation frequency at a given chord position is again higher in the pitch down cases than either the static or the pitch up cases. It also shows, in a similar manner to the pitch up cases, that the mean of the higher frequency band is insensitive to changes in incidence. In the pitch down cases this trend is more conclusive.

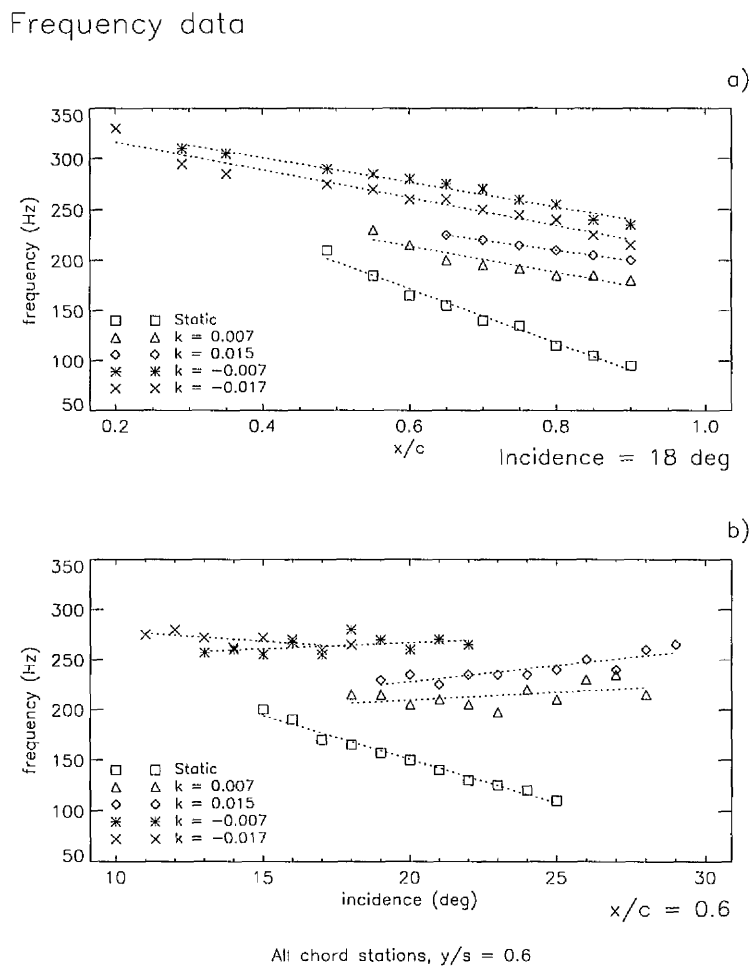

Figure 5.21 - Line plots showing the variation of central excitation frequency in static, two pitch up cases (k = 0.007 & k = 0.015) and two pitch down cases (k = -0.007 & k = -0.017) as: a) a function of chord position for an incidence of 18°. b) a function of incidence at chord station x/c = 0.6. Data collected during pressure measurement tests. Re = 2.7×10^6

5.1.4 *Frequency spectra - changes in sample window size*

For the results presented during this analysis of frequency spectra for pitch up and pitch down cases, the pressure sample window sizes, to which the FFT calculation was applied, remained constant at 1.5° for a pitch rate magnitude $|k| = 0.007$ and 2° for the pitch rate magnitudes of $|k| = 0.015/0.017$. These window sizes are similar to those used in the RMS pressure analysis. To investigate the effect of sample size variations on the frequency content, and in particular, the effect on the excitation frequency centre or mean value, a number of calculations were made using various incidence windows in pitch up and pitch down cases. Figures 5.22 to 5.25 show a series of frequency spectra for a single transducer located in the centre of the region of high RMS pressure inboard of the vortex core, labelled as (4) in Figures 4.39 and 4.42. The transducers chosen for pitch up cases, $k = 0.007$ (Figure 5.22) and $k = 0.015$ (Figure 5.23), were those positioned at span station, $y/s = 0.6$ and chord stations $x/c = 0.7$ and $x/c = 0.8$ respectively. For the pitch down cases, $k = -0.007$ (Figure 5.24) and $k = -0.017$ (Figure 5.25), the chosen transducers were located further inboard, (for reasons highlighted in the pitch down frequency analysis), at span station $y/s = 0.4875$ and chord stations, $x/c = 0.4875$ and $x/c = 0.3875$. Each figure shows frequency spectra from FFT calculations using four different window incidence sizes, such that, for the $|k| = 0.007$ cases, each plot shows an example of calculations using 1°, 1.5°, 2° and 3° incidence windows, and for the higher pitch rate cases, $|k| = 0.015/0.017$, the illustrated incidence windows were 1°, 2°, 3° and 4°. The plots as a whole show a general trend. That is, the increase in sample size increased the resolution of the frequency content and tended to reduce its overall power. However, in each case, the general form of the signal was largely unaffected and most importantly, the mean or central value of the excitation frequency band was not changed to any great degree.

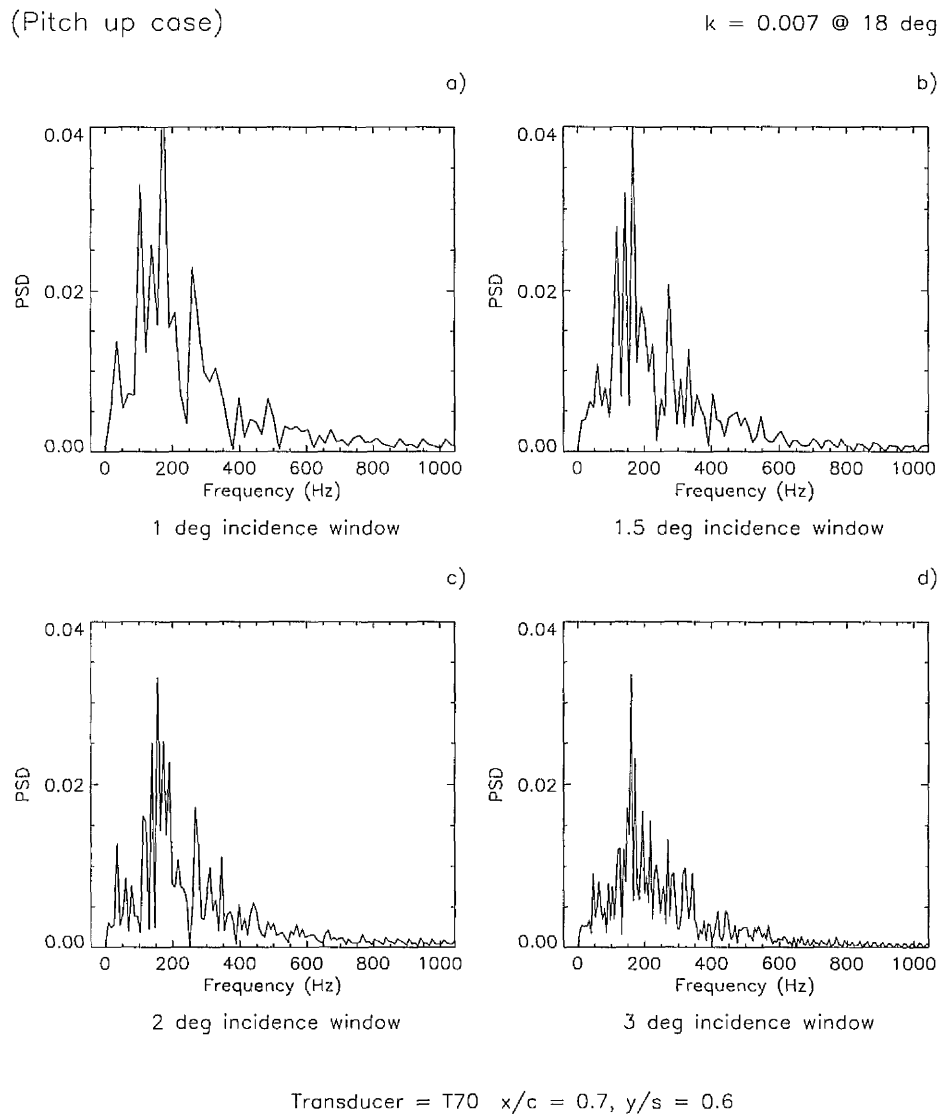

Figure 5.22 - Frequency spectra of pressure fluctuations for a single transducer located at x/c = 0.7, y/s = 0.6 at an incidence of 18° in the pitch up case k = 0.007, using incidence windows of 1° (314 samples), 1.5° (471 samples), 2° (628 samples) and 3° (942 samples). Data collected during pressure measurement tests. Re = 2.7×10^6.

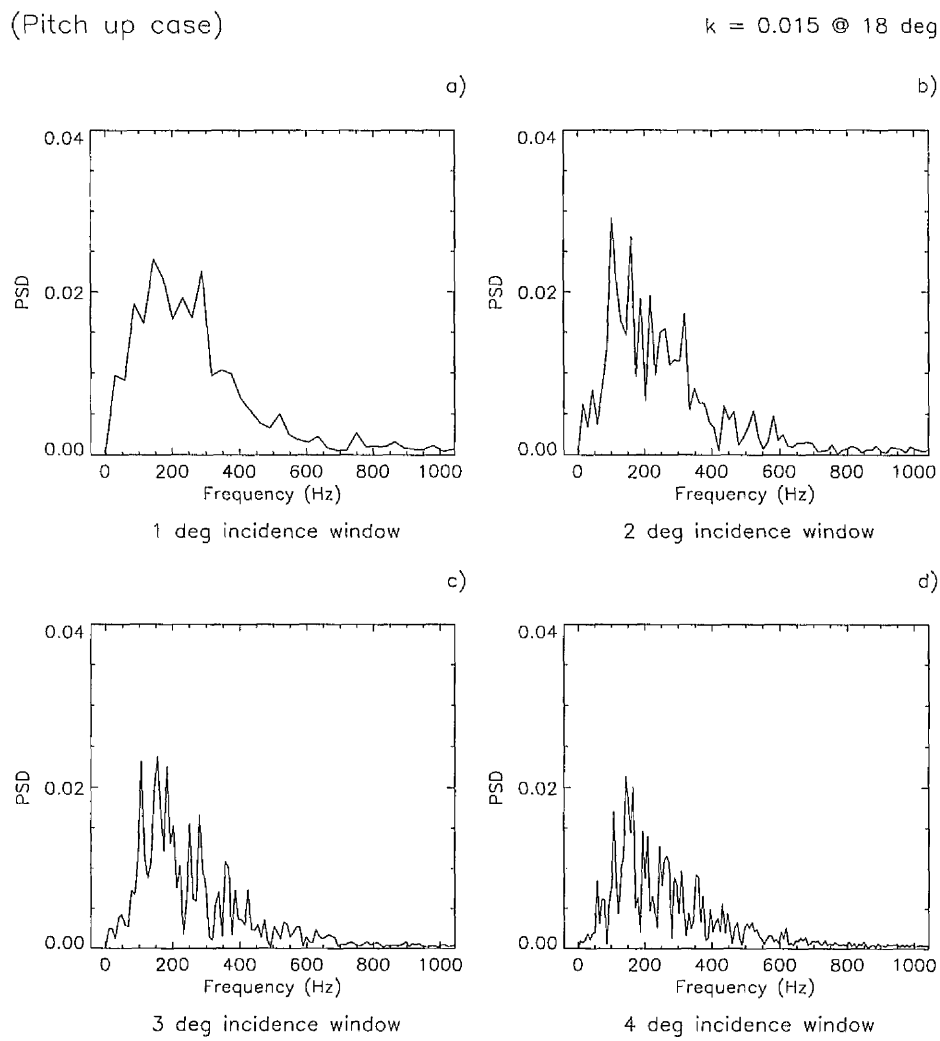

Figure 5.23 - Frequency spectra of pressure fluctuations for a single transducer located at **x/c = 0.8**, y/s = 0.6 at an incidence of 18° in the pitch up case **k = 0.015**, using incidence windows of **1°** (**362** samples), **2°** (**724** samples), **3°** (**1086** samples) and **4°** (**1448** samples). Data collected during pressure measurement tests. Re = 2.7×10^6.

Note: **bold** type denotes change of parameter from previous figure.

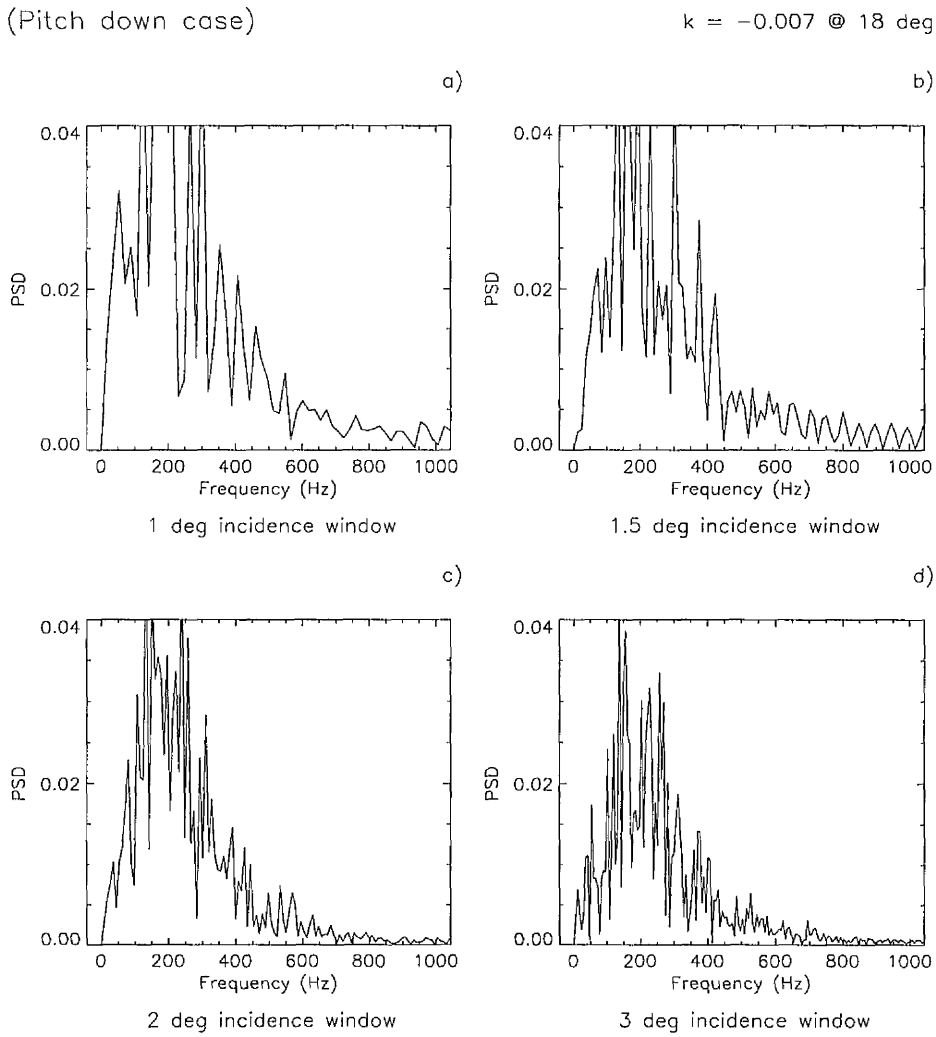

Figure 5.24 - Frequency spectra of pressure fluctuations for a single transducer located at **x/c = 0.4875, y/s = 0.4875** at an incidence of 18° in the pitch down case **k = -0.007**, using incidence windows of 1° (**296** samples), **1.5°** (**445** samples), **2°** (**592** samples) and **3°** (**890** samples). Data collected during pressure measurement tests. Re = 2.7×10^6.

Note: **bold** type denotes change of parameter from previous figure.

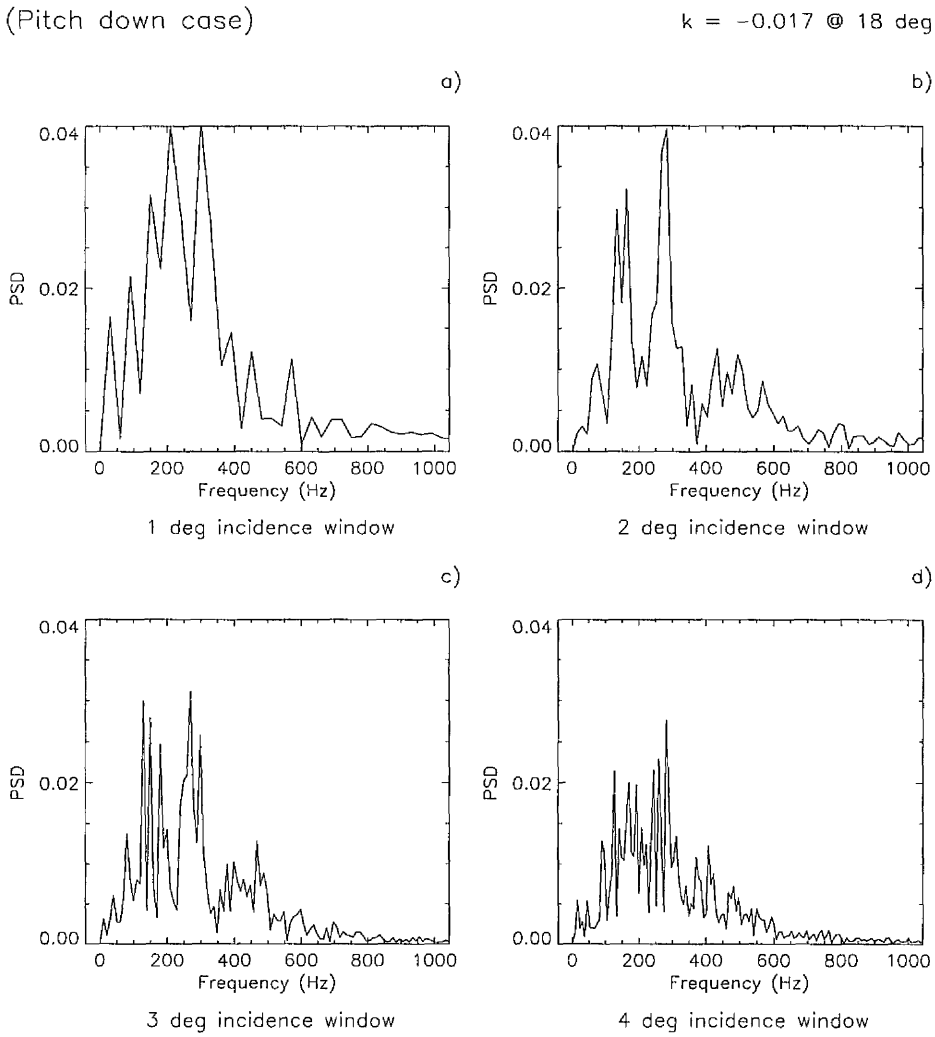

Figure 5.25 - Frequency spectra of pressure fluctuations for a single transducer located at **x/c = 0.3875**, y/s = 0.4875 at an incidence of 18° in the pitch down case **k = -0.017**, using incidence windows of **1°** (**346** samples), **2°** (**692** samples), **3°** (**1038** samples) and **4°** (**1384** samples). Data collected during pressure measurement tests. Re = 2.7×10^6.

Note: **bold** type denotes change of parameter from previous figure.

5.1.5 *Frequency spectra - changes in apex geometry*

Like the sharp-nosed static case, all frequency spectra examined for the round-nosed wing used all 2000 samples of data obtained for a given transducer at each incidence and all data were processed to remove the d.c. component prior to input into the FFT calculation. Again, no other filtering was applied. Figure 5.26 shows a series of frequency spectra for the same single transducer (at $x/c = 0.6$, $y/s = 0.6$) and at the same incidences (12°, 14°, 16° and 18°) shown for the sharp-nosed wing in Figure 5.1. At an incidence of 12° (plot a) and again at 14° (plot b), the low frequency component of around 5Hz, again, dominated the spectrum. The principle difference between the sharp and round-nosed cases at 12° incidence was in the magnitude of the low frequency spike, which was lower in the round-nosed case by as much as 30%. At 14° incidence, this trend continued and two further differences were apparent. Firstly, the excitation frequency was now very much in evidence in the round-nosed case, and secondly, the appearance of the excitation frequency seemed to have little effect on the low frequency spike magnitude which had fallen by only 14% at this incidence. In plot c) at 16° incidence, the magnitude of the low frequency component had dropped by a further 22%, compared with 50% in the sharp-nosed case over the same incidence range. At this incidence, the band of excitation frequencies have a magnitude almost twice that of the sharp-nosed wing, however, they are centred in the region of 180Hz - 200Hz which is similar to the sharp-nosed excitation frequency which, made its appearance at this incidence. This behaviour is typical of the transducers analysed in the round-nosed case, where the gradual drop in magnitude of the low frequency component occurs at a higher incidence towards the apex of the wing and the excitation frequency band appears later, closer to the apex. However, in each instance, these occur at a lower incidence than in the sharp-nosed case. In plot d) at 18° incidence, the excitation frequency band has come to dominate the frequency spectrum.

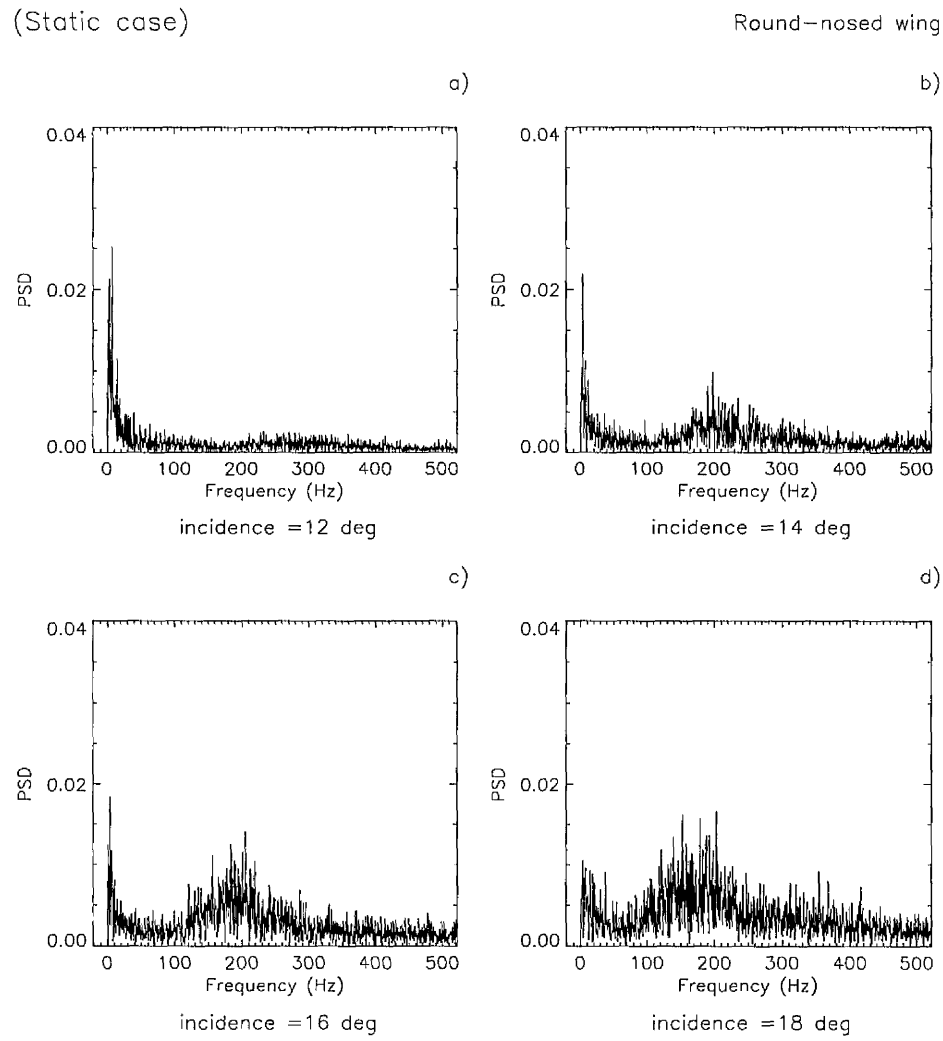

Figure 5.26 - Frequency spectra of pressure fluctuations for a single transducer located at x/c = 0.6, y/s = 0.6 at incidences of 12°, 14°, 16° and 18° in the round-nosed static case. For each plot, 2000 samples of data collected during pressure measurement tests. Re = 2.7×10^6.

Figure 5.27 illustrates the trends in the frequency data concerning the central frequency value in the round-nosed static case. Plot a) shows the variation in central frequency as a function of chord wise position at an incidence of 18° for both the sharp and round-nosed cases. Similarly, plot b) illustrates the variation of frequency with respect to incidence at a fixed chord location of x/c = 0.6, for the same two cases. It is clear from Figure 5.27, is that there is very little difference in

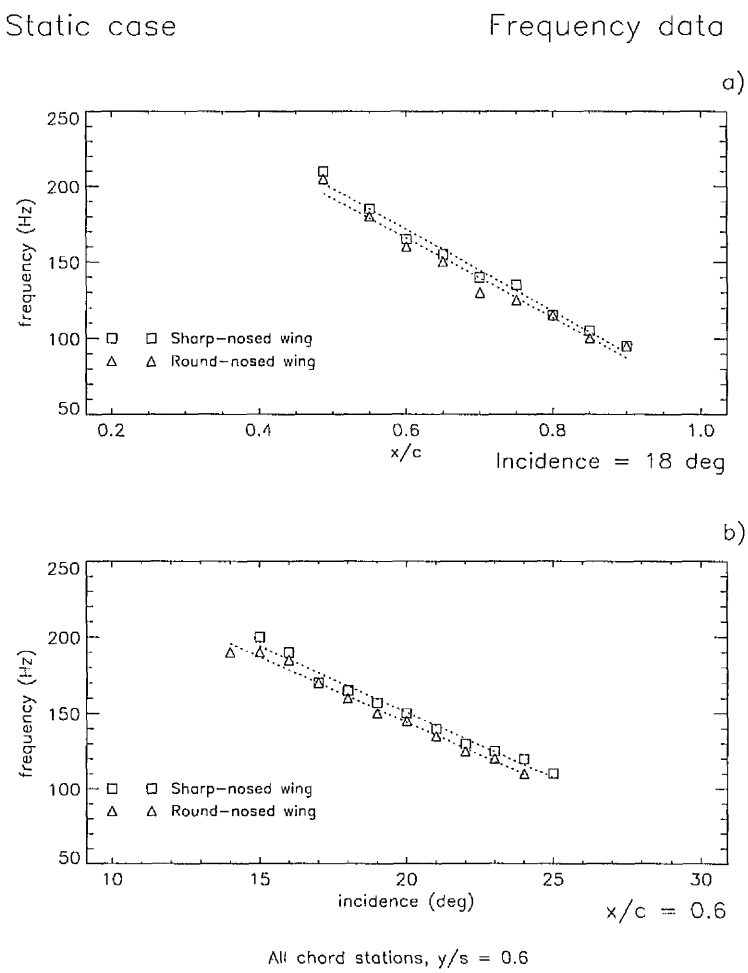

Figure 5.27 - Line plots showing the variation of central excitation frequency in sharp & round-nosed static cases as: a) a function of chord position for an incidence of 18°. b) a function of incidence at chord station x/c = 0.6. Data collected during pressure measurement tests. Re = 2.7×10^6

the values of excitation central frequency between the sharp and round-nosed static cases, such that, the non-dimensional constants identified by Mabey (1996) may also be applied to the round-nosed wing.

5.2 ANALYSIS OF THE PRESSURE SIGNAL CROSS-CORRELATION FUNCTION

The pressure signal cross-correlation function analysis programme was used to carry out a large number of cross-correlation calculations for a series of transducers on the leeward surface of the wing in static, pitch up and pitch down cases, over a range of incidences. The following section presents a selection of representative results from this analysis for a single mean or instantaneous incidence of 18°. At a given chord station downstream of vortex breakdown or vortex restoration, a 'fixed' transducer was chosen, to which other transducers across the span would be compared. This fixed transducer was located in all cases, at a spanwise location which was inboard of the centre of the region of high RMS pressure, labelled as (4) in Figures 4.39 and 4.42.

5.2.1 *Static tests*

For the static case, Figure 5.28 shows the Co-spectrum magnitude for cross-correlation calculations between transducers located at a chord station of $x/c = 0.6$. The four transducers chosen for comparison with the fixed transducer positioned at span station $y/s = 0.3875$, were located at $y/s = 0.4875$ (plot a), $y/s = 0.6$ (plot b), $y/s = 0.7$ (plot c) and $y/s = 0.8$ (plot d). Figure 5.28 reveals a dominant frequency band in the Co-spectra of pressure fluctuations centred in the region 140Hz - 200Hz, which indicates a clear correlation between a common group of frequencies in the pressure signals measured at span stations positioned progressively further outboard towards the leading-edge at a single chord station. This cross-correlation dominant frequency band compared well with the centre of the excitation frequency band, which was measured at this incidence and chord

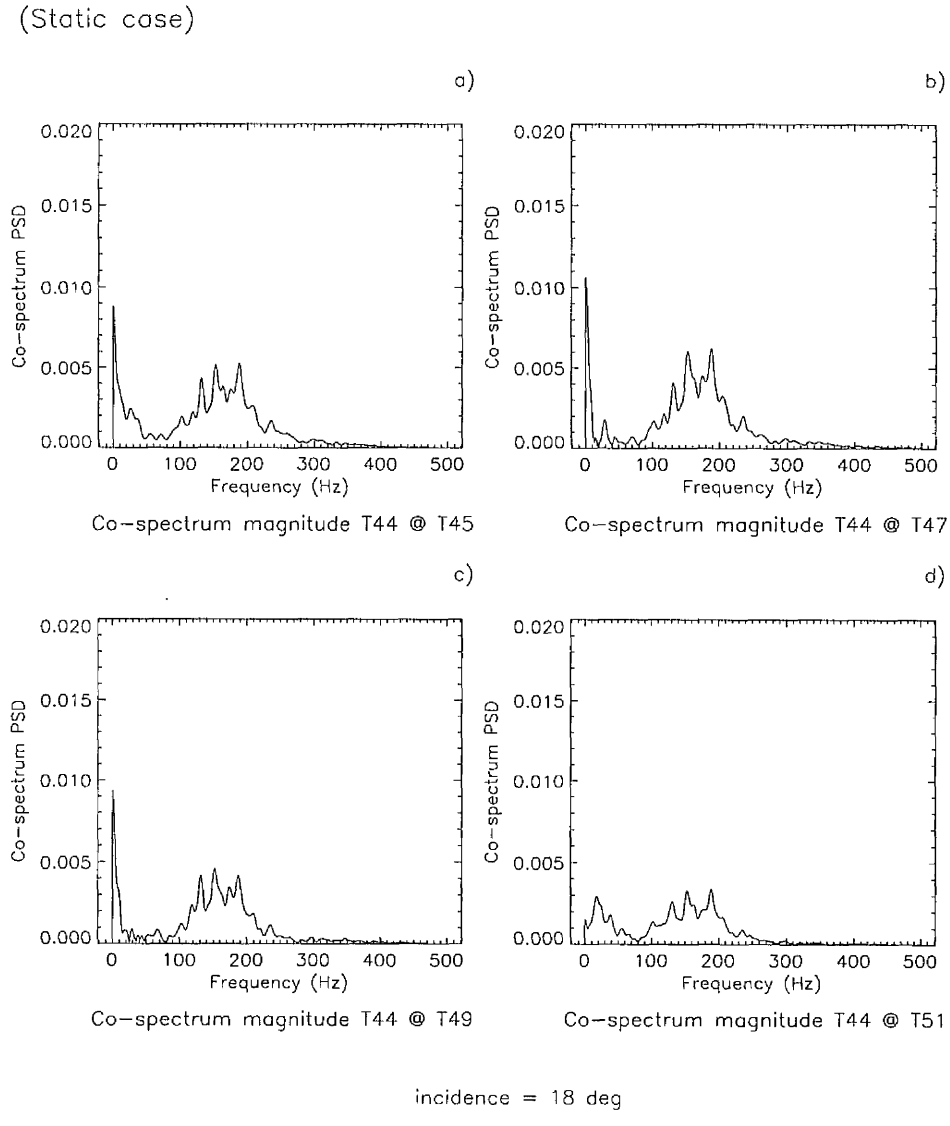

Figure 5.28 - Cross-correlation co-spectra of pressure fluctuations at an incidence of 18° in the static case between a fixed transducer T44 @ y/s = 0.3875 and four transducers across the span: T45 @ y/s = 0.4875, T47 @ y/s = 0.6, T49 @ y/s = 0.7 and T51 @ y/s = 0.8. All transducers at chord station x/c = 0.6. 2000 samples of data collected during pressure measurement tests. Re 2.7×10^6.

position in the single point frequency analysis, in the region 180Hz - 200Hz. Similarly, each dominant frequency in the cross-spectrum analysis displayed a tendency which saw the highest co-spectrum magnitude in the centre of the region of high RMS pressure inboard of the vortex core.

Figures 5.29 and 5.30 show two further static case sets of co-spectra for transducers at similar spanwise positions but located at $x/c = 0.7$ and $x/c = 0.8$ respectively. Figure 5.29 reveals, that at a chord station of $x/c = 0.7$, a dominant frequency band was again apparent, but this time centred in the region 125Hz - 160Hz. At $x/c = 0.8$, shown in Figure 5.30, a similar feature was centred in the region 110Hz - 140Hz. Both figures again showed good agreement with the single point analyses at the same incidence and chord location. The pattern of co-spectrum magnitude across the span which was seen at $x/c = 0.6$, was again observed at these chord stations. The trend apparent in the data, from chord station to chord station, saw a decrease in centre dominant frequency value and an increase in co-spectrum magnitude, as distance from the wing apex increased.

Figure 5.31 summarises the findings of the static case cross-correlation analysis at 18° incidence for the three chord stations $x/c = 0.6$, $x/c = 0.7$ and $x/c = 0.8$. Plot a) shows the co-spectrum dominant frequency band centre as a function of spanwise position, for each chord station case. Plot b) shows the corresponding quadrature-spectrum phase angle for the central frequencies shown in plot a). The figure shows a number of trends that were also observed for other transducer combinations and at other incidences. Plot a) shows two trends. Firstly, the co-spectrum dominant frequency is almost constant across the wing in a spanwise direction, and secondly, it tends to increase with upstream progression towards the apex of the wing. Plot b) however, shows three very different trends. Firstly, there was very little variation in phase lag measurements from chord station to chord station. Secondly, there was a steadily increasing phase lag between the

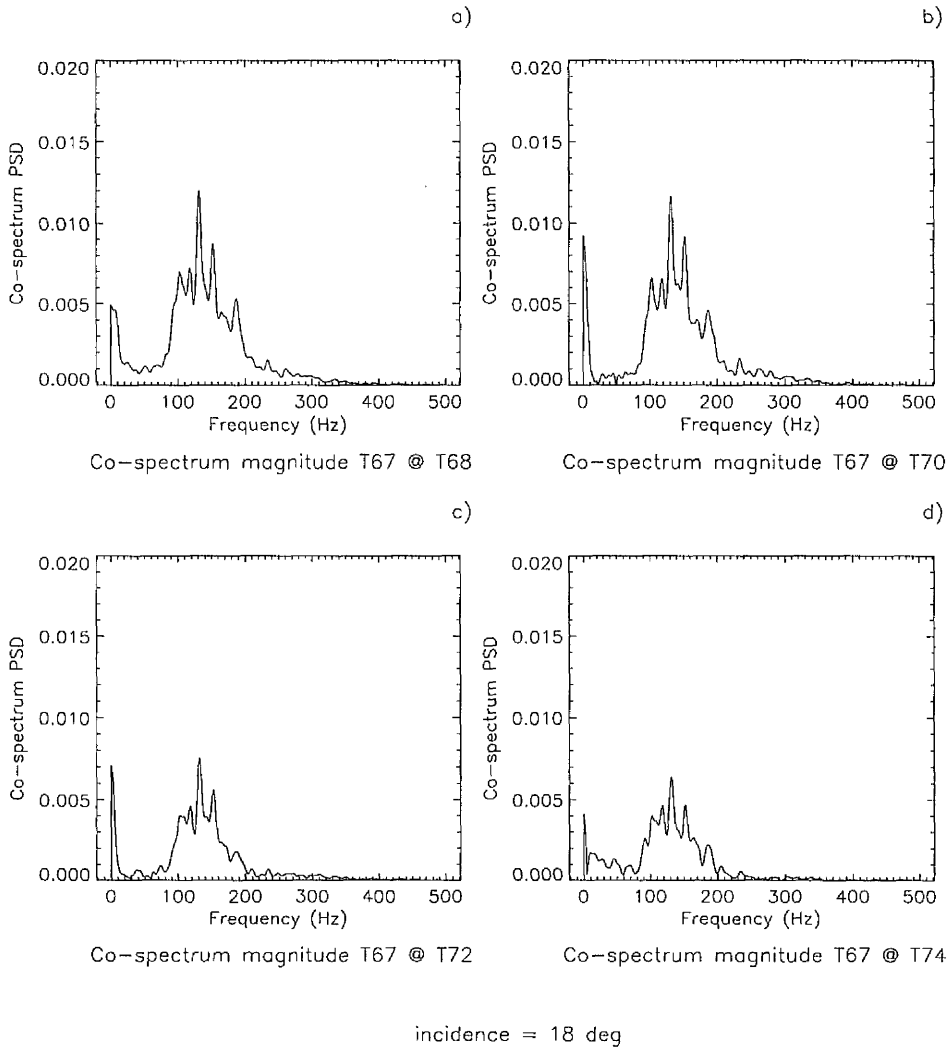

Figure 5.29 - Cross-correlation co-spectra of pressure fluctuations at an incidence of 18° in the static case between a fixed transducer **T67** @ y/s = 0.3875 and four transducers across the span: **T68** @ y/s = 0.4875, **T70** @ y/s = 0.6, **T72** @ y/s = 0.7 and **T74** @ y/s = 0.8. All transducers at chord station **x/c = 0.7**. 2000 samples of data collected during pressure measurement tests. Re 2.7×10^6.

Note: **bold** type denotes change of parameter from Figure 5.28.

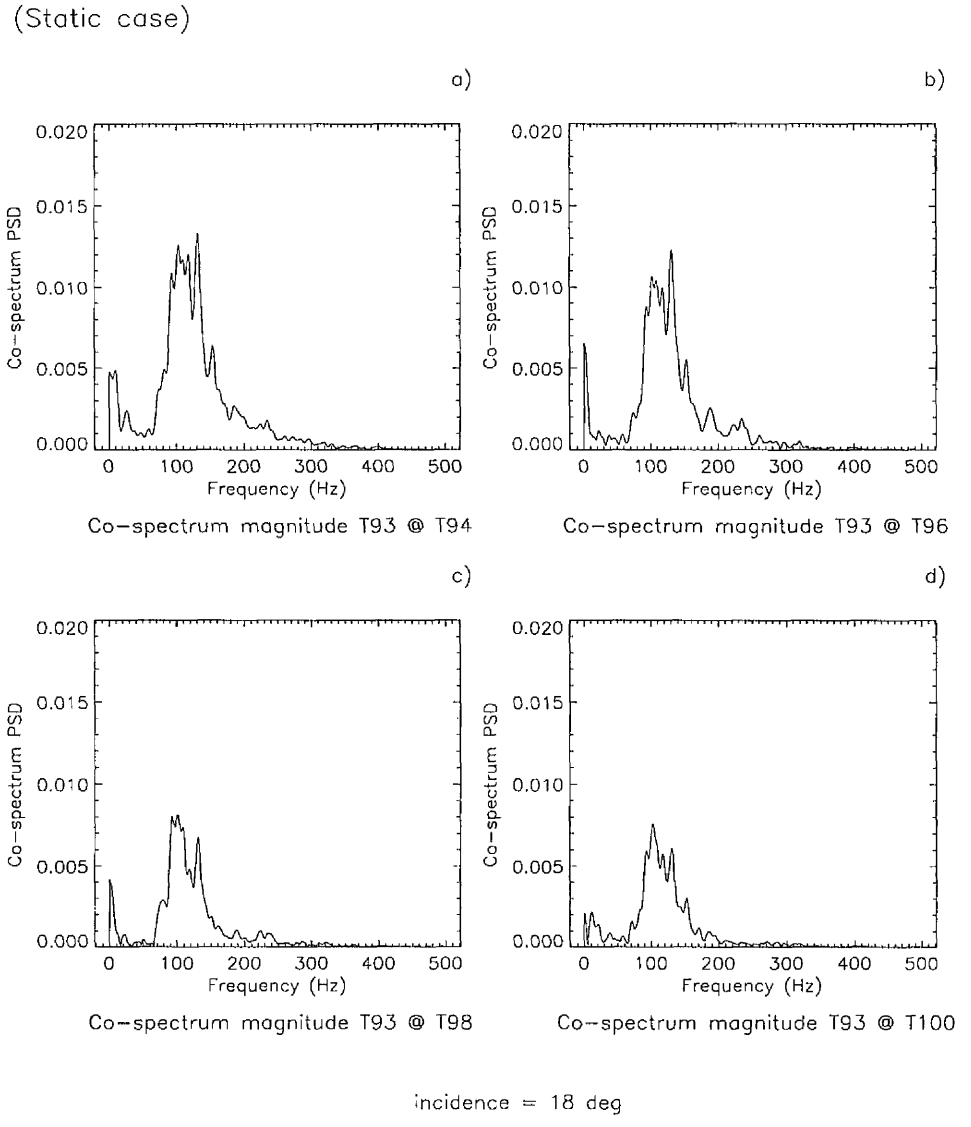

Figure 5.30 - Cross-correlation co-spectra of pressure fluctuations at an incidence of 18° in the static case between a fixed transducer **T93** @ y/s = 0.3875 and four transducers across the span: **T94** @ y/s = 0.4875, **T96** @ y/s = 0.6, **T98** @ y/s = 0.7 and **T100** @ y/s = 0.8. All transducers at chord station **x/c = 0.8**. 2000 samples of data collected during pressure measurement tests. Re 2.7×10^6.

Note: **bold** type denotes change of parameter from Figure 5.29.

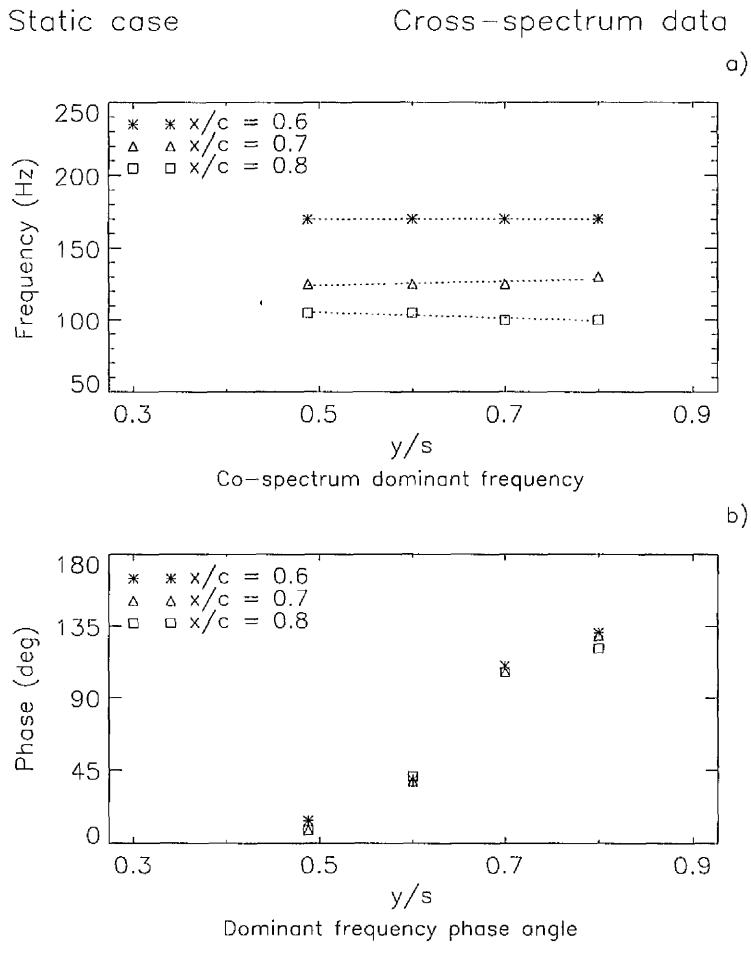

Figure 5.31 - Line plots showing the variation, at 18° incidence, in the static case, of a) the central cross-correlation dominant frequency and b) the central cross-correlation dominant frequency phase lag angle, each wrt spanwise position, for transducers located at three chordwise locations x/c = 0.6, 0.7 and 0.8. Data collected during pressure measurement tests. Re = 2.7×10^6.

pressure signals at the fixed transducer and successive transducers in an outboard direction. Gursul (1994), who observed a similar trend in his results, noted that this was indicative of the convection velocity of the flow underneath the vortex

in an outboard direction towards the leading-edge of the wing. It should also be noted that this implies that the flow field disturbances causing the pressure fluctuations were also travelling in the same direction. Thirdly, the plot reveals that this increase in phase angle from transducers located near the fixed transducer to those further outboard is not linear. At each chord station, there was seen a rapid increase in phase lag between the fixed transducer at y/s = 0.3875, and those located at y/s = 0.6 and subsequently at y/s = 0.7. This rapid increase over a short spanwise distance was followed by a much smaller increase in phase lag between y/s = 0.7 and y/s = 0.8.

5.2.2 *CCF analysis - pitch up tests*

It was shown in section 3.5 that the sample size index number, input into the FORTRAN library routine to calculate the FFT and cross-correlation functions, was limited by its prime factors, in that both the number of factors and their maximum value was restricted to 19. In order to carry out these calculations in either pitch up case at an incidence of 18°, this caused a problem. The 'natural' number of samples at this incidence, in the k= 0.007 case using a 1.5° incidence window, was 471 This has prime factors of 3, and 157 only. Similarly in the k = 0.015 case, using a 2° incidence window, the number of samples was 724 (prime factors = 2 (twice) and 181). In order to satisfy the input criterion, the respective sample sizes were increased to 475 (prime factors = 5 (twice) and 19) and 726, (prime factors = 2, 3 and 11 (twice)), by adding extra zeros to the input file prior to the FFT calculation described in Section 3.5.

Figures 5.32 and 5.33 show pitch up data sets of co-spectra for transducers located at x/c = 0.7, in the cases, k = 0.007 and k = 0.015 respectively. The spanwise locations of the fixed transducer and those to which it was compared, are the same transducers shown in the static case at the same chord station. Figure 5.32 reveals, that in the k = 0.007 case, a dominant frequency band was again

apparent in each plot but this time centred in the region 140Hz - 200Hz. In the k = 0.015 case, shown in Figure 5.33, a large cross-correlation frequency spike was centred in the narrow region 160Hz - 170Hz. Both figures again showed good agreement with the single point analyses for the same cases, at the same incidence and chord location. The spanwise pattern of co-spectrum magnitude seen in the static case, and in the respective pitch up single-point analyses, was again observed in the co-spectra at this chord station in both cases. The trend apparent in the data over the range of chord stations examined again saw a decrease in centre dominant frequency value and an increase in co-spectrum magnitude, as distance from the wing apex increased.

Figure 5.34, plot a) shows the co-spectrum dominant frequency band centre as a function of spanwise position, for the static and two pitch up cases (k = 0.007 and k = 0.015) at a chord station of x/c = 0.7 and an incidence of 18°. Like Figure 5.31, plot b) shows the corresponding quadrature-spectrum phase angle for the central frequencies shown in plot a). Plot a) shows that the co-spectrum dominant frequency is again, almost constant across the wing in a spanwise direction for each pitch rate. However, it tends to increase with an increase in pitch rate magnitude. Plot b) shows that the trends apparent in the spanwise distribution of phase measurements for the static case is also apparent for the pitch up cases, i.e., for each pitch up case, there was seen a rapid increase in phase lag between the fixed transducer at y/s = 0.3875, and those located at y/s = 0.6 and subsequently at y/s = 0.7. This rapid increase over a short spanwise distance was followed by a much smaller increase in phase lag between y/s = 0.7 and y/s = 0.8.

5.2.3 *CCF analysis - pitch down tests*

Like their counterparts in the pitch up tests, the sample size index number of each pitch down case fed into the FFT and cross-correlation calculations, suffered from the perennial problem of prime factor criterion failure. For the k = -0.007

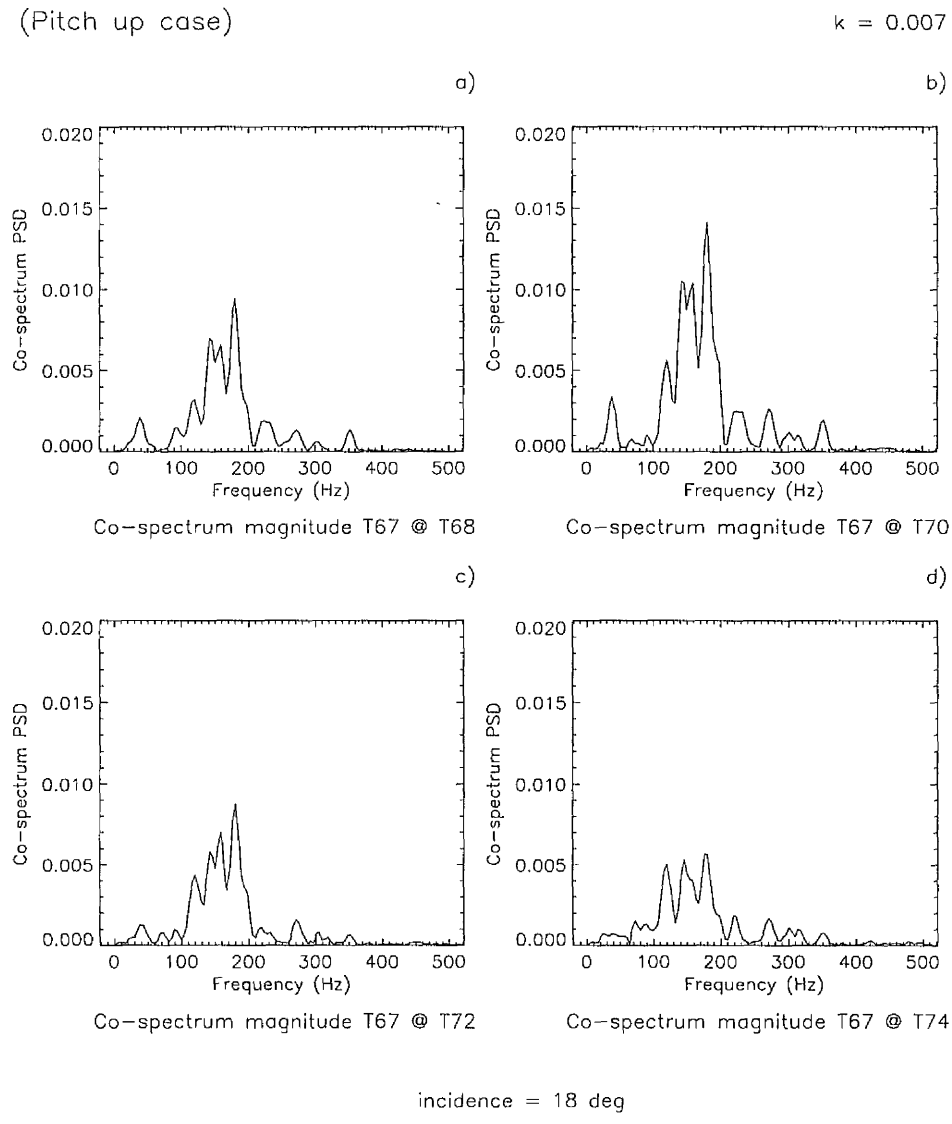

Figure 5.32 - Cross-correlation co-spectra of pressure fluctuations at an incidence of 18° in the pitch up case k = 0.007 between a fixed transducer T67 @ y/s = 0.3875 and four transducers across the span: T68 @ y/s = 0.4875, T70 @ y/s = 0.6, T72 @ y/s = 0.7 and T74 @ y/s = 0.8. All transducers at chord station x/c = 0.7. 475 samples of data collected during pressure measurement tests. Re 2.7×10^6.

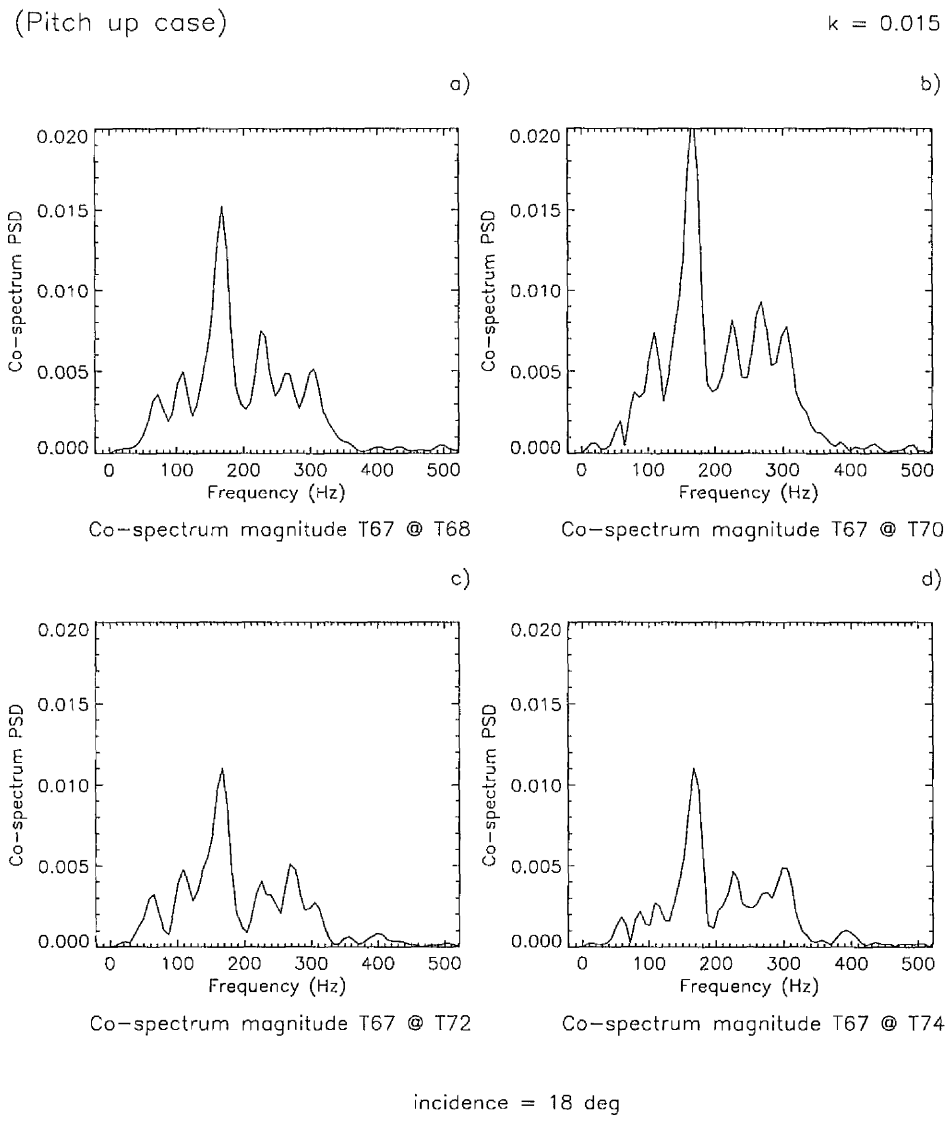

Figure 5.33 - Cross-correlation co-spectra of pressure fluctuations at an incidence of 18° in the pitch up case **k = 0.015** between a fixed transducer T67 @ y/s = 0.3875 and four transducers across the span: T68 @ y/s = 0.4875, T70 @ y/s = 0.6, T72 @ y/s = 0.7 and T74 @ y/s = 0.8. All transducers at chord station x/c = 0.7. **726** samples of data collected during pressure measurement tests. Re 2.7×10^6.

Note: **bold** type denotes change of parameter from Figure 5.32.

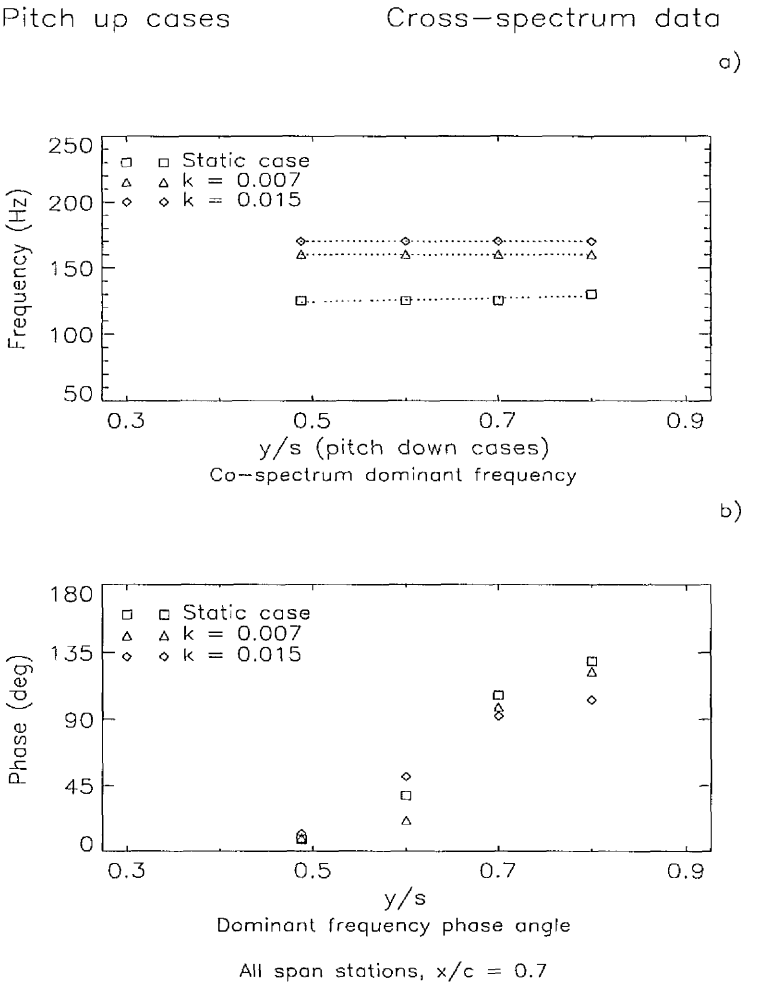

Figure 5.34 - Line plots showing the variation, at 18° incidence, in the static and two pitch up cases (k = 0.007 & k = 0.015), of a) the central cross-correlation dominant frequency and b) the central cross-correlation dominant frequency phase lag angle, each wrt spanwise position, for transducers located at a chordwise location of x/c = 0.7. Data collected during pressure measurement tests. Re = 2.7×10^6.

case using a 1.5° incidence window, the number of natural samples was 445 (prime factors = 5 and 89 only). This was solved by adding 3 zeros to make a

sample size of 448 (prime factors = 2 (6 times) and 7). Similarly, In the k = -0.017 case, an incidence window of 2° resulted in a sample count of 692, i.e., prime factors = 2 (twice) and 173. This was corrected by increasing the sample to 700 (prime factors = 2 (twice), 5 (twice) and 7).

Figures 5.35 and 5.36 show sets of co-spectra, for transducers located at x/c = 0.6, in the pitch down cases, k = -0.007 and k = -0.017 respectively. The spanwise locations of the fixed and subject transducers, chosen for the pitch down cross-correlation analysis, were positioned further inboard than those in the static and pitch up cases. Like the single point analysis, these were chosen to reflect the spanwise position of the region of high RMS pressure, Figure 4.43, label (4) seen in the RMS pressure analysis, at this incidence. The fixed transducer was located at y/s = 0.2 inboard of the centre of high RMS pressure, whilst the cross-correlation subject transducers were located at y/s = 0.3875 (plot a), y/s = 0.4875, (plot b), y/s = 0.6 (plot c) and y/s = 0.7 (plot d). Figure 5.35 reveals, that in the k = -0.007 case, a dominant frequency band was again apparent in each plot but this time centred in the region 250Hz - 350Hz. In the k = -0.017 case, shown in Figure 5.36, a large cross-correlation frequency spike was centred in the narrow region 260Hz - 300Hz. Like the static and pitch up cases, both pitch down cases showed good agreement with the single point analyses at the same incidence and chord location. The spanwise pattern of co-spectrum magnitude seen in the static and pitch up cases, and in the respective pitch down single-point analyses, was again observed in the co-spectra at this chord station in both cases. Similarly, the trend apparent in the data over the range of chord stations examined again saw a decrease in centre dominant frequency value and an increase in co-spectrum magnitude, as distance from the wing apex increased.

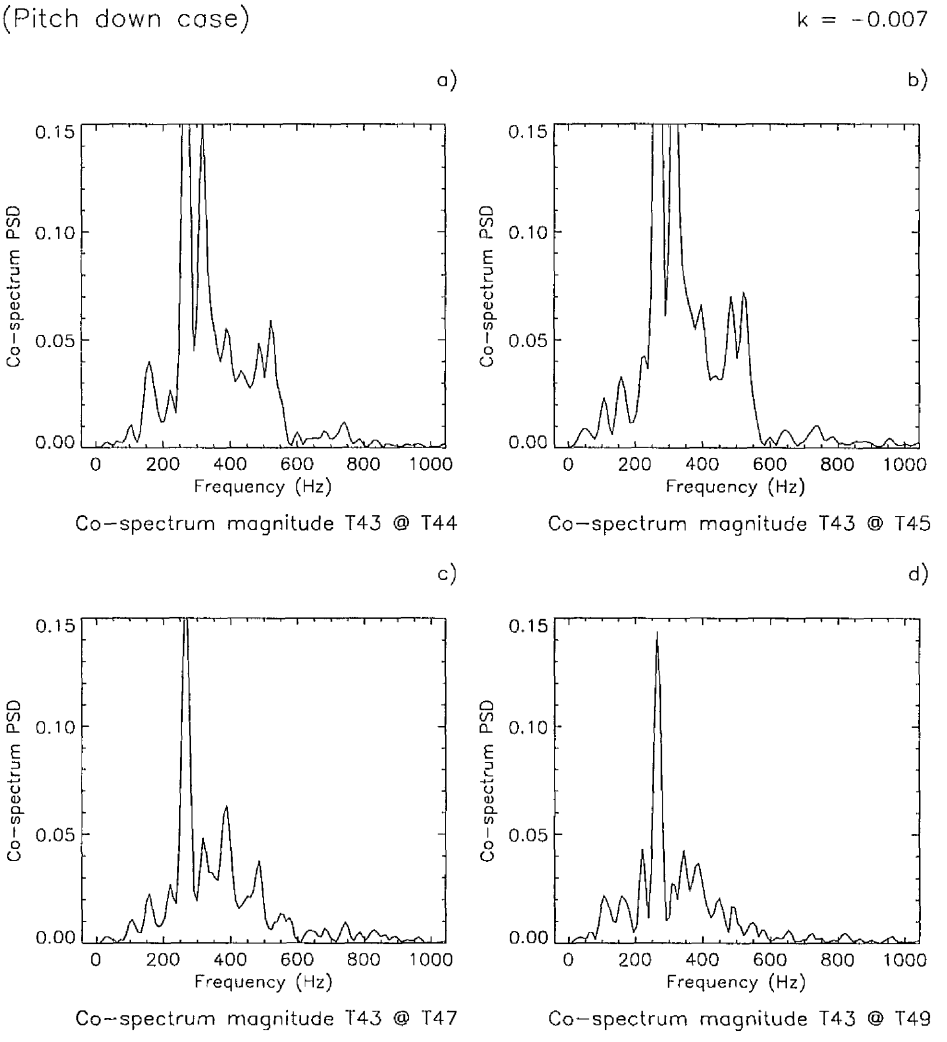

Figure 5.35 - Cross-correlation co-spectra of pressure fluctuations at an incidence of 18° in the pitch down case k = -0.007 between a fixed transducer T43 @ y/s = 0.2 and four transducers across the span: T44 @ y/s = 0.3875, T45 @ y/s = 0.4875, T47 @ y/s = 0.6 and T49 @ y/s = 0.7. All transducers at chord station x/c = 0.6. 448 samples of data collected during pressure measurement tests. Re 2.7×10^6.

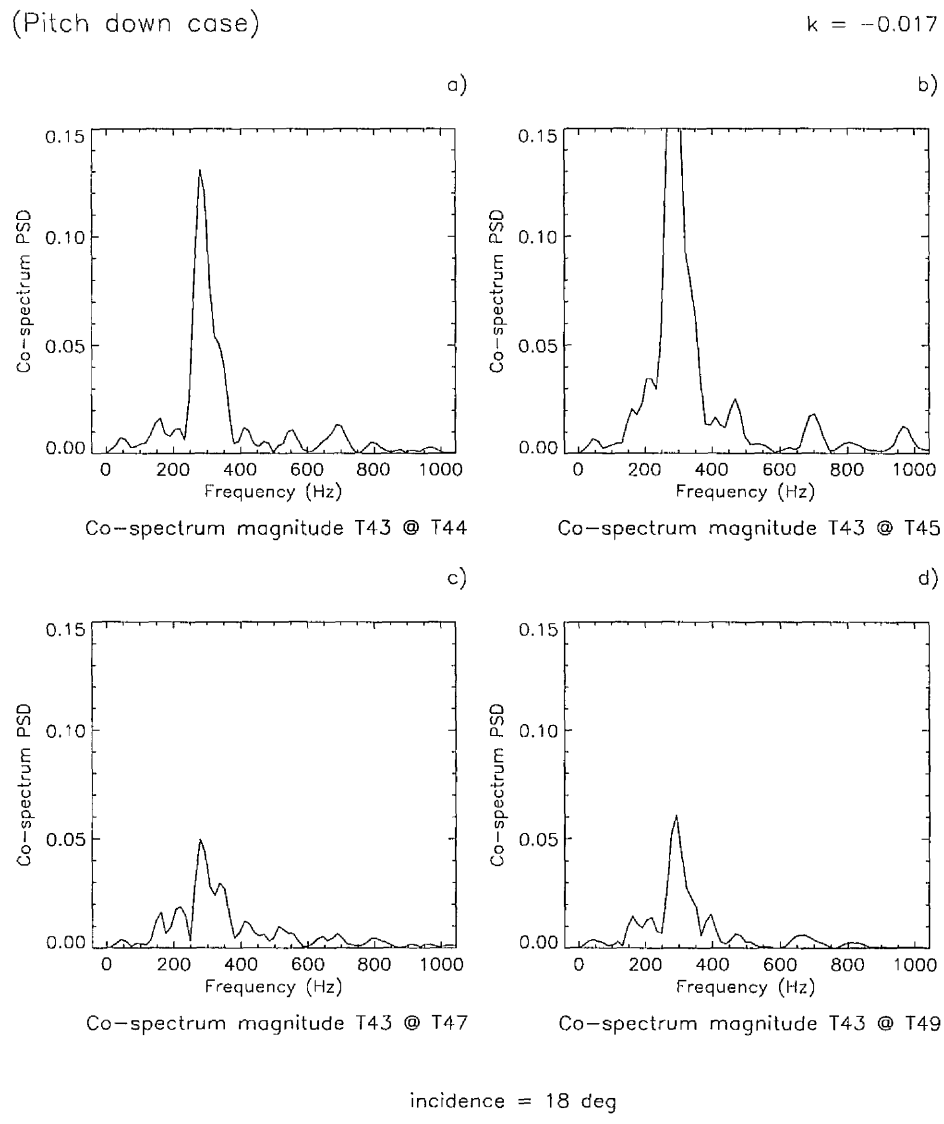

Figure 5.36 - Cross-correlation co-spectra of pressure fluctuations at an incidence of 18° in the pitch down case **k = -0.017** between a fixed transducer T43 @ y/s = 0.2 and four transducers across the span: T44 @ y/s = 0.3875, T45 @ y/s = 0.4875, T47 @ y/s = 0.6 and T49 @ y/s = 0.7. All transducers at chord station x/c = 0.6. **700** samples of data collected during pressure measurement tests. Re 2.7×10^6.

Note: **bold** type denotes change of parameter from Figure 5.35.

Figure 5.37, plot a) shows the co-spectrum dominant frequency band centre as a function of spanwise position, for the static and two pitch down cases (k = -0.007 and k = -0.017) at a chord station of x/c = 0.6 and an incidence of 18°. To enable the comparison of static and pitch down case plots at different spanwise stations, a second x-axis has been added at the top of the diagram, which has been spanwise shifted outboard with respect to the bottom axis and along which, the static case span positions are plotted. Plot b) shows the corresponding quadrature-spectrum phase angle for the central frequencies using the same x-axis convention. Figure 5.37 shows similar trends to those seen in Figure 5.34. Plot a) shows that the co-spectrum dominant frequency is again, almost constant across the wing in a spanwise direction for each pitch rate, and like the pitch up cases, it tends to increase with an increase in pitch rate magnitude. By comparing Figure 5.37, plot a) with the corresponding plot in Figure 5.34, it is evident that the cross-correlation dominant frequencies in the pitch down cases are higher than those observed in the pitch up cases, with a trend in both pitch up and pitch down, which suggests an increase in dominant frequency with an increase in pitch rate magnitude. Plot b) however, shows that there are significant variations in phase lag measurements with an increase in pitch rate magnitude, although the trends apparent in the static and pitch up cases with regard to the spanwise distribution of phase lag measurements are again apparent in both pitch down cases. This spanwise zone of rapid phase lag increase, in static and all pitching cases, corresponded to a transition from the centre of the region of high RMS pressure to a position underneath the vortex core centreline. The difference in the spanwise position of this zone in the static/pitch up and the pitch down cases, reflected the relative positions of these surface pressure features as indicated by the mean/instantaneous pressure and RMS pressure analyses.

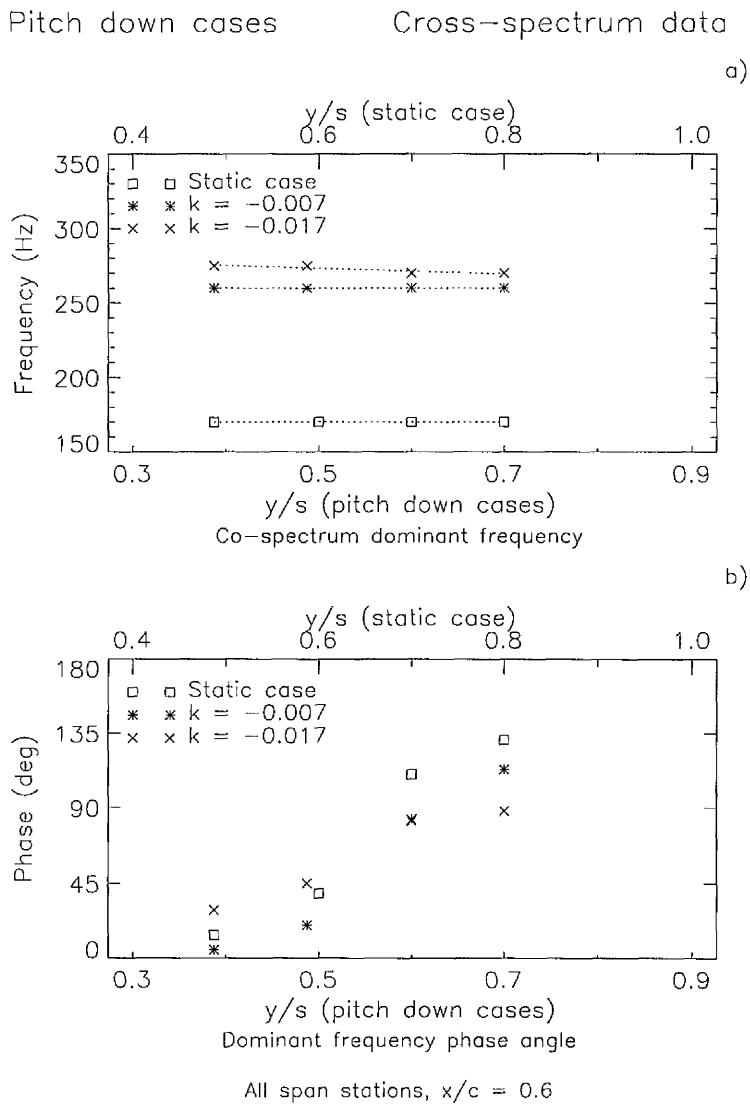

Figure 5.37 - Line plots showing the variation, at 18° incidence, in the static and two pitch down cases (k = -0.007 & k = -0.017), of a) the central cross-correlation dominant frequency and b) the central cross-correlation dominant frequency phase lag, each wrt spanwise position, for transducers located at a chordwise location of x/c = 0.6. Data collected during pressure measurement tests. Re = 2.7×10^6.

5.2.4 *CCF analysis - changes in apex geometry*

Like the sharp-nosed static case, all cross-correlation calculations for the round-nosed wing used all 2000 samples of data obtained for a given transducer at each incidence. Figures 5.38 shows sets of co-spectra for transducers located at $x/c = 0.7$, in the sharp-nosed static cases (plots a and b) and round-nosed static cases (plots c and d). The fixed transducer in each case was located at $y/s = 0.3875$, and the subject transducers were positioned at $y/s = 0.4875$ and $y/s = 0.6$ respectively. Figure 5.38 shows that the round-nosed case cross-correlation dominant frequency was centred in the region 110Hz - 130Hz, which was slightly lower than its sharp-nosed counterpart, however, the magnitude of this central frequency was significantly higher in the round-nosed case. These trends were typical for all transducer combinations and all incidences analysed.

Figure 5.39, plots a) and b) show the co-spectrum dominant frequency band centre as a function of spanwise position and the corresponding quadrature-spectrum phase lag measurements respectively, for the sharp and round-nosed static cases at a chord station of $x/c = 0.7$ and an incidence of 18°. Like all cases previously described, plot a) shows for the round-nosed static case, that the value of the cross-correlation central dominant frequency was largely constant across the span of the wing. What is also clearly shown is the slight decrease in central frequency from sharp nose to round. Similarly, plot b) shows that the spanwise trend in phase lag increase with distance from the fixed transducer was again apparent in the round-nosed case.

With the effect of changes in apex geometry, this concludes the presentation of results. Chapter 6 offers a discussion of the findings of Chapter 4 and Chapter 5 so that conclusions may be drawn.

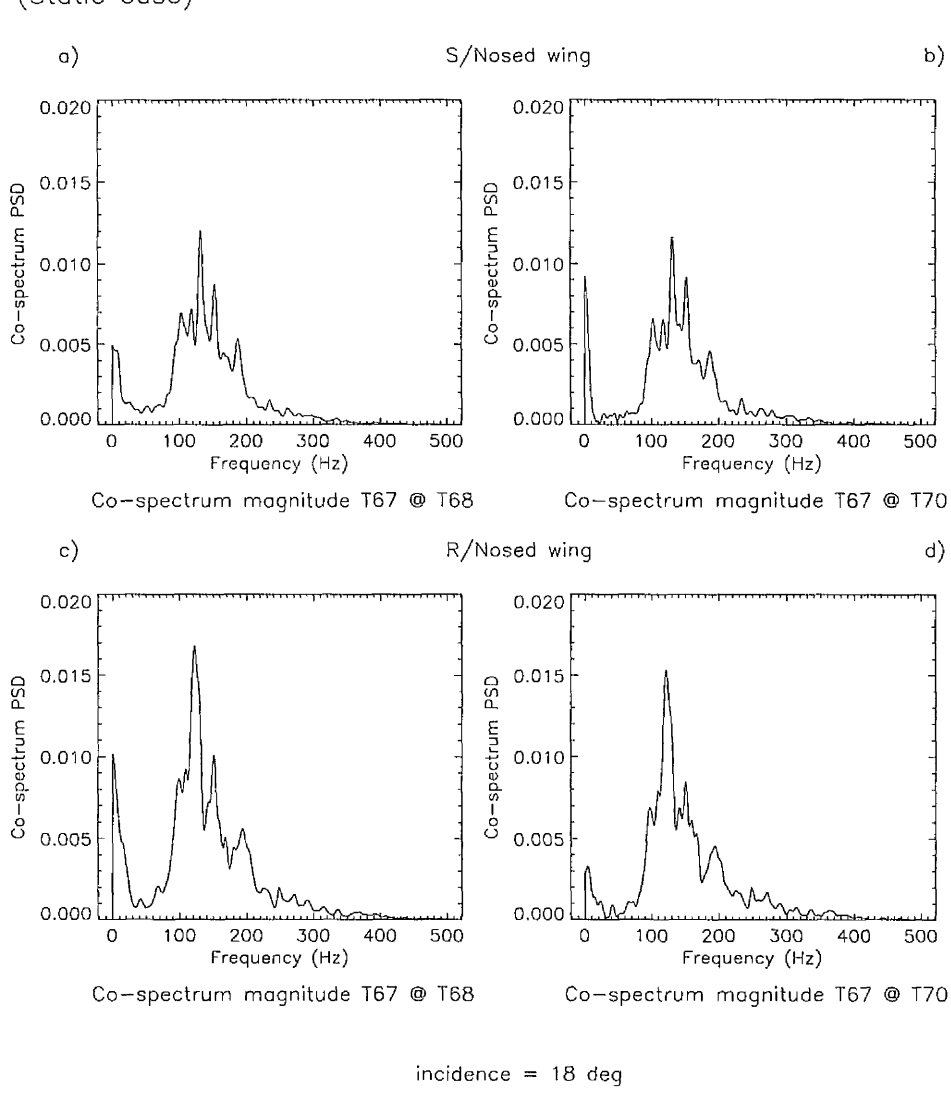

Figure 5.38 - Cross-correlation co-spectra of pressure fluctuations at an incidence of 18° in the sharp and round-nosed static cases between a fixed transducer T67 @ y/s = 0.3875 and two transducers across the span: T68 @ y/s = 0.4875 and T70 @ y/s = 0.6. All transducers at chord station x/c = 0.7. 2000 samples of data collected during pressure measurement tests. Re 2.7×10^6.

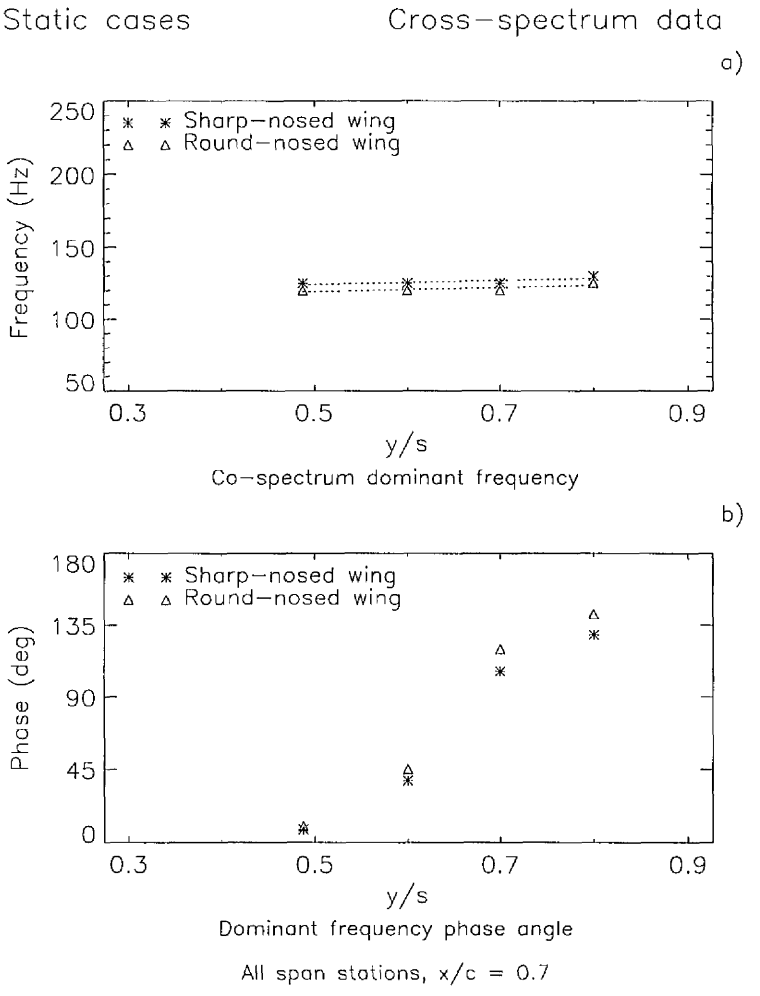

Figure 5.39 - Line plots showing the variation, at 18° incidence, in the sharp and round-nosed static cases of a) the central cross- correlation dominant frequency and b) the central cross-correlation dominant frequency phase lag, each wrt spanwise position, for transducers located at a chordwise location of x/c = 0.7. Data collected during pressure measurement tests. Re = 2.7×10^6.

Chapter 6

6. DISCUSSION

For the 60° wing tested in this study, the results of the mean and instantaneous C_P distribution analyses have been successful in determining the position of the primary vortex core and its growth during pitching motions. It is however, very difficult to pick out other significant features of the flow structure from these data alone. One example is the secondary vortex, whose presence is not discernible in either the static or pitching cases. This observation is supported by the smoke tunnel visualisation tests. These revealed only a small rotational component of velocity in the secondary vortex structure across the range of pitch rates. Similarly, it is not possible to detect the arrival of vortex breakdown over the trailing-edge of the wing. This is partly due to the inability of the analysis method to describe flowfield phenomena of a temporal nature and partly due to a departure from a purely 'conical' flow structure. Gursul (1994) and others have showed vortex breakdown to be characterised by a highly fluctuating component in the pressure signal, which does not necessarily affect its mean value in the long term. This means that an analysis method that can only detect changes in mean pressure values is likely to be ineffective in establishing the upstream movement of vortex breakdown over the wing surface. Similarly, a number of flow visualisation studies, notably, Parker (1977), Lowson (1991) and the smoke visualisations tests carried out in this study, have shown that the vortex inner core, where the axial velocity of the flow is at its highest and which acts as the principal source of the high suction ridge, lifts further and further away from the wing surface with downstream progression along the wing. This is a departure from the conical flow structure, which was first observed by Hall (1961), and is caused by the

continuous feeding of vorticity into the vortex along the entire length of the leading-edge. Continuous vorticity input induces the vortex to grow in size and strength with an increase in chordwise distance from the wing apex and tends to maintain the pressure footprint on the surface of the wing. In the pressure measurement tests, the departure from this conical flow manifests itself as a broadening and reduction in magnitude of the suction ridge over the length of the vortex. Hence, any eventual decrease in suction caused by a reduction in axial velocity prior to flow stagnation and vortex breakdown tends to be disguised by this flowfield effect.

6.1 CONDITIONS FOR VORTEX BREAKDOWN

The mean/instantaneous pressure data can be used in the context of vortex breakdown, to provide a highly useful qualitative assessment of pressure-related flowfield conditions, in particular, those which are measured upstream of the vortex breakdown point and can be associated with the root cause of the phenomenon. On a delta wing, a stationary leading-edge vortex is possible due to the swept leading-edge of the wing which provides a mechanism to continually transport generated vorticity downstream. Hence, a stationary and stable leading-edge vortex is achieved when the convection of vorticity along the core balances the vorticity generation from the boundary layer of the leading-edge. The importance of vorticity balance was first emphasized by Reynolds and Carr (1985), in their review of separation driven flows. This was applied to delta wing flows by Lee & Ho (1990), who observed that the amount of vorticity in a leading-edge vortex at a given chord station depends on a balance between the amount of bounded vorticity fed into the upstream shear layer and the magnitude of axial convection along the vortex core. Visser & Nelson (1993) showed that when this balance is no longer maintained, vortex stability at a given chordwise location is dependent on the level of distributed vorticity per unit area. If this

quantity, also known as the 'swirl' magnitude exceeds a critical value, then the vortex goes through a change of state to redistribute the excess vorticity.

The balance between vorticity generation and convection is controlled by a number of factors. Visser & Nelson (1993) showed that an increase in incidence leads to a higher rate of vorticity generation without necessarily an accompanying increase in axial velocity. When this happens, the magnitude of swirl tends to increase because the rate of vorticity transport remains largely constant. Similarly, the ability of the vortex to transport vorticity is a strong function of the pressure gradient along the vortex core and of the initial axial core velocity. That is, an increasingly adverse pressure gradient tends to reduce the flow axial velocity thus precipitating vortex breakdown and once it is established, induces the phenomenon to move further and further upstream. Conversely, a high axial velocity of the flow over the apex of the wing tends to combat the adverse pressure gradient and serves to redress the balance and reduce swirl magnitude. Earlier, Lee & Ho (1990) had argued that the magnitude of swirl is also decided by geometric factors. They showed that the rate of vorticity convection is partly determined by the component of freestream velocity parallel to the leading-edge of the wing. This velocity component is a geometric function of incidence and wing sweep angle in such a way that increasing the angle of incidence, or decreasing the angle of sweep, increases the 'helix' angle between the axial and circumferential velocity components of the flow and reduces the rate of vorticity transport.

In an earlier paper, Nelson & Visser (1990) suggested that the determination of a vortex breakdown position indicator could be based on several forms including, a local balance between vorticity generation and convection, a local balance of pressure forces with the acceleration of the fluid and an empirical fit parameter based on wing geometry and incidence. Given this proposal, and the findings of

Lee & Ho (1990) and Visser & Nelson (1993), this discussion will continue by using mean pressure measurements to examine the effect of incidence and the three flowfield conditions of vorticity generation, axial pressure gradient and initial axial velocity with a view to gaining an insight into the behaviour of vortex breakdown in the static, pitch up and pitch down cases.

6.1.1 *Conditions for vortex breakdown - static case*

On delta wings, vorticity is constantly fed into the free shear layer when the boundary layer flow on the windward surface of the wing separates along the leading-edge. Reynolds & Carr (1985) showed that the magnitude of vorticity flux generated over a short distance along a solid surface is a function of the local pressure gradient. Using an analogy to this method, it is suggested that at a given chord station, an effective indicator of the rate of vorticity generation is provided by the local pressure difference over a short spanwise distance as close as possible to the leading-edge on the windward surface of the wing. This is only a qualitative assessment however, as wing geometry and transducer locations dictate that the pressure value at the leading-edge be measured at the nearest transducer on the leeward surface, and it is recognised that pressure losses are likely to occur across the leading-edge. Figure 6.1 shows the pressure difference across the leading-edge at $x/c = 0.1$ as a function of incidence over the range 0° to 40°. The pressure values are those measured on the windward surface at $x/c = 0.1$, $y/s = 0.9$ and on the leeward surface at $x/c = 0.1$, $y/s = 0.7$. For chord position, $x/c = 0.1$, the figure indicates that the difference in pressure across the leading-edge increases with an increase in incidence up to 25°. After this, the pressure difference declines again to a plateau level at an incidence of 33°, whereafter, it has been observed in the mean pressure and RMS analyses, that the wing behaves like a bluff body. This is a general trend apparent for chord stations on the wing from $x/c = 0.1$

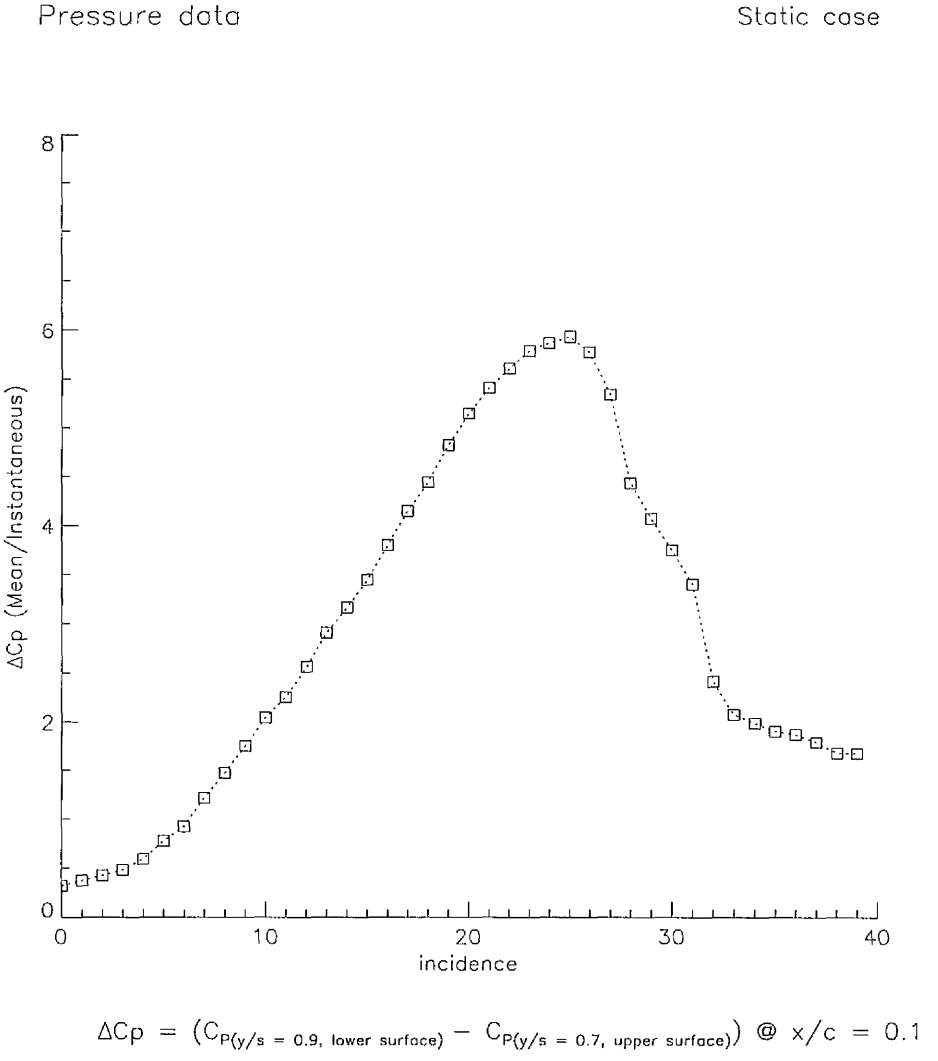

Figure 6.1 - Line plot showing the difference in mean pressure values between transducers located on the windward surface at y/s = 0.9 & on the leeward surface at y/s = 0.8 for a range of incidences from 0° to 40° in the static case. Both transducers at chord station x/c = 0.1 Data collected during pressure measurement tests. Re = 2.7×10^6.

to x/c = 0.6. However, for each successive chord station downstream of the wing apex, the magnitude of the pressure difference at a given incidence decreases and the turning points in the trace occur at an earlier incidence, such that at chord stations beyond x/c = 0.6, the pressure difference across the leading-edge declines to an almost constant value irrespective of incidence. The consistent nature of this trend, particularly over the front half of the wing, suggests that the rate of axial vorticity generation at each of these chord stations is likely to be following the same trend over the same incidence range.

An increase in adverse pressure gradient was shown by Brown & Lopez (1990) to result in increased vorticity diffusion. This leads to a radial redistribution of circulation which tends to 'stretch' and 'tilt' the stream surface that bounds the vortex core, and in doing so, induces the development of a negative azimuthal component of vorticity. This in turn, initiates a retardation in the axial velocity on the vortex axis which, by continuity, will lead to a further divergence of the stream surface and a further increase in negative azimuthal vorticity. Figure 6.2 is a line plot showing the difference in mean C_P values in the path of the suction ridge i.e., at the span station, $y/s = |C_P|_{(max)}$, in the static case, as a function of incidence from 0° to 40°. The pressure measurement positions are located at x/c = 0.8 and x/c = 0.2. This fixed portion of the suction ridge is not used to provide a quantitative measurement of the pressure gradient along the inner vortex core. Principally, this is because the core does not maintain a constant height over the length of the wing and tends to vary in height with pitch rate magnitude. Secondly, it is because the eventual arrival of vortex breakdown over the surface of the wing involves the measurement of the pressure difference across the breakdown boundary. A solution to this latter problem, would be to move the aft pressure measurement location upstream ahead of the breakdown point as incidence is increased. However, this serves to further complicate the pressure gradient calculation by introducing a 'rate of change of vortex' height

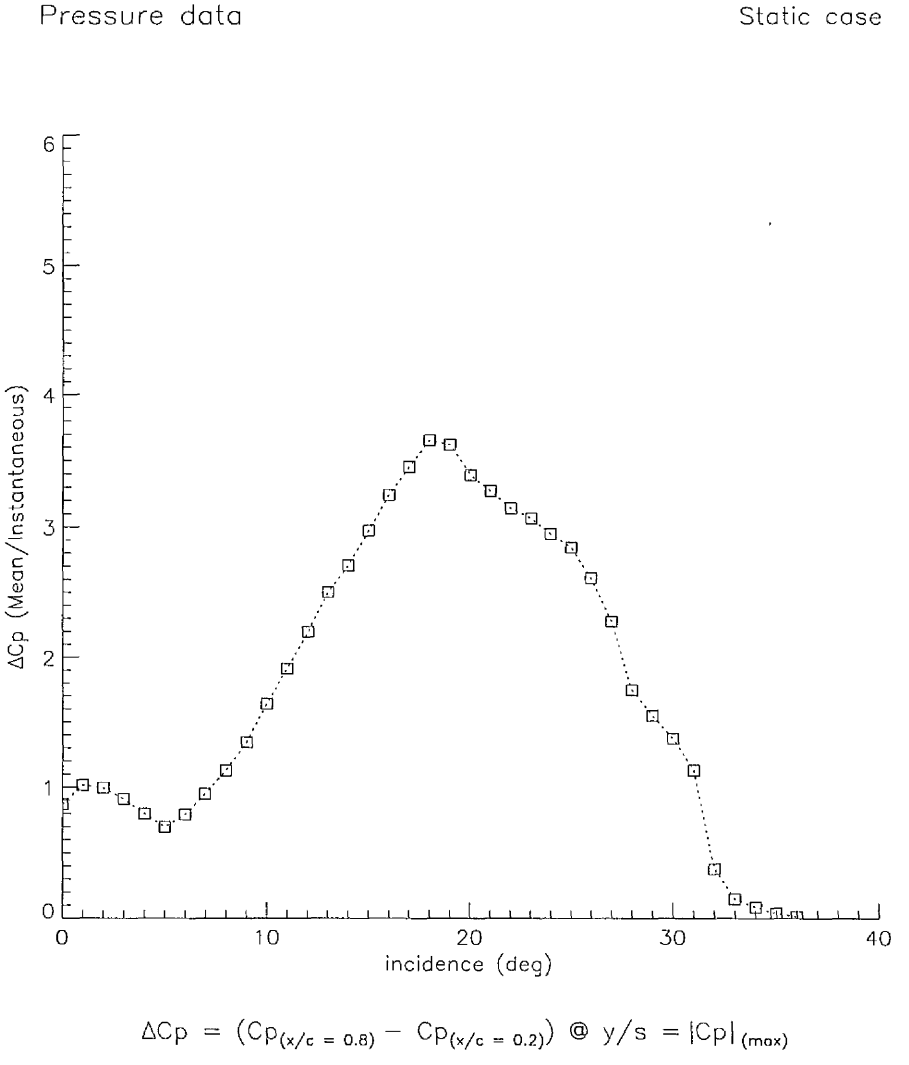

Figure 6.2 - Line plot showing the difference in mean pressure values between two transducers located along the ridge of peak suction at $y/s = |C_P|_{(max)}$ at chord stations x/c = 0.8 and 0.2, for a range of incidences from 0° to 40° in the static case. Data collected during pressure measurement tests. Re = 2.7×10^6.

parameter which again tends to vary with pitch rate magnitude. Rather, it is suggested that the measurement of streamwise pressure difference along the path of the vortex core can provide a simplified qualitative indication of vortex breakdown 'tendency' for each pitch rate case. Figure 6.2 shows for the static case, that the pressure difference along the vortex core between $x/c = 0.2$ and $x/c = 0.8$ increases over the incidence range from 5° to 18°, suggesting that the potential for axial velocity retardation, flow stagnation and vortex breakdown is increasing over this incidence range.

The third factor in the balance between vorticity generation and transport is the rate of streamwise vorticity transportation along the vortex core near to the wing apex. Brown & Lopez (1990) have shown that a higher axial velocity component or a reduced crossflow component near the apex of the wing tends to reduce the 'helix angle' of the flow velocity and induces a positive azimuthal vorticity component in the flow which can be seen as an aid to vorticity transport. This helix angle, α_v, was defined by Cornelius (1995) in terms of a 'vortex energy ratio', such that: $\alpha_v = \tan^{-1}(1/\sqrt{R_{mr}})$, where R_{mr} is the ratio of the integrated axial velocity and circumferential velocity profiles across the vortex inner core. It is clear that the suction peak on the surface of the wing is a function of the axial and crossflow velocity components. However, it has been shown by Brown & Lopez (ibid.) that the axial velocity of the flow at the edge of the vortex does not vary significantly with a change in incidence. Hence any variation in mean suction magnitude can be said to be indicative of crossflow velocity. Figure 6.3 shows the magnitude of suction at chord station $x/c = 0.2$ in the static case as a function of incidence from 0° to 40°. The figure shows that the suction magnitude at $x/c = 0.2$, $y/s = |C_P|_{(max)}$ increases over the incidence range from 5° to 18°. Using the data as a crossflow velocity indicator, it also suggests that the crossflow velocity perpendicular to the vortex core is increasing, thereby reducing the ability of the

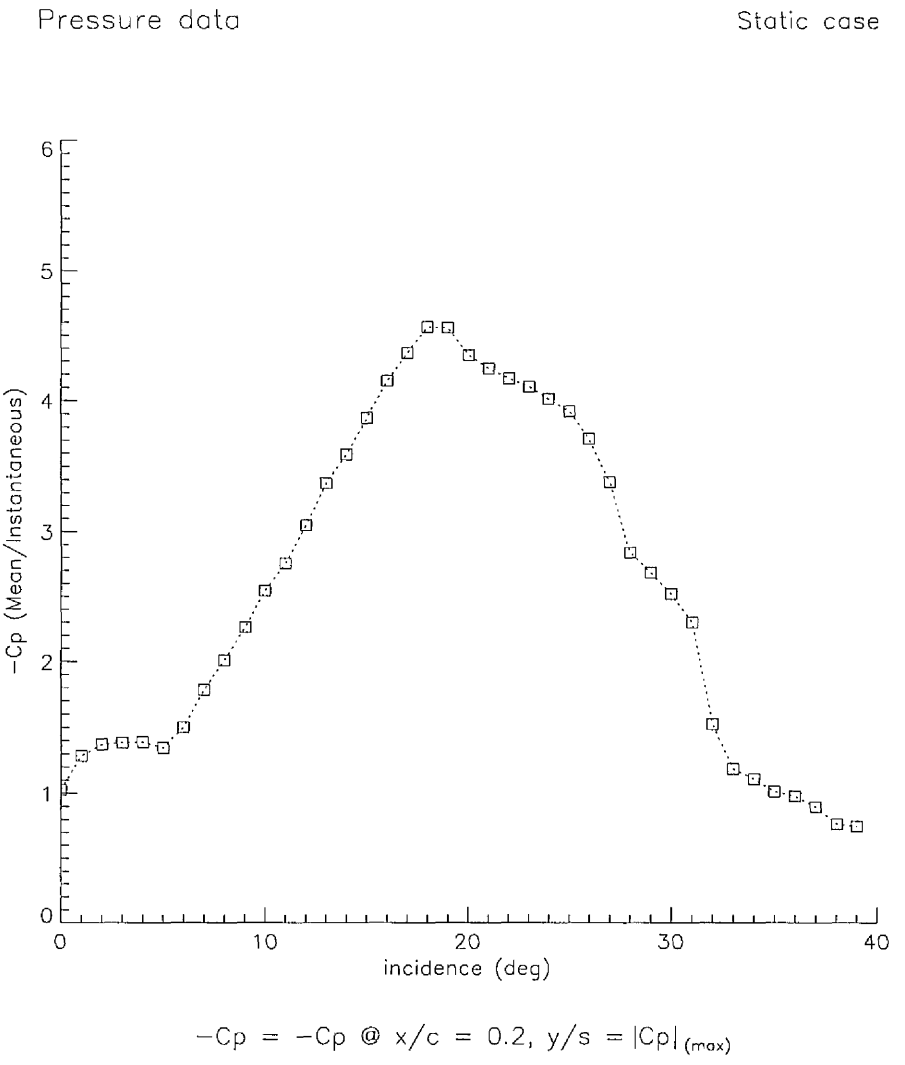

Figure 6.3 - Line plot showing the suction magnitude on the leeward surface of the wing at x/c = 0.2, y/s = $|C_P|_{(max)}$ for a range of incidences from 0° to 40° in the static case. Data collected during pressure measurement tests. Re = 2.7×10^6

vortex to transport vorticity downstream, increasing the likelihood of vortex breakdown. Figures 6.1 to 6.3 show for the static case, that with an increase in incidence from 0° to 25°, there is an increase in axial vorticity production in the boundary layer on the windward surface of the wing at the leading-edge separation point. The ability of the leading-edge vortex to transport the increasing levels of vorticity downstream is determined by the ratio of axial and crossflow flow velocity components near the wing apex and the adverse pressure gradient along the vortex core. These both increase with an increase in incidence over the range 5° to 18°. The results of the visualisation study indicate that at 11° incidence, vortex breakdown moves over the trailing-edge of the wing to $x/c = 0.9$. This indicates that at some point on the vortex core just upstream of this chord station, the generated crossflow component of velocity and the adverse pressure gradient are acting together to increase the helix angle of velocity beyond critical. Cornelius (1995) suggested that for a helix angle, in terms of an energy ratio value, in the range $1.39 \geq R_{mr} \geq 1.0$, the inner core flow is 'supercritical'. As $R_{mr} \Rightarrow 1.0$, i.e., as the helix angle $\alpha_v \Rightarrow 45°$, the flow goes through a transition from supercritical to 'subcritical', where a stagnation point is formed at the core centre and vortex breakdown ensues. Figures 6.1 to 6.3 show that, for an increase in incidence between 11° and 18° in the static case, the rate of vorticity production, the adverse pressure gradient and the crossflow component of velocity increase further, their combined effect overcoming the largely constant axial velocity of the flow to a greater and greater degree, causing the vortex breakdown point to move upstream. Between 18° and 25° incidence, the adverse pressure gradient and the crossflow velocity near the apex begin to decline, leaving the increasing vorticity production rate to increase swirl magnitude and drive vortex breakdown upstream to the wing apex. Beyond 25° incidence, the cross-flow velocity declines but the axial velocity of the flow has also fallen to a level where vortex recovery is apparently not possible.

6.1.2 *Conditions for vortex breakdown - pitch up cases*

An analysis of flowfield conditions can also be applied to the pitch up cases. Figure 6.4 shows the difference between mean C_P values on the windward surface at $x/c = 0.1$, $y/s = 0.9$ and on the leeward surface at $x/c = 0.1$, $y/s = 0.7$, in the static case and two pitch up cases, $k = 0.007$ and $k = 0.015$, as a function of incidence from 0° to 40°. Figure 6.5 shows the difference between mean C_P values in the path of the suction ridge between $x/c = 0.8$ and $x/c = 0.2$, at span station, $y/s = |C_P|_{(max)}$, and Figure 6.6 shows the magnitude of suction at chord station $x/c = 0.2$. The data sets plotted are for the same three cases over the same incidence range shown in Figure 6.4.

Figures 6.4 to 6.6 show that the pitching cases follow a similar trend to the static case, where the rate of vorticity production, the adverse pressure gradient and the crossflow velocity over the wing apex, all increase with an increase in incidence until such a point where vortex breakdown reaches the wing apex and bluff body behaviour ensues. The principal point of interest in Figures 6.4 to 6.6 concerns the magnitude of each parameter at a given incidence value. In the two pitching cases, each parameter lags the static case by a significant margin. This lag is generally consistent with the delay in the appearance and upstream progression of vortex breakdown with increasing pitch rate. This suggests for the pitch up cases at a given incidence, that the axial core velocity is more than able to overcome the reduced vorticity generation, adverse pressure gradient and crossflow velocity component, such that vortex breakdown is delayed. However, the values of leading-edge pressure difference, vortex core pressure difference and suction magnitude near the wing apex do not totally account for the differences in vortex breakdown location between the two pitch up cases. For example, vortex breakdown was observed on the wing at a chord location of $x/c = 0.8$ at an incidence of 15° in the $k = 0.007$ case, whereas its appearance at this chord

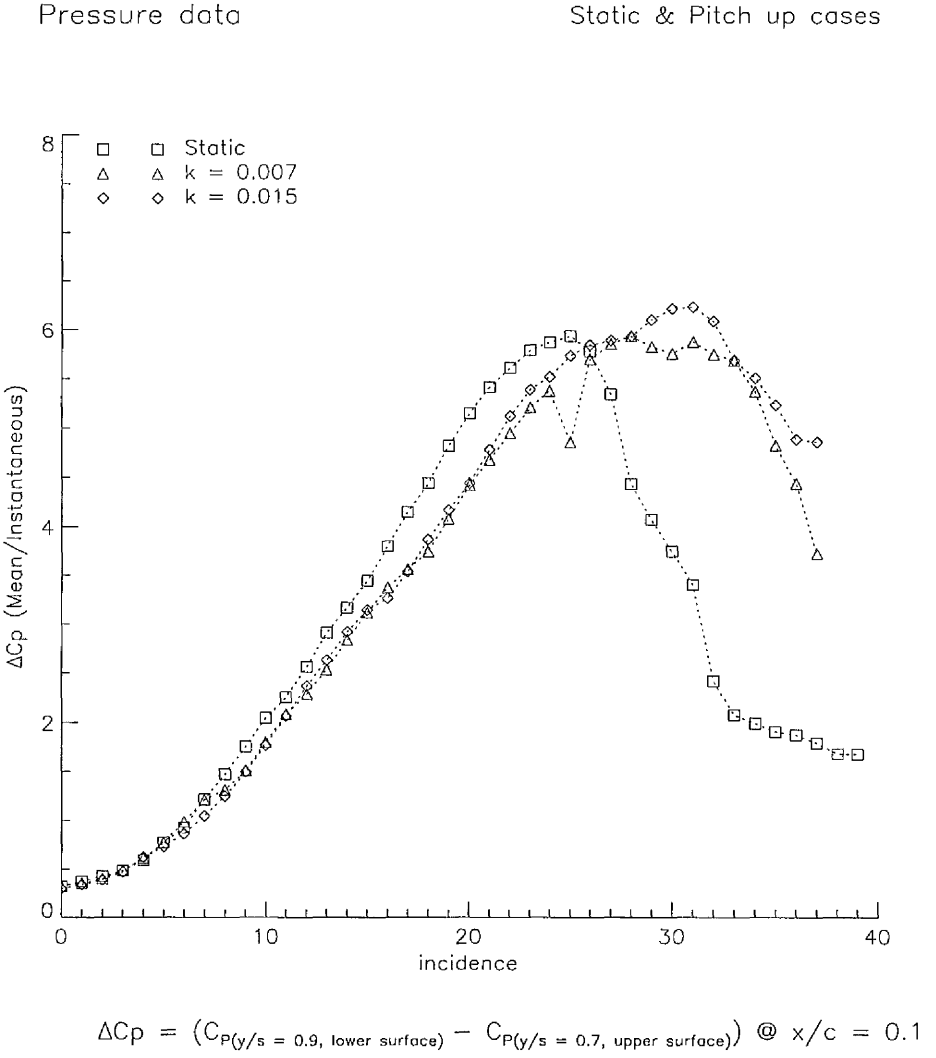

Figure 6.4 - Line plot showing the difference in mean pressure values between transducers located on the windward surface at y/s = 0.9 & on the leeward surface at y/s = 0.8 for a range of incidences from 0° to 40° in the static, k = 0.007 & k = 0.015 cases. Both transducers at chord station x/c = 0.1 Data collected during pressure measurement tests. Re = 2.7×10^6.

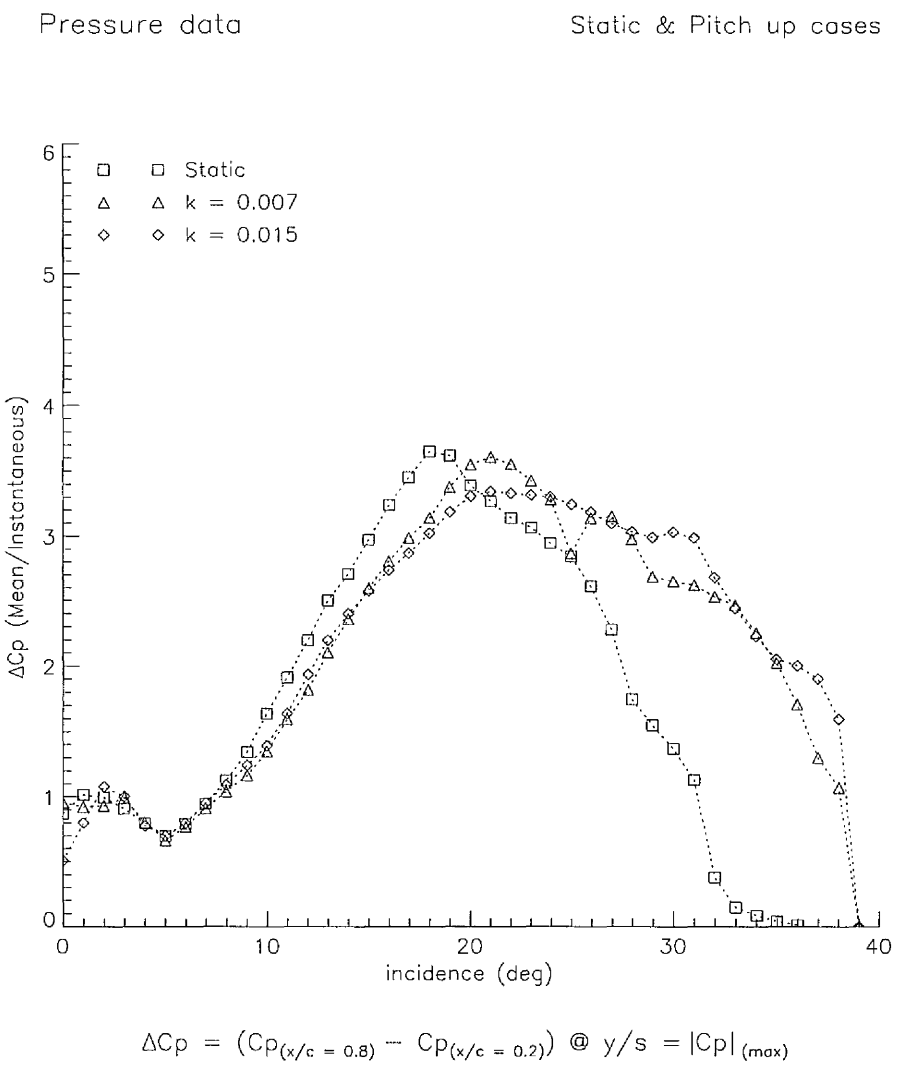

Figure 6.5 - Line plot showing the difference in mean pressure values between two transducers located along the ridge of peak suction at $y/s = |C_P|_{(max)}$ at chord stations $x/c = 0.8$ and 0.2, for a range of incidences from 0° to 40° in the static, $k = 0.007$ & $k = 0.015$ cases. Data collected during pressure measurement tests. $Re = 2.7 \times 10^6$.

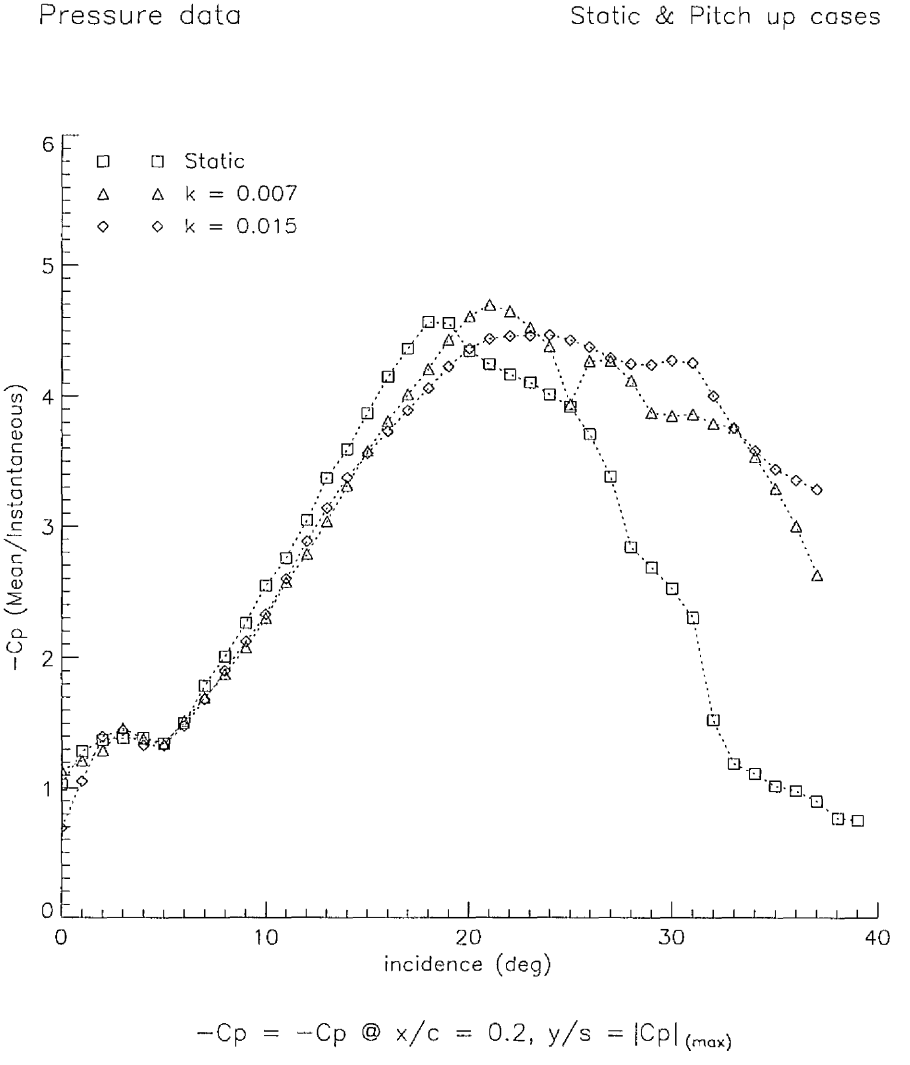

Figure 6.6 - Line plot showing the suction magnitude on the leeward surface of the wing at x/c = 0.2, y/s = $|C_P|_{(max)}$ for a range of incidences from 0° to 40° in the static, k = 0.007 & k = 0.015 cases. Data collected during pressure measurement tests. Re = 2.7×10^6

station in the k = 0.015 case does not occur until 17°. The value of each parameter shown in Figures 6.4 to 6.6, at an incidence of 15° for the two pitching cases is similar enough to suggest that at least a fourth parameter is responsible for the delay in breakdown in the higher pitch rate case. It is suggested that, in addition to variations in vorticity production, pressure gradient and crossflow velocity shown in Figures 6.4 to 6.6, an additional delay occurs, whereby the combined effect of the three parameters takes a nominally fixed period of time to influence the vortex condition at a given chord station. This delay is dependent on firstly, the chordwise distance between the origin of the flowfield parameter quantity and the location of the vortex breakdown point, and secondly, on pitch rate magnitude, as a given fixed time period covers an greater range of incidence as the pitch rate is increased. Therefore an increase in pitch rate magnitude results in a higher incidence, at which vortex breakdown arrives at a given location.

A second factor or effect, has been observed in the flow visualisation tests. The flow visualisation study revealed that during the pitch up movement, the vortex was observed to disintegrate and lose its coherent structure downstream of the trailing-edge of the wing irrespective of the location of vortex breakdown. This feature was contrary to that seen in the static case, where even a broken down vortex was observed to largely maintain its overall structure into the wake. It is suggested that the disintegration of the vortex downstream of the trailing-edge is likely to be the result of entrained, leading-edge vortex fluid mixing with fluid that has travelled over the windward surface and is subject to upwash due to the relative downward motion of the wing trailing-edge. This flow mixing is likely to provide an additional mechanism for vorticity diffusion and results in higher vorticity balance parameters at the trailing-edge of the wing. As vortex breakdown moves upstream away from the trailing-edge, the effect of upwash fluid mixing is likely to be reduced.

6.1.3 *Conditions for vortex breakdown - pitch down cases*

Figure 6.7 shows the difference in pressure across the leading-edge of the wing at chord station x/c = 0.1 as a function of incidence from 0° to 40° in the static and two pitch down cases k = -0.007 and k = -0.017. The pressure measurement locations on the leeward and windward surfaces are the same as those used in the pitch up analysis. For the same three cases, over the same incidence range, Figure 6.8 shows the pressure difference along the path of the peak suction ridge between chord stations, x/c = 0.2 and x/c = 0.8, and Figure 6.9 shows the suction magnitude at x/c = 0.2, y/s = $|C_P|_{(max)}$.

Figures 6.7 to 6.9 indicate for the pitch down cases, that the rate of vorticity production, the adverse pressure gradient and the crossflow velocity of the flow near the apex of the wing tend to increase as the wing is pitched down from 40°. Each parameter reaches a peak value before declining again thereafter. The general trend in the data shows that the peak value of each parameter occurs later during the pitch down motion as the pitch rate magnitude is increased. The results of the visualisation tests showed for the k = -0.007 and k = -0.017 cases, that vortex restoration moves downstream from the wing apex reaching a chord location of x/c = 0.3 at incidences of 17° and 14° respectively. Restoration then continues to move downstream, reaching a chord position of x/c = 0.8 at 10° incidence in the k = -0.007 case and later in the pitch down motion at 8° incidence in the k = -0.017 case. Figure 6.7 shows, for each pitch down case over these respective incidence ranges, that the rate of vorticity production is decreasing. This is contrary to the evidence shown by Figures 6.8 and 6.9, which reveal for the same incidence ranges, that the magnitude of the adverse pressure gradient and the crossflow velocity over the wing apex tend to increase.

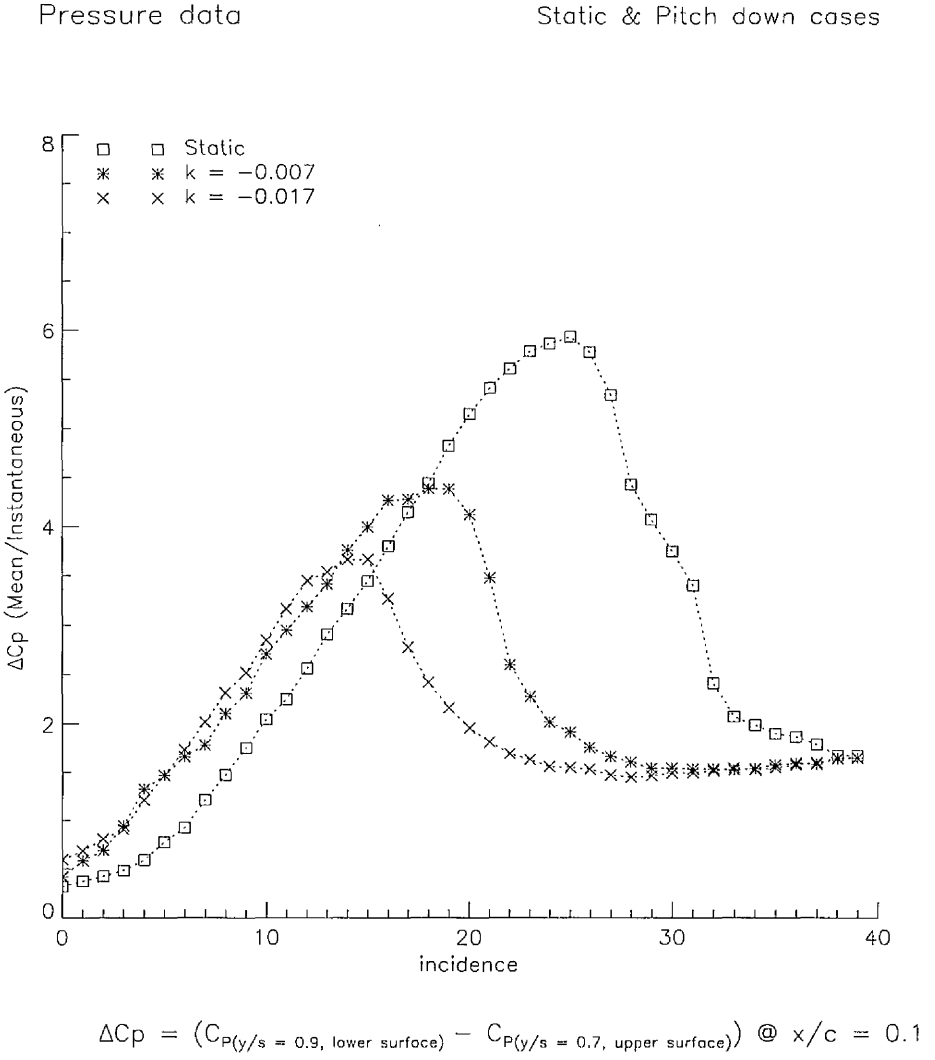

Figure 6.7 - Line plot showing the difference in mean pressure values between transducers located on the windward surface at y/s = 0.9 & on the leeward surface at y/s = 0.8 for a range of incidences from 0° to 40° in the static, k = -0.007 & k = -0.017 cases. Both transducers at chord station x/c = 0.1 Data collected during pressure measurement tests. Re = 2.7×10^6.

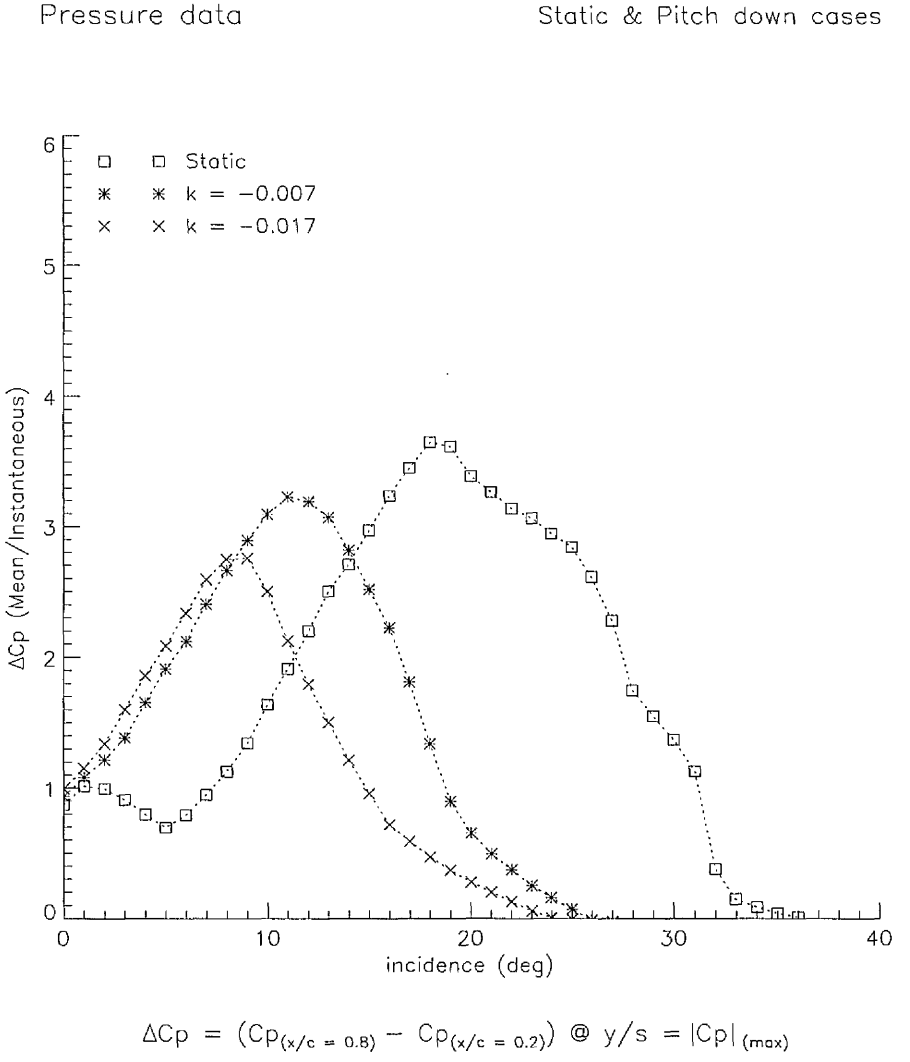

Figure 6.8 - Line plot showing the difference in mean pressure values between two transducers located along the ridge of peak suction at $y/s = |Cp|_{(max)}$ at chord stations x/c = 0.8 and 0.2, for a range of incidences from 0° to 40° in the static, k = -0.007 & k = -0.017 cases. Data collected during pressure measurement tests. Re = 2.7×10^6.

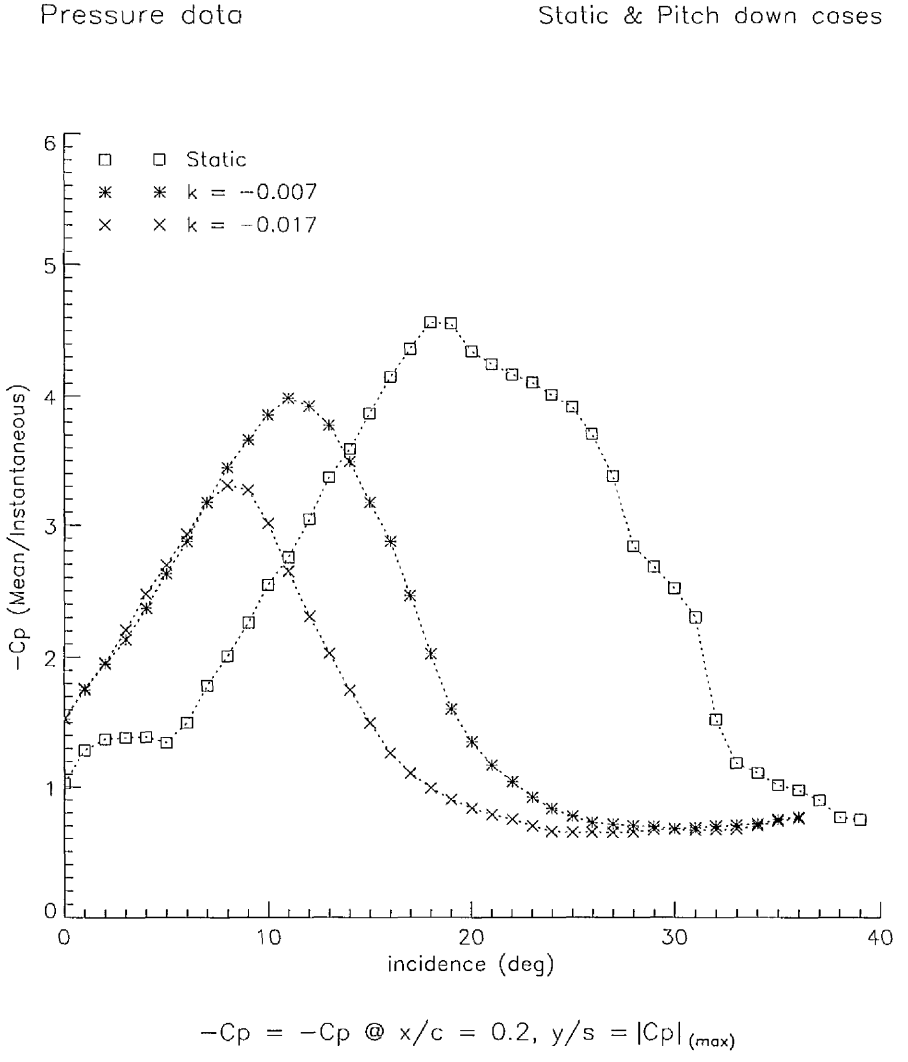

Figure 6.9 - Line plot showing the suction magnitude on the leeward surface of the wing at x/c = 0.2, y/s = $|C_P|_{(max)}$ for a range of incidences from 0° to 40° in the static, k = -0.007 & k = -0.017 cases. Data collected during pressure measurement tests. Re = 2.7×10^6

For each pitch down case, Figure 6.7 shows that the pressure difference across the leading-edge of the wing, and hence the rate of vorticity production, increases with a decrease in incidence over the initial stages of the pitch down motion. This increase coincides with the movement of the region of high RMS pressure, shown in Figure 4.43 and labelled as (4), away from the wing centreline towards its stable lateral position. At an incidence of 19° in the k = -0.007 case and 15° in the k = -0.017 case, the rate of vorticity production begins to level off and subsequently decreases as incidence is decreased further. The continued pitch down motion of the wing induces a relaxation of the rate of vorticity generation tending to reduce swirl magnitude. This results in a reduction in the negative azimuthal component of vorticity, which eventually switches sign. The subsequent generation of a positive component of azimuthal vorticity allows a restoration of a positive axial velocity component, as shown by the increase in suction magnitude at x/c = 0.2, and a reformation of the vortex structure at the apex of the wing. A continued relaxation of the swirl magnitude as the wing is pitched down further allows the 'reformation point' to move downstream. The speed of progress of the vortex reformation is tempered by the increasing adverse pressure gradient and the increase in crossflow velocity at the wing apex. It should be noted that one of the contributors to the adverse pressure gradient, the suction magnitude downstream at x/c = 0.8, is somewhat lower in the pitch down cases across the incidence range, than was observed in the static or pitch up cases.

It is interesting to contrast Figures 6.7, 6.8 and 6.8 with their counterparts for the pitch up cases, i.e. Figures 6.4, 6.5 and 6.6. Clearly, whilst the behaviour of the three parameters in the pitch up cases closely resembles the static case, the same cannot be said for the pitch down cases. This suggests, that in addition to parameters identified here, there must be other significant factors influencing the vortex restoration process. Green & Galbraith (1995) studied the dynamic recovery to fully attached flow on 2D aerofoil models during ramp down

motions. A short time after flow reattachment, they identified a weak disturbance which travelled from the leading-edge to the trailing-edge of the wing causing a characteristic wave on the pressure data. The speed of this wave was uniform along the chord and was independent of aerofoil profile and reduced pitch rate. It was suggested that this wave was indicative of the forced convection of 'dead' wake fluid over the aerofoil surface and that the reattachment of the flow at the leading-edge was important in speeding up the rate of this convection and in causing the observed wave. It is not suggested that the mechanism of vortex restoration in fully separated flows is in any way similar to 2D flow reattachment. However it is suggested, that the large body of 'dead' fluid observed in the wake of the 2D wing, may also be present over the leeward surface of the delta wing prior to the initiation of pitch down motion from a high angle of incidence. It is also suggested that the transition from bluff body behaviour to vortex restoration and increased axial velocity during the pitch down motion is analogous to 2D flow reattachment in that it may also herald a sudden rather than a steady downstream convection of wake fluid. It is possible for pitch down cases, that the convection of wake fluid is superimposed onto the restoration of the vortex flow and the ability of the vortex to transport vorticity is impaired. The independence of wake convection to pitch rate magnitude would suggest that the convection time occupies a greater range of incidence and an increased pitch rate magnitude case requires a higher inherent vorticity transport to generation ratio to achieve vortex restoration.

6.1.4 *Conditions for vortex breakdown - general*

It is suggested that a number of factors affect the location of vortex breakdown on the wing surface for static, pitch up and pitch down cases. These include vorticity balance, instantaneous incidence, pitch rate magnitude and the speed of flow convection over the wing surface, which is itself a function of freestream velocity and the angle of the wing surface to the freestream. A qualitative analysis

reveals an extremely complex interaction between all of these variables which does not at this stage, permit an overall 'vortex breakdown location' parameter to be deduced. However, it is hoped that the identification of these factors will provide a basis for an accurate quantitative analysis of the flowfield which may provide such a parameter in the future. The remainder of this discussion moves on from upstream flowfield features that may influence breakdown, to post-breakdown features that enable breakdown detection using more advanced temporal statistical methods.

6.2 VORTEX BREAKDOWN DETECTION

6.2.1 *Static case*

Previous work by Honkan & Andreopoulous (1997) which used velocity measurements to determine vorticity variations on a static wing, has identified a region of high turbulent kinetic energy ($0.5\ q^2/U^2$) on the surface of the wing inboard of the primary vortex core but outboard of the primary attachment zone. Similarly, two smaller regions of similar energy intensity have also been identified just above the surface of the wing, and these are located in areas which possibly correspond to the separation and reattachment zones of the secondary vortex. In the light of this, it is thought that the primary region of high RMS pressures, (an indication of the amplitude of the pressure fluctuations) observed inboard of the vortex core as shown in Figure 4.31, item (2), is associated with a region of localised but highly turbulent flow within the feeding vortex sheet between the vortex core and the primary attachment region. Similarly, it is thought that the secondary region of high RMS pressures observed outboard of the vortex core in Figure 4.31, item (3) is associated with the formation of the secondary vortex structure. It would appear that the arrival of vortex breakdown at the trailing edge of the wing and subsequently at chord stations upstream heralds a substantial increase in turbulent kinetic energy in this region. This may be associated with the

generation of a negative azimuthal component of vorticity, previously shown by Brown & Lopez (1990) to be necessary for the axial component of velocity in the vortex core to be brought to rest and for vortex breakdown to take place. Brown & Lopez showed that the development of negative azimuthal vorticity is a self-perpetuating process which leads to a retardation of the flow on the vortex axis and a rapid expansion of the vortex core. It is suggested that it is this mechanism that is associated with the rapid increase in magnitude of the high RMS pressure region downstream of breakdown as well as the broadening of the region across the wing in a spanwise direction, i.e., Fig. 4.33, item (4), as the wing incidence is increased.

Figure 5.2 indicates that the first appearance of the excitation frequency component in the frequency spectra follows a similar trend to the arrival of vortex breakdown at a given chordwise location, although the initiation of the phenomenon tends to occur ahead of the breakdown point. Similarly, Figure 4.35 shows that there is very good agreement between the upstream movement of the waist in the RMS contours, i.e., Figure 4.33, item (5), and the upstream progression of vortex breakdown shown by the visualisation data. It is suggested that the establishment of the excitation frequency following its very first appearance, the waisting of the RMS pressure contours and the associated localised trough of RMS pressure magnitude (described in section 4.3) are indicative of the first subinterval of the breakdown region first described by Leibovich (1978). This subinterval is characterised by an axial deceleration of the approach flow and the formation of a stagnation point on the vortex axis.

It is also possible that the above observations may be associated with an increase in the 'helix angle' of the vortex core velocity (Brown & Lopez (1990)) during the deceleration phase. A change in the flow direction from that with a greater chordwise component to that with a predominantly spanwise component would

align the flow more towards the surface normal direction at the primary reattachment point. It is suggested that this would tend to increase the frequency of pressure fluctuations, as any two pressure disturbances travelling at a similar velocity would cover a shorter distance in the same time-frame. Similarly, the 'sharpening' of the angle of reattachment would tend to reduce the RMS pressure 'footprint' immediately inboard of the reattachment point both in terms of magnitude and width.

It was also shown for the static case in Section 5.1, that the sudden drop in the magnitude of the low frequency component of the frequency spectra always follows the appearance of the excitation frequency. The cause of this low frequency component needs explanation. It could be associated with a very low frequency oscillation of the main vortex core during the post-vortex formation/pre-vortex breakdown phase. This oscillation may be caused by the cyclic expansion and contraction of the secondary vortex structure, which was observed in the visualisation tests described in Section 4.1, where the secondary vortex structure displaces the primary vortex inboard as it grows and allows reinstatement of the primary vortex position as it contracts. This phenomenon has been recorded previously by a number of researchers, particularly Gad-el-Hak & Blackwelder (1985), Payne *et al* (1986) and Lee & Ho (1990). It is suggested that the sudden drop in the magnitude of the low frequency component is associated with the breakdown point of the primary vortex, which immediately follows that of the secondary vortex, as shown by Atta & Rockwell (1987). At the point of vortex breakdown, the low frequency component associated with the formation and dissolution of the secondary vortex structure suddenly reduces in magnitude and the higher frequency component associated with the burst primary vortex becomes progressively stronger.

6.2.2 *Vortex breakdown detection - pitch up cases*

In the pitch up cases, two principle features initially dominate the RMS pressure distribution on the leeward surface of the wing during the pre-vortex breakdown phase. Firstly, a 'primary' ridge of high RMS pressure shown in Figure 4.38 to be located inboard of the vortex core. This was thought in the static case to be associated with a region of localised but highly turbulent flow within the feeding vortex sheet between the vortex core and the primary attachment region. The similarity in behaviour of this primary ridge of high RMS pressure in the pitch up case and that of the static case would suggest that these two regions have the same origin. Secondly, a 'secondary' ridge of high RMS pressure shown in Figure 4.38 to be located outboard of the main vortex core. This was thought in the static case to be somehow associated with the formation of the secondary vortex structure. Again, the similarity in behaviour of this secondary ridge of high RMS pressure in the pitch up case and that of the static case would suggest that these two regions also have the same origin.

For the pitch up cases, the establishment of the excitation frequency, the waisting of the RMS pressure contours and the associated trough of RMS pressure magnitude ahead of the expanded region of high RMS pressure reveals a similar behaviour to that of the static case, suggesting that these features are again indicative of the first interval of the breakdown region. Similarly, the appearance and the subsequent broadening and upstream movement of the additional peak of high RMS pressure coincides with the arrival of vortex breakdown at the trailing-edge of the wing and subsequently at chord stations upstream. Again, the similarity in behaviour between these features in the pitch up cases and those in the static case would indicate that these two sets of features can be explained by the same physical phenomenon. This explanation is supported by the pressure signal energy analysis results for the pitch up cases, which indicates a similarity in the trend of vortex breakdown position against incidence, as determined by the

smoke visualisation data, and the rapid increase in pressure signal energy over the same incidence range.

6.2.3 *Vortex breakdown detection - pitch down cases*

In the work of Gursul (1994), it was shown that the dominant buffet frequency in the spectra of pressure fluctuations observed on the wing ceased after vortex breakdown had reached the wing apex. An examination of the frequency power spectrum and RMS pressure data for the pitch down cases indicated that the first appearance of the dominant frequency coincided with the initial outboard movement of the region of high RMS pressure from the wing centreline towards the leading-edge. This initial movement immediately preceded the recession of the region of high RMS pressure from the apex of the wing towards the trailing-edge. Figure 4.48, plots b) & c) indicate a similarity in behaviour of the vortex restoration point determined by the smoke visualisation data and that obtained from the RMS pressure data analysis. It is suggested that the initial movement of the region of high RMS pressure away from the wing centreline heralds the end of bluff-body type behaviour and the beginning of the restoration of the vortex structure at the apex of the wing. This would explain the first appearance of the dominant frequency coinciding with the initial restoration of the vortex structure, showing agreement with Gursul's findings. Similarly, it was suggested in Section 6.1.3, that the relaxation of the rate of vorticity generation in the pitch down cases with a decrease in incidence is responsible for the reduction in negative azimuthal vorticity and a subsequent generation of a positive azimuthal vorticity component which allows the increase of flow axial velocity and the downstream progression of the point of vortex restoration. It is suggested that it is this mechanism that is associated with the decrease in peak magnitude in the high RMS pressure region, together with its recession downstream as the primary vortex is restored during pitch down motions. This is accompanied by a rapid decline in pressure signal

energy at a given location, the point of which, also recedes downstream in a similar manner.

6.3 VORTEX BREAKDOWN BUFFET FREQUENCIES

6.3.1 *Static case*

Figure 5.1 shows that a delay exists before the excitation frequency component in the spectra of pressure fluctuations becomes dominant. This apparently occurs after breakdown and as such may be associated with the fully broken down state. Once breakdown has fully developed the magnitude of the low frequency element drops considerably and the dominance of the higher excitation frequency ensues. Figure 5.5 reveals the behaviour of the dominant excitation frequency in the post-vortex breakdown state at a number of chord locations and incidences. The figure shows for the static case that, with an increase in distance from the wing apex at a given incidence, or alternatively, with an increase in incidence for a fixed chord location, the central frequency of the excitation band tends to have a lower frequency value. These characteristics have also been observed by a number of researchers including Gursul (1994), Woods and Wood (1996), Mabey (1996) and Woods (1999). These analyses however, did not necessarily have the benefit of full surface pressure measurement capability, and as such, may not have been able to fully explore the characteristics of the frequency content in post-breakdown pressure measurements. It is hypothesised that there is an alternative method of examining frequency spectra such that data obtained at pressure measurement locations a fixed distance behind the vortex breakdown point over a range of increasing incidence may also give a valuable insight into the behaviour of vortex flows in the post breakdown state. This method differs from previous analyses in that the distance between breakdown location and measurement point is kept constant but both are moving according to the movement of the vortex breakdown location. The following analysis tests this hypothesis by examining the

variation in excitation frequencies with respect to vortex breakdown location and downstream measurement point distance.

Figure 6.10 is a series of plots that show the central frequency in the excitation band of pressure fluctuations for pressure measurement points located a fixed distance downstream of the point of vortex breakdown as incidence is increased in the static case. The nominal fixed distances chosen are (x/c_{bd} + 0.1c), (x/c_{bd} + 0.2c) and (x/c_{bd} + 0.3c). Where the transducer arrangement on the wing precludes the calculation of the frequency spectra precisely at the point behind breakdown according to the nominal fixed distance, then the next transducer downstream is used instead. Using this criterion, a given fixed distance might be increased by up to 0.0125c. Plot a) indicates the chordwise location of vortex breakdown, as determined by the initial appearance of the excitation frequency band, shown as a function of incidence, together with the three fixed distance pressure measurement points on the wing surface. For each fixed distance behind the vortex breakdown point, plot b) shows the central frequency of the excitation band as a function of chord position. It should be noted, that the values of incidence which correspond to a given chord station, are increased by as much as 4° with an increase in fixed distance behind the breakdown location. Hence, this is a different data set to that shown in Figure 5.5. Plot b) indicates a trend in the data, which reveals that for a given fixed distance behind the vortex breakdown location, the frequency of pressure fluctuations increases towards the apex of the wing. This trend is in agreement with previous work and is similar to that shown in Figure 5.5. Plot c) on the other hand, shows the central frequency of the excitation band as a function of incidence. At a given incidence, the corresponding chord station of interest shifts in the direction of the wing trailing-edge. Plot c) indicates that for a given fixed distance behind the breakdown point, there is an increase in excitation frequency values with an increase in incidence. This is contrary to that shown in Figure 5.5 and to the work by Mabey (1996)

detailed in Chapter 5. Plot c) does however, show that the value of the central excitation frequency consistently decreases at a given incidence with an increase in fixed distance behind the vortex breakdown location. This suggests for the static case, that the decrease in excitation frequency previously attributed to an increase in incidence, both in this study and by the previous researchers, may instead be caused by the movement of the vortex breakdown position upstream and away from a fixed pressure measurement location. Similarly, maintaining a fixed position behind the breakdown location indicates that the increase in central frequency is a function of the upstream movement of the vortex breakdown location alone. Clearly, it is not possible to de-couple breakdown position and incidence in the static case for a fixed geometry, hence the consistency of the data shown in Figure 5.5 with the work of Mabey (ibid.) and other researchers on static wings. However, this finding has implications for pitching cases where breakdown position and incidence are de-coupled by the introduction of pitch rate.

The dependence of the excitation frequency value on breakdown location and distance behind it needs some explanation. Other experiments on vortex breakdown on static wings, notably Gursul (1994) and Cornelius (1995), have shown that overall circulation is affected only marginally after vortex breakdown, although the vorticity distribution changes dramatically. It was deemed reasonable to assume, even after breakdown, that the flow remains largely conical in nature and circulation continues to grow linearly due to the continuous feeding of vorticity from the leading-edge of the wing. At a fixed incidence for a given wing geometry, the excitation frequency of pressure fluctuations in its dimensionless form (fx/U) has been shown by Gursul (ibid.) to be a function of dimensionless circulation (Γ/Ux). Hence, the frequency of pressure fluctuations is strongly dependent on chordwise vortex breakdown position and on the post-breakdown growth of the vortex in a streamwise direction, and by inference, on the downstream measurement point distance.

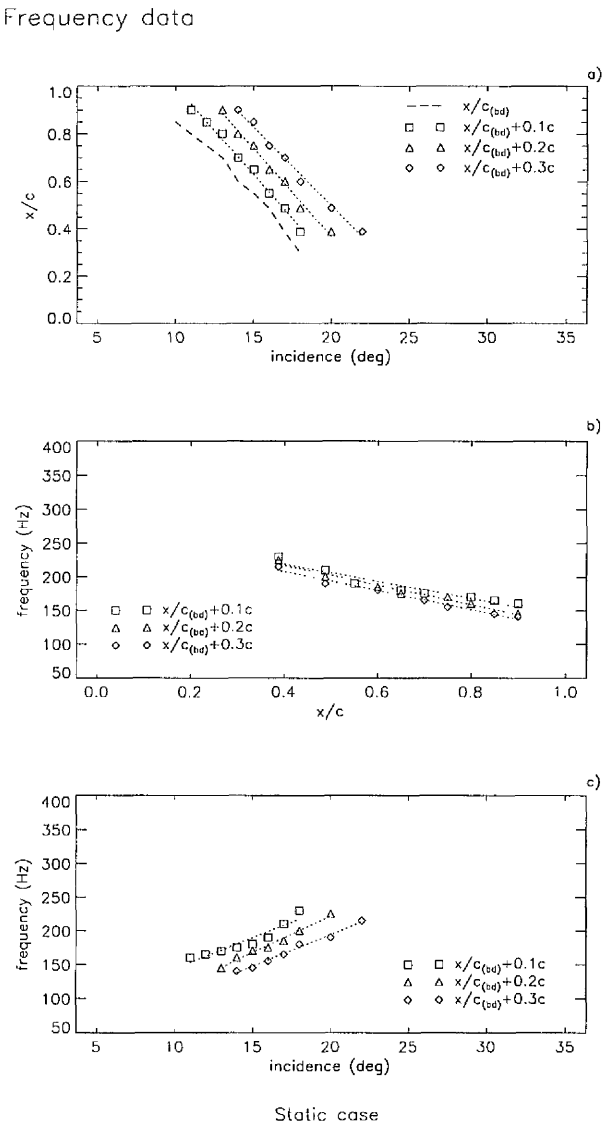

Figure 6.10 - Line plots showing: a) the variation in chordwise vortex breakdown location as a function of incidence. Together with the variation of central excitation frequency as: b) a function of chord position for varying incidences, and c) a function of incidence for a range of chord stations. Data collected during pressure measurement tests. Re = 2.7×10^6

6.3.2 *Buffet frequencies - pitch up cases*

A similar fixed distance frequency analysis has been carried out for the two pitch up cases, k = 0.007 and k = 0.015. The results reveal a similar trend in the pitch up case data to that observed in the static case. That is, little variation is observed in excitation frequency values at a given chord station, despite an increase in downstream distance from the breakdown location and the corresponding increase in incidence. Similarly, at a given incidence, a decrease in central frequency value is observed with an increase in fixed distance, indicating that the frequency of pressure fluctuations in the pitch up cases, also shows a strong dependency on vortex breakdown location and downstream measurement location distance.

Figure 6.11 shows pressure measurement locations as a function of incidence (plot a) and the central value of the excitation frequency band in the static case and two pitch up cases, k = 0.007 and k = 0.015, as a function of chord position (plot b), and incidence (plot c). Each frequency value plotted is measured 0.1c downstream of the vortex breakdown point. Figure 6.11, plot b) shows that in the pitch up cases, the centre of the high frequency band of pressure fluctuations associated with the post-vortex breakdown state are considerably higher than the static case at a given chord position. Similarly, Figure 6.11, plot c) shows that at a given incidence, the excitation frequency value for the static case is generally lower than the two pitching cases, although the highest frequency values would appear to be associated with the k = 0.007 case. Without the necessary quantitative flowfield information required to measure changes in flow velocity, vorticity and circulation for changes in pitch rate magnitude, it is difficult assess the impact of these variables on the frequency of pressure fluctuations. Therefore, the causes of frequency value variations can only be the subject of informed speculation using the evidence that is available.

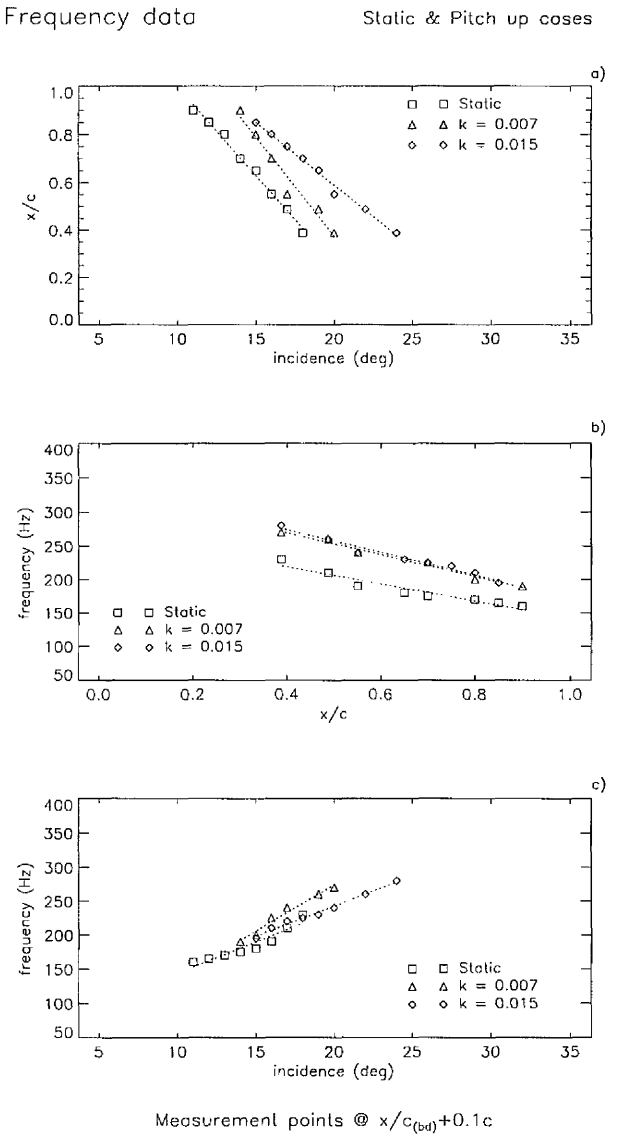

Figure 6.11 - Line plots showing: a) the variation in chordwise frequency measurement location as a function of incidence. Together with the variation of central excitation frequency for static , k = 0.007 & k = 0.015 cases, as: b) a function of chord position for varying incidences, and c) a function of incidence for a range of chord stations. Data collected during pressure measurement tests. Re = 2.7×10^6

The flow visualisation study revealed two distinct differences in the behaviour of the vortex between the static case and those cases subject to pitch up motion. In addition to vortex structure disintegration aft of the wing trailing-edge, alluded to in Section 6.1, the vortex was also observed to lie closer to the wing surface during the pitch up movement. The closer proximity of the vortex to the wing surface during the pitching motion manifests itself in the pressure data as an increase in suction magnitude near the trailing-edge at a given incidence. This is a feature of the instantaneous pressure distributions in the two pitch up cases, where the suction magnitude measured at $x/c = 0.8$ in the path of the suction ridge is generally higher than that for the static case across the incidence range under consideration. Visser & Nelson (1993), who published axial and tangential velocity profiles for a 60° delta wing in a plane normal to the vortex centreline, showed that closer proximity of the vortex core to the wing surface would bring faster moving fluid in contact with the wing surface, potentially inducing an increase in the frequency of disturbances. It is suggested that closer proximity of the vortex core to the wing surface would induce faster moving fluid at the wing surface and together may provide a partial explanation for an increase in pressure fluctuation frequency.

The effect of the flow disintegration and mixing, with regard to excitation frequency, on the upstream vortex is as yet unclear, but it is likely that any effect is largely independent of pitch rate magnitude and more likely to be dependent on freestream velocity. This may account for the similarity in excitation frequency values at a fixed distance downstream of a common breakdown location between the two pitch up cases, $k = 0.007$ and $k = 0.015$. It is suggested that the combination of these factors alone do not complete the mechanism which induces an increase in excitation frequency in the pitch up cases, although it is hoped that their identification may form the basis for further work in this area.

6.3.3 *Buffet frequencies - pitch down cases*

A fixed distance frequency analysis was carried out for the two pitch down cases, k = -0.007 and k = -0.017. The results revealed a trend in the pitch down case data that was similar to that observed in the static and pitch up cases. Again, little variation was observed in excitation frequency values at a given chord station, despite an increase in downstream distance from the vortex reformation location and the corresponding higher incidence value. Similarly, at a given incidence, a decrease in central frequency value was observed with an increase in fixed distance, indicating that the frequency of pressure fluctuations in the pitch down cases, also shows a strong dependency on the chordwise location of vortex reformation and the downstream measurement location distance.

Figure 6.12 shows pressure measurement locations as a function of incidence (plot a) and the central value of the excitation frequency band in the static case and two pitch down cases, k = -0.007 and k = -0.017, as a function of chord position (plot b), and incidence (plot c). Each frequency value plotted is measured 0.1c downstream of the point of vortex reformation. Figure 6.12, plot b) shows that in the pitch down cases, the centre of the high frequency band of pressure fluctuations associated with the pre-vortex reformation state are considerably higher than the static case at a given chord position. Similarly, Figure 6.12, plot c) shows that at a given incidence, the excitation frequency value is generally higher with an increase in pitch rate magnitude. In the absence of qualitative data, the causes of changes in frequency values in the pitch down cases, must be again be the subject of speculation. Section 6.1 introduced the work of Green & Galbraith (1995), who studied the dynamic recovery to fully attached flow on 2D aerofoil models during ramp down motions. It has been suggested in Section 6.1 for pitch down cases, in an analogy to the convection of wake fluid in 2D cases, that the convection of wake fluid is superimposed onto the restoration of the vortex flow, such that the ability of the vortex to transport vorticity is impaired. It is also

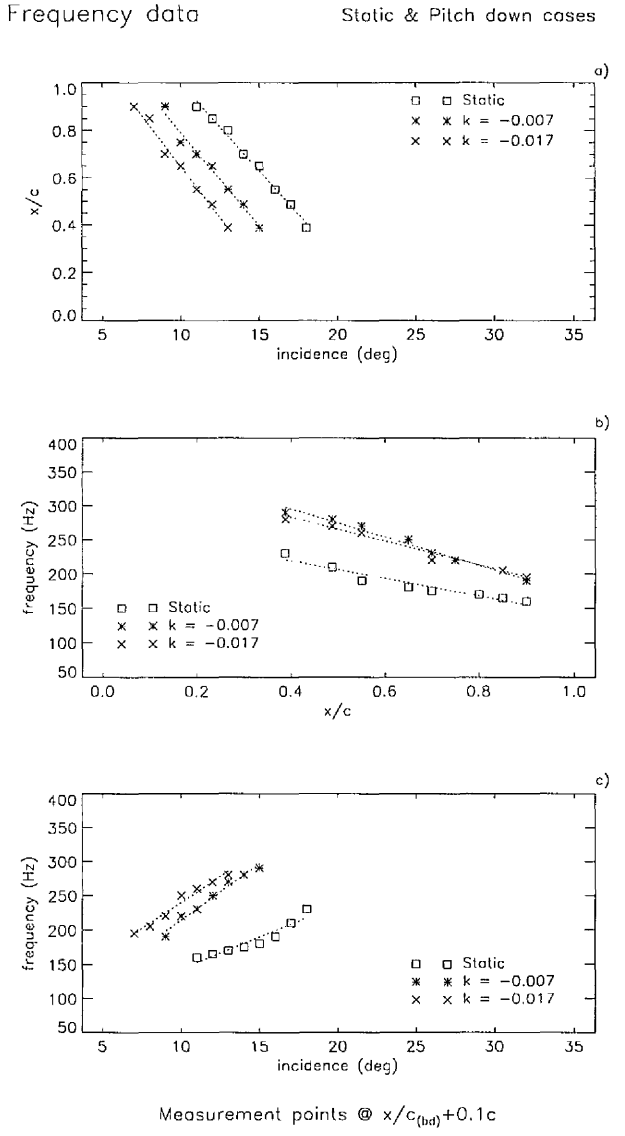

Figure 6.12 - Line plots showing: a) the variation in chordwise frequency measurement location as a function of incidence. Together with the variation of central excitation frequency for static , k = -0.007 & k = -0.017 cases, as: b) a function of chord position for varying incidences, and c) a function of incidence for a range of chord stations. Data collected during pressure measurement tests. Re = 2.7×10^6

suggested here that the same mechanism results in the flow disturbances that impinge on the wing surface to be convected from a position further upstream than is the case for the static wing under similar flowfield conditions. Hence, the increased frequency of pressure fluctuations in the pitch down cases.

Chapter 7

7. CONCLUSIONS AND RECOMMENDATIONS FOR FURTHER WORK

Detailed experiments have been carried out on a 60° delta wing with sharp leading-edges. The instantaneous pressure distribution on one half of the leeward surface of the wing has been successfully measured over a range of incidence using a large number of closely spaced pressure transducers coupled to an advanced data acquisition system capable of sampling at a high rate. The advantages of high spatial and temporal resolution pressure measurements lie in the ability to obtain high quality statistical data of the pressure fluctuations over the whole surface of the wing. This data has been used in a detailed statistical analysis involving the calculation of mean/instantaneous pressure, RMS pressure and signal power distributions, as well as frequency spectra of pressure fluctuations and the cross-correlation function of two pressure signals.

The calculation of the RMS pressure distribution and the frequency spectra of pressure fluctuations have been made complicated by the pitching motion of the wing. When carrying out these calculations, account must be taken of a pitch rate-dependent Nyquist frequency criterion which affects the low end of the frequency spectrum. Failure of this Nyquist criterion has been shown to cause aliasing which results in an inaccurate representation of the flowfield. This problem has been overcome in two stages. The first stage involves band-pass filtering the data prior to input into the frequency spectrum calculation. Subsequent analysis of the filtered frequency spectra provides necessary information regarding a characteristic excitation frequency of pressure fluctuations that have been shown

to be indicative of the presence of vortex breakdown over the surface of the wing. The second stage involves the calculation of the RMS pressure distributions using a line of best fit though the data over a given sample 'window'. This sample window is a function of incidence and pitch rate and is a measure of the minimum sample time period whose length allows the majority of the band of excitation frequencies identified in the frequency analysis to pass the low-end Nyquist criterion.

A number of observations have been made regarding the mean/instantaneous pressure, RMS pressure and signal power distributions, the power spectra of the pressure fluctuations and the cross-correlation spectra which have been supported by the results from smoke visualisation tests. In the static, pitch up and pitch down cases, it is suggested that the position and general condition of the leading-edge vortex are indicated by a localised ridge of high suction emanating from the apex of the wing extending towards the trailing-edge. Similarly, the rate of vorticity production, axial pressure gradient and the initial axial velocity of the flow are indicated by a local pressure difference across the leading-edge of the wing, the pressure difference along the ridge of high suction and the suction magnitude near the wing apex respectively. These three parameters, together with the wing incidence, determine the condition of the vortex flow at a given chord position. It has been shown for the pitch up cases, that a delay takes place whereby the incidence at which vortex breakdown arrives at a given chord station lags that of the static case. This delay is caused by two factors. The first factor is a lag in the generation of vorticity, axial pressure gradient and the initial axial velocity of the flow, the combination of which leads to a delay in the appearance and upstream progression of vortex breakdown. The second factor is that the vortex core at a given chord position, 'sees' the prevailing conditions at a progressively lower incidence with an increase in pitch rate magnitude. It has been shown that the former delay factor is not necessarily pitch rate dependent but

takes into account prevailing flow conditions. The second delay factor is, by its very nature, pitch rate dependent. For the pitch down cases, a similar delay occurs with an increase in pitch rate magnitude. It is suggested that this delay is caused by the superimposition of the convection of 'dead' wake fluid onto the restoration of the vortex flow, such that at a given vortex breakdown location the ability of the flow to transport vorticity is impaired and results in lower values of flowfield parameters at a given breakdown location.

For the static and pitch up cases, it is suggested that a 'primary' region of high RMS pressure located inboard of the vortex core is indicative of the attachment region of the primary vortex. Similarly, a secondary region of high RMS pressure located outboard of the primary vortex core is indicative of the separation region of the secondary vortex structure. The deceleration and eventual stagnation of the axial velocity within the vortex core, which acts as a pre-cursor to vortex breakdown, is indicated by a 'waisting' of the contours in the region of high RMS pressure inboard of the vortex core. Similarly, it is suggested that the onset of the fully broken down state is indicated by an expansion of the same RMS pressure contours immediately downstream of the waist and is accompanied by a characteristic change in the frequency signature of the pressure fluctuations.

In the pitch down cases, it is suggested that the change from bluff-body behaviour at high angles of incidence to the restoration of the primary vortex core at the apex of the wing is indicated by the outboard movement of a region of high RMS pressure situated along the wing centreline and its subsequent recession from the wing apex. Again, this change is accompanied by a characteristic change in the frequency signature of the pressure fluctuations. Following vortex restoration, two regions of high RMS pressure become apparent, suggesting that the 'primary' region of high RMS pressure located inboard of the vortex core is again indicative of the attachment region of the primary vortex and the secondary

region of high RMS pressure located outboard of the primary vortex core is again indicative of the separation region of the secondary vortex structure.

The results of a frequency analysis, carried out in a similar manner to a number of previous research programmes, revealed the behaviour of the dominant excitation frequency in the post-vortex breakdown state at a number of chord locations and incidences. For the static case, it has been shown that an increase in distance from the wing apex at a given incidence, or alternatively, an increase in incidence for a fixed chord location, leads to a lower frequency value of the central frequency of the excitation band. These characteristics are in agreement with the previous findings. However, this experimental system has the advantage of a total surface pressure measurement capability, which has enabled an extended analysis of frequency spectra. This analysis has been used to compare data for common breakdown locations and fixed measurement points downstream for a range of pitch rates and incidence values. It is suggested that, for static, pitch up and pitch down cases, the excitation frequency of pressure fluctuations is not only dependent on chordwise vortex breakdown position, but is also strongly dependent on the post-breakdown growth of the vortex in a streamwise direction, and is therefore, strongly dependent on the downstream measurement point distance.

At a given chord position, the frequency of pressure fluctuations has been shown to be higher during pitch up and pitch down motions compared with the static case. It is suggested for each motion type, that these characteristics are probably caused by different phenomena. It is suggested for pitch up cases, that the combination of closer proximity of the vortex core to the wing serves to increase the velocity of the flow impinging on the wing surface. It is also suggested for pitch up cases, that the termination of the vortex downstream of the trailing-edge due to the mixing of vortex and upwash fluid, may also influence the frequency of

pressure fluctuations to such a degree, that the frequency is largely independent of pitch rate and more dependent on freestream velocity. However, the effect of mixing is not as yet fully understood. It is suggested that increased flow velocity and flow mixing are together at least partly responsible for the increase in the frequency of pressure fluctuations in the pitch up cases. In the pitch down cases, it is suggested that the frequency of pressure fluctuations are also affected by the superimposition of the convection of 'dead' wake fluid onto the restoration of the vortex flow, such that at a given vortex breakdown location, flow disturbances that impinge on the wing surface are convected from a position further upstream than is the case for the static wing leading to an increased frequency of pressure fluctuations.

The work presented in this study has demonstrated the potential to investigate vortex breakdown and restoration using pressure measurements. The novel use of common vortex breakdown location to compare cases of different pitch rate magnitude has provided a number of important findings and trends in the data. These are not necessarily apparent when comparing cases using incidence as the common factor. It is suggested that flowfield similarity between pitching cases is an important criterion when carrying out comparative analyses of data and should be considered when carrying out analyses in the future. The high temporal resolution of the current data acquisition system provides the scope to extend the mean/instantaneous pressure, the RMS pressure and frequency spectra analyses to higher rate pitch up and pitch down cases and oscillatory cases. It is suggested that the understanding of the contribution of vorticity production rate, adverse pressure gradient and initial axial velocity to the arrival and upstream progression of vortex breakdown over the surface of the wing would be greatly enhanced by detailed flow-field surveys carried out at the same Reynolds numbers as the pressure measurement tests. Similarly, the quantitative measurement of flow helix angles for a range of static and dynamic cases using surface stress measurement

techniques, such as shear stress sensitive paint, would also provide further information regarding the vorticity production/transport balance. The provision of quantitative data ultimately may allow the calculation of an overall 'vortex breakdown location' parameter which will take into account the geometry of the wing, test conditions, vorticity generation, vorticity transport, wing motion and instantaneous incidence. It is suggested that the generation of this parameter will greatly enhance the understanding of vortex flows and will aid the analysis of new aircraft/wing designs well into the next millennium.

REFERENCES

AGRAWAL, S., BARNETT, R. M. & ROBINSON, B. A. 1992. Numerical investigation of vortex breakdown on a delta wing. *AIAA Journal* **30** (3): 584-591.

ANDERSON JR., J. D. 1997. A history of aerodynamics and its impact on flying machines. *Cambridge Aerospace Series 8*, Cambridge University Press, Cambridge, UK. ISBN 0-521-45435-2.

ASHLEY, H., KATZ, J., JARRAH, M.-A. M. & VANECK, T. 1991. Survey of research on unsteady aerodynamic loading of delta wings. *Journal of Fluids & Structures* : 363-390.

ATTA, R. & ROCKWELL, D. 1987. Hysteresis of vortex development and breakdown on an oscillating delta wing. *AIAA Journal.* **25** (11): 1512-1513.

ATTA, R. & ROCKWELL, D. 1990. Leading-edge vortices due to low Reynolds number flow past a pitching delta wing. *AIAA Journal* **28** (6): 995-1004.

BENJAMIN, T. B. 1962. Theory of the vortex breakdown phenomenon. *Journal of Fluid Mechanics* **14**: 593-629.

BOFFADOSSI, M. 1996. Calculation of vortex breakdown over a delta wing by a vortex-lattice method. *20th Congress of the International Council of the Aeronautical Sciences, Sorrento, Napoli, Italy. Paper No. ICAS-96-1.6.4.* ICAS/AIAA.

BOSSEL, H. H. 1969. Vortex breakdown flowfield. *Physics of Fluids* **12** (3): 498-508.

BROWN, G. L. & LOPEZ, J. M. 1990 Axisymmetric vortex breakdown, Part 2 - Physical mechanisms. *Journal of Fluid Mechanics* **221**: 553-576.

Continued...

CIPOLLA, K. M., LIAKOPOULOS, A. & ROCKWELL, D. 1998. Quantitative imaging in proper orthogonal decomposition of flow past a delta wing. *AIAA Journal* **36** (7): 1247-1254.

CIPOLLA, K. M. & ROCKWELL, D. 1995. Flow structure on a stalled delta wing subjected to small amplitude pitching oscillations. *AIAA Journal* **33** (7): 1256-1262.

CORNELIUS, K. C. 1995. Analysis of vortex bursting utilising three-dimensional Laser measurements. *Journal of Aircraft* **32** (2): 297-306.

DOLIGALSKI, T. L. 1994. Vortex interactions with walls. *Annual Review of Fluid Mechanics* **26**: 573-616.

ELLE, B. J. 1958. An investigation at low speed of the flow near the apex of thin delta wings with sharp leading edges. *Reports and Memoranda (R & M) No. 3176*, Aeronautical Research Council.

ELLE, B. J. 1960. On the breakdown at high incidences of the leading-edge vortices on delta wings. *Journal of the Royal Aeronautical Society* **64** (April): 491-493.

ER-EL, J., SETER, D. & WEIHS, D. 1989. Non-linear aerodynamics of a delta wing in combined pitch and roll. *Journal Of Aircraft* **26** (3): 254-259.

ERICKSON, G. E. 1982. Water-tunnel studies of leading-edge vortices. *Journal of Aircraft* **19** (6): 442-448.

ERICSSON, L. E. 1984. The fluids mechanics of slender wing rock. *Journal of Aircraft* **21** (5): 322-328.

ERICSSON, L. E. 1990. Various sources of slender wing rock. *Journal of Aircraft* **27** (6): 488-494.

Continued...

ESCUDIER, M. 1988. Vortex breakdown: Observations and explanations. *Progress in Aerospace Sciences* **25**: 189-229.

FALER, J. H. & LEIBOVICH, S. 1977. Disrupted states of vortex flow and vortex breakdown. *Physics of Fluids* **20** (9): 1385-1400.

FRIEMER M. 1996. Introduction to Eurofighter 2000. *IMechE Seminar Publication 1996-15; Eurofighter 2000 - Technology for the 21st Century, Paper S468/001/96.* Mechanical Engineering Publications Ltd., Bury St. Edmunds, Suffolk, UK. ISBN 1-86058-040-8.

GAD-EL-HAK, M. & BLACKWELDER, R. F. 1985. The discrete vortices from a delta wing. *AIAA Journal* **23** (6): 961-962.

GAD-EL-HAK, M. & BLACKWELDER, R. F. 1987. Control of the discrete vortices from a delta wing. *AIAA Journal* **25** (8): 1042-1049.

GAD-EL-HAK, M. & HO, C.-M. 1985. The pitching delta wing. *AIAA Journal* **23** (11): 1660-1665.

GARG, A. K., & LEIBOVICH, S. 1979. Spectral characteristics of vortex breakdown flowfields. *Physics of Fluids* **22**: 2053-2064.

GARTSHORE, I. S. 1962. Recent work in swirling incompressible flow. *National Research Council of Canada Report No. 6968* (formerly National Aeronautical Establishment Report No. LR-343).

GORDNIER, R. E. 1997. Numerical simulation of a 65 degree delta wing flowfield. *Journal of Aircraft* **34** (4): 492-499.

GRABOWSKI, W. J. B. & BERGER, S. A. 1976. Solutions of the Navier-Stokes equations for vortex breakdown. *Journal of Fluid Mechanics* **75** (3): 525-544.

Continued...

GREEN, R.B. 1998. A flow visualisation Study of a pitching delta wing. *Glasgow University Aero Report 9824*. University of Glasgow, UK.

GREENWELL, D. I. & WOOD, N. J. 1992. Determination of vortex burst location on delta wings from surface pressure measurements. *AIAA Journal* **30** (11) 2736-2739.

GUGLIERI, G. & QUAGLIOTTI, F. B. 1997. Experimental investigation of vortex dynamics on a 65 degree delta wing in sideslip. *The Aeronautical Journal* **101** (Mar): 111-120.

GURSUL, I. 1994. Unsteady flow phenomena over delta wings at high angle of attack. *AIAA Journal* **32** (2): 225-231.

GURSUL, I. 1995. Criteria for vortex breakdown location over delta wings. (Technical note). *The Aeronautical Journal* **99** (May): 194-196.

GURSUL, I. & YANG, H. 1995. Vortex breakdown over a pitching delta wing. *Journal of Fluids & Structures* **1995** (9): 571-583.

HALL, M. G. 1961. A theory for the core of a leading-edge vortex. *Journal of Fluid Mechanics* **11** : 209-228.

HALL, M. G. 1964. The structure of concentrated vortex cores. *Progress in Aeronautical sciences* **7**: 53-110.

HALL, M. G. 1972. Vortex breakdown. *Annual Review of Fluid Mechanics* **4**: 195-218.

HEMSCH, M. J. & LUCKRING J. M. 1990. Connection between leading-edge sweep, vortex lift and vortex strength for delta wings. (Engineering Note). *Journal of Aircraft* **27** (5): 473-475.

HERBST, W. B. 1983. Dynamics of air combat. *Journal of Aircraft* **20** (7): 594-598.

Continued...

HONKAN, A. & ANDREOPOULOUS, J. 1997. Instantaneous three-dimensional vorticity measurements in vortical flow over a delta wing. *AIAA Journal* **35** (10):1612-1620.

HUMMEL, D. & SRINIVASAN P. S. 1966. Vortex breakdown effects on the low speed aerodynamic characteristics of slender delta wings in symmetrical flow. *Journal of the Royal Aeronautical Society* **71** (April): 319-322.

JARRAH, M.-A. M. 1989. Low speed wind-tunnel investigation of flow about delta wings, oscillating in pitch to very high angle of attack. *AIAA 27th Aerospace Sciences Meeting, 9-12 January 1989, Reno, Nevada, USA. Paper No. 89-0295.* AIAA.

JARRAH, M.-A. M. 1990. Visualisation of the flow about a delta wing manoeuvring in pitch to very high angle of attack. *American Society of Mechanical Engineers Fluids Engineering Division (Publication) FED* **92** : 109-116.

JOBE, C. E., HSIA, A. H., JENKINS, J. E. & ADDINGTON G. A. 1996. Critical states and flow structure on a 65-deg delta wing. *Journal of Aircraft* **33** (2): 347-352.

JOBE, C. E. 1998. Vortex breakdown location over 65° delta wings empiricism and experiment. *AIAA 16th Applied Aerodynamics Conference, 15-18 June 1998, Albuquerque, New Mexico, USA. Paper No. 98-2526.* AIAA.

JOHARI, H. & MOREIRA J. 1998. Direct measurement of delta wing vortex circulation. *AIAA Journal* **36** (12): 2195-2203.

JONES, J. P. 1960. The breakdown of vortices in separated flow. *U.S.A.A. Report No. 140.*

Continued...

JUMPER, E. J., NELSON R. C. & CHEUNG, K. 1993. A simple criterion for vortex breakdown. *AIAA Paper No. 93-0866*. AIAA

JUPP, M. L., COTON, F. C. & GREEN, R. B. 1999. A statistical analysis of the surface pressure distribution on a delta wing. *The Aeronautical Journal* **103** (July): 349-358.

KOPECKY, R. M. & TORRANCE, K. E. 1973. Initiation and structure of axisymmetric eddies in a rotating stream. *Computers & Fluids* **1**: 289-300.

KUMAR, A. 1996. Accurate development of leading-edge vortex using an embedded conical grid. *AIAA Journal* **34** (10): 2038-2046.

LAMBOURNE, N. C. & BRYER, D. W. 1961. The bursting of leading-edge vortices - some observations & discussion of the phenomenon. *Aeronautical. Research. Council, Reports & Memoranda (R & M), No. 3282.*

LAMBOURNE, N. C., BRYER, D. W. & MAYBREY, J. F. M. 1969. The behaviour of the leading-edge vortices over a delta wing following a sudden change of incidence. *Reports & Memoranda (R & M) No. 3645*. Aeronautical Research Council.

LAPIN, L. L. 1993. Statistics for modern business decisions. 6th Ed. The Dryden Press, Orlando FL USA. ISBN 1-800-782-4479.

LAWFORD, J. A. & BEAUCHAMP, A. R. 1961. Low speed wind-tunnel measurements on a thin sharp-edged delta wing with 70° leading-edge sweep, with particular reference to the position of leading-edge vortex breakdown. *Reports & Memoranda (R & M) No. 3338*. Aeronautical Research Council.

LEE, M. & HO, C.-M. 1990. Lift force of delta wings. *Applied Mechanics Review* **43** (9): 209-221.

Continued...

LEIBOVICH, S. 1978. The structure of vortex breakdown. *Annual Revue of Fluid Mechanics* **10**: 221-246.

LEMAY, S. P., BATILL, S. M. & NELSON, R. C. 1990. Vortex dynamics on a pitching delta wing. *Journal of Aircraft* **27** (2): 131-138.

LESSEN, M., SINGH, P. J. & PAILLET F. 1974. The stability of a trailing line vortex, part 1 : Inviscid theory. *Journal of Fluid Mechanics* **63** (4): 753-763.

LEVIN, D. & KATZ, J. 1984. Dynamic load measurements with delta wings undergoing self-induced roll oscillations. *Journal of Aircraft* **21** (1) 30-36.

LIN, J.-C. & ROCKWELL, D. 1995. Transient structure of vortex breakdown on a delta wing. *AIAA Journal* **33** (1): 6-12.

LOWSON, M. V. 1963. The separated flows on slender wings in unsteady motion. *Reports & Memoranda (R & M) No. 3448*. Aeronautical Research Council.

LOWSON, M. V. 1964. Some experiments with vortex breakdown. *Journal of the Royal Aeronautical Society* **68** (May): 343-346.

LOWSON, M. V. 1991. Visualisation measurements of vortex flows. *Journal of Aircraft* **28** (5): 320-327.

LOWSON, M. V. AND A. J. RILEY 1995. Vortex breakdown control by delta wing geometry. *Journal of Aircraft* **32** (4): 832-838.

LUDWIEG, H. 1965. Erklarung des wirbellaufplatzens mit hilfe der stabilitatstheorie fur stromungenmit schraubenlinienformigen stromlinien. *Zeitschrift fur Flugwissenschaften* **13**: 437-442.

LYNN, P. A. 1982. The analysis and processing of signals. 2nd Ed. The MacMillan Press Ltd., London, UK. ISBN 0-333-34030-2.

Continued...

MABEY, D. G. 1996. Unsteady vortex flow phenomena on delta wings at high angles of incidence. *20th Congress of the International Council of the Aeronautical Sciences, 13-18 September 1996, Sorrento, Italy. Paper No. ICAS-96-1.6.1.* ICAS/AIAA.

MAGER, A. 1972. Dissipation & breakdown of a wing-tip vortex. *Journal of Fluid Mechanics* **55** (4): 609-628.

MAGNESS, C., ROBINSON, O. & ROCKWELL, D. 1992. Unsteady cross-flow on a delta wing using Particle Image Velocimetry. *Journal of Aircraft* **29** (4): 707-709.

MALTBY, R. L., ENGLER, P. B. & KEATING, R. F. A. 1963. Some exploratory measurements of leading-edge vortex positions on a delta wing oscillating in heave. *Reports & Memoranda (R & M) No. 3410.* Aeronautical Research Council.

MCKERNAN, J. F., PAYNE, F. M. & NELSON R.C. 1988. Vortex breakdown measurements on a 70 deg sweepback delta wing. *Journal of Aircraft* **25** (11): 991-992.

MIAU, J. J., CHANG, R. C., CHOU, J. H. & LIN, C. K. 1992. Non-uniform motion of leading-edge vortex breakdown on ramp-pitching delta wings. *AIAA Journal* **30**. (7): 1691-1702.

MODIANO, D. L. & MURMAN, E. M. 1994. Adaptive computations of flow around a delta wing with vortex breakdown. (Technical note). *AIAA Journal* **32** (7): 1545-1547.

NELSON, R. C. & VISSER, K. D. 1990. Breaking down the delta wing vortex - the role of vorticity in the breakdown process. *AGARD CP494.*

PARKER, A. G. 1977. Measurements on a delta wing in unsteady flow. *Journal of Aircraft* **14** (6): 547-552.

Continued...

PAYNE, F. M., NG, T. T., NELSON, R. C. & SCHIFF, L. B. 1986. Visualisation and flow surveys of the leading-edge vortex structure on delta wing planforms. *AIAA 24th Aerospace Sciences Meeting, 6-9 January 1986, Reno Nevada, USA. Paper No. 86-0330.* AIAA.

PAYNE, F. M., NG, T. T., NELSON, R. C. & SCHIFF, L. B. 1988. Visualisation and wake surveys of vortical flow over a delta wing. *AIAA Journal* **26** (2): 137-143.

PAYNE, F. M., NG, T. T. & NELSON, R. C. 1987. Experimental study of the velocity field on a delta wing. *AIAA Paper No. 87-1231.* AIAA

PECKHAM, D. H. 1958. Low speed wind tunnel tests on a series of uncambered slender pointed wings with sharp edges. *Reports and Memoranda (R & M) No. 3186.* Aeronautical Research Council.

PECKHAM, D. H. & ATKINSON S. A. 1957. Preliminary results of low speed wind tunnel tests on a gothic wing of AR = 1.0. *Current Papers (CP) No. 508.* Aeronautical Research Council.

POLHAMUS, E. C. 1971. Predictions of vortex-lift characteristics by a leading-edge suction analogy. *Journal of Aircraft* **8** (4): 193-199.

REDINIOTIS, O. K., STAPOUNTZIS, H. & TELIONIS, D. P. 1990. Vortex shedding over delta wings. *AIAA Journal* **28** (5): 944-946.

REYNOLDS, W. C. & CARR, L. W. 1985. Review of unsteady, driven separated flows. *AIAA Paper No. 85-0527.* AIAA

SARPKAYA, T. 1974. Effect of the adverse pressure gradient on vortex breakdown. *AIAA Journal* **12** (5): 602-607.

SPALL, R. E., GATSKI, T. B. & GROTSCH, C. E. 1987. A criterion for vortex breakdown. *Physics of Fluids* **30** (11): 3434-3440.

Continued...

SQUIRE, H. B. 1960. Analysis of the vortex breakdown phenomenon. *Imperial College of Science & Technology Report No. 102.* London.

THOMAS, J. L., KRIST, S. L. & ANDERSON, W. K. 1990. Navier-Stokes computations of vortical flows over low aspect ratio wings. *AIAA Journal* **28** (2): 205-212.

THOMPSON, S. A., BATILL, S. M. & NELSON, R. C. 1990. Delta wing surface pressures for high angle of attack manoeuvres. *Atmospheric Flight Mechanics Conference, 20-22 August 1990, Portland, Oregon, USA. Paper No. 90-2813.* AIAA.

THOMPSON, S. A., BATILL, S. M. & NELSON, R. C. 1991. Separated flow-field on a slender wing undergoing transient pitching motions. *AIAA Journal* **28** (8): 489-495.

THOMPSON, S. A. & NELSON, R. C. 1992. Wind tunnel blockage effects on slender wings undergoing large amplitude motions. *AIAA 17th Aerospace Ground Testing Conference, 6-8 July 1992, Nashville, Tennessee, USA. Paper No. 92-3926.* AIAA.

TRAUB, L. W. 1996. Simple prediction method for the location of vortex breakdown on delta wings. *Journal of Aircraft* **33** (2): 452-454.

VAUGHAN, J. P. & WOOD, N. J. 1995. Pressure measurements on a half delta wing oscillating in pitch. *Aeronautical Journal* **99** (990): 432-438.

VISBAL, M. R. 1994. Onset of vortex breakdown above a pitching delta wing. *AIAA Journal* **32** (8): 1568-1575.

VISSER, K. D. & NELSON, R. C. 1993. Measurements of circulation & vorticity in the leading edge vortex of a delta wing. *AIAA Journal* **31** (1): 104-111.

Continued...

WEINBERG, Z. 1992. Effect of tunnel walls on vortex breakdown location over delta wings. *AIAA Journal* **30** (6): 1584-1586.

WOLFFELT, K. W. 1986. Investigation on the movement of vortex burst position with dynamically changing AoA for a schematic delta wing in a water tunnel with correlation to similar studies in a wind-tunnel. *AGARD Conference Proceedings Publication (CPP) No. 413.* AGARD.

WOODS, M. I. 1999. An investigation of buffet over low-observable planforms. *PhD thesis, University of Bath.* Bath, UK.

WOODS, M. I. & WOOD, N. J. 1996. Unsteady aerodynamic phenomena on novel wing planforms. *20th Congress of the International Council of the Aeronautical Sciences, 13-18 September 1996, Sorrento, Italy. Paper No. ICAS-96-2.11.2.* ICAS/AIAA.

APPENDIX A

RIB Location	Static	Oscillatory	Ramp Up	Ramp Down
0	Run Number			
1	Date Of Test : Day			
2	Date Of Test : Month			
3	Date Of Test : Year			
4	Ambient Temperature (° C)			
5	Barometric Pressure (mm Hg)			
6	Motion Type (0)	Motion Type (1)	Motion Type (2)	Motion Type (3)
7	Starting Incidence (°)	Mean Incidence (°)	Starting Incidence (°)	
8	Arc (°)	Amplitude (°)	Ramp Arc (°)	
9	Empty	Oscillation Frequency (Hz)	Linear Pitch Rate (° s^{-1})	
10	Number Of Samples In One Block			
11	Number Of Total Samples			
12	Number Of Data Blocks (Cycles)			
13	Sampling Frequency (Hz)			
14	Dynamic Pressure (PSI)			
15	Reynolds Number			
16	Mach Number			
17	Empty	Reduced Frequency	Reduced Pitch Rate	
18	Incoming Velocity (ms^{-1})			
19	Dynamic Pressure (Nm^{-2})			
20	Model Number			
21	File ID			

Table A.1 - Layout Of Run Information Block